YEAR-END TECHNICAL REPORT (REVISION 1)

September 29, 2020 to September 28, 2021

Environmental Remediation Science and Technology

Date submitted:

December 3, 2021

Updated:

June 12, 2025

Principal Investigator:

Leonel E. Lagos, Ph.D., PMP®

Florida International University Collaborators:

Yelena Katsenovich, Ph.D.
Ravi Gudavalli, Ph.D.
John Dickson, Ph.D.
Shambhu Kandel, Ph.D.
Muhammad Alam, Ph.D.
Pieter Hazenberg, Ph.D.
Angelique Lawrence, M.S., GISP
Yan Zhou, Ph.D.
Hamid Bazgirkhoob, Ph.D.
Vadym Drozd, Ph.D.
DOE Fellows

Submitted to:

U.S. Department of Energy
Office of Environmental Management
Under Cooperative Agreement # DE-EM0005213

FIU | Applied Research Center
FLORIDA INTERNATIONAL UNIVERSITY

Addendum:

This document represents one (1) of five (5) reports that comprise the Year End Reports for the period of September 29, 2020 to September 28, 2021 prepared by the Applied Research Center at Florida International University for the U.S. Department of Energy Office of Environmental Management (DOE-EM) under Cooperative Agreement No. DE-EM0005213.

The complete set of FIU's Year End Reports for this reporting period includes the following documents:

Project 1: Chemical Process Alternatives for Radioactive Waste
Document number: FIU-ARC-2020-800012997-04b-009

Project 2: Environmental Remediation Science and Technology
Document number: FIU-ARC-2020-800013918-04b-004

Project 3: Waste and D&D Engineering and Technology Development
Document number: FIU-ARC-2020-800013919-04b-008

Project 4: DOE-FIU Science & Technology Workforce Development Initiative
Document number: FIU-ARC-2020-800013920-04b-017

Project 5: Long-Term Stewardship of Environmental Remedies: Contaminated Soils and Water and STEM Workforce Development
Document number: FIU-ARC-2020-800013922-04b-007

Each document will be submitted to OSTI separately under the respective project title and document number as shown above. In addition, the documents are available at the DOE Research website for the Cooperative Agreement between the U.S. Department of Energy Office of Environmental Management and the Applied Research Center at Florida International University: https://doeresearch.fiu.edu

NOTE: This report was updated on June 12, 2025 to include the DOI link for a published manuscript based on research conducted for Subtask 1.1. The link can be found under the "Major Technical Accomplishments" section on page 5 and also on page 14 under the section titled "Subtask 1.1: Conclusions".

TABLE OF CONTENTS

LIST OF FIGURES

LIST OF TABLES

PROJECT 2 EXECUTIVE SUMMARY

This project targets research to support environmental remediation and long-term monitoring of contaminated sediment, surface water and groundwater at Hanford Site, Savannah River Site, Oak Ridge Reservation and the Waste Isolation Pilot Plant (WIPP). The aim is to reduce the potential for contaminant mobility or toxicity in the surface and subsurface through the development and application of state-of-the-art environmental remediation technologies at DOE sites. In FIU Year 1, FIU ARC provided research and technical support on contaminant remediation efforts at the Hanford Site under Task 1, at SRS under Tasks 2 and 3, at the WIPP under Tasks 5 & 6, and at the ORR under Task 7. The research involved laboratory-scale studies which utilized novel analytical methods and microscopy techniques for characterization of various mineral samples. Tasks also included the implementation of hydrological models, which help to predict the behavior and fate of existing and potential contaminants in the surface and subsurface. Photogrammetry techniques were also applied for development of high-resolution digital elevation models (DEMs) to support hydrological model development.

DOE Fellows supporting this project include:

PhD students: Silvina Di Pietro (graduated with Ph.D. degree in Chemistry in Spring 2021), Juan Morales (graduate, Ph.D., Envirnomental Health Sciences), Mariah Doughman (graduate, Ph.D., Chemistry), Phuong Pham (graduate, Ph.D., Chemistry);

M.S. students: Alexis Vento (graduated with M.S. degree in Environmental Engineering in Summer 2021, Amanda Yancoskie (graduated with M.S. degree in Environmental Engineering in Fall 2021), Jonathan Williams (graduated with M.S. degree in Biomedical Engineering in Spring 2021), Gisselle Gutierrez (graduate, M.S. Environmental Engineering)

Undergraduate students: Katherine De La Rosa (graduated with B.S. degree in Environmental Engineering in Spring 2021), Nathalie Tuya (graduated with B.S. degree in Environmental Engineering in Spring 2021), Angel Almaguer (undergraduate, Chemistry), Caridad Estrada (undergraduate, Environmental Engineering), Aubrey Litzinger (undergraduate, Environmental Engineering), and Stevens Charles (undergraduate, Civil Engineering).

Task 1: Remediation Research and Technical Support for the Hanford Site

DOE EM has a critical need to understand the biogeochemical processes influencing the behavior of contaminants [uranium (U), iodine (I), technetium (Tc), chromium (Cr) and nitrate (NO_3^-)] in Hanford Site's deep vadose zone that can impact groundwater quality. These contaminants were accidentally released during production of atomic weapons at the Hanford Site from 1944 through the late 1980s, which has left a legacy of radionuclide contamination in soil and groundwater that poses technically complex environmental cleanup challenges that are unique to EM. The radioactive waste at Hanford Site contains about 195 million curies of radioactivity and 220,000 metric tons of chemicals. Of the 177 tanks onsite, sixty-seven have leaked about 3,800 cubic meters (1 million gallons) of liquids into the underlying sediment (Gephart, 2003). Most of this residual waste is in or near the 200 Area. These releases have created plumes that threaten groundwater quality due to potential downward migration through the unsaturated vadose zone (VZ) sediment. The fastest-moving contaminants in the subsurface are technetium-99, iodine-129, chromium, uranium and nitrate (Gephart, 2003).

This end of year report presents an overview of subtasks supporting the cleanup mission at the Hanford Site that can complement ongoing work at PNNL for a better understanding of the long-term behavior of contaminants in the subsurface.

Task 2. Remediation Research and Technical Support for Savannah River Site

Iodine-129 and uranium are the major risk drivers from radiological acid waste contaminants released at the Savannah River Site's F-Area. Radionuclides previously disposed of through unlined seepage basins as a constituent of acidic, aqueous waste are moving towards Fourmile Branch and Tims Branch wetlands with natural groundwater flow, where they may subsequently be interacting with natural organic materials present in the wetland or with humic materials injected for remediation purposes.

There is a need for the Savannah River Site to gather results to supplement permit requirements associated with the Area Completion Project (ACP), including the Phase 2 strategy to evaluate the performance of Phase 1 including "…downgradient of the F-Area inactive process sewer line and at Fourmile Branch". Per permitting requirements delineated in the corrective action plan, ^{129}I concentrations must be below groundwater standards in Fourmile Branch by October 31, 2025, and in the F-Area plume in surface water at the seepline by October 31, 2030. Because the DOE has no approved technology for remediation of subsurface iodine, it is essential to understand its long-term fate in plumes at the Savannah River Site. In addition, DOE-EM requires additional study of the fate of co-mingled contaminant plumes due to their complexity (McCabe, D., *et al.*, 2017). The experiments delineated in this subtask will contribute to both our understanding of the interactions of ^{129}I with organic materials and study the factors controlling the attenuation of ^{129}I in wetlands, as well as the potential for remediation of U via injection of modified humic materials, providing essential data for fulfillment of the abovementioned permitting requirements and goals for DOE-EM.

Savannah River Site (SRS) is also conducting synergistic research, funded by the Department of Energy's Environmental Management Office of Soil and Groundwater Remediation (EM-12), as part of the Attenuation-Based Remedies for the Subsurface Applied Field Research Initiative (ABRS AFRI). This applied research is geared towards developing science-based approaches to clean and close sites contaminated with combinations of metals, radionuclides, and other contaminants of concern. A primary objective of this program is to develop approaches for attenuation-based remedies, in this case, to investigate and validate the use of humate for subsurface stabilization of metals in contaminated groundwater plumes. SRS successfully conducted a field campaign that demonstrated the viability of dissolving and then injecting low cost agricultural humate into the subsurface and proposed that it may be a viable attenuation-based remedy for uranium and potentially for I-129 as well. Humic acid, which carries many functional groups, plays an important role in ion exchange and as a metal complexing ligand with a high complexation capacity, being able to affect the mobility of radionuclides in natural systems.

The fate and transport of uranium and iodine in the subsurface are controlled by various environmental factors such as pH, temperature, ORP, etc. A better understanding of the environmental conditions that affect these processes is critical to a more realistic risk assessment. During FIU Performance Year 1, FIU conducted research to investigate the factors controlling the attenuation of iodine in wetlands and continued ongoing research to investigate the impact of humic acid on U mobility at the Savannah River Site. Different types of humic substances such as KW-15 and KW-30 were used in this research to study their effect on uranium removal.

Task 3: Contaminant Fate and Transport Modeling for the Savannah River Site

This task involves the development and application of integrated hydrology and contaminant transport models for studying the fate of priority pollutants with emphasis on interactions between solute and sediment transport in the stream systems at SRS. The aim is to examine the response of these streams to historical discharges and environmental management remediation actions and to provide a means of assessment, evaluation and post-closure long-term monitoring of water quality and environmental conditions following remedial activities. In general, hydrological models are the standard tools used for investigating surface/subsurface flow behavior. They provide uncertainty quantification, risk and decision support for water resource management, and evaluation of water quality, erosion, deposition, and transport. The models being developed will serve as long-term monitoring tools that provide simulation capabilities to economically assess the fate and transport of heavy metals and radionuclides of concern (e.g., nickel, uranium, ^{137}Cs, I-129), that may have direct or indirect impact on the SRS environment. The outcome of such models can potentially determine spatial and temporal distribution of suspended particles or contaminants in the area when heavy rainfall or storms occur. This will assist DOE-EM in ensuring the achievement and maintenance of regulatory compliance goals for water quality in these SRS watersheds.

Task 5: Research and Technical Support for WIPP

The Waste Isolation Pilot Plant (WIPP) is a deep geologic repository used for permanent disposition of transuranic waste (TRU). It is characterized by high ionic-strength porewaters (up to 7.4 M). Every 5 years the WIPP is required to be recertified to demonstrate the safety underpinnings for the long-term stability of the stored TRU waste. Thus, a better understanding of the fate and transport of actinide in a high ionic-strength brine environment laden with metal chelating ligands is critical to developing accurate risk assessment models that address the low-probability scenario of potential brine inundation and contaminant release due to human intrusions. In a current Performance Assessment Inventory Report (Van Soest, 2018), ethylenediaminetetraacetic acid (EDTA), which forms strong, stable complexes with the lanthanides and actinides, was reported to be in high concentration in the WIPP waste (7.9×10^{-5} M), making it the largest concern for impact on contaminant mobility (Dunagan et al., 2007; Brush, 1990). Additional ligands of interest include degradation products such as gluconate, a cement additive, which has been identified in the hyperalkaline conditions expected in cementitious repositories (Gaona et al., 2008). Current Performance Assessment (PA) models do not include gluconate andiron oxide (corrosion product of steel containers) due to the expected low impact in WIPP-relevant conditions. However, additional experiments supporting the safety underpinning employed in the models will provide a better understanding of potential impacts from these ligands. In this study, FIU ARC is collaborating with Dr. Donald Reed, team lead of the Actinide Chemistry and Repository Science (ACRSP) group in Los Alamos National Laboratory's field office located at the Carlsbad Environmental Monitoring and Research Center (CEMRC) in Carlsbad, New Mexico. The main goal of this study is to generate accurate sorption data for interaction of actinides with minerals under conditions relevant to the WIPP as previous risk assessment models are characterized by high uncertainty.

Task 6: Hydrology Modeling for WIPP

Task 6 was developed to support research and development activities at the WIPP by scientists and researchers who are concerned about the impact of climate on the long-term vulnerability of this karst region and thus the eventual integrity and performance of this deep geologic transuranic waste repository due to the influence of characteristic surface features, such as sinkholes, swallets, and karst valleys on groundwater recharge over time. The task involves the development of a high-resolution digital elevation model (DEM) of Basin 6 of the Nash Draw, just west of the WIPP, to more accurately delineate surface hydrological features, and use of this DEM for development of regional hydrological models using the DOE-developed Advanced Simulation Capability for Environmental Remediation (ASCEM) modeling toolset. A high-resolution DEM will improve the ability of the coupled surface/subsurface flow models to simulate the hydrologic response to a range of storm events, compute the surface water balance and provide more accurate estimates of regional-scale infiltration rates/groundwater recharge. With improved estimates of the spatial and temporal patterns of recharge to force the groundwater model, predictions of halite dissolution and propagation of the shallow dissolution front will be made possible and the potential impact on repository performance quantified.

Task 7: Engineered Multi-Layer Amendment Technology for Hg Remediation on Oak Ridge Reservation

This task involves the development of a sorbent-based technology for cost-effective remediation of mercury on the Oak Ridge Reservation (ORR). The persistent geochemistry of mercury renders cleanup efforts costly and challenging across a vast number of mercury-contaminated sites globally. The existence of diffuse mercury sources further complicates technology development efforts for mercury remediation in freshwater stream systems, such as the East fork Poplar Creek (EFPC), Oak Ridge, Tennessee. As a case study, the EFPC ecosystem received large point-source discharges during the 1950s. Although upstream mercury discharges to EFPC have declined, mercury releases still persist from point sources within the industrial facility where mercury was used and from diffuse downstream sources, such as contaminated bank soils. Recent results suggest that releases from diffuse and historical downstream sources, such as bank soils and sediment, may be major drivers of mercury contamination in the stream system. Despite ubiquitous use of amendments for in-situ sequestration of organic contaminants, large-scale application of mercury sorbents is uncommon due to decreasing effectiveness in the presence of dissolved organic matter (DOM), cost and fouling problems that can potentially leach constituents and particles into waterbodies. Thus, the need to develop a sustainable, cost-effective solutions for mercury cleanup in EFPC is the main goal of this research. This multi-year, collaborative efforts will benefit DOE Office of Environmental Management (EM) in addressing its priority mission of reducing mercury flux to EFPC, resulting in an improved water quality and ecological health of EFPC.

MAJOR TECHNICAL ACCOMPLISHMENTS

Task 1: Remediation Research and Technical Support for the Hanford Site

- FIU completed Subtask 1.1 on ammonia gas injection and summarized results on the solid phase characterization and transformation of illite mineral with gas-phase ammonia treatment. This research demonstrated that NH_3 gas treatment has a potential for contaminant sequestration through mineral alterations. A manuscript based on this research was accepted for publication in the *Journal of Hazardous Material https://doi.org/10.1016/j.jhazmat.2021.127657*
- Completed modeling speciation for predicting solid phases upon application of ammonia gas injection technology using Geochemist's Workbench.
- Studied technetium (Tc-99) reoxidation comingled with uranium and nitrate following reduction in the presence of strong reductants, 0.1% of Hepure ZVI and 0.1% of sulfur modified iron. The study helped to determine reoxidation behavior of pertechnetate collocated with uranyl and nitrate after sediment samples prepared with the synthetic perched and groundwater solutions were exposed to the aerobic conditions. FIU also initiated SEM-EDS and XRD analyses.
- Determined that the co-location of I-127 and Cr(VI) had a minor impact on the Hanford sediment's capacity for adsorption. Specifically, the maximum adsorption decreased by 1 and 3 orders of magnitude for I-127 and Cr(VI) respectfully. I-127 adsorption followed the pseudo-second order kinetic model and Cr(VI) followed the pseudo-first order kinetic model. Uranium (VI) adsorption to Hanford formation sediment under site relevant conditions is minimal. This is due to the slightly alkaline pH and the presence of calcium and carbonate causing the formation of $Ca_2UO_2(CO_3)_3^0(aq)$ and $CaUO_2(CO_3)_3^{2-}$. These species make it difficult for U(VI) to sorb to minerals present in the sediment. Overall, this indicates that U(VI), I-127 and Cr(VI) present in the vadose zone at the Hanford Site are relatively mobile.
- Completed the glass dissolution experiments via a single-pass flow-through (SPFT) experiment using grout and silicon-amended solutions prepared in pH 12 adjusted buffer at 25°C, 40°C, 70°C. These experiments were conducted in support of the Hanford Lysimeter Test Facility (FLTF). The SPFT and static PCT tests determined that the dissolution rate of the glass waste forms was significantly reduced in the present of grout-contacted solution. The laboratory experiments showed that the addition of Si to the pH buffer slowed the dissolution rate only slightly, meaning that other dissolved species in the grout contacted solution play a controlling role in the decrease of glass dissolution.
- Presented one professional poster, one oral presentation and two graduate student posters at the 2021 Waste Management Symposia (WM2021). The team prepared and submitted pre-recorded videos for each of the poster and oral presentations as the conference was held virtually. A poster based on this research was also presented at the ACS Fall 2021 meeting held virtually in Atlanta, GA.

Task 2. Remediation Research and Technical Support for Savannah River Site

- Completed the characterization of Huma-K and modified humic acid KW-15 using dynamic light scattering (DLS), Brunauer-Emmett-Teller (BET), scanning electron microscopy coupled with energy dispersive X-ray spectroscopy (SEM-EDS), and potentiometric titration.
- Completed the characterization of organoclays, MRM and PM-199, for Subtask 2.1 via Fourier transform infrared (FTIR) spectroscopy, scanning electron microscopy coupled with energy dispersive X-ray spectroscopy (SEM-EDS) and the BET analysis. This data will help explain the results of iodine species (iodide and iodate) adsorption by the organoclays. The FTIR analyses indicate a similarity between organoclays PM-199 and MRM as they are quaternary amine-modified bentonite clays, which have common functional group moieties within their structures. The BET surface areas of PM-199 and MRM materials are similar to each other, 0.5278 m^2/g and 0.5193 m^2/g, respectively. The SEM-EDS spectra show that the two materials have common major and trace elements within their structures, however, MRM has ~ 1% of normalized mass of sulfur in it as expected since MRM has been modified with sulfur containing compound(s). Based on the characterization results, these materials have shown a potential for iodine adsorption primarily via electrostatic interactions with the quaternary amine groups intercalated between the clay layers. Moreover, the MRM with sulfur moiety in its structure can potentially reduce iodate to iodide, which can then be adsorbed easily by the clay particles.
- Characterized SRS wetland sediment via Fourier transform infrared spectroscopy (FTIR) and scanning electron microscopy coupled with energy dispersive X-ray spectroscopy (SEM-EDS). These sediment characterization results provide information on the elemental and mineralogical compositions that could potentially impact the speciation and interaction of iodine in the wetland sediment.
- Presented one professional poster and two student posters (one graduate and one undergraduate) at 2021 Waste Management Symposia (WM2021). As the conference was held virtually, the team prepared and submitted pre-recorded videos for each of the poster and oral presentations.
- Abstract submitted to ACS Fall 2021 meeting and was selected for the Sci-Mix session. This is a large poster session and mixer held at each ACS national meeting. The poster session consists of abstracts selected by division program chairs and represents the most exceptional abstracts submitted to participating divisions.

Task 3: Contaminant Fate and Transport Modeling for the Savannah River Site

- FIU completed the sensitivity analysis for calibration of the Tims Branch (TB) MIKE 11 ECO Lab module for the uranium (U) transport process, which determines the controlling variables and optimum values for parameters affecting U geochemical processes in the Tims Branch stream system. Additionally, FIU conducted scenario testing to simulate and forecast uranium transport associated with contaminated sediments for different storm events.
- FIU conducted an in-depth review of available contaminant data for tin and nickel focusing on the acquisition of data related to tin and nickel concentration and determination of significant parameters that influence their mobility in the environment under extreme

meteorological conditions. The data was used to perform theoretic mass balance calculations and will be used to assign the boundary and initial conditions for contaminant transport models of tin and nickel in Tims Branch, which will be based on the existing model framework developed for modeling the uranium transport process.

- A DOE Fellow travelled to SRS to perform routine maintenance and calibration of the remote monitoring devices (HOBO units) deployed in Tims Branch. These sensors record water level timeseries data required for hydrological model calibration and validation in order to increase confidence in the ability of the model being developed to estimate flow depth and velocity. The Fellow also integrated a turbidity sensor into the HOBO unit located at the Tims Branch catchment outlet to aquire additional data to improve the calibration of the sediment transport component and subsequently the performance of the Tims Branch model developed by FIU.
- The Fourmile Branch watershed modeling boundary was determined and justified using surface water and groundwater flow patterns. A clipping model was then developed based on this study domain using ArcGIS ModelBuilder and applied to several GIS data layers that were acquired during the preliminary data collection process for mapping and visualization of the FMB study area. Several thematic maps were subsequently generated to support the development of a conceptual model of the Fourmile Branch watershed. A Flood Frequency Analysis (FFA) was also conducted using historical discharge data from 1976-2002 from a USGS stream gauge in the downstream portion of Fourmile Branch to calculate average recurrence intervals (ARIs), which describe the probability that a certain precipitation event will occur. Two FFA methods were used for comparison that resulted in maximum estimated ARIs of 48 years using the Gumbel Distribution in MS Excel and 45 years using the FLIKE statistical software for a storm event that occurred in 1980.

Task 5: Research and Technical Support for WIPP

- Completed batch sorption studies investiging the impact of gluconate and ionic strength on the sorption of Nd(III), Th(IV), and U(VI) to iron oxides. An actinide concentration representative of understauration (10 μg/L), a range of ionic strength systems (0.1, 1.0, 5.0 M) and salt solutions (NaCl, $CaCl_2$, $MgCl_2$) were utilized in these experiments. Study results showed that the addition of gluconate to magnetite-amended brines did not enhance the solubility of U, Th, Nd as there were no discernable differences in aqueous concentration of U, Th, Nd among evaluated batch samples, suggesting insignificant formation of tertiary gluconate complex with contaminants.
- Submitted one full length paper to 2021 Waste Management Symposia (WM 2021), which was presented virtually as a poster presentation in the professional track and was published in the conference proceedings. A student poster was also presented based on this research at WM 2021. Another poster was presented virtually at the International Symposium on Solubility Phenomena and Related Equilibrium Processes (ISSP-19).
- DOE Fellow Alexis Vento successfully defended his Master's thesis in July, 2021 and will graduate with a Master's degree (MS) in Environmental Engineering in the Fall of 2021. His Master's thesis was wholly based on this research work.

Task 6: Hydrology Modeling for WIPP

- FIU completed the workflow to evaluate various vegetation removal methods to generate the best bare-ground digital elevation model to be used in the regional hydrology model development. A draft document was then created which outlines the entire photogrammetry process workflow, which included field data collection, image processing and point cloud generation, DSM development and finally, an evaluation of various RGB-based vegetation removal methods to generate the best bare ground high-resolution DEM.
- An FIU research team traveled to Carlsbad, NM (Aug. 2021) to collect the imagery dataset for Basin 6 study area (~ 24 km^2) and was successful in capturing ~ 22 km^2. The site will be revisited in December 2021 to complete the survey. The final data set will be processed as per the established photogrammetry work flow.
- Training of the hydrological modeling team on the ATS model by LANL scientists was initiated in the form of a DOE Fellow summer internship and began with an introduction to the open-source software and tools required for developing the input files for the ATS model.

Task 7. Engineered Multi-Layer Amendment Technology for Hg Remediation on Oak Ridge Reservation

- Completed kinetic studies and determined pertinent kinetic parameters for eight sorbent media. Model-calculated kinetic parameters indicate the nonlinear pseudo-second-order model as the best predictor of kinetic parameters for mercury sorption onto the evaluated sorbents. Kinetic data suggest that liquid film diffusion was the rate-limiting step governing mercury sorption. Higher sorbent dosages resulted in faster kinetics of mercury sorption. Based on kinetic data, the sorbent media were ranked in decreasing order as follows: PAC > Sorbster > FeS+PAC > Si-thiol ≅ RemBind > Biochar > Filtrasorb 300 > Organoclay PM 199. These evaluated sorbents hold promise for cost-effective remediation of mercury in contaminated environments.
- Submitted an abstract titled *"Sorbent-Based Technology for Mercury Remediation in a Freshwater Aquatic System"* to the American Geophysical Union (AGU) Fall 2021 meeting based on this research.

TASK 1: REMEDIATION RESEARCH AND TECHNICAL SUPPORT FOR THE HANFORD SITE

Subtask 1.1: Remediation Research of Ammonia Gas for Uranium Treatment

Subtask 1.1: Introduction

FIU evaluated uranium (U) sorption and partitioning in SGW of phyllosilicate minerals and Hanford Site sediments using traditional batch experiments to assess the association of mobile and immobile U species to the solid phase. The goal of this study was to determine whether the application of the reactive gas, ammonia (NH_3), could be effective for sequestration of U in vadose zone conditions such as those at the Hanford Site in Washington State, U.S. Results of this investigation demonstrate U removal upon calcite formation and secondary coatings, such as Fe-oxides and aluminosilicates, upon NH_3 leaving the system. In addition, extensive solid phase characterization techniques were employed to understand the mineral transformations and U behavior upon the reactive gas remedy. For example, absorption spectroscopy X-ray absorption near edge structure (XANES) analysis showed a significant fraction of U (26±11%) in the reduced U form for the phyllosilicate illite mineral investigated during the short-term contact time batch experiment. The goal of FIU Year 1 was geochemical speciation modeling that provided a way to predict U species and secondary mineral phases upon treatment. Overall, this promising technology may be capable of immobilizing U in solid phases as these secondary phases may remove the contaminant via adsorption, precipitation, and co-precipitation processes and may coat uranium phases with low solubility minerals as the pH returns to Hanford Site's natural conditions.

Subtask 1.1: Objectives

The objective of Year 1 research was to identify the major physicochemical changes of aluminosilicate minerals, illite and montmorillonite, following NH_3 gas and subsequent aeration treatments. This report presents Geochemist's Work Bench (GWB) modeling results that predict the formation of solid phases upon ammonia gas technology.

Subtask 1.1: Methodology

Speciation modeling to predict the formation of uranium solid phases likely to be present in this system was conducted using the Geochemist's Workbench® (GWB) version 12.0 with the Visual *MINTEQ* database (thermo-minteq) formatted by Jon Petter Gustafsson (KTH Royal Institute of Technology). The database was previously updated manually with the most recently published thermodynamic equilibrium constants for aqueous complexation reactions for relevant uranyl species. The equilibrium constants for ternary complexes of uranyl carbonate, $Ca_2UO_2(CO_3)_{3(aq)}$ and $CaUO_2(CO_3)_3^{2-}$, and polynuclear U(VI) hydroxide-carbonate complexes were updated based on the recommendations from OECD's NEA TDB (Emerson et al., 2017; Katsenovich et al., 2018). Concentrations of Al, U, and Si were kept constant in all modeling simulations at 0.185 mM, 0.02 mM, and 1.50 mM, respectively. Dissolved oxygen was set at 8.4 mg/L at a constant temperature of 25 °C based on saturation with air. The simulations were repeated by sliding pH from 8 to 12, imitating the pH values reached after the injection of 5% of NH_3 [5% NH_3/95% N_2; 3.1 mol/L of $NH_{3(aq)}$)]. The modeling of the treated solid samples with NH_3 gas was assumed to be closed from the atmosphere, applicable to the core of the gas injection in the field in the short term.

Subtask 1.1: Results and Discussion

Geochemist's Workbench® (GWB) thermodynamic equilibrium modeling was used to calculate mineral saturation indices and to identify U-solid phases potentially in equilibrium with the SGW compositions and NH_3 gas application, simulating Hanford Site conditions. These modeling results do not predict adsorption, incorporation, or coating processes but can be used to identify important mineral phases with and without U that are predicted to form based on the solution phase species measured in these experiments. The saturation index (SI or Ω) is used to quantify the distance a system is from equilibrium (Schott et al., 2009). Defined by Eq. 1, Q stands for the activity product and K_{sp} is the mineral solubility product at equilibrium at the temperature of interest.

$$\Omega = \log (Q/K_{sp}) \quad \text{Eq. 1}$$

Ω is dimensionless and, as in standard thermodynamics, a value of 1 represents equilibrium. With a quotient less than 1, reactants are undersaturated with respect to the solution composition and the reaction will tend to go towards the product side. When Ω is greater than 1, the reactants are supersaturated, and the reaction will tend towards the reactants or solid phase precipitates in this discussion (Cantrell et al., 2011; Schott et al., 2009). The GWB speciation modeling predicted that the SGW solution was saturated (i.e., $\Omega > 1$) with respect to five major minerals at pH ~10.8 as shown by Figure 1. Table 1 lists the relevant U-bearing mineral phases and their structural formulae predicted by the GWB software. Consistent with literature, the speciation modeling identified the formation of Na-boltwoodite and uranophane, the most common uranyl silicate solid phases found in the vadose zone environment at the Hanford Site (Szecsody et al., 2012; Um et al., 2009; Zachara et al., 2007). Further, detailed spectroscopic studies on U(VI)-contaminated Hanford sediments indicated that the precipitates were uranophane, K-boltwoodite (Z. Wang et al., 2005), and Na-boltwoodite (Catalano et al., 2004). In the case of Na-boltwoodite, its formation was expected in some areas of the Hanford Site as the local porewater reached U concentrations in the range of $10^{-4} – 10^{-3}$ M, near saturation with respect to the uranyl silicate (Catalano et al., 2004). It is important to note that this concentration range is two orders of magnitude higher than the added U in the presented experiments.

When free uranyl ions are present in alkaline environments, anionic aqueous species such as $UO_2(CO_3)_2^{2-}$ and $UO_2(CO_3)_3^{4-}$ are formed. According to Liu *et. al.*, the latter aqueous species accounted for greater than 78% of the dissolved U in all of Hanford Site porewater, with the remainder occurring as $Ca_2UO_2(CO_3)_3$ and $(UO_2)(CO_3)_2^{2-}$ (Liu et al., 2004). Such stable and water-soluble uranyl species tend to coprecipitate with the $CaCO_3$ formed at circumneutral pH. Thus, it is expected to form calcium carbonate polymorphs (e.g., vaterite, aragonite, calcite) and uranyl carbonates, such as liebigite, as shown in the GWB speciation diagrams in Figure 1 and Figure 2.

Lastly, a recent study proved U retardation on comparative alkaline treatments in the presence of various minerals and natural Hanford sediments. Results suggest that U removal from the aqueous phase increases from NaOH < NH_4OH < NH_3 gas in the SGW solution (Emerson et al., 2018). These results are of relevance to the presented study as the background electrolytes in the SGW solution are equal in composition (i.e., Na^+, Ca^{2+}, HCO_3^-, etc.) and both at elevated pH (~11.5). The researchers state that under these conditions, the SGW solution is saturated with respect to calcite. Thus, we can conclude that the U co-precipitation with calcite phenomena presented in their work is highly likely to occur in batch experiments, supporting our previous results on calcite formation.

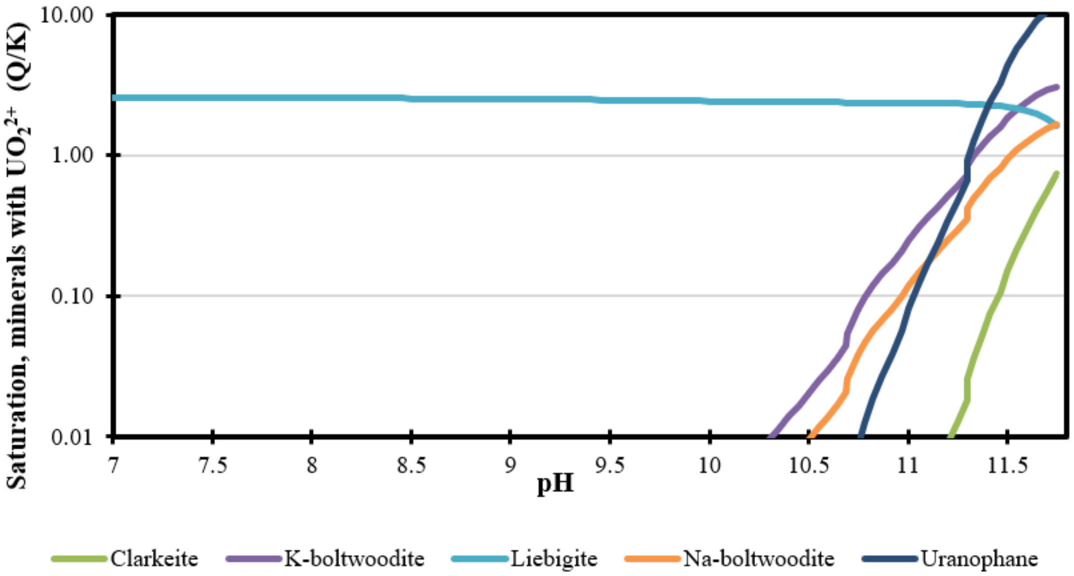

Figure 1. Saturation index of U-bearing mineral phases diagram plotted as a function of pH for 5.0% of NH_3 [3.1 mol/L $NH_3(aq)$] in SGW.

Table 1. Uranyl mineral phases used in the Geochemist's Workbench® speciation modeling

Mineral Phase	Structural Formula
Uranyl Carbonates	
Liebigite	$Ca_2UO_2(CO_3)_3 \cdot 10H_2O$
Uranyl hydroxides	
Clarkeite	$Na(UO_2)O(OH)$
Uranyl Silicates	
K-Boltwoodite	$KH_4SiO_4\ UO_2\ \cdot 1.5H_2O$
Na-Boltwoodite	$NaHSiO_4\ UO_2\ \cdot 1.5H_2O$
Uranophane	$Ca(UO_2)_2(HSiO_4)_2\ 5H_2O$

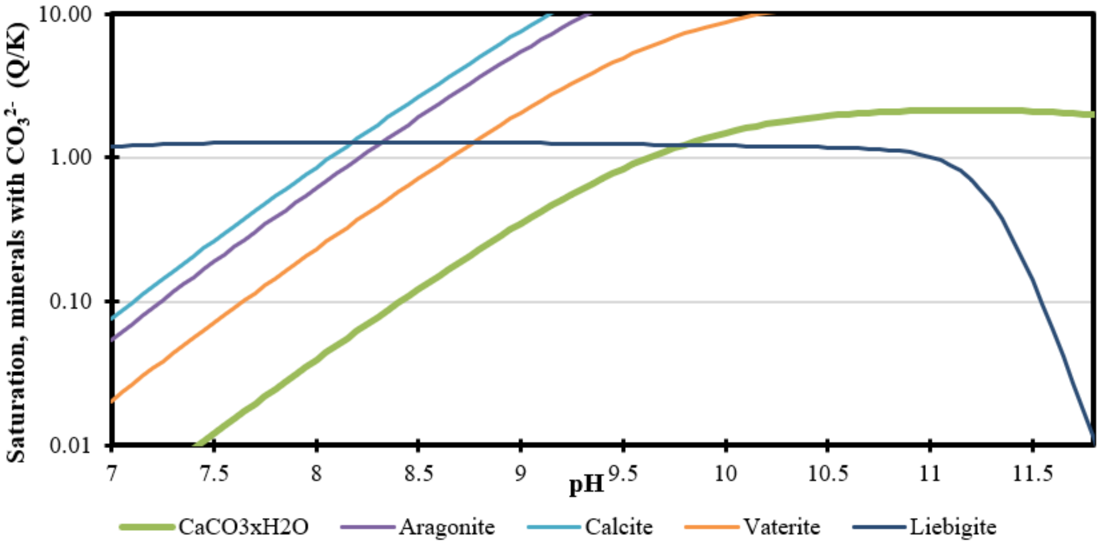

Figure 2. Saturation index of Ca-bearing mineral phases diagram plotted as a function of pH for 5.0% of NH_3 [3.1 mol/L $NH_{3(aq)}$] in SGW.

Subtask 1.1: Conclusions

This research was aimed at understanding and predicting the fate of U at contaminated sites when alkaline ammonia (NH_3) gas injection is chosen as a remediation technique. The focus of this study was to identify (1) mineral alteration of phyllosilicates and Hanford sediments after contact with 5% NH_3/95% N_2 gas treatment; (2) secondary precipitates; and (3) changes in the mobility of U. By using a wide range of characterization and spectroscopic techniques prior, during, and post-treatment, U behavior in the solid phase was monitored. These overall results of the study are indicative of U removal due to multiple mechanisms, including:

i. co-precipitation of U(VI) with secondary phases (e.g., $CaCO_3$ and Fe-oxides),

ii. co-precipitation of reduced U(IV),

iii. U precipitation (e.g., Na-boltwoodite or uranophane),

iv. adsorption of U, and

v. coating of U phases with secondary phases (e.g., Al/Si from incongruent dissolution and secondary precipitation).

These mechanisms are contingent upon NH_3 gas leaving the system (i.e., pH 8). Co-precipitation mechanisms, such as $CaCO_3$ and Fe-oxide co-precipitation and incongruent dissolution phenomenon due to the aqueous phase being saturated with Si, Al, or similar ions, are primordial for immobilization. FIU's research proved the co-precipitation of uranium with secondary phases. Experiments discussed in previous reports also showed a significant fraction of reduced U(IV) for the illite mineral investigated (26±11%) and $CaCO_3$ formed (26±4%). In addition, Fe-oxide impurities in clays along with the re-precipitated Al-Si aluminosilicates provided evidence for a valid U-sequestration mechanism. Lastly, non-radioactive low solubility mineral (e.g., cancrinite, sodalite, etc.) formation and significant Al/Si ratio phyllosilicate transformations during subsequent pH decrease, are expected to coat the U phases present at the Hanford Site.

These removal mechanisms were supported by apparent partitioning coefficient (K_d) calculations and geochemical speciation. When describing the distribution of the contaminant at the liquid–solid interface, observation data from batch experiments showed K_d values during aeration treatment higher ($K_d > 107$ mL/g) than those of natural conditions ($K_d < 8.0$ mL/g). Further, simulation models predicted U- and Ca-bearing mineral phase upon NH_3 gas treatment, indicative of U removal at the investigated conditions.

Overall, this study demonstrated effective U removal and U-sequestration mechanisms from resulting precipitates. It was hypothesized that the phyllosilicate minerals and Hanford Site sediments analyzed would be transformed to U-bearing phases and have calcite co-precipitated on the solid phase under conditions designed to mimic those under leaking high-level waste tanks. These batch experiments and predictive model simulations improve our understanding of U contaminant interactions in highly alkaline systems. Nonetheless, further studies are warranted to evaluate U fate and transport focusing on U reduction and immobilization in systematic studies.

FIU has completed Subtask 1.1 “Remediation Research of Ammonia Gas for Uranium Treatment”. The research results based on this task were included in two Master’s theses by Robert Lapierre (May 2018, chemistry) and Alberto Abarca (December 2018, environmental engineering) and two PhD theses defended by Claudia Cardona (May 2017, environmental engineering) and most recently, Silvina Di Pietro, who successfully defended her thesis and graduated with a PhD degree in chemistry in April 2021.

Major technical accomplishments for the duration of this subtask include:

- FIU completed the speciation modeling simulations to correlate results with SEM/EDS and XRD analysis on the selected precipitate samples and investigated the stability of the multicomponent uranium-bearing precipitates mimicking those created in sediments as a result of alkaline ammonia gas treatment in the vadose zone. The amount of water adsorbed on uranium-bearing precipitates was determined gravimetrically by the isopiestic method. The results indicate that gravimetric measurements of moisture uptake as a function of increasing relative humidity can provide reasonable estimates of the deliquescence point of solid phases or its components.
- FIU investigated phyllosilicate clay mineral alteration in variable redox conditions and alkaline treatments. Results showed significant dissolution occurs upon exposure of phyllosilicate clay minerals to highly alkaline (pH > 11) solutions with slightly greater dissolution under anaerobic conditions. Alkaline-treated mineral samples were characterized via XRD, SEM-EDS, and EPMA analyses. These observations suggest secondary precipitation may be an effective method for sequestration of contaminants within newly formed, low solubility minerals. This information provides critical fundamental aspects on identification of secondary minerals to evaluate their abilities to incorporate contaminants.
- FIU identified the major physicochemical changes of aluminosilicate minerals following NH_3 gas treatment and subsequent aeration. This systematic investigation used a range of characterization and spectroscopic techniques that demonstrated an alteration in morphology and recrystallization following aeration upon microscopic (SEM and TEM) and surface area (BET) analysis. These physical changes were further supported by MAS NMR analysis, where edge-site Al and $[SiO_4]^{n-}$ groups display charges in local structure

for ammonia- and aerated-treated samples.

- The FIU results highlighted the importance of mineral alteration upon *in situ* remediation with NH_3 gas, particularly following treatment as NH_3 was removed from the aqueous phase by adsorption to sediments and diffusion through gas phases as pH returned to natural soil conditions. For environmental remediation applications, these mineral alteration and co-precipitation processes could remove soluble contaminant cations from the aqueous phase and coat minerals with adsorbed contaminants on the surface such as illite and montmorillonite. Overall, injection of NH_3 gas treatment of aluminosilicate minerals demonstrates potential for contaminant sequestration through mineral alterations. This work provided technical support to a potential treatability test affecting Hanford Site decisions.

The research results out of this competed subtask were summarized in the peer-reviewed publications and presentations as followed :

- Di Pietro, et al., Solid phase characterization and transformation of illite mineral with gas-phase ammonia treatment, 2021. Accepted by the *Journal of Hazardous Materials.* The manuscript DOI link *https://doi.org/10.1016/j.jhazmat.2021.127657*
- Di Pietro, et al., Phyllosilicate mineral dissolution upon alkaline treatment under aerobic and anaerobic conditions, 2020. Applied Clay Science, v.189, p.105520
- Emerson, H.P et al., 2018 Uranium immobilization in the presence of minerals following remediation via base treatment with ammonia gas, Journal of Environmental Management, 223, 1, 108-114. DOI: 10:1016/jenvman.2018.06.12
- Katsenovich, et al., 2018. Assessment of Calcium Addition on the Removal of U(VI) in the Alkaline Conditions Created by NH_3 Gas. Applied Geochemistry, 92, p.94-103.
- Emerson, et al., 2017. Effects of ammonium on uranium partitioning and kaolinite mineral dissolution. Journal of Environmental Radioactivity 167,150-159.
- Katsenovich, et al., 2016. The effect of Si and Al concentrations on the removal of U(VI) in the alkaline conditions created by NH_3 gas. Applied Geochemistry, 73, p. 109-117
- Seven presentations at WM conferences and proceeding manuscripts including one awarded as a "Paper of Note" (2016)
- Student posters at WM and other student poster competitions.
- Katsenovich et al., 2018. Uranium Sequestration with pH Manipulation by Ammonia Gas. Presentation at Goldschmidt conference, August 2018.

Subtask 1.1: References

Cantrell, K. J., Deutsch, W. J., & Lindberg, M. J. (2011). Thermodynamic Model for Uranium Release from Hanford Site Tank Residual Waste. *Environmental Science & Technology*, *45*(4), 1473–1480. https://doi.org/10.1021/es1038968

Catalano, J. G., & Brown, G. E. (2005). Uranyl adsorption onto montmorillonite: Evaluation of binding sites and carbonate complexation. *Geochimica et Cosmochimica Acta*, *69*(12), 2995–3005. https://doi.org/10.1016/j.gca.2005.01.025

Catalano, J. G., Heald, S. M., Zachara, J. M., & Brown, G. E. (2004). Spectroscopic and diffraction study of uranium speciation in contaminated vadose zone sediments from the Hanford site, Washington state. *Environmental Science & Technology*, *38*(10), 2822–2828

Emerson, H. P., Di Pietro, S., Katsenovich, Y., & Szecsody, J. (2017). Effects of ammonium on uranium partitioning and kaolinite mineral dissolution. Journal of Environmental Radioactivity, 167.

Emerson, H. P., Di Pietro, S., Katsenovich, Y., & Szecsody, J. (2018). Potential for U sequestration with select minerals and sediments via base treatment. Journal of Environmental Management, 223.

Katsenovich, Y. P., Cardona, C., Szecsody, J., Lagos, L. E., & Tang, W. (2018). Assessment of calcium addition on the removal of U(VI) in the alkaline conditions created by NH3 gas. Applied Geochemistry, 92, 94–103.

Liu, C., Zachara, J. M., Qafoku, O., McKinley, J. P., Heald, S. M., & Wang, Z. (2004). Dissolution of uranyl microprecipitates in subsurface sediments at Hanford Site, USA. Geochimica et Cosmochimica Acta, 68(22), 4519–4537

Szecsody, Truex, M. J., Zhong, L., Johnson, T. C., Qafoku, N. P., Williams, M. D., Greenwood, W. J., Wallin, E. L., Bargar, J. D., & Faurie, D. K. (2012). Geochemical and Geophysical Changes during Ammonia Gas Treatment of Vadose Zone Sediments for Uranium Remediation. Vadose Zone Journal, 11(4).

Um, W., Wang, Z., Serne, R. J., Williams, B. D., Brown, C. F., Dodge, C. J., & Francis, A. J. (2009). Uranium phases in contaminated sediments below Hanford's U tank farm. Environmental Science & Technology, 43(12), 4280–4286.

Zachara, J., Brown, C., Christensen, J., Davis, J. A., Dresel, E., Kelly, S., Liu, C., McKinley, J., Serne, J., & Um, W. (2007). A Site-Wide Perspective on Uranium Geochemistry at the Hanford Site.

Subtask 1.2: Re-oxidation of Redox Sensitive Contaminants Immobilized by Strong Reductants

Subtask 1.2: Introduction

Technetium-99 (^{99}Tc) management is a high-priority activity for the EM complex due to its high aqueous solubility, toxicity and environmental mobility. Approximately 700 Ci of ^{99}Tc have been released to the Hanford subsurface and its remediation is challenging due to the variability of waste chemistries and heterogeneity of the deep vadose zone. A perched water zone located beneath 200-DV-1 Operable Unit at Hanford contains ^{99}Tc as pertechnetate ($Tc^{VII}O_4^-$) that can potentially migrate to the underlying aquifer. Reducing conditions without or with sulfides may temporarily immobilize ^{99}Tc as one or more Tc^{IV} precipitates. Previous research has shown that ^{99}Tc, as pertechnetate that has been reduced to $Tc^{IV}O_2$ or TcS_x precipitates, reoxidizes and will eventually remobilize back to the aqueous phase (Lukens, Bucher et al. 2005). Previous research has also shown that reduced Tc precipitates that have been coated with other low solubility precipitates can be effective for preventing Tc remobilization, so may be useful for remediation (Pearce, Serne et al. 2018). In addition,Tc can be incorporated into low solubility precipitates such as iron oxides (Boglaienko, Soltis et al. 2020) or tin oxides (Luksic, Riley et al. 2015), which may have application for ex-situ treatment. For this reason, there is a need for additional research under the specific conditions of subsurface remediation for the Hanford Site as other Tc species may form.

Recent bench scale evaluations provided insights on the pertechnetate reduction process using strong reductants in the sediment mixture (Lawter, Garcia et al. 2018); however, this process was not evaluated for the re-mobilization of ^{99}Tc under aerobic conditions. The study conducted at FIU between 2019 – 2020, investigated the re-oxidation behavior of ^{99}Tc to mimic field conditions, where the groundwater and perched water zone were slowly re-oxidized to naturally occurring conditions. Laboratory experiments evaluated re-oxidation behavior of ^{99}Tc initially reduced by strong reductants such as zero valent iron (ZVI, Hepure Technologies), sulfur modified iron (SMI-PS Inc), and calcium polysulfide (CPS) in batch scale experiments under sequential anaerobic conditions followed by aerobic conditions. In FIU Year 1, experimental work was extended to investigate the reoxidation behavior of ^{99}Tc in in the presence of collocated uranyl (UO_2^{2+}) and nitrate (NO_3^-) ions.

Sediment samples obtained from the Hanford Site Ringold Formation were sieved and the ≤ 2 mm size fraction was used in the batch experiments. The batch experiments were conducted in two phases: Phase 1 – reduction of ^{99}Tc collocated with NO_3^- and UO_2^{2+} in the presence of strong reductants, 0.1% ZVI or 0.1% SMI, under anaerobic conditions; and Phase 2 – re-oxidation of reduced ^{99}Tc and other contaminants, NO_3^- and UO_2^{2+}, under aerobic conditions. Two contacting solutions were used in these experiments: (1) a synthetic perched water solution amended with 10 µg/L (34 pCi/L) of ^{99}Tc collocated with 150 mg/L of U(VI) and (2) a synthetic groundwater solution amended with 420 µg/L (122.3 pCi/L) of ^{99}Tc collocated with 124 mg/L NO_3^-.

Subtask 1.2: Objectives

The objective of this subtask is to study re-oxidation kinetics of perched and groundwater contaminants, such as ^{99}Tc(VII) comingled with NO_3^- and UO_2^{2+} that have been initially reduced by strong reductants such as 0.1% ZVI and 0.1% SMI, in batch-scale experiments under anaerobic initial conditions followed by aerobic conditions. This report presents results on Tc reduction and reoxidation behavior when ^{99}Tc is comingled with UO_2^{2+} in perched water and NO_3^- in groundwater solutions.

Subtask 1.2: Methodology

These batch experiments studied re-oxidation behavior of reduced forms of technetium [$^{99}Tc^{(IV)}$ oxides and/or sulfides] in the presence of UO_2^{2+} and NO_3^- after treatment with strong reductants, including ZVI and SMI. Ringold Formation non-contaminated sediment samples sent from PNNL were obtained near the Hanford Site. The sediment was dried in an oven at 30˚C for 48 hours and sieved through a 2 mm sieve (Saslow et al., 2018).

The ≤ 2 mm sediment fraction was used in the batch experiments conducted in two phases: Phase 1 - Reduction of ^{99}Tc comingled with UO_2^{2+} and NO_3^- in the presence of strong reductants under anaerobic conditions; and Phase 2 - Identification of the re-oxidation rates of reduced ^{99}Tc comingled with UO_2^{2+} and NO_3^- under aerobic conditions.

Initial set up

Ultrapure deionized water (> 18 MΩ-cm, DIW, 5 L) was purged with N_2 for 30 minutes and transferred into the anaerobic chamber (Coy Laboraotory) to prepare 2.5 L of each of the two contacting solutions of synthetic perched and groundwater solutions. An anaerobic CAM-12 meter inside the anaerobic chamber monitored oxygen (ppm) and hydrogen (%) levels. The anaerobic glove box was connected to two cylinders: (i) high purity nitrogen and (ii) nitrogen (95%) mixed with hydrogen (5%). The level of H_2 was kept as ~2% and $O_2 < 50$ ppm. A palladium catalyst in the anaerobic chamber was replaced and regenerated weekly by heating in the oven at 180 °C for 4-5 h. The pH adjustment solutions were prepared based on the information presented in Table 2.

Table 2. HCl volume (mL) to prepare 100 mL of pH- adjustment solutions

MW$_{HCl}$ =36.46 g/mol, density 1.18 g/cm^3, purity- 35-38%		
0.1 M	1 M	2 M
0.835 mL	$V = \frac{36.46 * 100 * 100}{1.18 * 37 * 1000} = 8.35\ mL$	16.7 mL

The perched water (PW) and groundwater (GW) simulants were prepared inside the glovebox, using salts defined in Table 3, and diluted using DIW purged with N_2. These solutions were then pH-adjusted by using small quantities of hydrochloric acid (HCl, TraceMetal™ Grade, 0.1 M, 1 M and 2 M) to a pH of 7.8 ± 0.1 and 8.2 ± 0.1 for the artificial GW and PW solutions, respectively. The pH electrode was calibrated using three buffers (pH: 4.01, 7.00, and 10.01) immediately before measuring the pH of the solutions.

Table 3. Recipes for Simulant Solutions (Saslow et al., 2018)

Synthetic Perched Water (PW) Recipe (~pH 8.2)			
Chemical	mmol/L	g/L	Mass to prepare 2.5 L solution, g
$NaHCO_3$	10.708	0.9	2.25
$KHCO_3$	0.310	0.031	0.0775
(anhydrous) $MgSO_4$	2.703	0.325	0.8125
$CaSO_4$ $2H_2O$ (dite)	0.561	0.097	0.2425
Na_2SO_4	1.744	0.248	0.62
NaCl	3.3006	0.193	0.4825
Add 100 µL of 2M HCl to 1L solution to lower pH to ~8.2			

Artificial Groundwater (GW) recipe (~pH 7.8)			
Chemical	mmol/L	g/L	Mass to prepare 2.5 L solution, g
$NaHCO_3$	1.586	0.133	0.3325
$KHCO_3$	0.123	0.012	0.03
$MgSO_4$	0.366	0.090	0.225
$MgCl_2$ $6H_2O$	0.247	0.050	0.125
$CaCl_2$ $2H_2O$	1.071	0.157	0.3925

The simulant solutions were spiked with contaminants of concern, 150 mg/L U and 10 µg/L ^{99}Tc for the PW and 420 µg/L of ^{99}Tc in addition to 124 mg/L NO_3^- for the GW. These Tc concentrations are consistent with previous work conducted at PNNL (Lawter et al., 2018) and experiments conducted in FY Year 10 (2020) by FIU (Table 4).

Table 4. Amounts of U, NO_3^- and Tc added from stock solutions to 2.5 L of artificial GW or PW solutions

Volume of stock to prepare 2.5 L solution	**Tc (stock concentration 4.217 mM/417.483 mg/L)**	**U [uranyl acetate solution (depleted U)], $UO_2(OCOCH_3)_2 \cdot 2H_2O$, stock solution, 2%)***	**$NaNO_3^-$, 0.01 M** (0.62 g/L of NO_3)**
Groundwater (420 µg/L of ^{99}Tc and 124 mg/L NO_3^-	2515 µL		500 µL
Perched water (150 mg/L U and 10 µg/L ^{99}Tc)	59 µL	33.52 mL	

*2% of $UO_2(OCOCH_3)_2 \cdot 2H_2O$ solution (MW= 424.14 g/mol) is 0.047 mol/L. This requires 13.4 mL per L to have 0.15 g/L of U.

**0.01 M $NaNO_3$ (MW= 90.104) requires 0.0901 g of salt dissolved in 100 mL D IW.

Each 250 mL bottle contained 10 ± 0.01 g of sieved homogeneously mixed sediment prepared in triplicate for a 1:10 solid to liquid ratio. The sediment-free control samples with GW and PW synthetic solutions contained the same concentrations of ^{99}Tc, U, and NO_3^- as those used in the experimental samples. These samples were treated the same as the experimental samples to determine the initial content of ^{99}Tc, U and NO_3^- in GW and PW solutions. In addition, control bottles amended with reductants but without contaminants were prepared for solid characterization studies to compare iron products formed with and without contaminants. These samples were treated the same as other experimental samples. Each of the tested reductants were weighed to prepare for batch experiments within ± 0.01 (0.1% ZVI and 0.1% SMI (Table 5 and Table 6).

Table 5. Mass of reductants in GW and PW bottles

Reductant per 100 mL	ZVI	SMI
GW (Tc=420 µg/L), 0.1%	100 mg, Tc/Fe molar ratio=0.00023	100 mg, Tc/Fe molar ratio=0.00023
PW (Tc= 10 µg/L), 0.1%	100 mg, Tc/Fe molar ratio=0.0000056	100 mg, Tc/Fe molar ratio=0.0000056

Table 6. The amount of experimental and control bottles

<table>
<tr><th></th><th>ZVI</th><th>SMI</th></tr>
<tr><td rowspan="4">GW, 0.1%</td><td>3 experimental bottles. Monitored changes in pH, oxidation reduction potential (ORP), dissolved oxygen (DO), and contaminant concentrations (Tc, NO_3^-). Use for solid characterization studies after the completion of reoxidation experiments</td><td>3 experimental bottles. Monitored changes in pH, ORP, DO, and contaminant concentrations (Tc, NO_3^-). Use solids for the characterization studies after the completion of reoxidation experiments</td></tr>
<tr><td colspan="2">1 reductant- free GW control monitored changes in pH, ORP, DO, and contaminant concentrations</td></tr>
<tr><td>1 sediment-free control monitored changes in contaminant concentrations</td><td>1 sediment-free control monitored changes in contaminant concentrations</td></tr>
<tr><td>1 contaminant-free control to be used for solid characterization at the end of experiment</td><td>1 contaminant-free control to be used for solids characterization at the end of experiment</td></tr>
</table>

	ZVI	SMI
	1 bottle of sacrificial control with contaminants for solid characterization after phase 1 in anaerobic glove box	**1** bottle of sacrificial control with contaminants for solid characterization after phase 1 in anaerobic glove box
PW, 0.1%	changes in pH, ORP, DO, and contaminant concentrations (Tc, U). Use for solid characterization studies after the completion of reoxidation experiments	**3** experimental bottles. Monitored changes in pH, ORP, DO, and contaminant concentrations (Tc, U). Use for solid characterization studies after the completion of reoxidation experiments
	1 reductant- free PW control to monitor changes in pH, ORP, DO, and contaminant concentrations (Tc, U)	
	1 sediment-free control to monitor changes in contaminant concentrations (Tc, U)	**1** sediment-free control to monitor changes in contaminant concentrations (Tc, U)
	1 contaminant-free control to be used for solids characterization	**1** contaminant-free control to be used for solids characterization
	1 bottle of sacrificial control with contaminants for solid characterization after phase 1 in anaerobic glove box	**1** bottle of sacrificial control with contaminants for solid characterization after phase 1 in anaerobic glove box
Total experimental	4	4
Total controls	8	6
Total bottles	22	

Phase 1: ^{99}Tc reduction experiment

Triplicate samples with sediment and reductant in 250 mL bottles were transferred into an anaerobic glovebox for 48 hours before contacting with 100 mL of deoxygenated synthetic GW and PW solutions amended with ^{99}Tc, UO_2^{2+} and NO_3^-. Samples were manually shaken several times per day for a period of 30 days (Saslow et al., 2018). An aliquot of 0.4 mL was collected at variable times, including 7 days, 15 days, 21 days and 28 days until nearly all ^{99}Tc, U and NO_3^- removal was achieved. Collected samples were filtered via 0.2 µm syringe filters and stored in a refrigerator (4°C) until analysis. Anions (NO_3^-, NO_2^-, and SO_4^-) were analyzed by ion chromatography (IC, Integrion Dionex), and ^{99}Tc, U, and Fe were measured by inductively coupled plasma mass spectrometry (ICP-MS, Thermo Fisher Scientific, iCAP RQ). Tc and U samples were prepared in 2 % nitric acid and NO_3^-, NO_2^-, and SO_4^- samples were prepared in DIW. In addition, measurements were taken for ORP, DO, and pH at each sampling time. After completion of Phase 1, the supernatant was removed from the sacrificial samples containing sediment, contaminants, and reductants, and solids were dried in the vaccum oven at 35ºC to prepare for solid phase characterization by XRD and SEM-EDS. These analyses would suggest changes in sediment solid phases in the anaerobic conditions due to presence of ZVI, SMI and CPS reductants. The results will be compared with solid samples analyzed after the completion of the reoxidation experiments (Table 6).

Phase 2: Re-oxidation of redox sensitive contaminants

After the $Tc^{(VII)}$, $U^{(VI)}$ and NO_3^- reduction in Phase 1, experimental bottles, sediment-free controls and contaminant-free controls were removed from the anaerobic glovebox to study the re-oxidation behaviour of redox sensitive contaminants under aerobic conditions. The experiment was continued under a fume hood in FIU ARC's radiation laboratory. Capped samples were placed on a shaker for proper mixing (110 rpm, ThermoScientific) and kept for 45 days under slow aeration to allow sufficient oxygen presence in the aqueous phase throughout Phase 2 experiments, and for slow re-oxidation of the redox sensitive contaminants. Samples of 0.4 mL were collected once a week at 1 day, 7 days, 14 days, 21 days, 28 days, 35 days and 45 days and filtered via 0.2 µm syringe filters before being refrigerated (4°C) until analysis. Measurements were continued for the solution pH, ORP and DO at each sampling event in aerobic conditions conducted on the bench.

Liquid Analysis (ICP-MS, LSC, IC)

Anion analyses by IC**:**

Ion chromatography (IC, Integrion Dionex) was used to analyze anions, NO^-_3, NO_2^- and SO_4^-. Calibration standards were prepared from a solid sodium nitrate, sodium nitrite and sodium sulfate in DIW using special IC vials. The concentrations of NO_3^- and NO_2^- in the combined stock solution were 100 mg/L. The concentration range for NO_3^- and NO_2^- calibration standards were 50 – 1,000 µg/L for the sample volume of 5 mL.

The Dionex IonPac AS11 analytical column (2x250 mm) and an Anion Dynamically Regenerated Suppressor (ADRS) (2 mm) were used for analyses.

ICP-MS analyses for Tc, U and Fe

^{99}Tc calibration standards ranged from 0.005 µg/L to 50 µg/L through a serial dilution from 1mg/L stock solution that was prepared from 4.217 mM (417.483 mg/L) stock solution (Table 7).

Table 7. Preparation of Tc standards

Standard concentration, µg/L	Volume from the stock, µL	Volume of 2 % HNO_3, µL Total volume 40 mL
1.0 mg/L	96	39,904
50 (from 1 mg/L stock)	2,000	38,000
25 (from 1 mg/L stock)	1000	39,000
10 (from 1 mg/L stock)	400	39600
5 (from 10 µg/L std)	20,000	20,000
1 (from 5 µg/L std)	8,000	32,000
0.5 (from 1 µg/L std)	20,000	20,000
0.01 (from 0.5 µg/L std)	800	39,200
0.005 (from 0.01 µg/L std)	20,000	20,000

ICP-MS U standards were prepared from 1,000 mg/L commercial uranyl nitrate stock solution purchased from High Purity Standards by the dilution to 1 mg/L stock (0.01 -500 µg/L). Fe calibration standards were prepared from a 100 mg/L Fe standard stock solution to measure aqueous iron in the samples (0.1 – 1000 µg/L).

The remaining aqueous fraction of contaminant (unitless) was calculated as the ratio of concentration in the solution to the initial concentration.

Calculation of rate constants

The oxidation rate constants for Tc^{VII} were calculated using the first-order and second-order rate equations according to Eqns. 1 and 2, respectively (H Scott, 2006). Other kinetic models to calculate reoxidation rate constants will be also considered.

$$ln\left(\frac{[C_t]}{[C_0]}\right) = -K_t \tag{1}$$

$$\frac{1}{[Ct]} - \frac{1}{[C0]} = Kt \tag{2}$$

Where C_t = concentration at the time, t, in mol L^{-1}
C_0 = initial concentration, mol L^{-1}
t =time, min
K = pseudo-first-order rate, min^{-1} fo r Eq. 1 and pseudo-second-order rate, $M^{-1}min^{-1}$ for Eq. 2.

Subtask 1.2: Results and Discussion

$Tc^{(VII)}$, $U^{(VI)}$, and NO_3^- are redox sensitive contaminants and the reduction of $Tc^{(VII)}$ to $Tc^{(IV)}$, $U^{(VI)}$ to $U^{(IV)}$ and NO_3^- to NH_4 is described by the following equations 1, 2, and 3 (Fiedor et al., 1998; Kobayashi et al., 2013; Yang and Lee, 2005)

$$TcO_4^- + 3e^- + 4H^+ = TcO_2\ xH_2O(s) + (2-x)\ H_2O \quad E^o = 0.75V \qquad \text{Eq. 1}$$

$$Fe^0 + 1.5UO_2^{2+} + 6H^+ = Fe^{3+} + 1.5U^{4+} + 3H_2O \quad E° = +0.17\ V \qquad \text{Eq. 2}$$

$$NO_3^- + 4Fe^0 + 10H = 4Fe^{2+} + NH_4 + 3H_2O \qquad \text{Eq. 3}$$

This study assessed the ability of ZVI and SMI to simultaneously reduce Tc(VII) in the presence of U(VI) and NO_3^- in groundwater or perched water typical for Hanford Site. ZVI is readily oxidized in an anaerobic Fe^0- H_2O system by the following reactions (Agrawal and Tratnyek, 1995):

$$Fe^0 + 2H^+ = Fe^{2+} + H_2 \qquad \text{Eq. 4}$$

$$Fe^0 + 2H_2O = Fe^{2+} + H_2 + 2OH^- \qquad \text{Eq. 5}$$

Under aerobic conditions, dissolved oxygen is the electron acceptor and the primary reaction yields OH^- (Zhao et al., 2016):

$$2Fe^0 + O_2 + 2H_2O = 2Fe^{2+} + 4OH^- \qquad \text{Eq. 6}$$

Sediment Sieving and Fraction Analysis

Most of the sediment in the Hanford soil was classified as sand.

Table 8 depicts the results from the fraction analysis done. A coarser soil particle size seen in the Hanford soil, is expected to lead to less sediment suspension in the batch experiments. The clay fraction was the smallest fraction measured by a significant margin.

Table 8. Fraction Analysis of Hanford Soil

Fraction	Soil Weight (g)	Weight Percentage
2000µm-500µm (Sand)	7.52	7.5
500µm-63µm (Sand)	87.15	87.2
63µm-20µm (Silt)	4.06	4.1
<20µm (Clay)	1.22	1.2

Aqueous Removal of ^{99}Tc by different reductants

Under anaerobic conditions, reduction of ^{99}Tc in the presence of $U^{(VI)}$ and NO_3^- occurred very quickly (Figure 3 and Figure 4). Before entering the aerobic phase of the experiments, all batches had less than 2% of Tc remaining as $Tc^{(VII)}O_4^-$ in the aqueous phase. The results obtained for triplicate GW sediment-amended samples in anaerobic conditions revealed that remaining aqueous fractions of Tc after 0.1% SMI and ZVI treatment was 0.003±0.002 and 0.008±0.003, respectfully. This was expected, as there was a high reductant loading versus initial concentration of Tc. ZVI was a slightly more effective reductant than SMI. In the aerobic phase, ZVI and SMI reductants led to varying reoxidation behavior of Tc. In aerobic conditions, however, SMI was more effective in resisting reoxidation. Sediment containing samples treated with SMI showed an increase of the Tc fraction remaining in the solution after samples were exposed to aerobic conditions; however, the Tc aqueous fraction slowly decreased and stabilized on the level of 0.015-0.02. The remaining fractions of Tc in SMI samples were slightly less than values measured in ZVI-treated samples (0.01 vs. 0.02) by day 75 at the end of sampling in aerobic conditions (Figure 3).

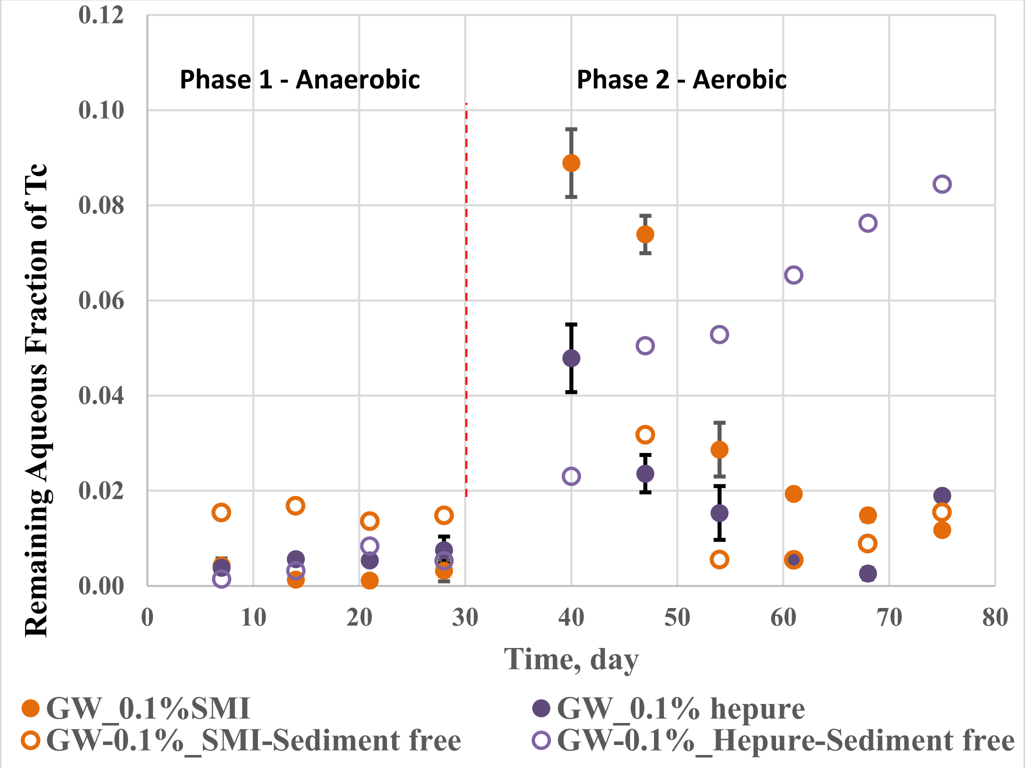

Figure 3. Reductive removal of Tc over time in aerobic and anaerobic conditions in GW samples amended with 0.1% of ZVI or SMI. Note: The remaining aqueous fraction of Tc (Y-axis, unitless) was calculated as the ratio of Tc concentration in the solution to the initial Tc concentration in the control.

This tendency was the same in sediment-free samples suggesting that ZVI was a more effective reductant in anaerobic conditions, while SMI was more effective in resisting re-oxidation in aerobic conditions. The remaining aqueous fraction of Tc was detected as <0.02 at the end of the aerobic sampling period compared to ~0.09 remaining in sediment-free ZVI samples (Figure 4).

For PW solutions, both reductants were effective in reducing Tc to less than 0.002 of the remaining aqueous fraction in the anaerobic conditions. For the sediment-containing samples, SMI was slightly more effective in resisting re-oxidation than ZVI; SMI remaining aqueous fraction was 0.06 vs. 0.11 for ZVI by the end of Phase 2 (Figure 5).

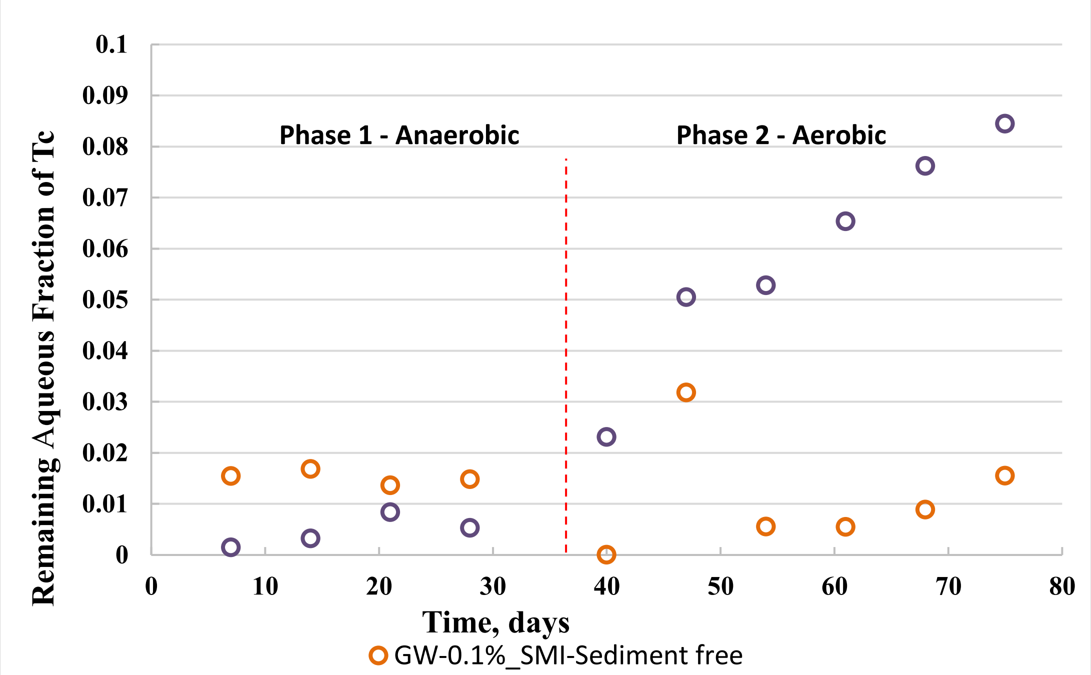

Figure 4. Reductive removal of Tc over time in aerobic and anaerobic conditions in GW sediment-free samples amended with 0.1% ZVI or 0.1% SMI. Note: The remaining aqueous fraction of Tc (Y-axis, unitless) was calculated as the ratio of Tc concentration in the solution to the initial Tc concentration in the control.

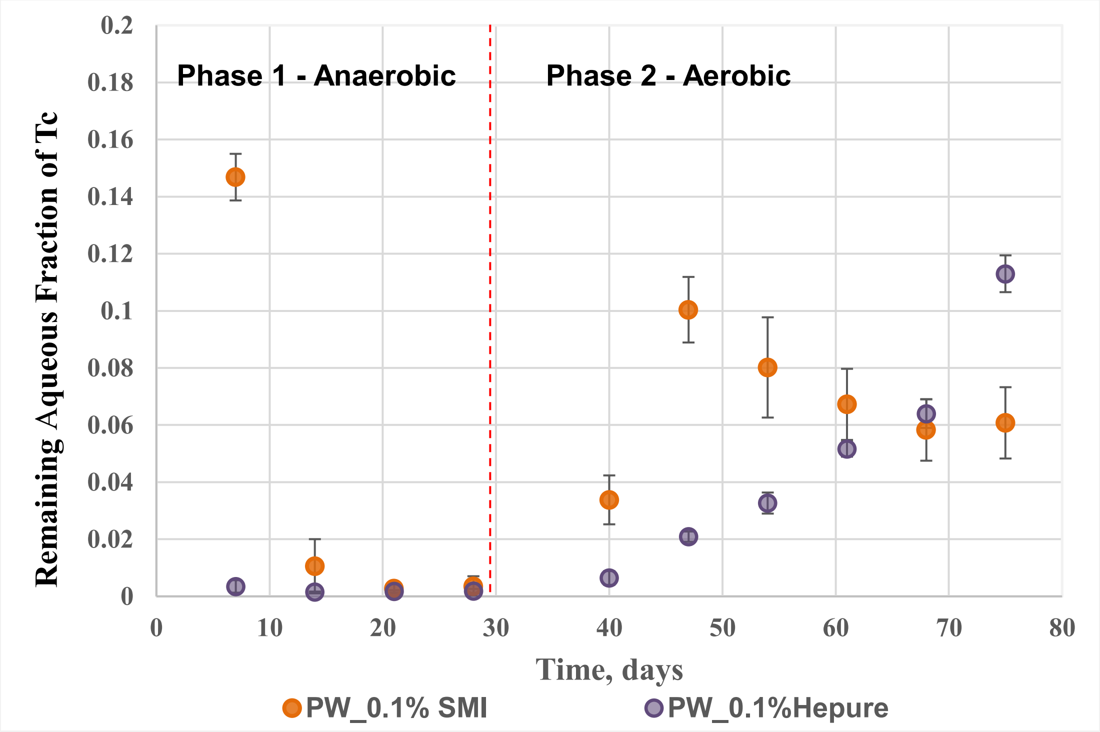

Figure 5. Reductive removal of Tc over time in aerobic and anaerobic conditions in PW amended with 0.1% ZVI or 0.1% SMI. Note: The remaining aqueous fraction of Tc (Y-axis, unitless) was calculated as the ratio of Tc concentration in the solution to the initial Tc concentration in the control.

Measurements of Tc remaining aqueous fractions in PW sediment-free controls revealed a similar trend as in the sediment-bearing samples. The reduction of Tc in SMI sediment-free samples continued throughout the aerobic period. SMI–treated samples contained the remaining aqueous fraction of Tc as 0.08 by day 75, compared to the ZVI samples containing 0.28 of the remaining aqueous fraction Tc by the end of the aerobic Phase 2. Overall, SMI was more effective in resisting re-oxidation than ZVI. Tc re-oxidation was higher in sediment–free samples compared to sediment-bearing samples (Figure 6).

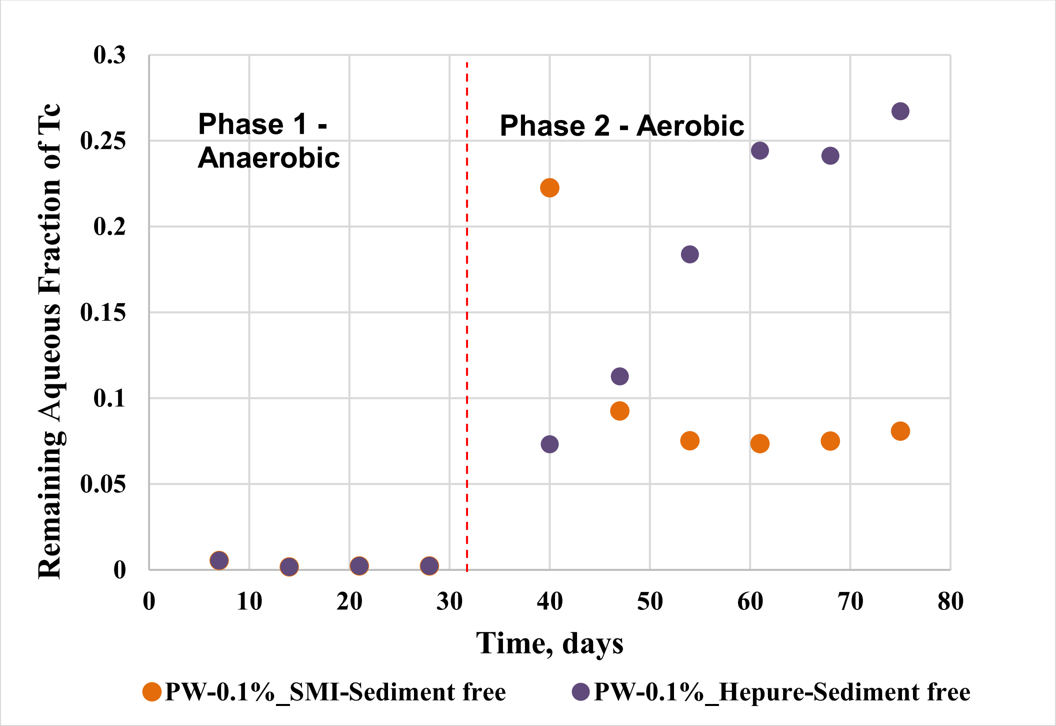

Figure 6. Reductive removal of Tc over time in aerobic and anaerobic conditions in PW sediment-free samples amended with 0.1% ZVI or 0.1% SMI. Note: The remaining aqueous fraction of Tc (Y-axis, unitless) was calculated as the ratio of Tc concentration in the solution to the initial Tc concentration in the control.

Evaluation of U(VI) reduction from the synthetic PW solutions in the presence of 0.1% ZVI and SMI suggested that ZVI was more effective than SMI for U reduction in sediment-amended samples in anaerobic conditions, leaving a remaining aqueous fraction of ~0.14±0.3 by the end of anaerobic Phase 1. In the same conditions, SMI-treated PW samples contained 0.37±0.11 remaining aqueous fraction of U by the end of the anaerobic sampling period (Phase 1) (Figure 7). In aerobic conditions, SMI was more effective than ZVI in resisting re-oxidation. The remaining aqueous fraction of U in SMI samples was measured as 0.32±0.01 by day 75 at the end of the aerobic sampling period (Phase 2). However, the remaining aqueous fraction of U was increased from 0.14 up to 0.40±0.01 in ZVI–treated samples by day 75 at the end of the aerobic Phase 2 (Figure 7).

In the sediment-free samples, ZVI was more effective than SMI in reducing U in anaerobic conditions with a remaining aqueous fraction <0.001 by the end of Phase 1. SMI samples contained a remaining aqueous fraction of ~0.02 by the end of anaerobic Phase 1. The remaining aqueous fraction of U in ZVI and SMI samples in aerobic conditions averaged as 0.3 for both reductants by the end of sampling in Phase 2 at day 75 (Figure 7).

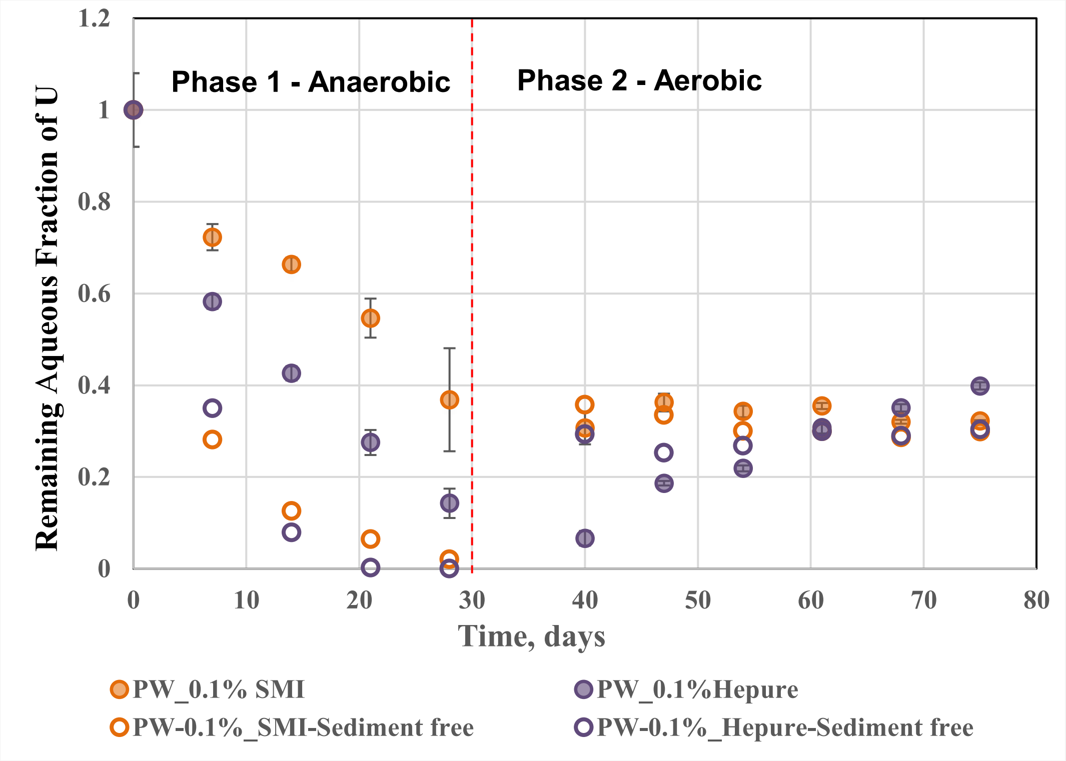

Figure 7. Reductive removal of U over time in aerobic and anaerobic conditions in PW samples amended with 0.1% ZVI or 0.1% SMI. Note: The remaining aqueous fraction of U (Y-axis, unitless) was calculated as the ratio of Uconcentration in the solution to the initial U concentration in the control.

Further analysis was conducted for the kinetic behavior of Tc in sediment-free GW & PW samples amended with 0.1% ZVI and SMI. The kinetic behavior was determined as first-order with respect to Tc. Sediment-free control samples revealed that Tc steadily oxidized in ZVI-containing samples in aerobic conditions, while Tc SMI-containing samples resisted re-oxidation to a greater degree (Figure 8).

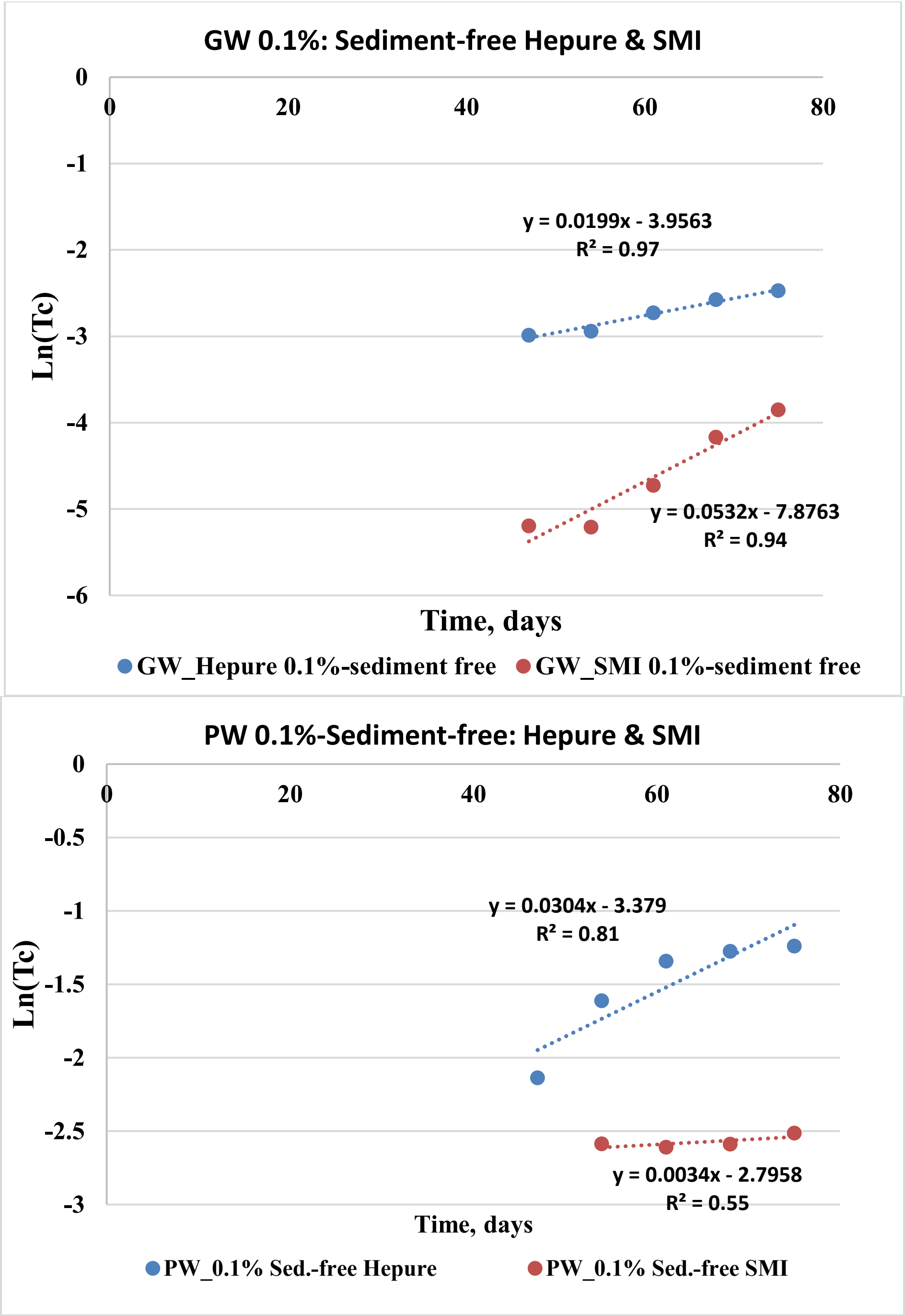

Figure 8. Re-oxidation behavior of Tc in PW and GW sediment-free samples.

The results for anion analysis by IC to evaluate the amount of NO_3^-, NO_2^-, & SO_4^{2-} in GW samples amended with 124 mg/L of NO_3^- collocated with Tc during treatment with ZVI and SMI are presented in Figure 9.

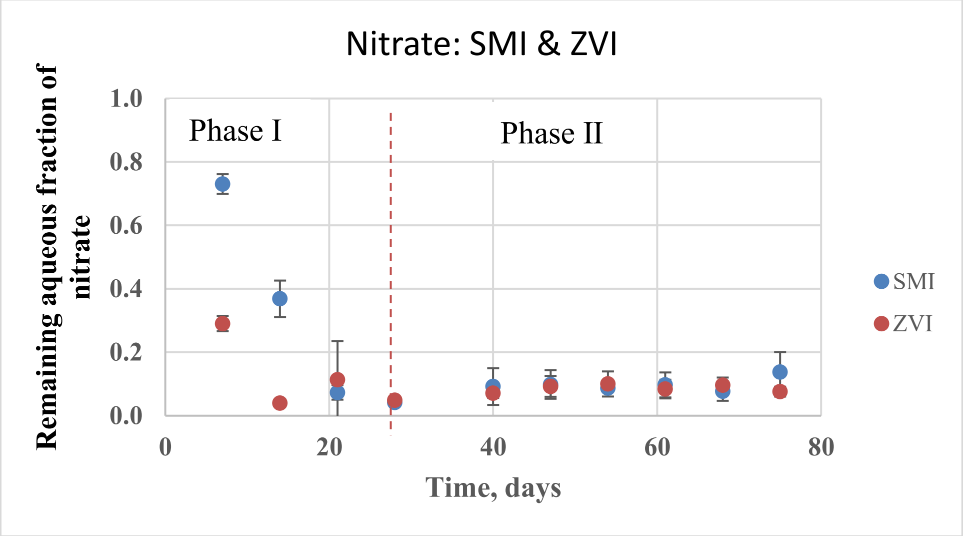

Figure 9. Remaining fraction of NO_3^- in groundwater samples treated with 0.1% SMI and 0.1% ZVI. The remaining aqueous fraction of NO_3^- (Y-axis, unitless) was calculated as the ratio of NO_3^- concentration in the solution to the initial NO_3^- concentration in the control.

Both ZVI and SMI were effective in NO_3^- removal by the end of the anaerobic Phase 1. The results do not show the re-oxidation of NO_3^- at the end of aerobic Phase 2 and both reductants showed similar removal of NO_3^-.

The increase in NO_2^- was larger in the SMI amended samples at the end of the Phase 1; however, NO_2^- concentrations were similar in samples amended with ZVI or SMI at the end of Phase 2.

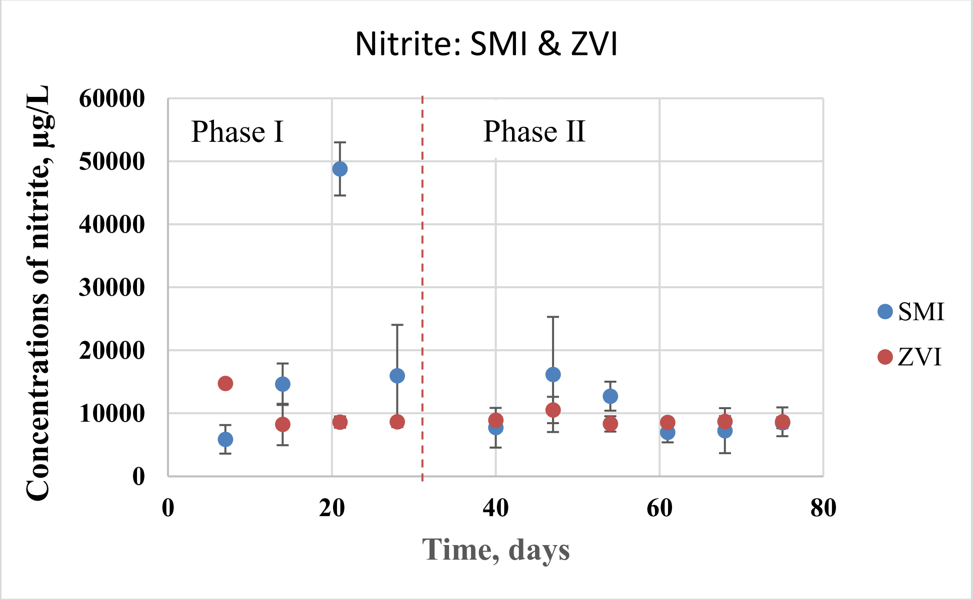

Figure 10. Concentrations of NO_2^- in groundwater samples treated with 0.1% SMI and 0.1% ZVI.

Measurements of SO_4^{2-} concentrations in aerobic and anaerobic conditions suggested a decrease of SO_4^{2-} content from the initial value of 75.14±5.07 mg/L in ZVI and SMI treated samples during first week of experiments (Figure 11). Then the concentrations of SO_4^{2-} in anaerobic conditions was increased from 19.9 mg/L at day 7 to 41.5 mg/L at day 28 in ZVI samples and from 31.8 mg/L to 62.8 mg/L for the same time period in SMI samples (Figure 11). The decrease in SO_4^{2-} concentrations might be due to formation of iron sulfate minerals, for example schwertmannite, prior to formation of green rust (Reinsch et al., 2010). The reaction with $Fe^{(II)}$ in the presence of SO_4^{2-} results in the formation of green rust (Su and Puls, 2001, 2004):

$$4Fe^{2+} + 2Fe^{3+} + SO_4^{2-} + 12H_2O \rightarrow Fe_6(OH)_{12}SO_4 + 12H^+ \qquad \text{Eq.7}$$

In aerobic conditions, the concentration of SO_4^{2-} in ZVI-treated samples was approximately on the level of 31.1- 40.6 mg/L but deacreased to 26.4-27.5 mg/L by the end of the experiment. However, in SMI-treated samples, the concentration of SO_4^{2-} was increased from an average value of 62.8 mg/L at day 28 to 90.5 mg/L at day 54, and then decreased to 67-68 mg/L by the end of the experiments. Thus, the concentration of SO_4^{2-} between 47-61 days was larger in SMI-amended samples compared to ZVI in both anaerobic and aerobic conditions (Figure 11). SMI is treated during its production by powdered elemental sulfur or other sulfur compounds such as sulfide. SMI includes about 2-8% of sulfur that may oxidize in aerobic conditions to SO_4^{2-}. Measurements showed that SO_4^{2-} concentrations between 47-61 days of experiment were on the level of 87.2-90.5 mg/L, which is larger compared to the value of 75.14±5.07 mg/L measured in the initial GW simulant solution. However, this concentration decreased to 67-68 mg/L, possibly due to formation of iron sulfate minerals. The mineral phases will be determined by x-ray diffraction analysis.

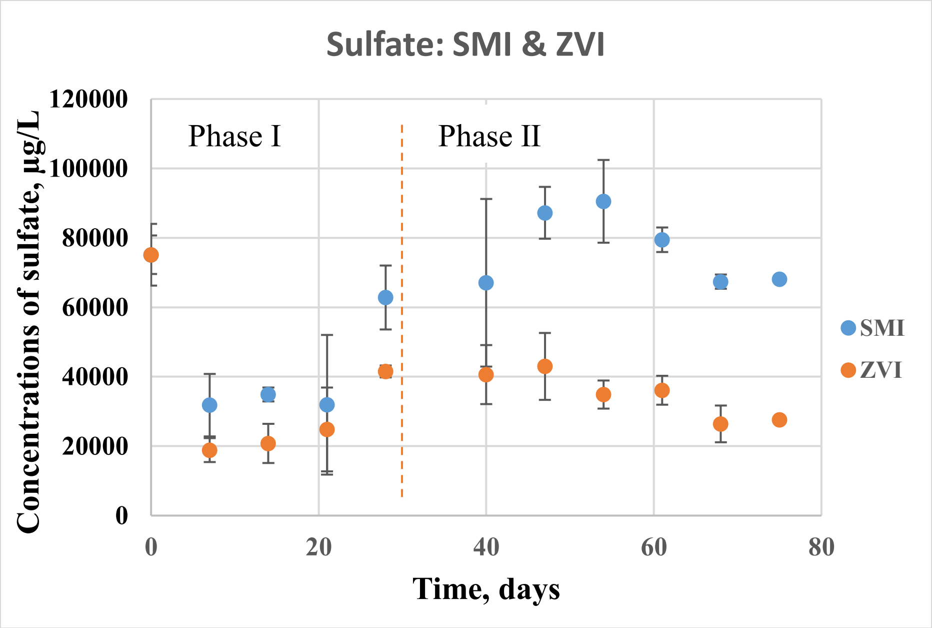

Figure 11. SO_4^{2-} concentrations over time in groundwater samples treated with 0.1% SMI and 0.1% ZVI.

Analysis of Dissolved Iron in Batch Experiments

In batches containing 0.1% iron-based reductants, tracking the dissolved total iron over the span of the experiment provides insight into the effect that aqueous Fe(II) and Fe(III) have on the rates of reductions of ^{99}Tc and other contaminants in the prepared simulants. Samples containing SMI revealed Fe concentrations ranging between 0.5-3.3 µM in anaerobic conditions, however, after entering the aerobic phase, Fe concentrations were below the detection limit of the ICP-MS. In

ZVI-amended samples, Fe concentrations increased up to 6 µM by day 21 and then dropped to 3.3 µM. In aerobic conditions Fe concentrations were below the detection limits. ORP values were measured in mV against a Ag/AgCl reference electrode and were consistent with reducing conditions during Phase 1 of the experiments. The relationship between the change in iron (Fe) concentration over time, as well as change in ORP values vs Fe concentration, are given in Figure 12 and Figure 13.

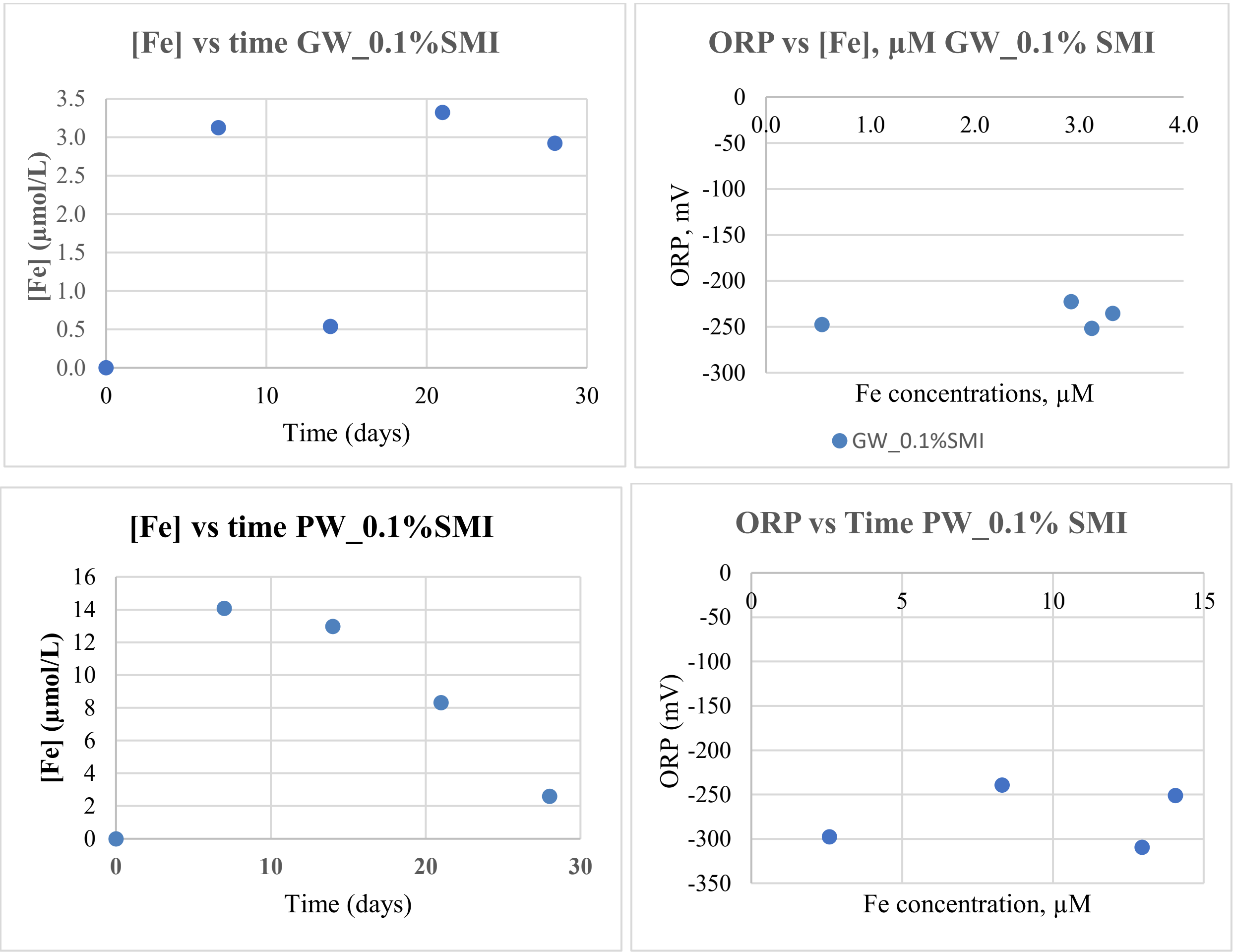

Figure 12. Total Fe concentrations vs time and ORP values for samples amended by SMI in PW and GW synthetic solutions.

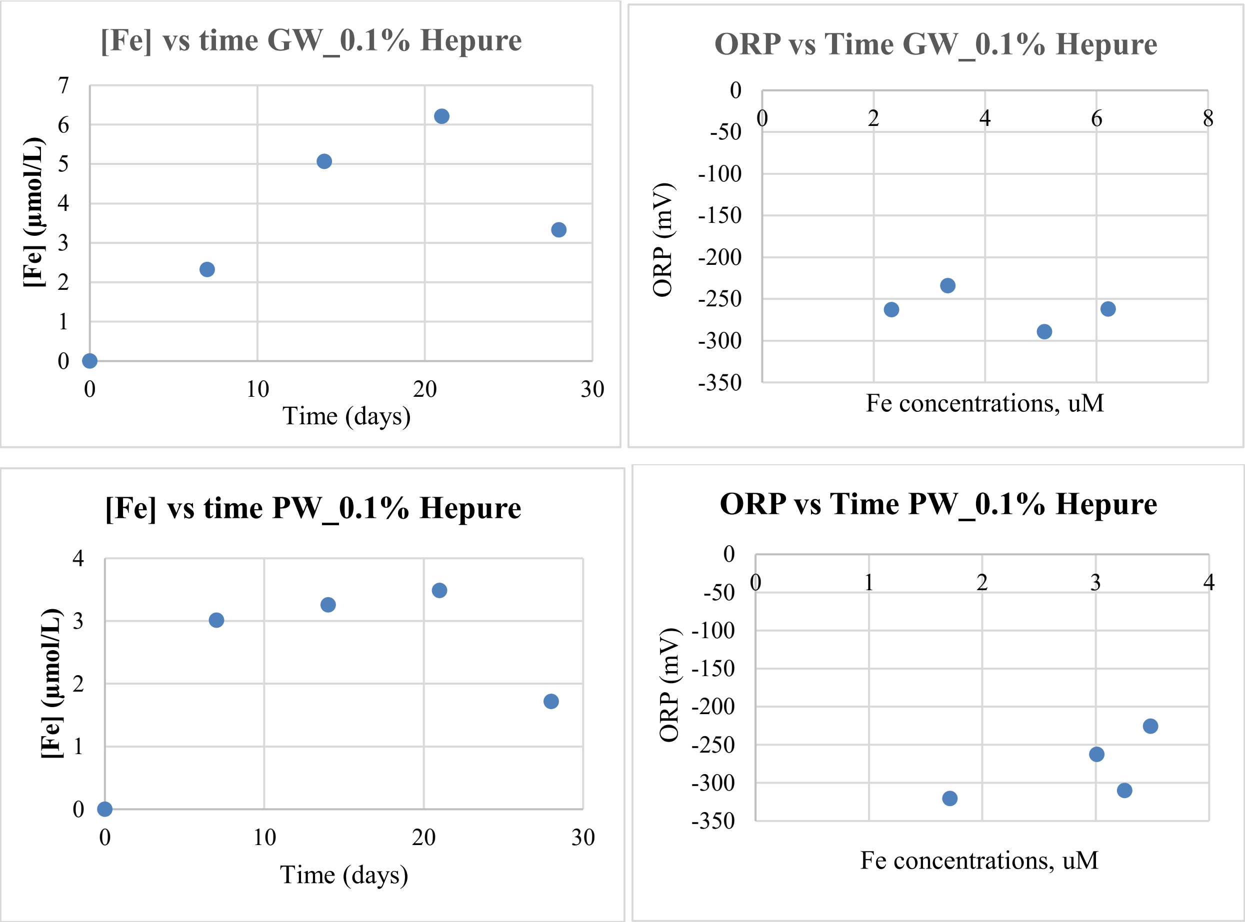

Figure 13. Total iron concentrations vs time and ORP values for samples amended by ZVI in PW and GW synthetic solutions.

Oxidation Reduction Potential (ORP), pH and Dissolved Oxygen (DO)

Readings for pH, ORP and DO are presented in Figure 14. The initial pH of the PW of 8.3 decreased after 7 days to pH 7.6 and then gradually increased during 30 days in the anaerobic conditions to pH 8.3-8.5 for both reductants; these values were not changed under aerobic conditions by the end of the experiment. For GW samples, pH was increased from initial 7.8 to 8.1±0.06 and 8.98±0.05 after 7 days under anaerobic conditions for SMI and ZVI, respectively. By day 30, pH values were stabilized at 9.1-9.14 for both SMI and ZVI. After switching to aerobic conditions, the pH gradually decreased to 7.6±0.2 and 8.22±0.37 by day 64 for SMI and ZVI, respectively.

Measuring the ORP can provide information into the reductive/oxidative behavior of species in the system. The observed trend ORP for GW (0.1% iron reductant amended samples) solutions revealed values ranging from about -200 to -300 mV during the anaerobic period, indicating that reducing conditions were present throughout. The ORP values measured during the aerobic phase were consistent with oxidizing conditions, yielding ORP values ranging from about +200 to +500 mV. The observed trend of the DO concentrations throughout the anaerobic period revealed very low concentrations of about 0.03-0.05 mg/L, while the trend observed throughout the aerobic period revealed an increase of DO concentrations up to 5-6 mg/L (Figure 14).

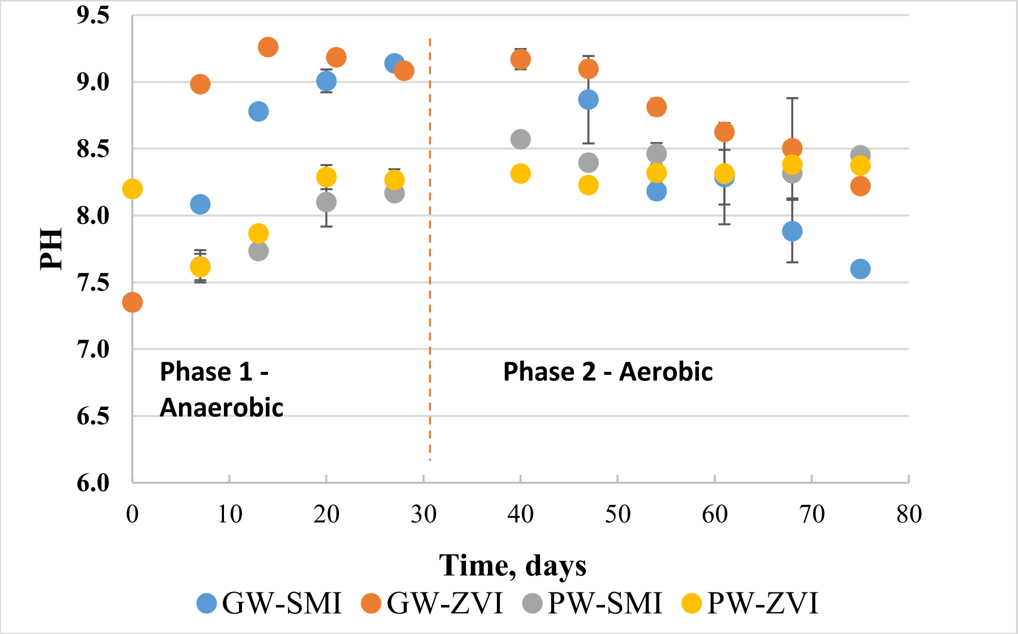
PH
9.5
9.0
8.5
8.0
7.5
7.0
6.5
6.0
0
10
20
30
40
50
60
70
80
Time, days
Phase 1 - Anaerobic
Phase 2 - Aerobic
GW-SMI
GW-ZVI
PW-SMI
PW-ZVI

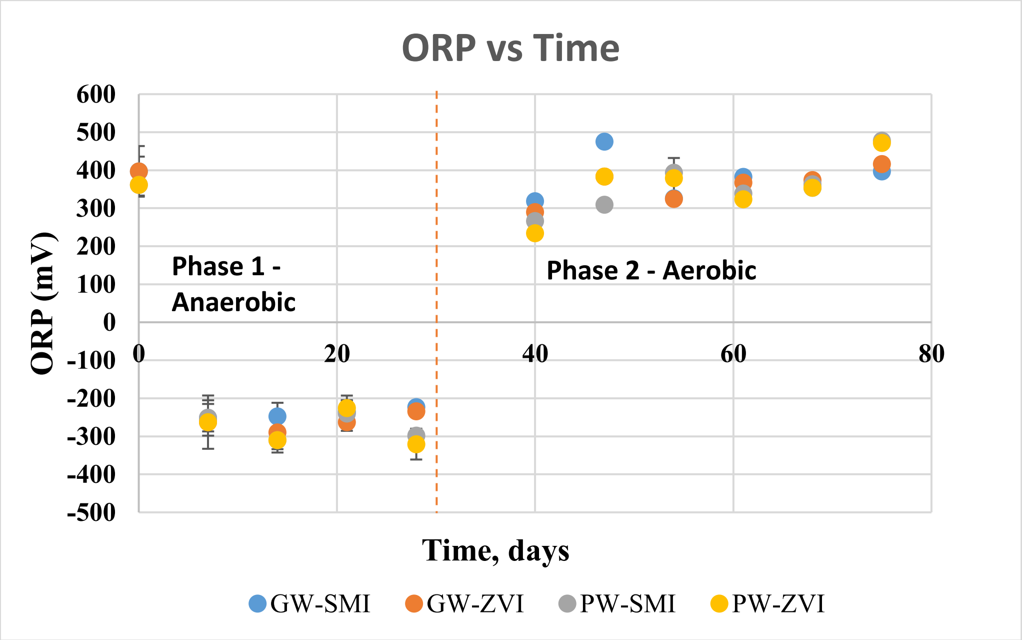
ORP vs Time
ORP (mV)
600
500
400
300
200
100
0
-100
-200
-300
-400
-500
0
20
40
60
80
Time, days
Phase 1 - Anaerobic
Phase 2 - Aerobic
GW-SMI
GW-ZVI
PW-SMI
PW-ZVI

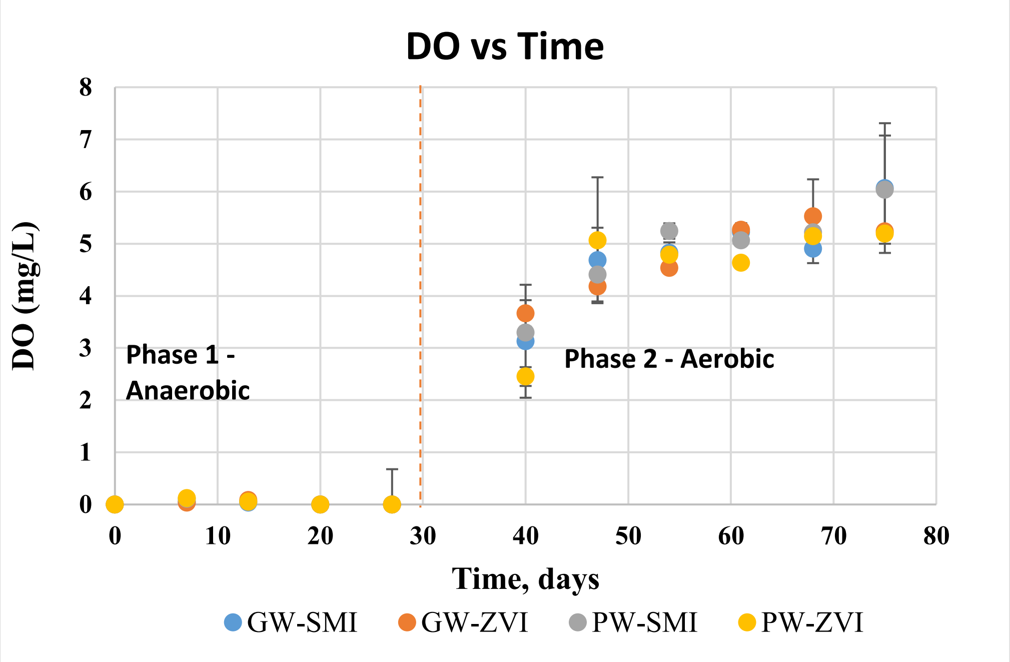

Figure 14. Changes in pH, ORP, and DO content over time. The ORP values were measured against Ag/AgCl reference electrode.

Subtask 1.2: Conclusions

These experiments provided insights on the re-oxidation behavior of immobilized ^{99}Tc, ^{238}U, and NO_3^- with 0.1% Hepure ZVI and SMI. Experimental data revealed that reduction of all contaminants occurred in the presence of both reductants when in anaerobic conditions. The results obtained through ICP-MS analyses showed that in sediment-bearing samples, ZVI was the stronger reductant of U(VI) and Tc(VII) in anaerobic conditions, but SMI-treated samples were found to be more effective in resisting reoxidation of U(VI) and Tc(VII) in aerobic conditions. Sediment-free GW samples treated with SMI were more effective in resisting reoxidation of U(VI) and Tc(VII) in aerobic conditions. The reoxidation of Tc(VII) observed in aerobic conditions was higher in sediment-free compared to sediment-bearing samples.

Both ZVI and SMI were effective in NO_3^- removal by the end of the anaerobic Phase 1. The results do not show the reoxidation of NO_3^- at the end of aerobic Phase 2 and both reductants showed similar removal of NO_3^-. The results obtained through IC revealed that the concentration of NO_2^- was larger in the SMI-amended samples at the end of Phase 1; however, NO_2^- concentrations were similar in samples amended with ZVI or SMI at the end of Phase 2. Measurements of total SO_4^{2-} concetrations in aerobic and anaerobic conditions suggested a decrease of SO_4^{2-} content from the initial value in GW simulant. The decrease in SO_4^{2-} concentrations might be due to formation of iron sulfate minerals, green rust or schwertmannite.

Results obtained through measurements of ORP (mV) in anaerobic conditions supported this data, with average ORP values ranging from -200 to -300 mV; indicating strong reducing conditions. Similarly, the average ORP values in aerobic conditions ranged from +200 to +500 mV, indicating that oxidizing conditions were present throughout.

Future work will involve solid characterization studies of solid samples recovered from batch solutions at the end of each phase and the initiation of the next round of batch experiments using a 1% ZVI and SMI solid to liquid ratio in GW and PW solutions.

Subtask 1.2: References

Agrawal, A., and Tratnyek, P. G., 1995, Reduction of nitro aromatic compounds by zero-valent iron metal: Environmental Science & Technology, v. 30, no. 1, p. 153-160.

Boglaienko, D., Emerson, H. P., Katsenovich, Y. P., and Levitskaia, T. G., 2019, Comparative analysis of ZVI materials for reductive separation of 99Tc (VII) from aqueous waste streams: Journal of hazardous materials, v. 380, p. 120836.

Emerson, H. P., Gebru, A., Boglaienko, D., Katsenovich, Y. P., Kandel,['{: S., and Levitskaia, T. G., 2020, Impact of zero valent iron aging on reductive removal of technetium-99: Journal of Environmental Chemical Engineering, v. 8, no. 3, p. 103767.

Fiedor, J. N., Bostick, W. D., Jarabek, R. J., and Farrell, J., 1998, Understanding the mechanism of uranium removal from groundwater by zero-valent iron using X-ray photoelectron spectroscopy: Environmental science & technology, v. 32, no. 10, p. 1466-1473.

Gephart, R. E., 2003, A short history of Hanford waste generation, storage, and release: Pacific Northwest National Lab.(PNNL), Richland, WA (United States).

Gu, B., Liang, L., Dickey, M., Yin, X., and Dai, S., 1998, Reductive precipitation of uranium (VI) by zero-valent iron: Environmental Science & Technology, v. 32, no. 21, p. 3366-3373.

H Scott, F., 2006, Elements of chemical reaction engineering, Prentice Hall Profesional.

Kobayashi, T., Scheinost, A. C., Fellhauer, D., Gaona, X., and Altmaier, M., 2013, Redox behavior of Tc (VII)/Tc (IV) under various reducing conditions in 0.1 M NaCl solutions: Radiochimica Acta, v. 101, no. 5, p. 323-332.

Lawter, A. R., Garcia, W. L., Kukkadapu, R. K., Qafoku, O., Bowden, M. E., Saslow, S. A., and Qafoku, N. P., 2018, Technetium and iodine aqueous species immobilization and transformations in the presence of strong reductants and calcite-forming solutions: remedial action implications: Science of the Total Environment, v. 636, p. 588-595.

Pearce, C. I., Cordova, E. A., Garcia, W. L., Saslow, S. A., Cantrell, K. J., Morad, J. W., Qafoku, O., Matyáš, J., Plymale, A. E., and Chatterjee, S., 2020, Evaluation of materials for iodine and technetium immobilization through sorption and redox-driven processes: Science of The Total Environment, v. 716, p. 136167.

Reinsch, B. C., Forsberg, B., Penn, R. L., Kim, C. S., and Lowry, G. V., 2010, Chemical transformations during aging of zerovalent iron nanoparticles in the presence of common groundwater dissolved constituents: Environmental science & technology, v. 44, no. 9, p. 3455-3461.

Saslow, S. A., Lawter, A. R., Gartman, B. N., Zhang, Z., Snyder, M., Zhong, L., Cantrell, K. J., and Brown, C. F., 2018, Evaluation of Perched Water Post-Extraction Remedy Technologies: Interim Status Report: Pacific Northwest National Lab.(PNNL), Richland, WA (United States).

Su, C., and Puls, R. W., 2001, Arsenate and arsenite removal by zerovalent iron: effects of phosphate, silicate, carbonate, borate, sulfate, chromate, molybdate, and nitrate, relative to chloride: Environmental science & technology, v. 35, no. 22, p. 4562-4568.

Su, C., and Puls, R. W., 2004, Nitrate reduction by zerovalent iron: effects of formate, oxalate, citrate, chloride, sulfate, borate, and phosphate: Environmental science & technology, v. 38, no. 9, p. 2715-2720.

Szecsody, J. E., Jansik, D. P., McKinley, J. P., and Hess, N. J., 2014, Influence of alkaline co-contaminants on technetium mobility in vadose zone sediments: Journal of environmental radioactivity, v. 135, p. 147-160.

Szecsody, J. E., Truex, M. J., Zhong, L., McKinley, J. P., Qafoku, N. P., Lee, B. D., and Saurey, S. D., 2015, Remediation of technetium in vadose zone sediments using ammonia and hydrogen sulfide gases: Vadose Zone Journal, v. 14, no. 7, p. 1-12.

Yang, G. C., and Lee, H.-L., 2005, Chemical reduction of nitrate by nanosized iron: kinetics and pathways: Water research, v. 39, no. 5, p. 884-894.

Zhao, X., Liu, W., Cai, Z., Han, B., Qian, T., and Zhao, D., 2016, An overview of preparation and applications of stabilized zero-valent iron nanoparticles for soil and groundwater remediation: Water research, v. 100, p. 245-266.

Subtask 1.3: Evaluation of Competing Attenuation Processes for Mobile Contaminants in Hanford Sediments

Subtask 1.3: Introduction

Weapons production at the Hanford Site has created large volumes of legacy radioactive and chemical waste. Some contaminants were released to the environment through discharges to liquid disposal sites, cribs and trenches, or accidental leakages from single-shell tanks. Contaminants, including uranium (U), technetium-99 (^{99}Tc), iodine-129 (^{129}I), chromium (Cr) and nitrate (NO_3^-), migrated to the vadose zone creating subsurface plumes at the Hanford 200 Area located in the Central Plateau. These mobile contaminants persist in the subsurface and have potential to enter the groundwater via downward migration through the vadose zone. If allowed to reach the groundwater, contaminants will flow towards the Columbia River (a major water resource in the Pacific Northwest and a path for public exposure). U is in the form of hexavalent uranium [U(VI)] primarily existing as tertiary neutral and anionic carbonate complexes ($Ca_2UO_2(CO_3)_3$ aq and $CaUO_2(CO_3)_3^{2-}$) in the natural oxic vadose zone environment at solution pH of ~ 8 (Gorman-Lewis, D. et al, 2009). Tc is primarily in the form of anionic mobile pertechnetate (TcO_4^-) under oxidizing conditions (Peretyazhko, T. S. et al, 2012). Chromium is typically present in the hexavalent form (the most mobile form of chromium) [Cr(VI)] as chromate (CrO_4^{2-}) (Zachara, J. et al, 2004). Major aqueous species of iodine (I) have been distributed as 76% IO_3^-, 22% organo-iodine, and 2% I^- (Xu, C. et al, 2015). NO_3^- is stable and mobile in oxygenated environments (Martin, C. J., 2011).

These co-contaminants (all above the maximum contaminant level [MCL]) in subsurface plumes at the 200 Area are currently being remediated with pump and treat technology. Once active remediation is completed, a transition to more passive approaches, such as monitored natural attenuation (MNA), is needed. This will allow us to determine if the concentrations of these contaminants are behaving as predicted and if mobility is reduced by natural processes. Effective MNA requires a thorough understanding of the contaminant immobilization processes that keep the contaminants stable and resistant to remobilization during any changes in environmental conditions or groundwater chemistry. Quantifying contaminant attenuation processes via competitive adsorption mechanisms on vadose zone sediment will assess competitive attenuation processes. This was initiated by conducting batch adsorption studies of Cr, I-127, Tc-99, and U(VI) in artificial groundwater (AGW) onto Hanford Formation sediment and a competition batch study with Cr and I-127 in AGW onto Hanford Formation sediment. Attention was turned towards U(VI) and the effect aqueous speciation has on its ability to adsorb to the sediment at the site.

Many studies have been conducted to understand the adsorption mechanisms of U(VI) onto a variety of different minerals and even natural sediment. Their findings have indicated that in the pH range of 6-9, the presence of calcium carbonate in sediment (from calcite) reduces U (VI) ability to sorb. This is due to the blockage of reactive sites by Ca^{2+} and the formation of neutral uranyl complexes ($Ca_2UO_2(CO_3)_3^0$(aq)) (Stewart, B. D. et al, 2010; Zheng, Z. et al, 2003; Dong, W. et al, 2005; Fox, P. M. et al, 2006). However, there is still a need to incorporate the presence of collocated contaminants into these studies to understand the true adsorption capacity of sediment present at the Hanford Site. These contaminants include Tc-99, iodate, Cr (VI), and NO_3^- which may compete for reactive sites on the same minerals in the vadose zone. There, mineralogy is mainly comprised of quartz and feldspars; the finer-grained sediment includes a variety of phyllosilicates (Um, W. et al, 2010). The objectives of this research effort are to provide (i) a better understanding of the species-dependent mechanisms of U(VI) interaction with sediments in the absence and presence of co-contaminants; (ii) the necessary parameters to predict U(VI) mobility in the vadose zone; and (iii) the technical basis for MNA at the site.

Subtask 1.3: Objectives

This research is focused on competitive adsorption between contaminants of concern onto the Hanford Formation vadose zone sediment as an assessment of their mobility and fate.

Subtask 1.3: Methodology

After completion of solid characterization (described in the 2020 year-end report), competitive adsorption experiments were conducted with the ≤2 mm bulk size fraction. Individual batch sorption experiments with Cr, I-127, Tc-99, and U(VI) and a competitive adsorption experiment with Cr and I-127 were initiated using the following methodology. Artificial groundwater (AGW, 2L) used in the experiment was created using the formulation found in Table 9. AGW was placed in 5 different 100 mL bottles and were then spiked with the concentrations of Cr, I, Tc, and U listed in Table 10. These five bottles were stored in the refrigerator.

Table 9. AGW Formulation (Serne, R. et al, 2015)

Constituent	Formula Weight (g/mol)	Conc. (mmol/L)	Mass (g/L)
$NaHCO_3$	84.006	1.586	0.1333
$KHCO_3$	100.114	0.1231	0.0123
$MgSO_4{\cdot}7H_2O$	246.466	0.3660	0.0902
$MgCl_2{\cdot}6H_2O$	203.351	0.2468	0.0502
$CaCl_2{\cdot}2H_2O$	147.036	1.0708	0.1574
1M HCl add 0.150 mL for pH 7.8			

Table 10. Concentrations of Each Contaminant Used in Experiments (Hanford Site Groundwater Monitoring Report for 2018; Hanford Site 2018 Pump and Treat Report)

Contaminant	I-127, µg/L	Tc-99, µg/L	Cr(VI) µg/L	NO_3^- mg/L	U(VI) mg/L	U(VI) µg/L
1	100	2.6	532	1990	99	9000
2	80	2.6	400	1600	80	5000
3	60	2.6	300	1200	60	2500
4	40	2.6	200	800	40	1000
5	20	2.6	100	400	20	100
6						50

Tabletop dried sediment (20.00±0.02 g) was placed in 50 mL centrifuge tubes in triplicate for each concentration. Spiked AGW (20.0±0.1 mL) was then added to the sediments. A control without any sediment was also done for each concentration to measure the amount of contaminant absorbed on the tube and the cap. A control with non-spiked AGW was also conducted to establish the concentration of water soluble naturally occurring I-127 currently present in the sediment. Centrifuge tubes were then placed on an end-over-end tube revolver at 30 rpm as shown in Figure 15. For preliminary sorption equilibrium experiments, samples were taken at the following times to establish equilibrium time: 1 hour, 3 hours, 8 hours, 1 day, 2 days, 3 days, 4 days, 5 days, and 7 days after the addition of the spiked AGW to sediment. During these sampling times, the sediment was allowed to settle for up to 40 minutes before 0.5mL of supernatant was taken and filtered through a 0.2 mm syringe filter into a 1.5 mL centrifuged vial. I-127 samples were stored in the freezer while all other samples were stored in the refrigerator prior to chemical analyses.

Figure 15. Sediment samples in an end-over-end tube revolver at 30 rpm.

Cr, Tc-99, and U(VI) samples from individual and competitive batch sorption experiments were diluted 10x with 2% HNO_3^-. I samples from individual and competitive batch sorption experiments were diluted 10x with 0.1% TMAH. All samples were then analyzed via a ThermoFisher Scientific iCAP RQ inductively coupled plasma-mass spectrometer (ICP-MS).

Due to change in the sediment to solution ratio during the batch sorption experiments, U(VI) batch adsorption studies were repeated with sacrificial sampling. AGW was placed in 50 mL centrifuge tubes and spiked with concentrations of U(VI) listed in Table 10. The pH of solutions was measured using a Thermo Scientific Orion Versastar pH meter with a Thermo electrode calibrated using standard pH buffers 4.01, 7.00, 10.00 (Fisher). After minor adjustments with NaOH (0.1 M) and HCl (1 M), the final pH for each concentration was 7.90 ± 0.03 for the lower concentration range and 7.94 ± 0.03 for the higher concentration range. Tabletop dried sediment (0.752 g ±0.001 g) was placed in 15 mL polypropylene centrifuge tubes in triplicate. Spiked AGW (0.750±0.001 mL) was added to the sediments. A control without any sediment was also prepared to measure the amount of U(VI) absorbed on the tube and the cap. Centrifuge tubes were placed on an end-over-end tube revolver at 8 rpm, as shown in Figure 16.

Figure 16. Sediment samples in an end-over-end tube revolver at 8 rpm.

For preliminary sorption equilibrium experiments, samples were sacrificed at the following times to establish equilibrium time: 1 hour, 3 hours, 8 hours, 1 day, 2 days, 3 days, 4 days, 5 days, 7 days, and 14 days after the addition of the spiked AGW to sediment. During these sampling times, the samples were centrifuged at 4,500 RPM for 30 minutes (Sorvall ST Thermo Scientific Centrifuge). The supernatant was removed from the sediment and placed in a new vial for storage. Samples were stored in the refrigerator before chemical analyses.

Samples collected during the batch adsorption experiment were diluted with 2% nitric acid (HNO_3) prior to analyses on the ThermoFisher Scientific iCAP RQ inductively coupled plasma - mass spectrometer (ICP-MS). U(VI) samples (20-100 ppm, 1000-9000 ppb and 50-100 ppb) were diluted 250x,100x, and 10x with 2% HNO_3 respectively.

Geochemical speciation modeling using the Geochemist's Workbench software (version 12) was conducted to determine the distribution of uranyl aqueous species and to analyze the saturation state of uranium in AGW. Visual MINTEQ (thermo-minteq) thermodynamic database formatted by Jon Petter Gustafsson (KTH Royal Institute of Technology) was used in this modeling. Artificial groundwater composition included four cations and one anion along with counter ions. Concentrations of uranium ranged from 50 ppb-100 ppm. Dissolved oxygen was set at 8.0 mg/L at a constant temperature of 25°C. The speciation modeling assumed that the system was open to the atmosphere by including the presence of carbon dioxide. This best represents the environment in the vadose zone at the Hanford site.

The partition (or distribution) coefficient, K_d, a measure of sorption of contaminants to sediments, was determined from batch adsorption data. It is defined as the ratio of the concentration of the contaminant adsorbed to the solid ([s]) to the concentration of the contaminant remaining in solution ([C]) at equilibrium as shown in Equation 1.

$$K_{id} = \frac{[S]}{[C]} \qquad \text{Eq 1}$$

Removal percentage of contaminants from solution was also evaluated by using Equation 2:

$$Removal\ \% = \frac{(C_0 - C_e)}{C_0} x100 \qquad \text{Eq 2}$$

where C_0 is the initial concentration of contaminant in solution and C_e is the concentration of contaminant in solution at equilibrium. Adsorption data was fit to the Langmuir and Freundlich models as shown in Equations 3 and 4 respectively:

$$q_e = \frac{K q_m C_e}{1 + K C_e} \qquad \text{Eq 3}$$

$$q_e = K' C_e^n \qquad \text{Eq 4}$$

where q_e is the concentration of contaminant on the sediment at equilibrium, K is the Langmuir and Freundlich constant, q_m, is the maximum concentration of contaminant that can be adsorbed to the sediment, and n is the Freundlich exponential constant. The Langmuir model is generated from kinetic parameters and assumes homogenous adsorption sites and only considers a system with a monolayer or less. It also assumes that there is no interaction between sites or the sorbate (our contaminants). The Freundlich model is an empirical derivation and considers heterogeneous type adsorption sites. It also considers systems with multilayer adsorption.

Adsorption data was also fit to the pseudo-first, pseudo-second order, and intraparticle diffusion kinetic models as shown in equations 5-7 respectively:

$$q_t = q_e(1 - e^{-k_1 t}) \qquad \text{Eq 5}$$

$$q_t = \frac{k_2 q_e^2 t}{1 + k_2 q_e t} \qquad \text{Eq 6}$$

$$q_t = K_t t^{1/2} + C \qquad \text{Eq 7}$$

where k_1, k_2, k_t are the pseudo first order, pseudo second order, and intraparticle rate constants. q_t and q_e are the amounts of adsorbed dye at time t and the equilibrium time and C is the intercept that represents the boundary layer thickness.

Subtask 1.3: Resuls and Discussion

It appears that the co-location of Cr and I-127 has a minor impact on the adsorption capacity of the sediment for both contaminants. The percent removal and log Kd of Cr as shown in Figure 17 is not altered, most likely due to the small concentrations used in the batch studies. The same trend is present for I-127 in Figure 18. However, it appears that capacity of the sediment is reached faster than if the contaminants were present separately.

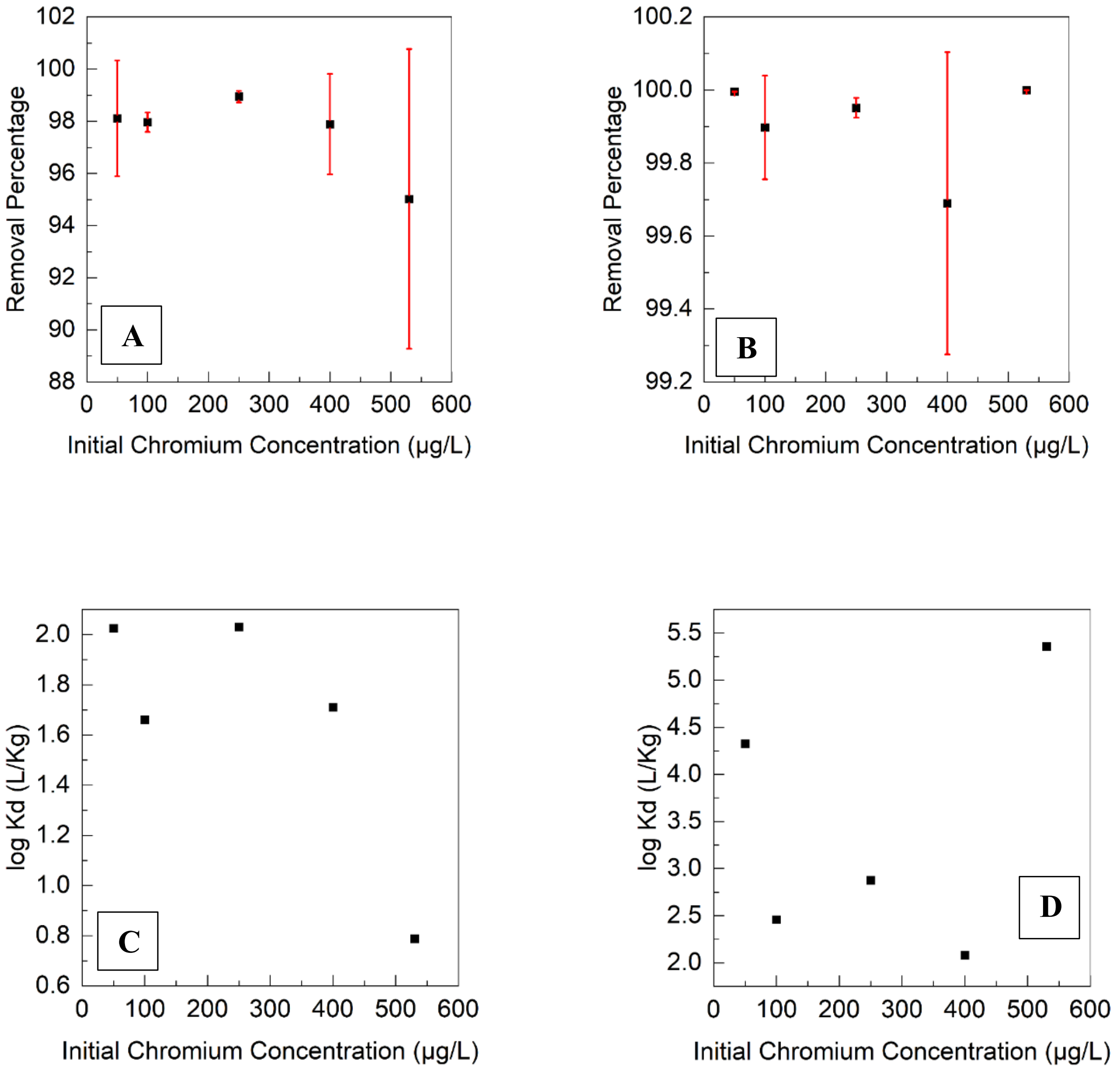

Figure 17. A and C: Removal percentage and log Kd vs initial Cr only concentration (50-530 µg/L); B and D: Removal percentage and log Kd vs Initial Cr in the presence of I-127 concentration (50-530 µg/L).

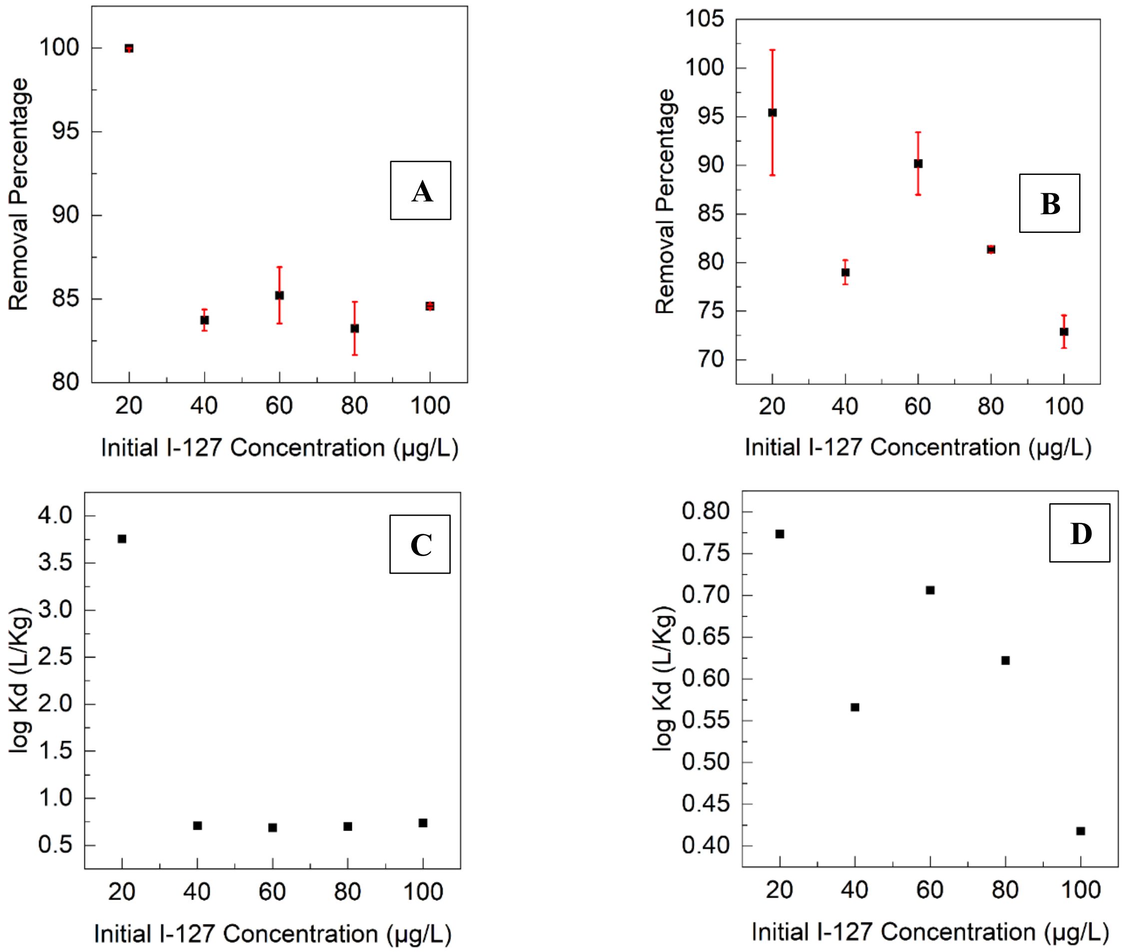

Figure 18. A and C: Removal percentage and log Kd vs Initial I-127 only concentration (20-100 µg/L); B and D: Removal percentage and log Kd vs Initial I-127 in the presence of Cr concentration (20-100 µg/L).

The pseudo-first order kinetic model appears to best fit data for Cr alone and in the presence of I-127. The regression coefficients can be found in Table 11. A pseudo-second order kinetic model appears to best fit data for I-127 alone and in the presence of Cr. The regression coefficients can be found in Table 12.

Table 11. Pseudo-First Order (PFO) and Pseudo-Second Order (PSO) Kinetics of Cr Alone and in the Presence of I-127 Spiked AGW Adsorption onto Hanford Formation Sediment

Concentration (ppb)	**Regression Coefficient, R^2**			
	Cr PFO	**Cr PSO**	**Cr+I-127 PFO**	**Cr+I-127 PSO**
530	0.99	0.98	0.99	0.97
400	0.98	0.96	0.99	0.97
250	0.61	0.85	0.99	0.97
100	0.99	0.97	0.98	0.95
50	0.98	0.95	0.97	0.92

Table 12. Pseudo-First Order (PFO) and Pseudo-Second Order (PSO) Kinetics of I-127 alone and in the Presence of Cr Spiked AGW Adsorption onto Hanford Formation Sediment

Concentration (ppb)	Regression Coefficient, R^2			
	I-127 PFO	I-127 PSO	I-127+Cr PFO	I-127+Cr PSO
100	0.80	0.91	0.80	0.91
80	0.69	0.85	0.77	0.89
60	0.76	0.89	0.74	0.85
40	0.57	0.78	0.71	0.84
20	0.77	0.87	0.79	0.89

Speciation results presented in Figure 19 predicted that $Ca_2UO_2(CO_3)_3{}^0(aq)$ and $CaUO_2(CO_3)_3{}^{2-}$ are the dominant uranyl aqueous species present in AGW. The speciation modeling predicted the over saturation/precipitation formation (Q/K >1) of swartzite (calcium magnesium uranyl carbonate mineral). This indicates that not all aqueous U(VI) removal is due to adsorption, and some is due to precipitation in the form of these minerals. All other minerals were considered undersaturated in the system (Q/K <1).

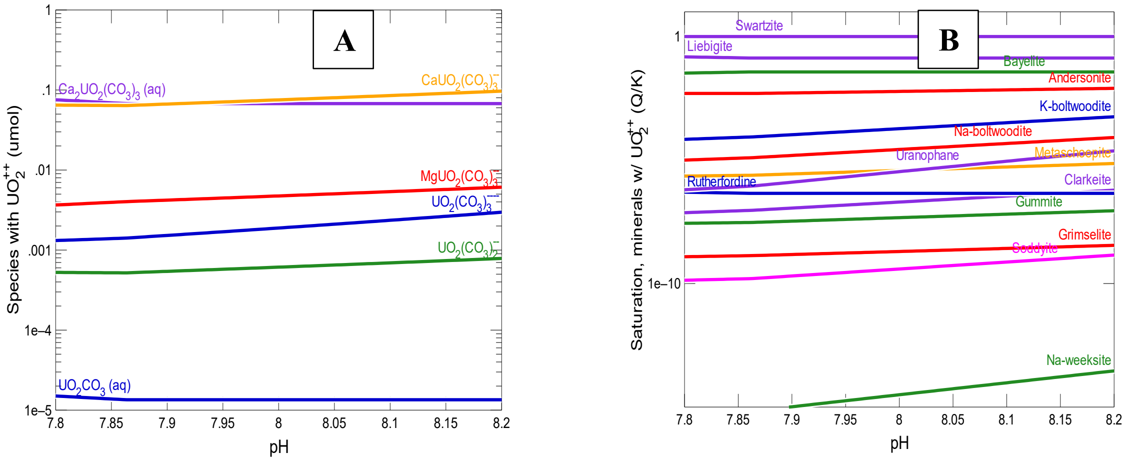

Figure 19. A: Uranium aqueous species; B: Saturation indices of uranium-bearing mineral phases as a function of pH. Sample composition includes 1.586 mmol/L of Na^+, 0.1231mmol/L K^+, 0.62 mmol/L Mg^{2+}, 1.0708 mmol/L Ca^{2+}, 0.366 mmol/L $SO_4{}^{2-}$, and 10 g of quartz.

Due to change in the sediment to solution ratio during the batch sorption experiments, U(VI) batch adsorption studies were repeated with sacrificial sampling. Figure 20 illustrates the difference in results between sampling strategies. Percent removal and log Kd of U(VI) decreased in the sacrificial sampling compared to the first strategy.

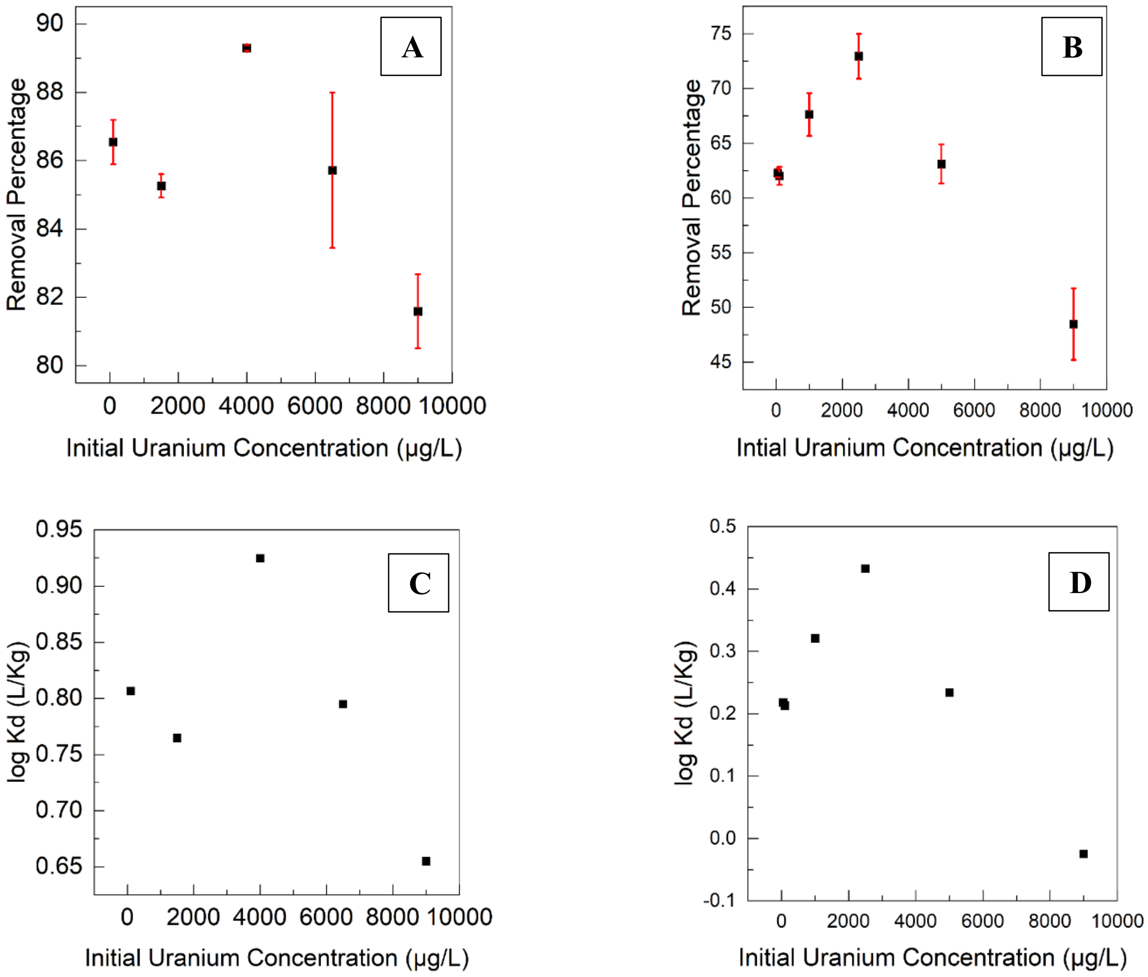

Figure 20. A and C: Removal percentage and log Kd vs initial U(VI) concentration (100-9000 µg/L); B and D: Removal percentage and log Kd vs Initial U(VI) (100-9000 µg/L) sacrificial samples.

Sacrificial sampling continued to be used for the U(VI) batch adsorption experiment with higher concentrations (20-100 mg/L). Sorption becomes weaker at higher initial U(VI) concentrations and can be seen in Figure 21. This agrees with previous observations (Payne, T. E., 1999; Waite, T.D. et al, 2000; Giammar, D. E. and Hering, J. G., 2001; Ho, C. H. and Doern, D. C, 1985; Zheng, Z. et al, 2003).

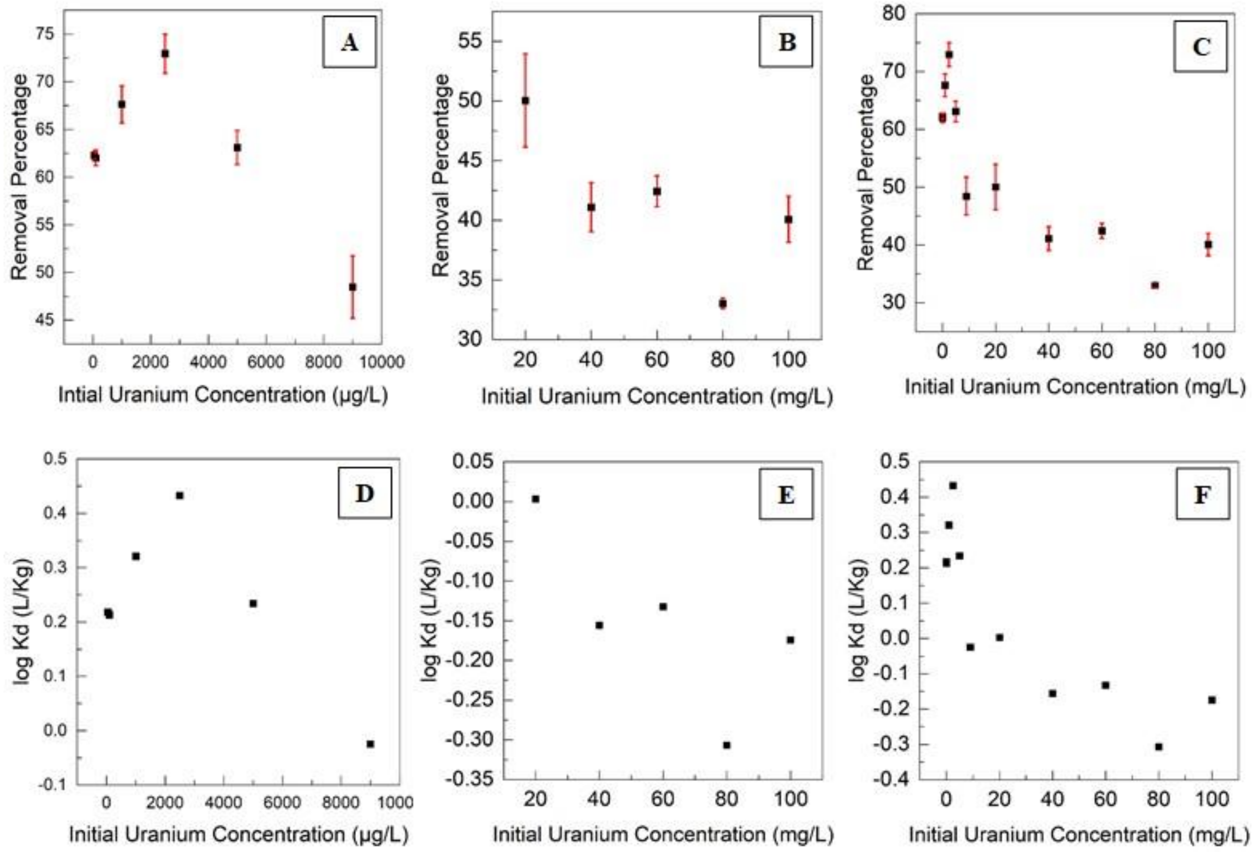

Figure 21. A and D: Removal percentage and log Kd vs Initial U(VI) concentration (µg/L) for initial concentration range of 50-9000 µg /L; B and E: Removal percentage and log Kd vs Initial U (VI) concentration (mg/L) for initial concentration range of 20-100 ppm; C and F: Removal percentage and log Kd vs Initial U(VI) concentration (mg/L) for initial concentration range of 0.05-100 mg/L.

The small amount of adsorption observed in batch experiments can be assumed to be due to the dominant $Ca_2UO_2(CO_3)_3^0(aq)$ and $CaUO_2(CO_3)_3^{2-}$ species. It is unlikely that $Ca_2UO_2(CO_3)_3^0(aq)$ will be able to adsorb well to the surface of quartz due to its neutral charge and is unlikely to bond with the surface via the Ca atoms because they are already bonded to oxygen atoms of the carbonate anions (Bernhard, G. 2001). For these same reasons, $CaUO_2(CO_3)_3^{2-}$ is also unlikely to bond to the surface of quartz.

Fe oxides were most likely responsible for the majority of U(VI) adsorption to Hanford Formation sediment. This is due to their high specific areas as high as several hundreds of m^2g^{-1} and their point of zero charge being located in the neutral or slightly basic pH range (Cornell, R. and Schwertmann, U., 1996; Sposito, G., 1984; Sposito, G., 1989). Unlike quartz, Ca has the ability to adsorb to the surface of ferrihydrite (Kinniburg, A. D. G. et al, 1975; Dempsey, B. A. and Singer, P. C., 1980; Cowan, C. E. et al, 1991). This can lead to a change in surface charge on ferrihydrite and also cause a decrease in U(VI) ability to adsorb to its surface.

Pseudo-first and pseudo-second order kinetic models were investigated. The pseudo-second order gave the best fit in most cases; kinetic models and their respective correlation coefficients are illustrated in

Table 13. This agreed with previous findings (Shi, Y. L. et al, 2019).

Table 13. Pseudo-First Order (PFO) and Pseudo-Second Order (PSO) Kinetics of U(VI) Spiked AGW Adsorption onto Hanford Formation Sediment

Concentration (ppm)	Regression Coefficient R^2	
	PFO	PSO
100	0.87	0.86
80	0.78	0.78
60	0.87	0.93
40	0.93	0.17
20	0.88	0.92
9	0.88	0.95
5	0.87	0.94
2.5	0.91	0.96
1	0.94	0.99
0.1	0.92	0.97
0.05	0.92	0.97

Subtask 1.3: Conclusions

The co-location of I-127 and Cr had a minor impact on the sediment's capacity for adsorption. Specifically, the maximum adsorption decreased by 1 and 3 orders of magnitude for I-127 and Cr respectfully. I-127 followed the pseudo-second order kinetic model and Cr followed the pseudo-first order kinetic model. Uranium (VI) adsorption to Hanford formation sediment under site relevant conditions is minimal. This is due to the slightly alkaline pH and the presence of calcium and carbonate causing the formation of $Ca_2UO_2(CO_3)_3^0$(aq) and $CaUO_2(CO_3)_3^{2-}$. These species make it difficult for U(VI) to sorb to minerals present in the sediment. Overall, this indicates that U(VI), I-127 and Cr present in the vadose zone at the Hanford Site is relatively mobile. This should be considered while developing future MNA procedures. Future work will include a competitive batch adsorption experiment with the co-location of U(VI), NO_3^-, Cr, I-127, and Tc-99. Solid phase characterization of post treated sediment will also be conducted.

Subtask 1.3: References

Gorman-Lewis, D.; Shvareva, T.; Kubatko, K.-A.; Burns, P. C.; Wellman, D. M.; Mcnamara, B.; Szymanowski, J. E. S.; Navrotsky, A.; Fein, J. B. Thermodynamic Properties of Autunite , Uranyl Hydrogen Phosphate , and Uranyl Orthophosphate from Solubility and

Calorimetric Measurements. Environ. Sci. Technol. 2009, 43 (19), 7416–7422. https://doi.org/10.1021/es9012933.

Peretyazhko, T. S.; Zachara, J. M.; Kukkadapu, R. K.; Heald, S. M.; Kutnyakov, I. V; Resch, C. T.; Arey, B. W.; Wang, C. M.; Kovarik, L.; Phillips, J. L.; et al. Pertechnetate (TcO4-) Reduction by Reactive Ferrous Iron Forms in Naturally Anoxic, Redox Transition Zone Sediments from the Hanford Site, USA. Geochim. Cosmochim. Acta 2012, 92, 48–66. https://doi.org/10.1016/j.gca.2012.05.041.

Zachara, J.; Ainsworth, C.; Brown, G.; Catalano, J.; McKinley, J.; Qafoku, O.; Smith, S.; Szecsody, J.; Traina, S.; Warner, J. Chromium Speciation and Mobility in a High Level Nuclear Waste Vadose Zone Plume. Geochim. Cosmochim. Acta 2004, 68 (1), 13–30. https://doi.org/10.1016/S0016-7037(03)00417-4.

Xu, C.; Kaplan, D. I.; Zhang, S.; Athon, M.; Ho, Y. F.; Li, H. P.; Yeager, C. M.; Schwehr, K. A.; Grandbois, R.; Wellman, D.; et al. Radioiodine Sorption/Desorption and Speciation Transformation by Subsurface Sediments from the Hanford Site. J. Environ. Radioact. 2015, 139, 43–55. https://doi.org/10.1016/j.jenvrad.2014.09.012.

Martin, C. J. Overview of Hanford Hydrogeology and Geochemistry; 2011.

Stewart, B. D.; Mayes, M. A.; Fendorf, S. Impact of Uranyl - Calcium - Carbonato Complexes on Uranium(VI) Adsorption to Synthetic and Natural Sediments. Environ. Sci. Technol. 2010, 44 (3), 928–934. https://doi.org/10.1021/es902194x.

Zheng, Z.; Tokunaga, T. K.; Wan, J. Influence of Calcium Carbonate on U(VI) Sorption to Soils. Environ. Sci. Technol. 2003, 37 (24), 5603–5608. https://doi.org/10.1021/es0304897.

Dong, W.; Ball, W. P.; Liu, C.; Wang, Z.; Stone, A. T.; Bai, J.; Zachara, J. M. Influence of Calcite and Dissolved Calcium on Uranium(VI) Sorption to a Hanford Subsurface Sediment. Environ. Sci. Technol. 2005, 39 (20), 7949–7955. https://doi.org/10.1021/es0505088.

Fox, P. M.; Davis, J. A.; Zachara, J. M. The Effect of Calcium on Aqueous Uranium(VI) Speciation and Adsorption to Ferrihydrite and Quartz. Geochim. Cosmochim. Acta 2006, 70 (6), 1379–1387. https://doi.org/10.1016/j.gca.2005.11.027.

Um, W.; Icenhower, J. P.; Brown, C. F.; Serne, R. J.; Wang, Z.; Dodge, C. J.; Francis, A. J. Characterization of Uranium-Contaminated Sediments from beneath a Nuclear Waste Storage Tank from Hanford, Washington: Implications for Contaminant Transport and Fate. Geochim. Cosmochim. Acta 2010, 74 (4), 1363–1380. https://doi.org/10.1016/j.gca.2009.11.014.

Serne, R.; Westik, J.; Williams, B.; Jung, H.; Wang, G. Simulated LAW Cast Stone Monoliths; Richland, Washington, 2015.

Hanford Site Groundwater Monitoring Report for 2018; Richland, Washington, 2019.

Hanford Site 2018 Pump and Treat Report; Richland, Washington, 2019.

Payne, T. E. Ph.D. Dissertation, University of South Wales, 1999.

Waite, T. D.; Davis, J. A.; Fenton, B. R.; Payne, T. E. No Title. Radiochim. Acta 2000, 88, 687–693.

Giammar, D. E.; Hering, J. G. Time Scales for Sorption - Desorption and Surface Precipitation of Uranyl on Goethite. Environ. Sci. Technol. 2001, 35 (16), 3332–3337. https://doi.org/10.1021/es0019981.

Ho, C. H.; Doern, D. C. No Title. Can. J. Chem 1985, 63, 1100–1104.

Bernhard, G. Uranyl(VI) Carbonate Complex Formation: Validation of the Ca2UO2(CO3)3(Aq.) Species. Radiochim. Acta 2001, 89, 511–518.

Cornell, R.; Schwertmann, U. The Iron Oxides; VCH Publ, Weinheim, 1996.

Sposito, G. The Surface Chemistry of Soils; Oxford University Press: New York, 1984.

Sposito, G. The Chemistry of Soils; Oxford University Press: New York, 1989.

Kinniburg, A. D. G.; Jackson, M. L.; Syers, J. K. Selective Sorption of Trace Amounts of Calcium and Strontium by Hydrous Oxides of Iron and Aluminum. Soil Sci. Soc. Amer. Proc 1975, 39, 464–470.

Dempsey, B. A.; Singer, P. C. The Effects of Calcium on the Adsorption of Zinc by MnOx(s) and Fe(OH)3(Am). In Contaminants and Sediments, vol 2 Ann Arbor Science; 1980; pp 333–352.

Cowan, C. E.; Zachara, J. M.; Resch, C. T. Cadmium Adsorption on Iron Oxides in the Presence of Alkaline-Earth Elements. Environ. Sci. Technol. 1991, 25 (3), 437–446. https://doi.org/10.1021/es00015a009.

Shi, Y. L.; He, J.; Yang, X.; Zhou, W.; Wang, J.; Li, X.; Liu, C. L. Sorption of U(VI) onto Natural Soils and Different Mineral Compositions: The Batch Method and Spectroscopy Analysis. J. Environ. Radioact. 2019, 203 (March), 163–171. https://doi.org/10.1016/j.jenvrad.2019.03.011.

Subtask 1.4: Experimental Support of Lysimeter Testing

Subtask 1.4: Introduction

Vitrification is one of the preferred technologies to solidify millions of gallons of mixed radioactive waste by the U.S. Department of Energy (DOE). Vitrification involves melting waste materials with glass-forming additives to immobilize contaminants in the structure of a final vitreous product. Borosilicate glasses immobilize larger quantities of actinides, are less corrosive compared to molten phosphate glasses, and are considered a leading candidate for a permanent disposal in geologic repositories (Grambow, 2006; Ojovan and Lee, 2011). The chemical durability of borosilicate glasses expressed as a dissolution rate, k (g $m^{-2}day^{-1}$), is the most important requirement for acceptance of glass waste forms for geological disposal (Jantzen et al., 2010).

The corrosion of glass is traditionally evaluated using ASTM Method C1662-18, *Standard Practice for Measurement of the Glass Dissolution Rate Using the Single Pass Flow Through (SPFT) Test Method* and the static Product Consistency Test (PCT) (Standard, 2014). The rate of corrosion is then calculated from elemental analysis of the glass components in a solution. The mechanisms of corrosion can be explored using surface characterization techniques to document details of alteration layers thickness and composition.

One of the planned configurations at Hanford Field Lysimeter testing units is a co-disposal of grout waste forms above glass waste forms. The grout waste forms placed above the glass is expected to strongly affect both the glass corrosion mechanisms and rate. It is presumed that the alkaline water resulting after contact with the grout waste forms may increase the dissolution rate of the glass waste forms below and pre-experimental modeling suggested such behavior. The grout-contacted water has elevated pH (~12) and contains dissolved species from the grout (e.g., Si, Al, Ca, K) that may affect the rate of glass dissolution through a common ion effect or precipitation reactions. In the presence of silicon, the observed drop in the alteration rate can be associated with the formation of the silica gel that restricts water accessibility to the pristine glass (Frugier et al., 2009; Gin, 2001; Jégou et al., 2000). If the pore water composition contacting the glass is dominated by the grout, the formation of calcium-silicate-hydrates is expected due to a very strong affinity between calcium and silica gels in alkaline media (Armelao et al., 2000).

Subtask 1.4: Objectives

The objective of this study is to determine the effect of temperature, pH and dissolved components on the borosilicate glass dissolution rate in the presence of grout-contacted solution. This would help to evaluate if the dissolution behavior of the glass is controlled by a pH-mediated effect by the sediment or by the chemical makeup of the grout-contacted groundwater. The results of these experiments will provide information to support the design of future FTLF units to investigate the dissolution of waste forms at the Hanford Site Integrated Disposal Facility (IDF).

Subtask 1.4: Methodology

Materials

The glass used in this study was borosilicate ORLEC28 glass which is one of the two glasses being tested in the FLTF (Neeway et al., 2018). The grout used to prepare the grout-contacted solutions was Cast Stone (47 wt. % ground granulated blast furnace slag, 45 wt. % class F fly ash and 8 wt. % ordinary Portland cement) which is used to immobilize simulated LAW and its fabrication is described elsewhere (Asmussen et al. 2018). Buffer solution with pH 12 was prepared by dissolving LiCl and LiOH in DI water (both were purchased from Fischer Scientific). Sodium metasilicate nonahydrate (Fischer Scientific) was used to prepare silicon-amended solution (~ 5 mg/L Si) and ACS grade 67-70 wt. % HNO_3 reagent was used for solution preparation and analytical measurements.

Preparation of glass and grout

The bulk glass was crushed with an agate mortar and pestle and sieved to the desired size fraction 149 - 74 µm (-100 to +200 mesh). Glass powder was washed with DI water and ethanol according to the *Section 19.6* of *ASTM C1285-14* to remove fines. The glass particles were then dried in an oven overnight at 90ºC and, finally, tested by SEM for the absence of any fines adhered to the surface of glass particles. The grout-contacted solution was prepared by first crushing the bulk grout sample with a hammer and sieving the powder to $\leq$2 mm particle size. DI water (1000.0 g) was contacted with the powdered grout (25.0 g) for 7 days on a mechanical shaker. The filtrate with pH 12.40 ± 0.08 was used as a grout-contacted solution.

Collection and analysis of samples

Corrosion of the glass was monitored using ASTM Method C1662-18, *Standard Practice for Measurement of the Glass Dissolution Rate Using the Single Pass Flow Through (SPFT) Test Method and* and the static Product Consistency Test (PCT) (Standard, 2014). The SPFT samplings were performed using an IS-95 Interval sampler with a 4-column adapter (Fischer Scientific). An Isometric Peristaltic Pump (IPC Series) was employed for pumping solution into the reactors (Teflon^{TM}, ID: 40.8 mm, h = 63.6 mm) at a controlled flow rate.

Three experiments at 25 ºC, 40 ºC, and 70 ºC were conducted under identical conditions. Each experiment included a control reactor with pH 12 adjusted buffer and two reactors with grout-contacted or Na_2SiO_3 (5 ppm of Si) in pH 12 buffer solutions as leachate. The ratio of surface area of glass to solution volume was calculated as 34.17 m^{-1}. The pump peristaltic cartridges were carefully calibrated before starting sample collection to have a flow rate of 40 mL/day. About 40-50 samples were collected from each glass reactor between 1.69 days and 6 days.

Static experiments at 90ºC was performed in three solutions: pH 12 buffer, Na_2SiO_3 in pH 12 buffer and grout-contacted solution. Each solution was triplicated: 9 reactors in total with glass samples and, in addition, three reactors with solutions without glass. The test was run for 7 days at 90±1ºC with ratio V_{soln}/m_{solids} = 10:1 (11.000 mL solution and 1.100 g of glass), which corresponds to S/V ratio of 2000 m^{-1}. After the experiment, containers were removed from the oven one by one, weighed, and opened. Immediately after opening 5 samples, 0.250 mL of aliquots were collected from hot leachate and diluted by 6.00 mL (3 samples) and 4.00 mL (2 samples) of 2 wt.% HNO_3. The pH in each reactor was measured after cooling down the solution to room temperature. Every third reactor, in addition to the glass powder, contained polished glass coupons for SEM/EDS analysis in cross-section.

The concentrations of B and Re, which is a chemical surrogate of Tc, in the samples and blanks were measured by inductively coupled plasma mass spectroscopy (Thermo Fisher Scientific, iCAP RQ ICP-MS). The concentration of Si was measured by inductively coupled plasma optical emission spectroscopy (ICP-OES, Perkin Elmer, Optima 7300 DV). The ICP-MS estimated limits of quantification (LOQ) for B and Re as 9.2 μg/L and 0.013 μg/L, respectively. The LOQ for Si by the ICP-OES was determined as 50 μg/L. Solutions were diluted with 2% HNO_3 before analysis. Micrographs and elemental analysis of used glass from each experiment were taken from a JEOL JSM-5900LV scanning electron microscopy/energy-dispersive X-ray spectroscopy (SEM/EDS) at 25.0 kV and a takeoff angle of 35.0°. SEM/EDS study was done on the powdered glass samples mounted in epoxy resin and polished using Al_2O_3 abrasive powder. Due to the non-conductive nature of the samples, specimens were coated with gold using cold sputter coater to avoid charging of the surface under the electron beam.

Subtask 1.4: Results and Discussion

Prepared glass powder was tested by SEM for the absence of any fines adhered to the glass surface. An SEM image collected is shown in Figure 22. It confirms both the absence of fines and the uniform particle size of crushed glass.

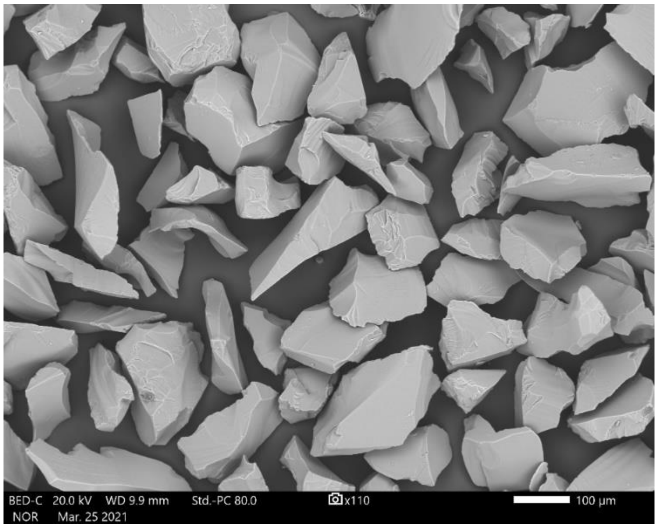

Figure 22. SEM image of glass particles after crushing and washing with DI water and ethanol.

Table 14. Chemical composition of grout contacted solution according to ICP-OES analysis.

Analyte	mg/L
Si	6.350
Na	28.660
K	28.434
Ca	132.544
Fe	1.336
Al	6.840

Our previous results indicated that borosilicate glass has a lower dissolution rate of Re and B in the grout-contacted solution (Figure 23) compared to the pH 12 buffer solution. Grout-contacted solution contains various dissolved species, which causes sluggish glass dissolution kinetics. Chemical composition of a grout-contacted solution was measured using the ICP-OES instrument and is presented in

Table 14. Grout powder was characterized before and after contact with deionized water (DIW). As-received grout powder and grout powder after prepation of the grout-contacted solution were analyzed by a powder XRD instrument (Figure 23). Table 15 summarizes results on the phase composition of each powder sample by fitting of obtained XRD patterns. The major phases in as-received grout were calcite, gypsum, quartz and ettringite. After grout was contacted with DIW, the ettringite phase disappeared and a large amount of vaterite was formed. Vaterite is a metastable polymorph of calcium carbonite, which has higher solubility compared to either calcite or aragonite and transforms to one of these phases under prolonged exposure to liquid.

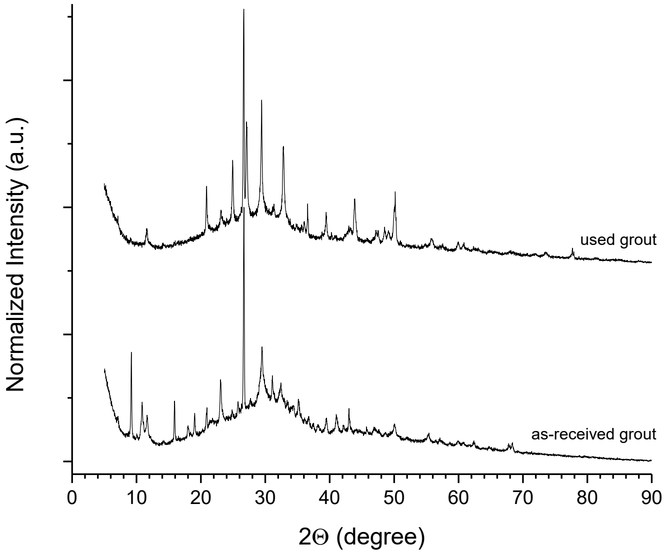

Figure 23. XRD patterns of as-received and used grout powders.

Based on measured concentrations of dissolved cationic and anionic species in the grout-contacted solutions, Si-amended solution in pH 12 buffer was prepared (5ppm Si) and tested in SPFT experiment with ORLEC28 glass. Figure 24 shows release rates of Re (Tc surrogate), B, Si and Al by borosilicate glass at different temperatures in grout-contacted, pH 12 buffer and Si-amended solutions. As seen, the dissolution of glass in grout contacted solution was reduced by a factor of ~10 compared to the pH 12 buffer solution. Addition of silicon (5 ppm) to the buffer solution reduces slightly the release of B and Re at low temperature of 25°C and has almost no effect at elevated temperatures. These results indicate that presence of Si in the grout-contacted solution has limited impact on the stability of borosilicate glass at high pH.

Table 15. Phase composition of as-received and used grout powders according to XRD analysis

Phase	As-received grout	Used grout
Calcite ($CaCO_3$)	11.1	17.0
Vaterite ($CaCO_3$)	0	52.0
Gypsum ($CaSO_4 \cdot 2H_2O$)	16.3	8.5
Quartz (SiO_2)	30.2	22.5
Ettringite ($Ca_6Al_2(SO_4)_3(OH)_{12} \cdot 26H_2O$)	42.3	0

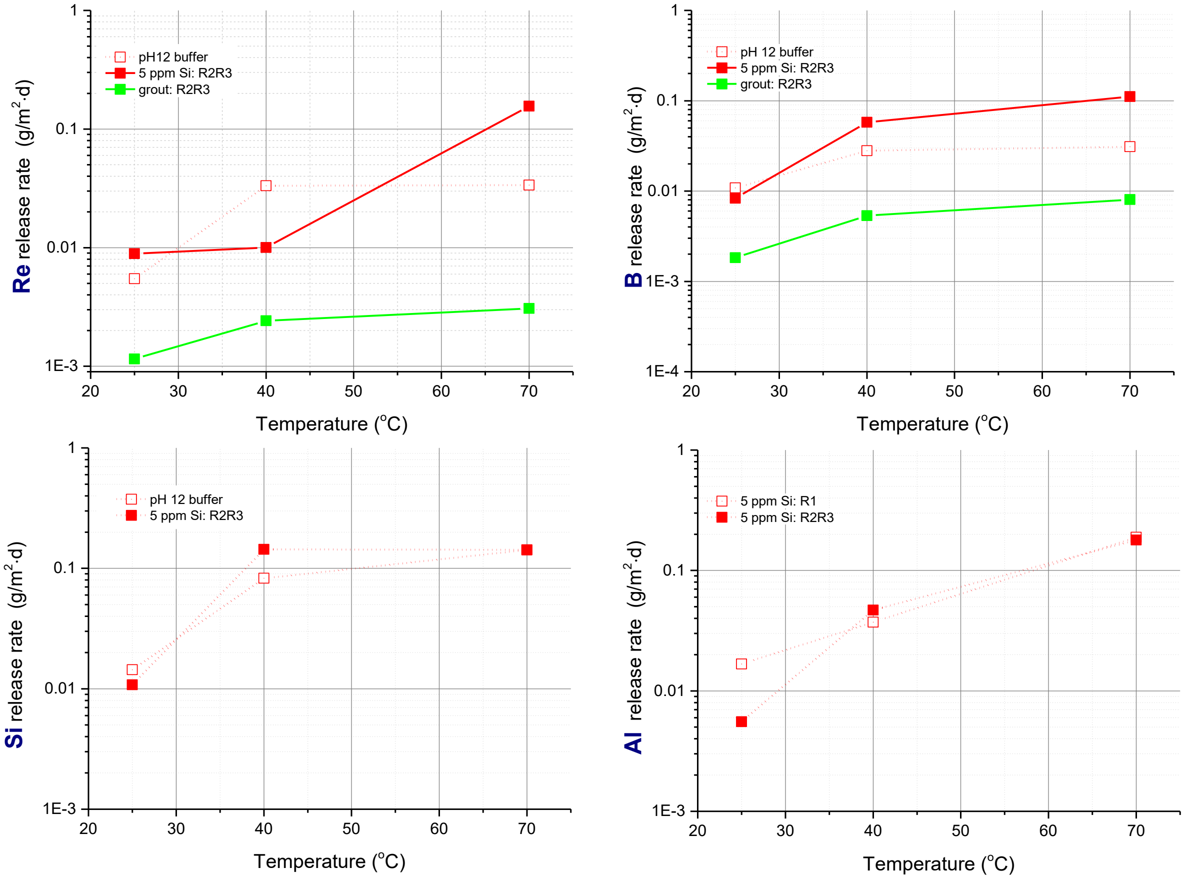

Figure 24. Release rates of major elements (Si, B and Al) and Tc tracer (Re) by the ORLEC28 borosilicate glass in SPFT experiment at different temperatures in grout-contacted, Si- amended solutions and pH 12

buffer.

The Static Product Consistency Test (PCT) at 90ºC was conducted as an accelerated approach to test glass stability at different conditions of chemical environment and presence of variable ionic species in the solution. This test was performed with grout-contacted, pH 12 buffer, Ca-, Si-, Ca+Si-, Al+Si- and Ca+Al+Si-amended solutions. Concentrations of dissolved species (Ca, Al and Si) corresponds to their concentration in grout-contacted solution (

Table 14).

Figure 25 shows results of ICP-MS analysis of the leachate solution for ^{187}Re, ^{11}B, ^{57}Fe and ^{26}Mg. As seen, the dissolution of glass is strongly reduced in a grout-contacted solution compared to the pH 12 adjusted buffer and the pH 12 adjusted buffer amended with Na$_2$SiO$_3$. Results suggested that Ca^{2+} ions have a dramatic effect on the glass dissolution. However, presence of Si alone or in a combination with Al^{3+} does not notably affected the release rate of B and Re.

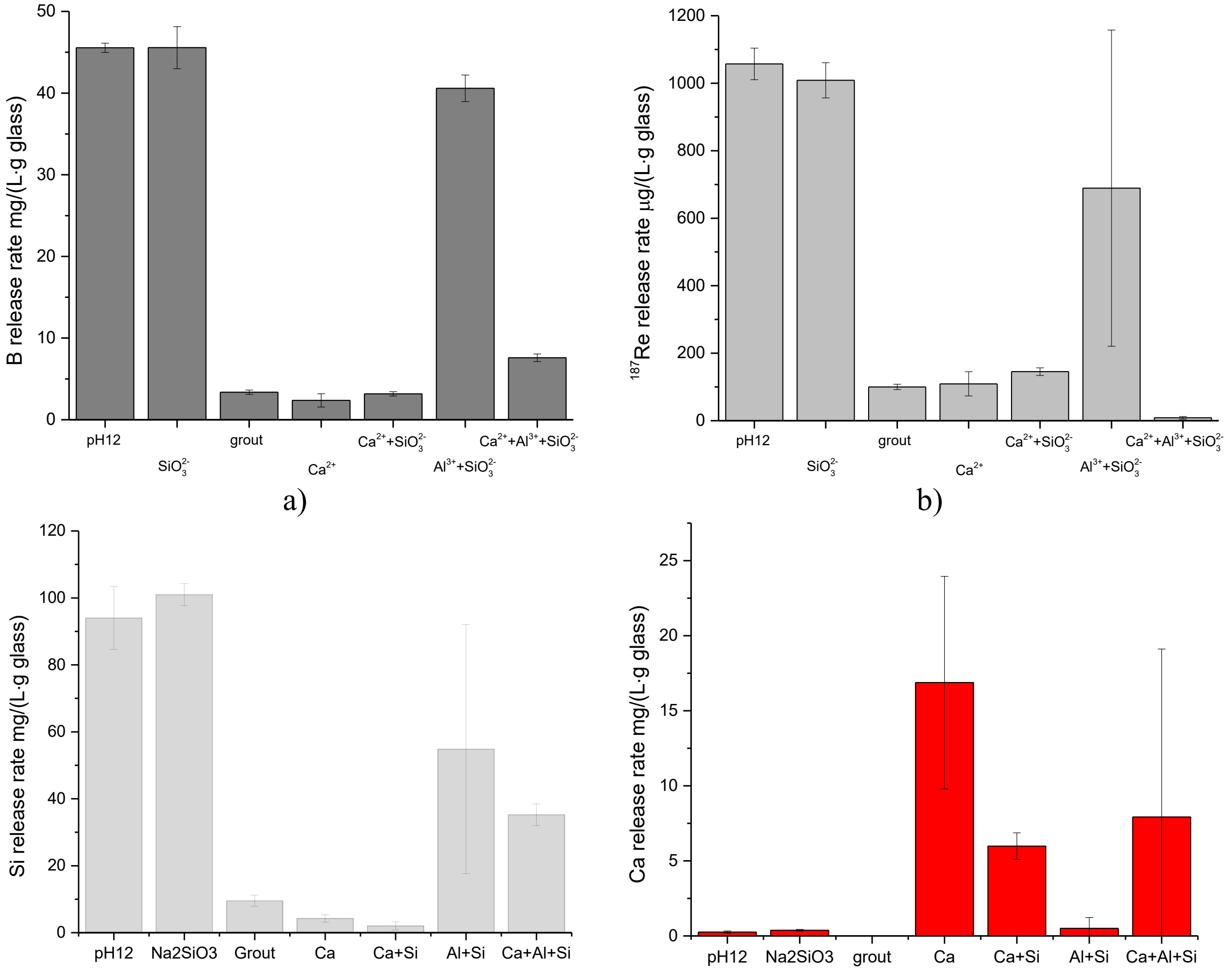

a) b)

c) d)

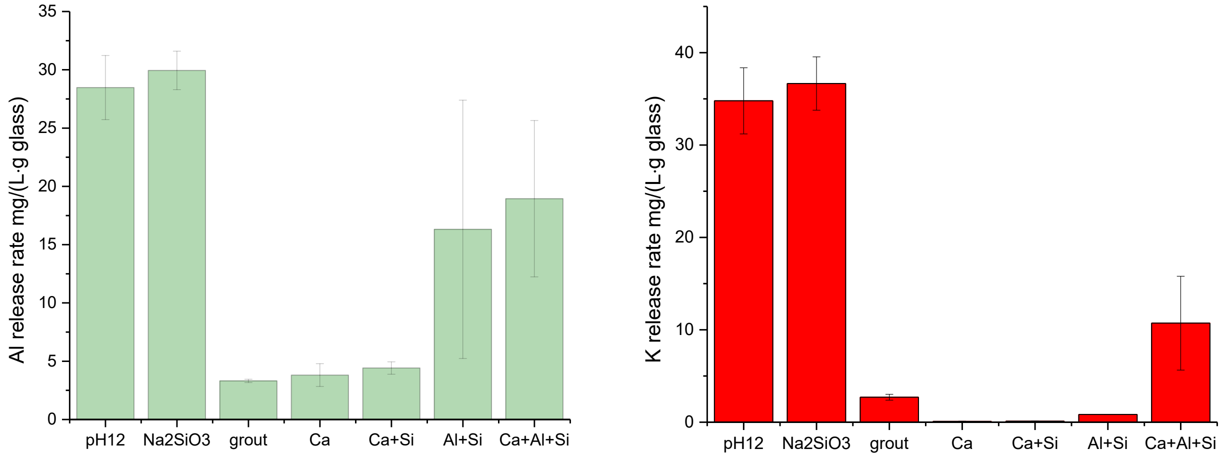

e) f)

Figure 25. Results of ICP-OES (Si, Ca, Al and K) and ICP-MS (B and Re) analysis of the leachates collected after 7 days static test at 90ºC in different solutions.

All glass powders used in static experiments at 90ºC were also characterized by powder XRD analyses. Results are summarized in Figure 26 which shows collected XRD patterns. No change in the XRD patterns were detected as a result of glass treatment.

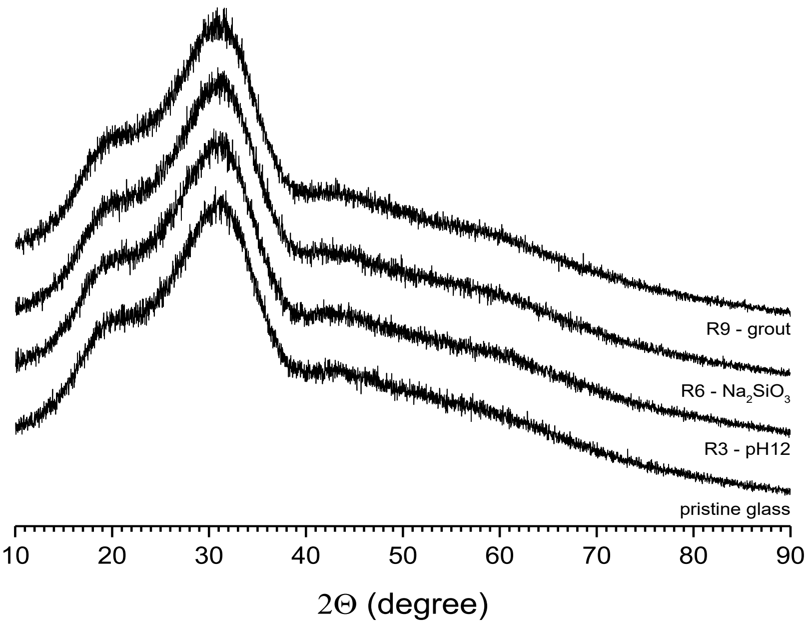

Figure 26. Powder XRD patterns of the pristine and used in the static experiment at 90ºC glass powders.

Three glass samples used in SPFT experiment at 40ºC in pH 12 buffer, sodium silicate and grout-contacted solutions were analyzed via SEM/EDS. EDS analysis of precipitates and fine particle adhered to the surface of used glass particles after 40ºC SPFT experiment in Na_2SiO_3 solution was performed (Figure 27). Most of the fines on the surface have irregular shape, however, small number of particles with acicular morphology was observed.

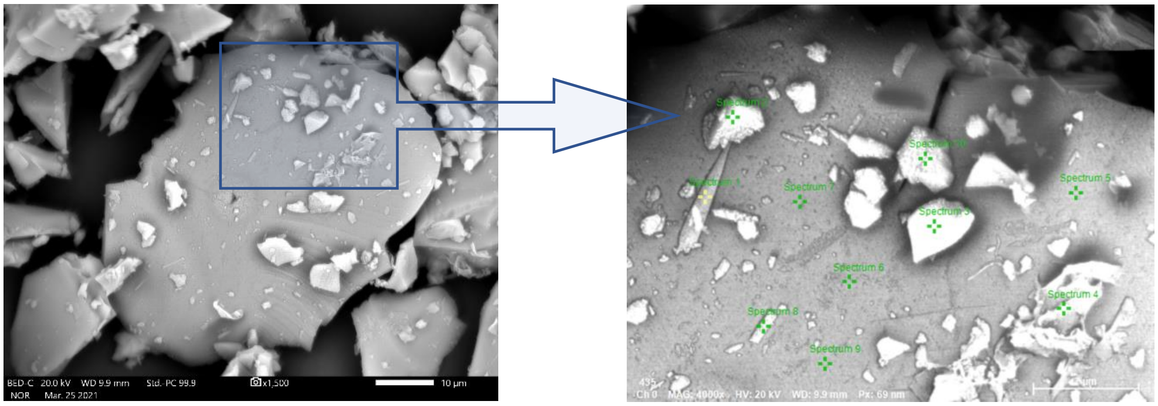

Figure 27. SEM images of the precipitates on the glass particles after 40°C SPFT experiment in Na_2SiO_3 solution (right image). Image on the left shows points where EDS spectra were taken from.

The EDS composition of precipitates included potassium, magnesium, aluminum, calcium, and silicon implying the formation of aluminosilicates. The SEM image of a polished glass sample used in the SPFT experiment at 40°C in pH 12-adjusted buffer amended with sodium metasilicate solution is shown in Figure 28.

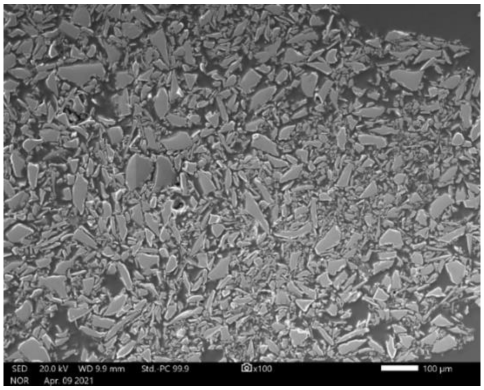

Figure 28. SEM image of glass mounted in epoxy resin and polished for SEM/EDS study in cross-section. Glass sample was used in SPFT experiment at 40°C in Na_2SiO_3 solution.

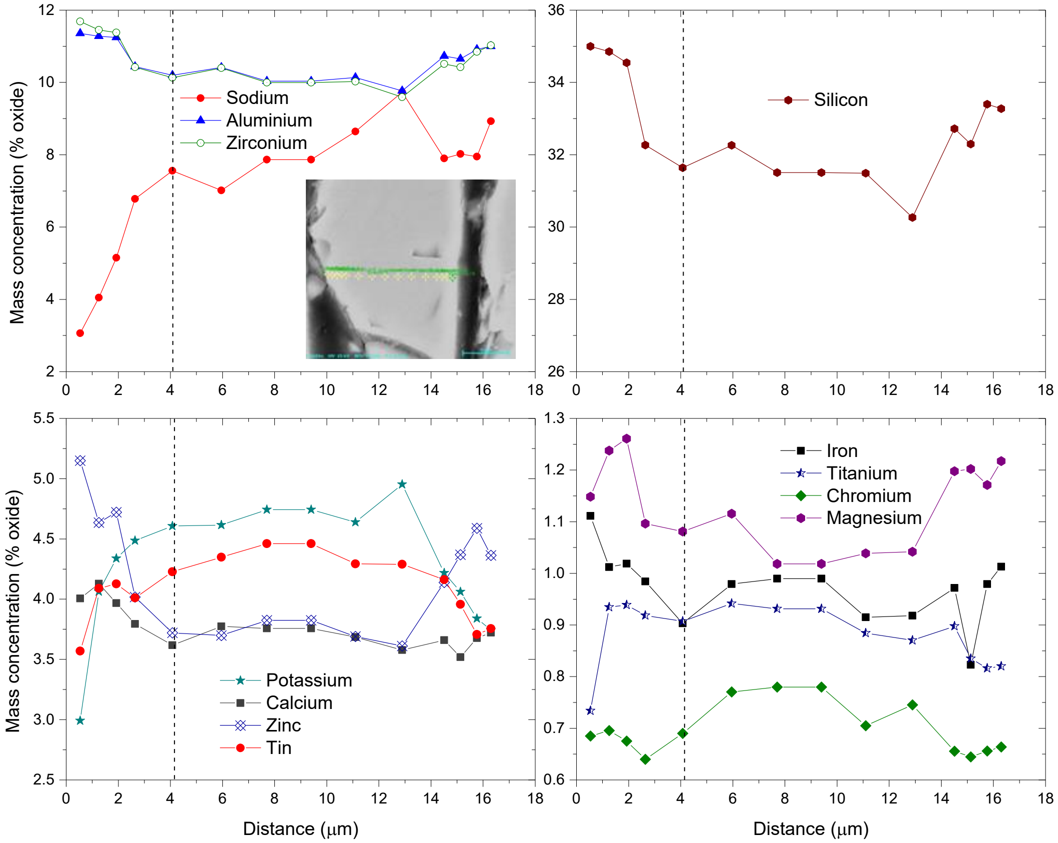

Figure 29. Distribution of the elements as a function of distance from the sample's edge. Sample is treated in pH 12 buffer solution at 40°C glass powder (SPFT experiment). Inset shows points on the polished glass particle where EDS spectra were collected.

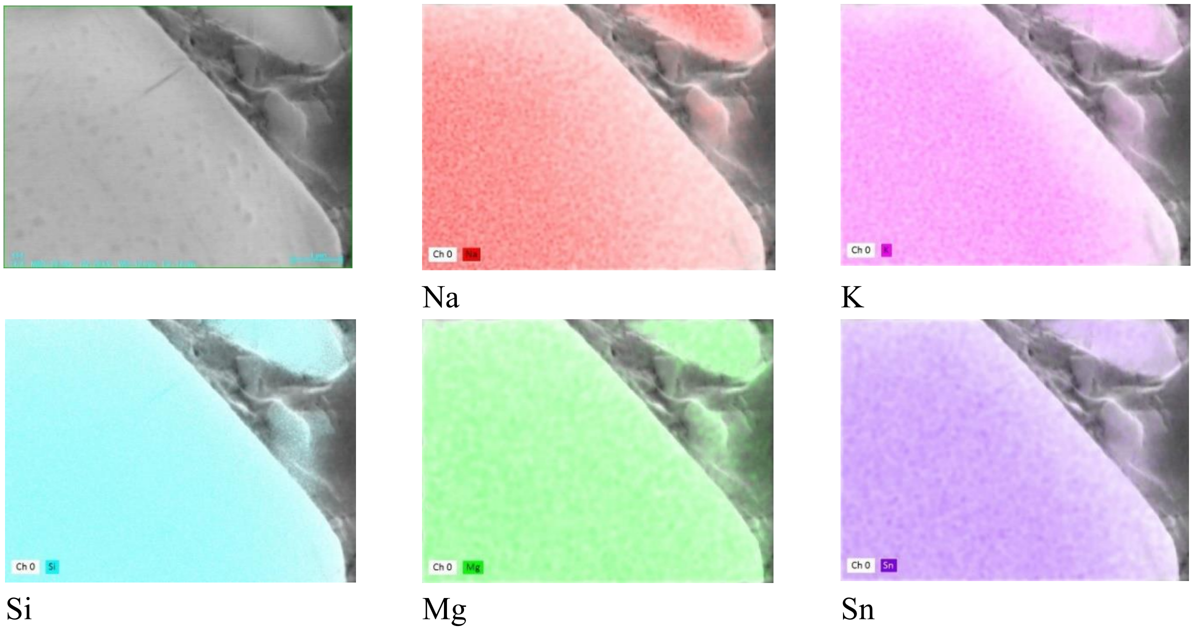

Na

K

Si

Mg

Sn

Figure 30. SEM micrograph and elemental maps for Na, K, Si, Mg and Sn of cross-sectioned ORLEC28 particles used in SPFT experiment at 40°C in pH 12 buffer.

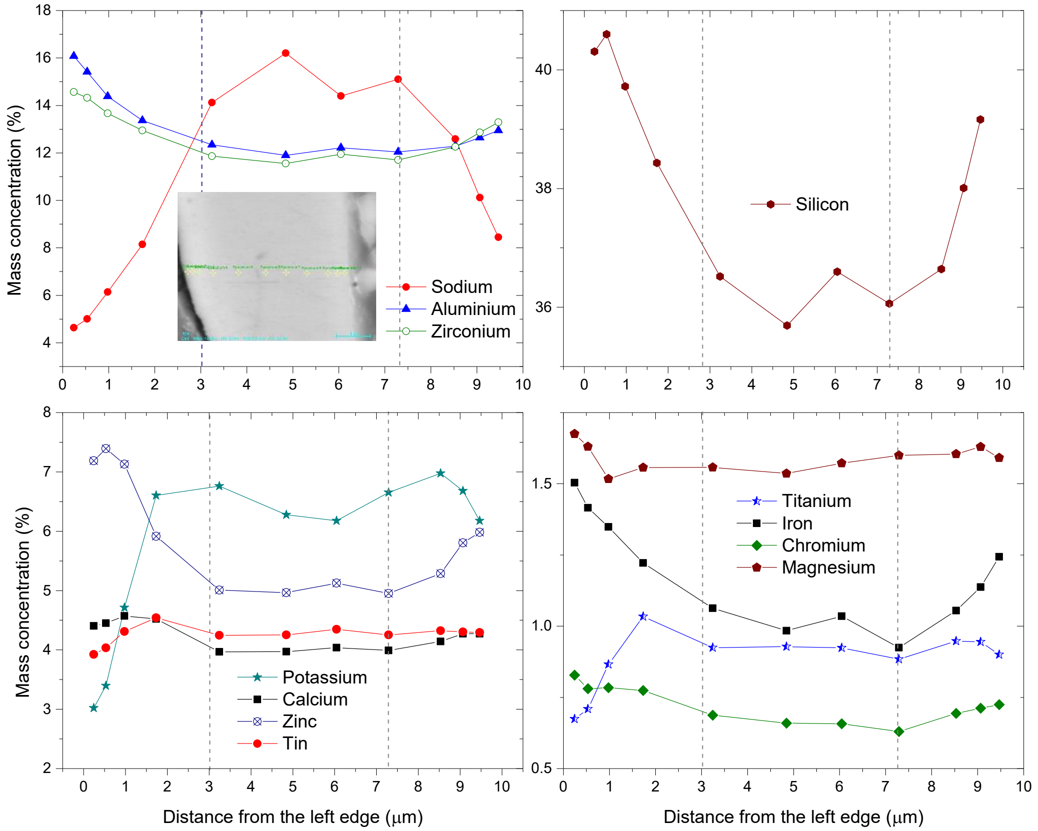

Figure 31. Distribution of the elements as a function of distance from the sample's edge. Sample is treated in Na_2SiO_3 solution at 40^{o}C glass powder (SPFT experiment). Inset shows points on the polished glass particle where EDS spectra were collected.

Figure 29 and Figure 30 report concentration profiles of major elements by means of mass concentration of corresponding oxide as a function of a distance from the edge of a glass particle and EDS elemental maps of Na, K, Si, Mg and Sn collected on the glass powder treated in pH 12 buffer solution, respectively. Figure 31 shows concentration profiles of major elements for the glass sample after treatment in Na_2SiO_3-amended solution. The alternation layers of about 4 μm and 3 μm thickness are clearly detectable in the pH 12 buffer and Na_2SiO_3 amended leachate solution, respectively. It is evident from the depleted amount of sodium, potassium and possibly tin, resulting from the ion exchange process. Although no alternation layer is visually detected in SEM images, the images of elemental maps show no uniformity in the distribution of sodium, potassium and tin (Figure 30). It is notable that potassium concentrations in the glass treated in pH 12 buffer recover within about 2 μm distance from the glass particle edge, while the depletion depth of sodium extends to about 4 μm. This observation is attributed to the difference in diffusion coefficients for sodium and potassium in the glass. Similar trends hold for other elements in Figure 29 and Figure 30.

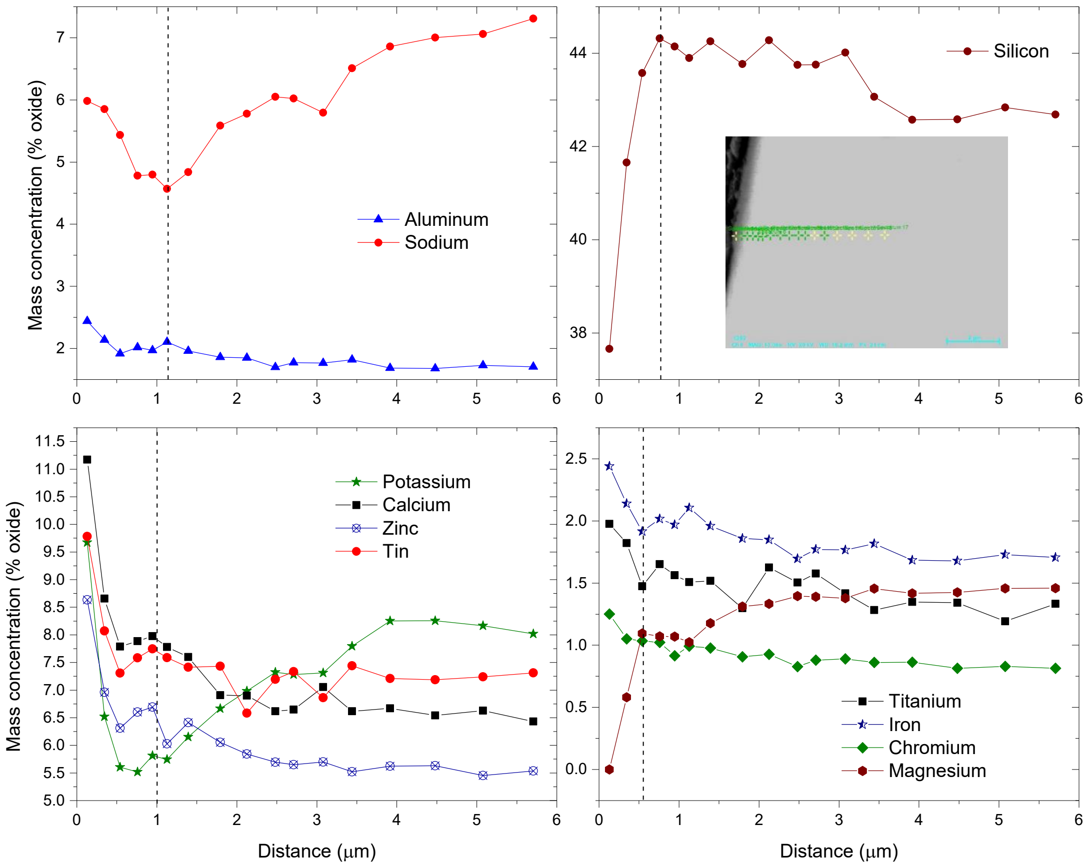

Figure 32. Distribution of the elements as a function of distance from the sample's edge. Sample is treated in grout-contacted solution at 40ºC glass powder (SPFT experiment). Inset shows points on the polished glass particle where EDS spectra were collected.

EDS results obtained on the glass treated in grout-contacted solution are presented in Figure 32. This sample has several distinctive features compared to the other two samples: (1) no significant alternation layer is observed on this sample; (2) opposite trends are observed for sodium and silicon compared to the two other samples; and (3) the surface layer is enriched in calcium. These results indicated that the dissolution behavior in grout-contacted solution is significantly different from the other two solutions and suggest that there could be other elements in addition to silicon in the solution which control the dissolution rate of the glass. For example, calcium in the solution could affect dissolution of glass. This suggestion is supported by the literature (Suzuki-Muresan et al. 2018), who showed that solutions enriched with calcium influence glass alternation by precipitation of either calcium borate or calcium silicate hydrates.

a) b)

Figure 33. (a) Glass coupons cut and polished for the SEM/EDS study after the static experiment at 90ºC; and (b) glass coupons mounted in epoxy resin and polished for cross-sectional SEM/EDS analysis.

Results of the SEM/EDS study of glass coupons used in the static test are summarized in Table 16, which report changes in alternation layer thickness for different elements in the static PCT test at 90ºC for Ca- Ca+Si- Al+Si- and Ca+Al+Si-amended solutions. A negative sign corresponds to a decreased concentration of the element compared to its concentration in the bulk glass, and a positive sign corresponds to an increased amount of the element as compared with the concentration in the bulk glass. More details on this SEM/EDS study will be reported in Year 2.

Table 16. Alternation layer thickness for different elements in the static PCT test at 90°C

Solution	Na	K	Si	Al	Ca	Zn
Ca^{2+}	-4.05	-3.31	-1.84	-1.6	+3.3	+3.3
$Ca^{2+} + SiO_3^{2-}$	+0.85; -3.5	+0.72; -3.5	-0.91	-0.84	+2.05	+0.72
$Al^{3+} + SiO_3^{2-}$	-4.4	-3.8	-1.2	-0.71	0.0	0.0
$Ca^{2+} + Al^{3+} + SiO_3^{2-}$	-4.15	-3.36	0.0	0.0	+2.2	+2.2

Subtask 1.4: Conclusions

A single-pass flow-through (SPFT) at 25ºC, 40ºC and 70ºC and a static Product Consistency Test (PCT) at 90ºC experiments were conducted in support of the Hanford Lysimeter Test Facility (FLTF). The effect of a grout-contacted, pH 12 buffer and Si-amended solution on the glass dissolution was evaluated via a SPFT test. Grout-contacted, pH 12 buffer and Si-, Ca-, Ca+Si- Al+Si- and Ca+Al+Si-amended solutions were used in the static PCT test. Glass tested in SPFT and PCT experiments was analyzed by SEM/EDS analysis in cross-section. It was shown that an alternation layer 3-4 µm thick is present in the glass samples tested in pH 12 buffer and sodium metasilicate solutions, however, it is much less noticeable after glass treatment in the grout-contacted and Ca-amended solutions. Future work will focus on SPFT tests using Ca-amended solutions at variable temperatures.

Subtask 1.4: References

ASTM (2018). Standard practice for measurement of the glass dissolution rate using the single-pass flow-through test method (Designation: C1662-18). Philadelphia, PA: ASTM

Armelao, L., Bassan, A., Bertoncello, R., Biscontin, G., Daolio, S., and Glisenti, A., 2000, Silica glass interaction with calcium hydroxide: a surface chemistry approach: Journal of Cultural heritage, v. 1, no. 4, p. 375-384.

Asmussen, R.M., et al., 2018, Getters for improved technetium containment in cementitious waste forms. Journal of hazardous materials. v. 341, p. 238-247.

Frugier, P., Chave, T., Gin, S., and Lartigue, J.-E., 2009, Application of the GRAAL model to leaching experiments with SON68 nuclear glass in initially pure water: Journal of Nuclear Materials, v. 392, no. 3, p. 552-567.

Gin, S., 2001, Protective effect of the alteration gel: a key mechanism in the long-term behaviour of nuclear waste glass.

Grambow, B., 2006, Nuclear waste glasses-How durable?: Elements, v. 2, no. 6, p. 357-364.

Jantzen, C. M., Brown, K. G., and Pickett, J. B., 2010, Durable glass for thousands of years: International Journal of Applied Glass Science, v. 1, no. 1, p. 38-62.

Jégou, C., Gin, S., and Larché, F., 2000, Alteration kinetics of a simplified nuclear glass in an aqueous medium: effects of solution chemistry and of protective gel properties on diminishing the alteration rate: Journal of Nuclear Materials, v. 280, no. 2, p. 216-229.

Neeway, j.j., et al., 2018, FY2017 ILAW Glass Corrosion Testing with the Single-Pass Flow-Through Method: Pacific Northwest National Lab. (PNNL), Richland, WA (United States).

Ojovan, M. I., and Lee, W. E., 2011, Glassy wasteforms for nuclear waste immobilization: Metallurgical and Materials Transactions A, v. 42, no. 4, p. 837-851.

Standard, A., 2014, C1285-14, Standard Test Methods for Determining Chemical Durability of Nuclear, Hazardous, and Mixed Waste Glasses and Multiphase Glass Ceramics: The Product Consistency Test (PCT): ASTM International, West conshohocken, PA.

TASK 2: REMEDIATION RESEARCH AND TECHNICAL SUPPORT FOR THE SAVANNAH RIVER SITE

Subtask 2.1: Environmental Factors Controlling the Attenuation and Release of Contaminants in the Wetland Sediments at Savannah River Site

Subtask 2.1: Introduction

The Savannah River Site (SRS) is a nuclear separation facility built in the 1950's to refine nuclear materials for nuclear weapons production. The F-Area Seepage Basins, located within the General Separation Area of the SRS consisted of three unlined basins. These basins received low-level radioactive wastewater originating from the reprocessing of uranium slugs and irradiated fuel in the F-Area Separation Facility. A large amount of ^{129}I and other radionuclides migrated to the vadose zone and contaminated the groundwater and the contamination was transported to the wetlands associated with a local stream, Fourmile Branch (Kaplan et al. 2014 (a, b), Zhang et al. 2014). Wetlands at the F-Area have been an important sink for ^{129}I and other contaminants, but changes in biogeochemical conditions could cause the release of these contaminants into the surrounding areas (Xu et al. 2011, Zhang et al. 2011, Chang et al. 2014, Emerson et al. 2014, Kaplan et al. 2014, Santschi et al. 2017, Neeway et al. 2019). Denham and Amidon (2016) found that during the periods of high rainfall ^{129}I concentrations tend to increase, while tritium does not increase but at times instead decreases. The increase in surface water and groundwater flow during the rainy periods might have released the bounded ^{129}I into the environment. Their results are consistent with a study conducted by Xu et al. (2011) of the speciation of ^{129}I in F-Area wetland soils.

During the migration of ^{129}I within the groundwater plume from the basins toward the wetland areas, several studies have observed ^{129}I can undergo various transformations changing its speciation (Schwehr et al. 2009, Otosaka et al. 2011, Zhang et al. 2014). Different iodine species exhibit dramatically different mobility, bioavailability, and behavior in the environment. There is little data or information about how these transformation processes and environmental factors affect iodine species fate and transport in the aquatic environments. The biogeochemical conditions such as variations in microbial activity, redox conditions, soil temperature, soil moisture, and pH, may cause the seasonal release of organically bound ^{129}I from wetland soils.

Subtask 2.1: Objectives

The research objective of this study is to better understand the dominant attenuation mechanisms for ^{129}I in the wetlands, how strong is the attenuation, and what conditions would reverse it. The potential findings will improve the understanding of the effect of environmental factors on the adsorption and release of iodine species. It will also help to determine if organoclays are feasible amendments for in-situ remediation of iodine species in the SRS wetland environments and whatconditions are optimal for iodide, iodate, and organo-iodine removal from the aqueous phase.

Subtask 2.1: Methodology

Materials:

This study utilized commercially available organoclays, PM-199 and MRM, that were obtained from CETCO. For I^-, a commercial 1,000 ppm iodide stock solution was used to prepare working solutions. A commercial stock solution consisting of 1,000 ppm of IO_3^- was used in the preparation of working solutions. The pH of the samples was adjusted using 0.1 M HCl or 0.1 M NaOH. The 25% tetramethylammonium hydroxide (TMAH) was obtained from Fisher Scientific.

Experimental Procedures:

Characterization of organoclays PM-199 and MRM

The attenuated total reflectance Fourier transform infrared spectroscopy (ATR-FTIR) spectra of the organoclays, PM-199 and MRM, were obtained using an Agilent FTIR (Santa Clara, CA, USA) in the spectral range of 400 - 4000 cm^{-1} with 16 scans per spectrum. The surface areas of the organoclays were measured by Brunauer-Emmett-Teller (BET) analysis. The morphology and elemental characterization of organoclays PM-199 and MRM were performed using the scanning electron microscopy coupled with energy dispersive X-ray spectroscopy (SEM-EDS). The SEM-EDS spectra and mapping of elements in organoclays were analyzed by the JEOL IT-500HR FE-SEM coupled with the Bruker Quantax 400 EDS.

Characterization of topsoil collected from SRS wetlands

The attenuated total reflectance Fourier transform infrared spectroscopy (ATR-FTIR) spectra of the SRS wetland's topsoil were obtained using an Agilent FTIR (Santa Clara, CA, USA) in the spectral range of 400 – 4.000 cm^{-1} with 16 scans per spectrum. The characterization of morphological structure and elemental distribution of the topsoil was done using the scanning electron microscopy coupled with energy dispersive X-ray spectroscopy (SEM-EDS). The SEM-EDS spectra and mapping of elements in organoclays were analyzed by the JEOL IT-500HR FE-SEM coupled with the Bruker Quantax 400 EDS. The soils were also analyzed by the Bruker D2 PHASER X-ray diffraction (XRD) analyzer with the 2Θ ranging from 5° to 90° with the step size of one second.

Sorption of iodine species (iodide and iodate) on the organoclays PM-199 and MRM

Stock solutions of 1000 ppb of iodide and iodate were prepared in MilliQ water. A series of iodate standard solutions ranging from 0.5 to 15 ppb was prepared using commercial stock solution for the ICP-MS calibration curve. A series of control solutions and working solutions were prepared by dilution of stock solution. The adsorption experiments were performed by adding 0.04 g of organoclays PM-199 or MRM into 40 mL of 50, 100, and 150 ppb iodide/iodate solutions in the 50 mL centrifuge vials. The initial adsorption studies were conducted at room temperature and at solution pH of 5.5 ± 0.1. The solution pH was varied in subsequent experiments to probe the effects of pH on the adsorption. The mixtures were placed in the platform shaker at the agitation rate of 100 rpm for a total of 7 days to ensure that the adsorption equilibrium was reached. The aliquots collected at a specific time interval were filtered with a 0.45 μm of syringe filter, mixed with 0.1% TMAH and analyzed by the iCAP RQ Quadrupole ICP-MS (Thermo Fisher).

Sorption of iodide and iodate on SRS topsoil

The adsorption experiments were performed by adding 4.0 g of SRS's wetland topsoil into 40 mL of 100 ppb iodide/iodate solutions in the 50 mL centrifuge vials. The soil samples were equilibrated in ultrapure water at pH ~ 4.5±0.1 for a period of 7 days on a platform shaker at the agitation rate of 100 rpm before the analytes (I^- and IO_3^-) were spiked into the solutions to reach the final concentration of 100 ppb. The aliquots from the samples were collected at specific time interval during the adsorption time of 20 days and filtered with a 0.45 µm of syringe filter. The filtrate samples were mixed with 0.1% TMAH finally analyzed by the iCAP RQ Quadrupole ICP-MS (Thermo Fisher).

Subtask 2.1: Results and Discussion

Characterization of organoclays PM-199 and MRM

The morphological structure and particle sizes of MRM and PM-199 were determined by SEM. Figure 34 shows that the organoclays have a wide range of shapes and particle size distribution; however, PM-199 has a slightly larger particle size than MRM.

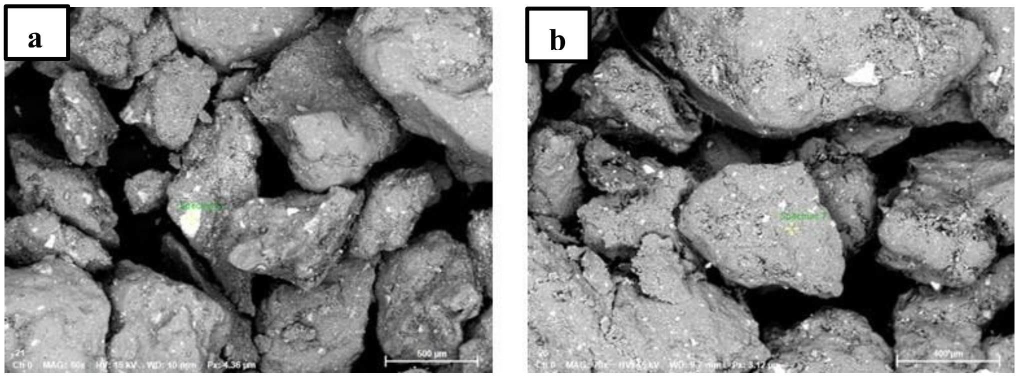

Figure 34. SEM spectra of (a) MRM and (b) PM-199.

Elemental analyses of MRM and PM-199 (Figure 35) indicated that the primary metal was aluminum (Al) as these materials were modified bentonite clay. The elements carbon (C), oxygen (O), and silicon (Si) were related to the functional groups (carboxyl groups, hydroxyl/phenolic groups, aromatic rings, aliphatic chains, and silanol groups) present in clays. There are trace amounts of sodium (Na), iron (Fe), and chlorine (Cl) present in both MRM and PM-199; however, the presence of sulfur (S) in MRM is as a result of the modification of organoclay MRM with sulfur moiety.

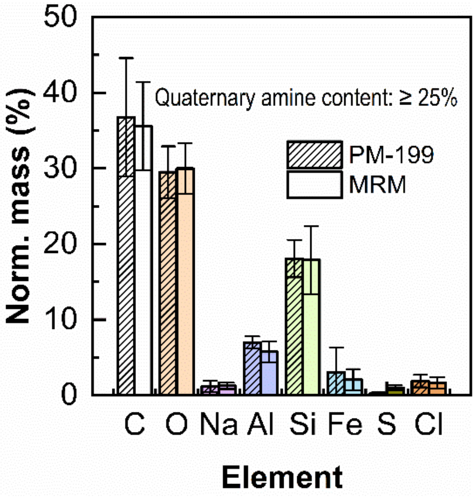

Figure 35. Elemental distribution of PM-199 and MRM.

The Brunauer-Emmet-Teller (BET) analysis of organoclays PM-199 and MRM show the BET surface area of 0.5278 m^2/g and 0.5193 m^2/g, respectively. The surface areas of these materials are similar to each other. Figure 36 shows the FTIR spectra of PM-199 and MRM. In ATR-FTIR spectra, the band at 3641 cm^{-1} and broad peak at 3378 cm^{-1} in organoclays corresponds to the O-H stretching of the Al-OH groups and the O-H stretching vibration of bound water, respectively. The peak at 1639 cm^{-1} is assigned to the bending of O-H bonds of water molecules in the silicate matrix. Peaks at 1021 cm^{-1}, 914 cm^{-1}, and 790 cm^{-1} correspond to stretching vibrations of functional groups Si-O-Al, Si-O, Al-Al-OH, and Al-O, respectively, on tetrahedral and octahedral sheets of the clays.

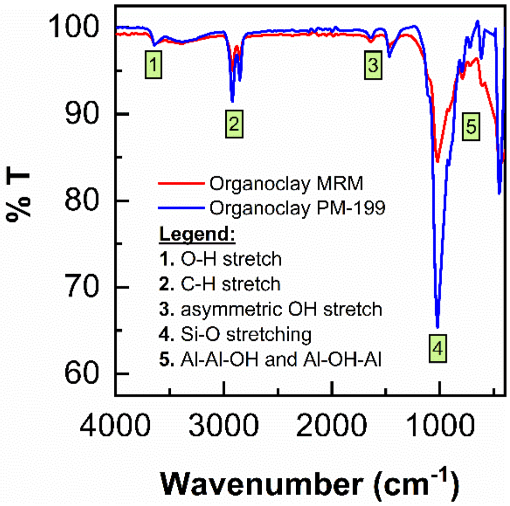

Figure 36. FTIR spectra of organoclays PM-199 and MRM.

Characterization of topsoil collected from SRS wetlands

The SRS bulk topsoil was collected from an uncontaminated area in the wetland of Fourmile Branch. The soil was collected using a hand auger for 0 – 2 feet samples. The soil samples were dried at room temperature for at least a week. Once the soil samples dried, the soils were analyzed by the X-ray diffraction (XRD) technique. In XRD spectra (Figure 37), the peak patterns of the soils were matched with peak patterns of quartz and kaolinite minerals. The quartz was estimated to be the major mineral in the soils while kaolinite made up ~ 7% of the characterized soils. Although iron was detected using SEM-EDS analysis, iron minerals were not detected in the bulk samples using XRD. The bulk soil samples may need to be fractionated to further characterize the soils.

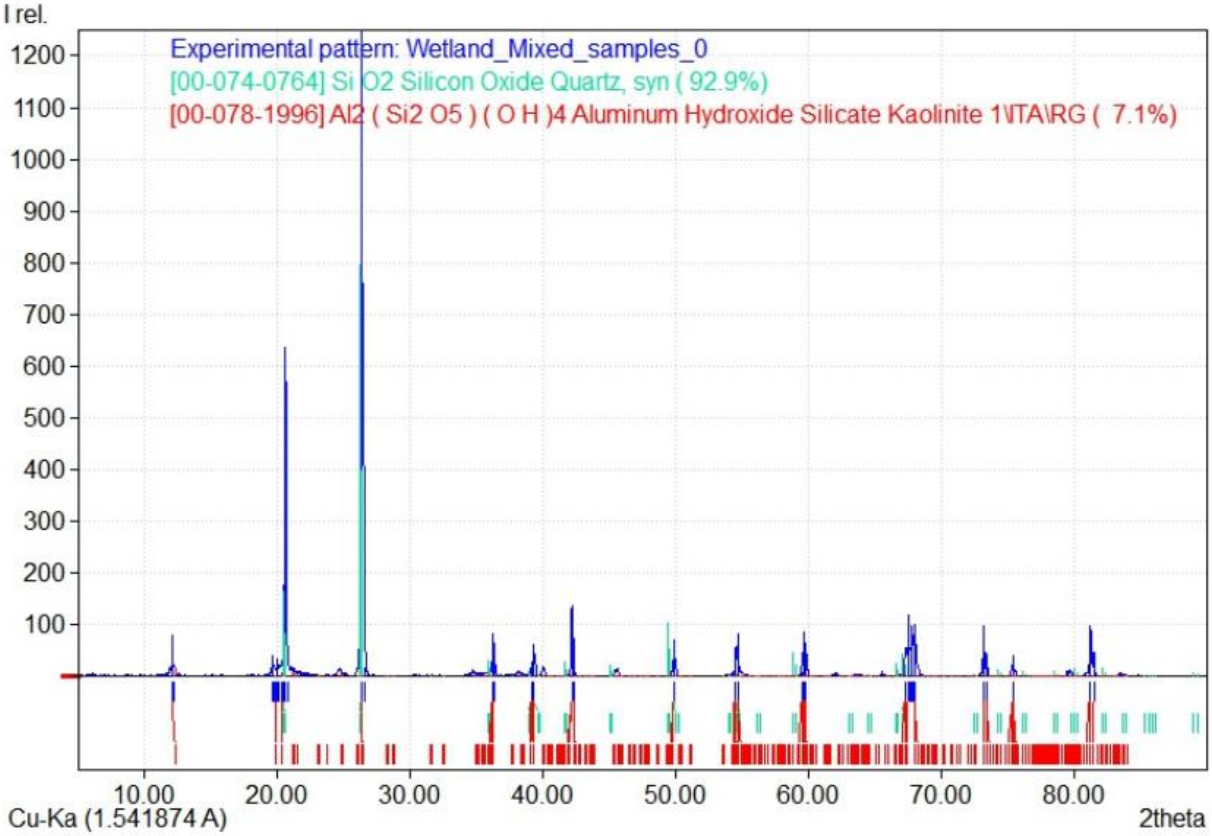

Figure 37. XRD spectra of SRS's wetland topsoil.

The quartz mineral was the most abundant in the bulk soil followed by kaolinite, which was confirmed by using EDS mapping in Figure 38 (top). The overlapping regions of silicon (Si) and oxygen (O) could be denoted to quartz minerals in bulk samples. The kaolinite mineral was also detected using the EDS mapping technique as shown in Figure 38 (bottom). The overlapping regions of aluminum, silicon, and oxygen can be assigned to kaolinite mineral.

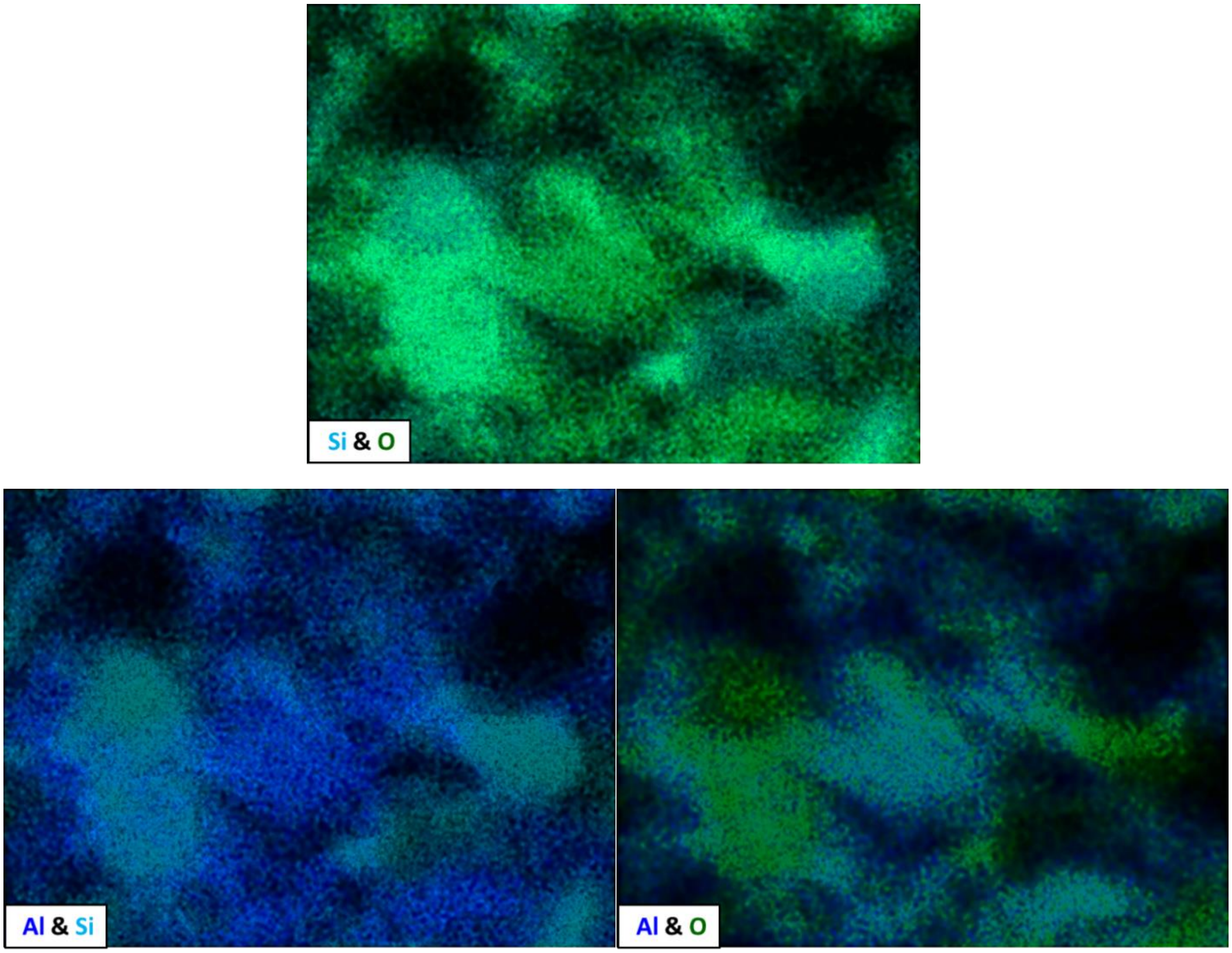

Figure 38. EDS mapping of silicon and oxygen (top) and aluminum, silicon, and oxygen (bottom) in bulk wetland soil.

The FTIR characterization of bulk SRS wetland topsoil was carried out using room air dried topsoil. In FTIR spectra (Figure 39), the characteristic bands of kaolinite are observed at ~3690 cm^{-1}, ~3650 cm^{-1} and ~3620 cm^{-1}, corresponding to interlayer -OH functional groups in the clay structure (Bich et al. 2009); hence, these functional groups are inaccessible for interaction with guest molecules (Irfan Khan et al. 2017). The FTIR spectra of the wetland soils exhibit a broad band at 3600–3200 cm^{-1}, which is attributed to –OH stretching of alcohol and/or phenol in the humic substances presented in the soils. Carboxyl groups constitute a major functional group of humic substances presented in the soils (Perdue 1998). The C=O stretching of free carboxylate groups typically appear at ~ 1700 cm^{-1}, however, when the carboxylate groups form a complex with metal ions in the soils, the C=O bond is weakened and the peak shifts at ~ 1630 cm^{-1}. The appearance of strong bands in the soils at ~1000 cm^{-1} can be assigned to Si-O asymmetric stretch of quartz mineral presented in the soils (Müller et al. 2014, Irfan Khan et al. 2017). The Al-OH-Al bending vibration of kaolinite minerals is evident at 915 cm^{-1} (Müller et al. 2014). The bands at ~ 795, 777 and 751 cm^{-1} are assigned to Si – O – Al^{IV} in the soils (Bich et al. 2009).

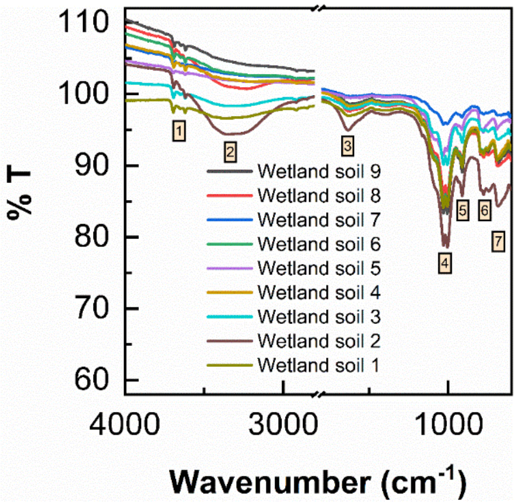

Figure 39. FTIR Spectra of SRS wetland topsoil.

Sorption of iodine species (iodide and iodate) on the organoclays PM-199 and MRM

The adsorption kinetic studies of iodide (I^-) onto 1.0 g/L of PM-199 and MRM at 3 different concentrations (50, 100, and 150 ppb) were carried out for a period of 7 days. Sorbent-free control solutions were included as the initial concentrations and to provide information on the adsorption of iodide onto glassware. The data showed that the adsorption of iodide on PM-199 and MRM reached equilibrium within the first 12 hours (Figure 40). Two iodine-free control solution samples consisting of sorbents were included to monitor the release of natural iodine within the organoclays to the solution. The results showed that no iodine was detected in the solutions over the course of the experiment. The adsorption of iodide onto MRM sorbent slightly decreased over time, however, the overall removal percentage of iodide by MRM is ~ 70% (Figure 40). The adsorption of iodide on PM-199 reached equilibrium within 12 hours with more than 90% removal percentage and stayed constant throughout the course of 7 days.

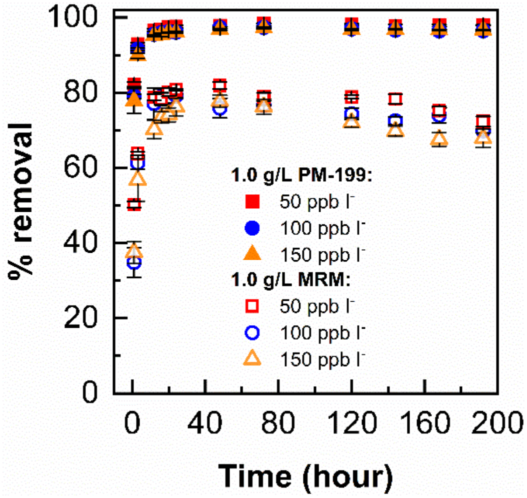

Figure 40. The percentage of removal of iodide on PM-199 and MRM over 7 days.

The kinetic studies of iodate (IO_3^-) onto 1.0 g/L of PM-199 and MRM at 3 different concentrations (50, 100, and 150 ppb) were carried out for a period of 7 days. Sorbent-free control solutions were included as the initial concentrations and to provide information on the adsorption of iodide onto glassware. The data showed that the adsorption of iodide on PM-199 has reached equilibrium within the first 24 hours with ~40% removal percentage, whereas the kinetic of iodate sorption on MRM took ~ 5 days to reach equilibrium with >70% removal percentage (Figure 41). The adsorption of iodide on PM-199 stayed constant throughout the course of 7 days.

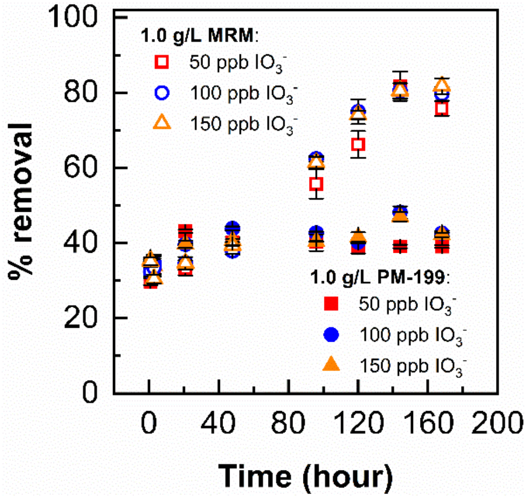

Figure 41. The percentage of removal of iodate on PM-199 and MRM over 7 days.

The adsorption isotherm studies of iodide on PM-199 and MRM was carried out. Figure 42 shows the isotherms of iodide on 1.0 g/L of PM-199 and MRM. Although the initial concentrations of iodide ranged from 10 to 1000 ppb, the equilibrium had not been reached.

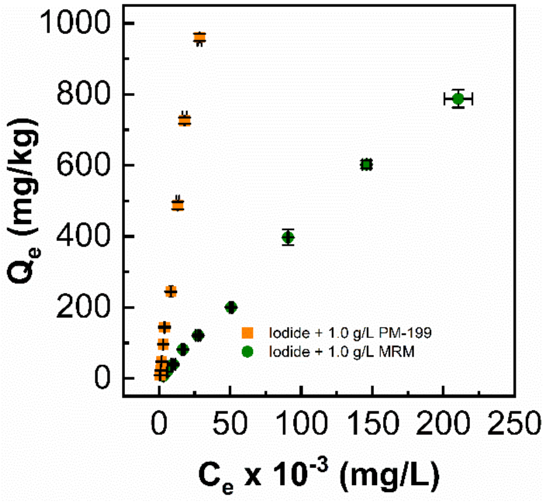

Figure 42. The isotherms of iodide on PM-199 and MRM.

The effect of pH on the adsorption of iodide on 1.0 g/L organoclays PM-199 and MRM were carried out using the 100 ppb iodide solutions. The removal of iodide by PM-199 and MRM under different pHs is shown in Figure 43. The removal of iodide does not change significantly in the pH 4-6 range; however, the removal slightly decreased at pH greater than 7. The proposed hypothesis for this phenomenon is that the isoelectric points of PM-199 and MRM are around pH 6, therefore, the surface charges of PM-199 and MRM are more negatively charged as the pH increases. This can be confirmed by performing potentiometric titration or dynamic light scattering to figure out the isoelectric points of organoclays.

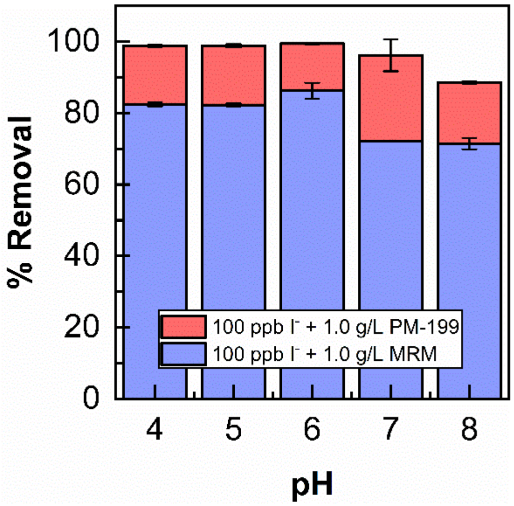

Figure 43. The effects of pH on adsorption of iodide on PM-199 and MRM.

Sorption of iodide and iodate on SRS topsoil:

As shown in Figure 44a, the sorption of 100 ppb iodide onto 100 g/L of soil reached equilibrium within 48 hours. Meanwhile, the sorption of 100 ppb iodate onto 100 g/L soil reached equilibrium after 5 days. The kinetic data of the sorption of iodate onto soil were fitted into the kinetic models, pseudo-first and pseudo-second models, to provide insights of adsorption mechanisms such as mass transfer and chemical reaction (Figure 44b). The pseudo-first-order kinetic model in general fits better to the initial stage of processes especially those with rapid adsorption (Ho and McKay 1998), whereas the pseudo-second-order model (Ho and McKay 1999) considers adsorption behavior over longer contact times with chemisorption as the rate-controlling step. Under our experimental conditions, the experimental data exhibit a reasonably good correlation to the pseudo-second-order kinetic model with good linearity ($R^2 > 0.98$) and in agreement between the experimental and calculated Q_e values, 0.9686 mg/kg and 0.9656 mg/kg, respectively.

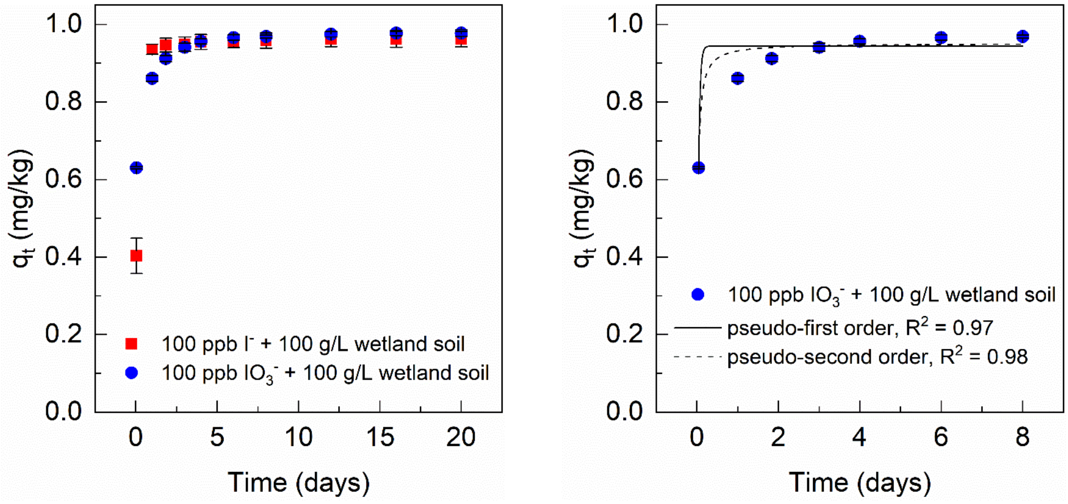

Figure 44. The adsorption kinetic of iodide and iodate onto the SRS F-Area's wetland soil (a) and the pseudo first and pseudo-second orders fitting for adsorbed iodate onto F-Area's wetland soil.

Subtask 2.1: Conclusions

Two low cost and environmentally friendly organoclays (PM-199 and MRM) were studied as potential sorbents for *in-situ* remediation of iodine species, i.e., iodide (I^-) and iodate (IO_3^-), in the SRS wetlands. The adsorption of iodine species was studied using organoclays MRM and PM-199 as the sorbents. Detailed characterization of the organoclays was carried out before the treatment of the iodine species. Approximately 40% of the IO_3^- was adsorbed to the organoclay PM-199, while the I^- was mostly (~99%) removed from the aqueous solution within 12 hours. The separation of iodide from the aqueous solution is primarily driven by the strong adsorption onto the PM-199. In contrast, approximately 80% removal of IO_3^- and I^- by organoclay MRM was achieved within 7 days. The results demonstrate that the organoclays can be used to facilitate iodine species adsorption in the Fourmile Branch wetlands.

Subtask 2.1: References

Bich, C., J. Ambroise and J. Péra (2009). "Influence of degree of dehydroxylation on the pozzolanic activity of metakaolin." Applied Clay Science 44(3): 194-200.

Chang, H.-s., C. Xu, K. A. Schwehr, S. Zhang, D. I. Kaplan, J. C. Seaman, C. Yeager and P. H. Santschi (2014). "Model of radioiodine speciation and partitioning in organic-rich and organic-poor soils from the Savannah River Site." Journal of Environmental Chemical Engineering 2(3): 1321-1330.

Denham, M. E. and M. B. Amidon (2016). Analysis of concentration versus time trends for selected contaminants in groundwater and wetland surface water assocaited with the F-Area and H-Area Seepage Basins Aiken, SC, Savannah River National Laboratory.

Emerson, H. P., C. Xu, Y.-F. Ho, S. Zhang, K. A. Schwehr, M. Lilley, D. I. Kaplan, P. H. Santschi and B. A. Powell (2014). "Geochemical controls of iodine uptake and transport in Savannah River Site subsurface sediments." Applied Geochemistry 45: 105-113.

Ho, Y. S. and G. McKay (1998). "A Comparison of Chemisorption Kinetic Models Applied to Pollutant Removal on Various Sorbents." Process Safety and Environmental Protection 76(4): 332-340.

Ho, Y. S. and G. McKay (1999). "Pseudo-second order model for sorption processes." Process Biochemistry 34(5): 451-465.

Irfan Khan, M., H. U. Khan, K. Azizli, S. Sufian, Z. Man, A. A. Siyal, N. Muhammad and M. Faiz ur Rehman (2017). "The pyrolysis kinetics of the conversion of Malaysian kaolin to metakaolin." Applied Clay Science 146: 152-161.

Kaplan, D. I., M. E. Denham, S. Zhang, C. Yeager, C. Xu, K. A. Schwehr, H. P. Li, Y. F. Ho, D. Wellman and P. H. Santschi (2014). "Radioiodine Biogeochemistry and Prevalence in Groundwater." Critical Reviews in Environmental Science and Technology 44(20): 2287-2335.

Kaplan, D. I., S. Zhang, K. A. Roberts, K. Schwehr, C. Xu, D. Creeley, Y.-F. Ho, H.-P. Li, C. M. Yeager and P. H. Santschi (2014). "Radioiodine concentrated in a wetland." Journal of Environmental Radioactivity 131: 57-61.

Müller, C. M., B. Pejcic, L. Esteban, C. D. Piane, M. Raven and B. Mizaikoff (2014). "Infrared Attenuated Total Reflectance Spectroscopy: An Innovative Strategy for Analyzing Mineral

Components in Energy Relevant Systems." Scientific Reports 4(1): 6764.

Neeway, J. J., D. I. Kaplan, C. E. Bagwell, M. L. Rockhold, J. E. Szecsody, M. J. Truex and N. P. Qafoku (2019). "A review of the behavior of radioiodine in the subsurface at two DOE sites." Science of The Total Environment 691: 466-475.

Otosaka, S., K. A. Schwehr, D. I. Kaplan, K. A. Roberts, S. Zhang, C. Xu, H.-P. Li, Y.-F. Ho, R. Brinkmeyer, C. M. Yeager and P. H. Santschi (2011). "Factors controlling mobility of 127I and 129I species in an acidic groundwater plume at the Savannah River Site." Science of The Total Environment 409(19): 3857-3865.

Perdue, E. M. (1998). Chemical Composition, Structure, and Metal Binding Properties. Aquatic Humic Substances: Ecology and Biogeochemistry. D. O. Hessen and L. J. Tranvik. Berlin, Heidelberg, Springer Berlin Heidelberg: 41-61.

Santschi, P. H., C. Xu, S. Zhang, K. A. Schwehr, R. Grandbois, D. I. Kaplan and C. M. Yeager (2017). "Iodine and plutonium association with natural organic matter: A review of recent advances." Applied Geochemistry 85: 121-127.

Schwehr, K. A., P. H. Santschi, D. I. Kaplan, C. M. Yeager and R. Brinkmeyer (2009). "Organo-Iodine Formation in Soils and Aquifer Sediments at Ambient Concentrations." Environmental Science & Technology 43(19): 7258-7264.

Xu, C., S. Zhang, Y.-F. Ho, E. J. Miller, K. A. Roberts, H.-P. Li, K. A. Schwehr, S. Otosaka, D. I. Kaplan, R. Brinkmeyer, C. M. Yeager and P. H. Santschi (2011). "Is soil natural organic matter a sink or source for mobile radioiodine (129I) at the Savannah River Site?" Geochimica et Cosmochimica Acta 75(19): 5716-5735.

Zhang, S., J. Du, C. Xu, K. A. Schwehr, Y. F. Ho, H. P. Li, K. A. Roberts, D. I. Kaplan, R. Brinkmeyer, C. M. Yeager, H.-s. Chang and P. H. Santschi (2011). "Concentration-Dependent Mobility, Retardation, and Speciation of Iodine in Surface Sediment from the Savannah River Site." Environmental Science & Technology 45(13): 5543-5549.

Zhang, S., Y.-F. Ho, D. Creeley, K. A. Roberts, C. Xu, H.-P. Li, K. A. Schwehr, D. I. Kaplan, C. M. Yeager and P. H. Santschi (2014). "Temporal Variation of Iodine Concentration and Speciation (127I and 129I) in Wetland Groundwater from the Savannah River Site, USA." Environmental Science & Technology 48(19): 11218-11226.

Subtask 2.2: Humic Acid Batch Sorption Experiments with SRS Soil

Subtask 2.2: Introduction

In the 1950s, Savannah River Site (SRS), located 13 miles south of Aiken in South Carolina, was a defense nuclear processing facility owned by the U.S. government. During the Cold War, from 1953 to 1988, SRS produced a large amount of radioactive and hazardous acidic waste from the production of plutonium and irradiated fuel (Evans, et. al., 1992). Approximately 1.8 billion gallons of acidic waste solutions containing low-level radioactivity from numerous isotopes were discharged into a series of unlined seepage basins in the F/H Area. At that time, it was believed that most of the radionuclides present in the waste solution would bind to the soil, precluding the migration of the radionuclides. However, sufficient quantities of uranium isotopes, ^{129}I, ^{99}Tc, and tritium migrated into the groundwater, creating an acidic plume with a pH between 3 to 5.5. The groundwater remains acidic with uranium concentrations surpassing the Environmental Protection

Agency (EPA) maximum contaminant levels (Dong et. al., 2012). In an effort to remove the contaminants from the groundwater, pump-and-treat and re-inject systems were implemented in 1997. Downgradient contaminated groundwater was pumped up to a water treatment facility, treated to remove metals (through osmosis, precipitation/flocculation, and ion exchange), and then re-injected upgradient within the aquifer. The pump-and-treat water treatment unit eventually became less effective generating large amounts of radioactive waste. The maintenance of the pump-and-treat water treatment unit was very expensive, and this prompted the research for new remedial alternatives. In 2004, the pump-and treat system was replaced by a funnel and gate system in order to create a treatment zone via injection of a solution mixture composed of two components, sodium hydroxide and carbonate. The injections were done directly into the gates of the F-Area groundwater to raise pH levels. The purpose of the treatment zone was to reverse the acidic nature of the contaminated sediments, thereby producing a more negative net charge on the surface of sediment particles and enhancing the adsorption of cationic contaminants. This amplified the adsorption of cationic contaminants on the sediment and resulted in the decrease of Sr-90 and U-238 concentrations but had no effect on the treatment of iodine. To maintain the pH neutral within the treatment zone, systemic injections were required. Carbonate forms strong complexes with uranium and could remobilize uranium that was already adsorbed within the treatment zone (Gudavalli et. al., 2013).

Humic substances (HS) are major components of soil organic matter, which are polyfunctional organic macromolecules that are formed from the decomposition of biomass or dead organic matter (Trevisan, et. al., 2010). Humic substances can be divided into three main fractions: humin, which is insoluble at all pHs, humic acid (HA), soluble at pHs greater than 3.5, and fulvic acids, which are soluble at all pHs (Choppin et. al., 1992). Humic acid is an important ion exchange and metal complexing ligand with a high complexation capacity, allowing it to chemically bind to metals and influence their migration behavior (Davis et. al., 2002). Previous studies suggest that the sorption of U(VI) in the presence of humic acid is a complex process (Perminova et. al., 2002). Ivanov et al (2012) studied U(VI) sorption onto bentonite with and without humic acid and proved enhanced uranium sorption at pHs lower than 3.8, while it was reduced at pHs above 3.8. In another study, U(VI) sorption proved to be influenced by pH, the U(VI) concentration, humic acid, and inorganic carbon species (Krepelova et al., 2007).

Chemically modified humate materials, commercially known as KW-15 and KW-30, are being tested for its use in remediation techniques to reduce the mobility of uranium in the subsurface at SRS. This project focuses on studying the characterization of humate materail and the sorption of uranium in the presence of humate onto SRS sediments, with parameters set to evaluate the effect of pH, time, and concentrations of U and HA. This study aims to determine if humic substances containing humic/fulvic acids of different molecular weights can be used to control uranium mobility and to understand the different interactions and mechanisms occurring in the presence of the modified humic acid. These interactions affect the adsorption of uranium onto the sediments that impacts U(VI) mobility in SRS groundwater. This study evaluates if humic substances could be used for in-situ remediation of uranium in acidic environments and determine optimal conditions for U(VI) removal from the aqueous phase.

This research also suggests if modified humic substances can be used as potential amendments at other DOE sites, where soil and groundwater conditions are less acidic compared to SRS.

Subtask 2.2: Objectives

The objective of this research is to investigate the sorption behavior of humic substances via batch experiments and evaluate the effect of sorbed humic substances on uranium sorption to support groundwater remediation strategies. The outcome of these studies will help to determine approaches to deploy humate technology under varying site-specific conditions.

Subtask 2.2: Methodology

Materials:

This study utilized sediment samples that were collected from the F-Area at SRS (FAW1 70-90 ft) and sieved through a 2mm sieve. The fraction ≤ 2 mm was used in the experiments. This sediment was chosen due to its comparability to the soil composition in the uranium-contaminated aquifer layer. For U(VI), a commercial 1000 ppm uranyl stock solution in 2% nitric acid was used. A humate stock solutions (KW-15 and KW-30) consisting of 1000 mg in 1000 mL of deionized water (DIW) was prepared for use in the experiments. The pH of the samples was adjusted using 0.1 M HCL or 0.1 M NaOH.

Experimental Procedures:

Characterization of Mod-HA

The attenuated total reflectance Fourier transform infrared spectroscopy (ATR-FTIR) spectra of the mod-HA and Huma-K were obtained using an Agilent FTIR (Santa Clara, CA, USA) in the spectral range of 400 - 4000 cm^{-1} with 16 scans per spectrum. The zeta potentials and hydrodynamic sizes of mod-HA and Huma-K were determined using a Malvern Zetasizer Nano Z (Malvern, Worcestershire, United Kingdom). The differential potentiometric titrations (DPT) provide useful information on the protonation/deprotonation properties of functional groups, which can be involved in the sorption process.

The dynamic light scattering (DLS), Brunauer-Emmett-Teller (BET), scanning electron microscopy coupled with energy dispersive X-ray spectroscopy (SEM-EDS), and potentiometric titration were used to further characterize humic materials. The zeta potentials and hydrodynamic sizes of mod-HA and Huma-K were determined using a Malvern Zetasizer Nano Z. The surface areas of the humic substances were measured by the Brunauer-Emmett-Teller (BET) analyzer. The spectra and mapping of elements in Huma-K and mod-HA were analyzed by the JEOL IT-500HR FE-SEM coupled with the Burker Quantax 400 EDS.

Uranium Sorption and Desorption Experiments

Batch humate sorption experiments were conducted in triplicates, with 200 mg of SRS sediments spiked with 50 ppm of humate (KW-15 and KW-30) with a total volume of 20 mL in 50 mL polypropylene centrifuge tubes. Samples were pH adjusted to pH 4 daily and placed on a platform shaker at 100 rpm to equilibrate. After 5 days, samples were centrifuged at 2700 rpm for 30 minutes and the supernatant was analyzed via a UV-Vis spectrophotometer.

Sediment coated with humic acid was then contacted with 20 mL of 0.5 mg/L of U(VI) solution at pH 4. Similar to the sorption of HA step, the pH of the samples was adjusted to pH 4 daily for 7 days. After 7 days, samples were centrifuged for 30 minutes at 2700 rpm, supernatant was carefully removed, and unfiltered samples as well as samples filtered through 0.45 µm filters were stored in the refrigerator to measure the uranium concentration. After the supernatant was removed, fresh

DIW, pH adjusted from pH 3 to 8, was introduced to study the effect of pH during the desorption process. The pH of the samples was monitored and adjusted and left on the platform shaker daily for 7 days. The samples were then centrifuged. The supernatant was removed, and half was filtered while the other half was left unfiltered. To study the desorption, 20 mL of DIW at pH 4-8 was added to the samples and left on the platform shaker at 100 rpm for 7 days. After the 7 days, the samples were centrifuged at 2700 rpm for 30 minutes and the supernatant removed and analyzed via ICP-MS.

A control experiment was performed by preparing 20 mL samples with 0.5 mg/L of U(VI) that were kept on the platform shaker at 100 rpm. The pH of these samples was monitored and adjusted to pH 3-8 daily for 7 days. After 7 days, samples were centrifuged at 2700 rpm for 30 minutes and the supernatant was removed and analyzed via ICP-MS.

The effect of pH on uranium removal was studied by following the same procedure while pH was adjusted to 3-8.

Subtask 2.2: Results and Discussion

Characterization of Humic Material

The differential potentiometric titrations (DPT) provide useful information on the protonation/deprotonation properties of functional groups, which can be involved in the sorption process. Figure 45 shows the differential potentiometric titration (DPT) of mod-HA. In the DPT curve, the band at pH ~ 9.5 to 10.3 in mod-HA corresponds to hydroxyl/phenolic functionality of HA. The DPT curve of mod-HA reveals a broad peak at pH ~ 3 to 6.5 denoting the carboxylic groups arranged in different configurations within mod-HA. The sharp peaks at ~ 6.0 can be assigned to the out-of-plane silanol group (pKa = 5.6) of the mod-HA (Sulpizi, et al., 2012 and Gonzalez-Raymat et al., 2018). The peaks at 7.1 and 10.5 can be assigned to the pKa values of carbonic acid (H_2CO_3) (Gonzalez-Raymat et al., 2018). The mod-HA could have been extracted from leonardite using the highly alkaline solution KOH. The HCO_3^- could have formed because of highly alkaline solutions where the CO_2 in the atmosphere reacted with OH^- and then precipitated in the mod-HA (Gonzalez-Raymat et al., 2018).

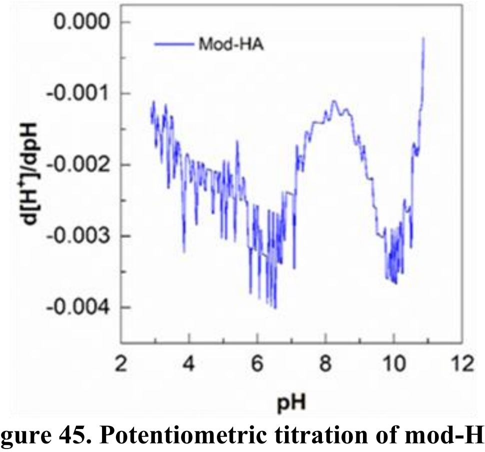

Figure 45. Potentiometric titration of mod-HA.

The zeta potentials of both humate materials are shown in Figure 46. The zeta potential of Huma-K and mod-HA show the same trend: at higher pH range, HA is more negatively charged compared to the lower pH range indicating higher stability than the lower pH range. Figure 47 shows the averaged hydrodynamic size of Huma-K in water is 330.1 nm with a little amount of aggregate at

5305 nm, while approximately 65% of modified-HA hydrodynamic size in water is 428.3 nm, 29% of mod-HA is 122.3 nm, and a small amount of aggregate at 5285 nm. The BET analysis shows the surface area of mod-HA is significantly larger than Huma-K, 1.1507 m^2/g and 0.0277 m^2/g, respectively. The low surface area of Huma-K could be attributed to the impurities leached from leonardite during the alkaline extraction of humic substances (Gonzalez-Raymat et al., 2018).

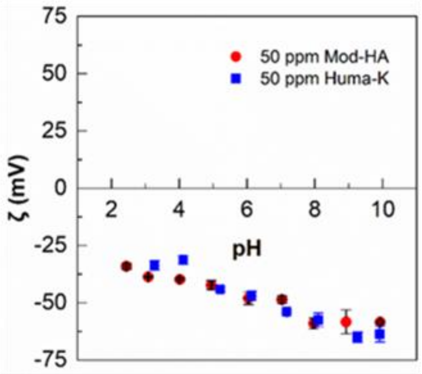

Figure 46. Zeta potential of mod-HA (●) and Huma-K (■).

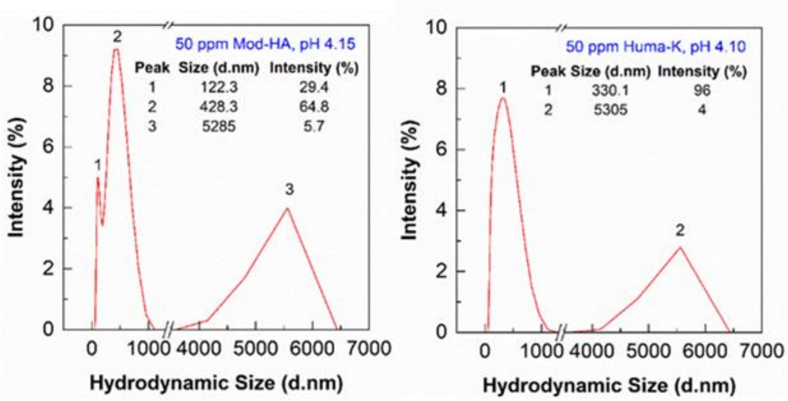

Figure 47. Hydrodynamic sizes of mod-HA (left) and Huma-K (right).

In ATR-FTIR spectra (Figure 48), the broad peak at 3000-3600 cm^{-1} denotes the O-H stretching of the phenols, alcohols, and carboxylic acids for mod-HA and Huma-K. The sharp bands at 2916 and 2848 cm^{-1} can be attributed to the aliphatic sp^3 C-H stretching. The band at 1559 cm^{-1} in mod-HA corresponds to the asymmetric C=O stretching of carboxylate anion (COO^-) and the N-H of HA (Jiang et al., 2014). The energies of the COO^- absorption band depend on several factors such as the electron density, intra- and inter-molecular H bonding, interactions with metal ions, and coupling with other vibrational modes in the molecule. The study reported by Hay et al., 2007 shows that the structural environment of the carboxyl group affects the energies of the asymmetric stretching vibrations of the COO^- in natural organic molecules. Due to a lower COO^- vibrational energy, 1559 cm^{-1}, it was concluded that the dominant fraction of carboxyl groups in the mod HA and Huma-K are substituted aromatics. The COO^- symmetric stretching frequency and N-H of the HAs is 1379 cm^{-1}, which is within the range of 1368 and 1382 cm^{-1} for the reported natural organic molecules (Hay et al., 2007). The strong peak at 1100 cm^{-1} denotes the C-O stretching vibration of the humic substances. The peaks at 1100 - 925 cm^{-1} can also be assigned to the Si-O-Si and Si-O-C moieties (Zhou et al., 2018).

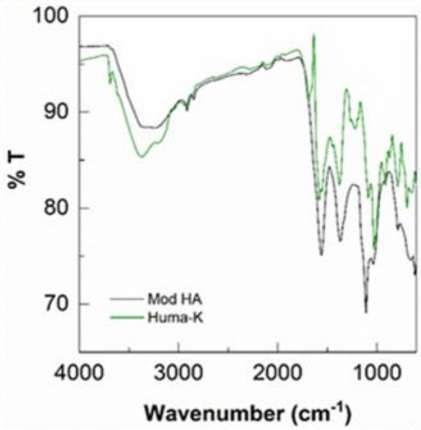

Figure 48. FTIR Spectra of mod-HA and Huma-K.

The morphological structure and particle sizes of the Huma-K and mod-HA were determined by SEM. Figure 49a shows that the modified humic acid has a spherical shape and a wide range of particle-size distribution. The floc on the surface texture of mod-HA indicates a large surface area. Figure 49b shows that the Huma-K has a larger size distribution and a smaller surface area which is consistent with our BET results since it is the unrefined commercial product used in agriculture (Gonzalez-Raymat et al., 2018).

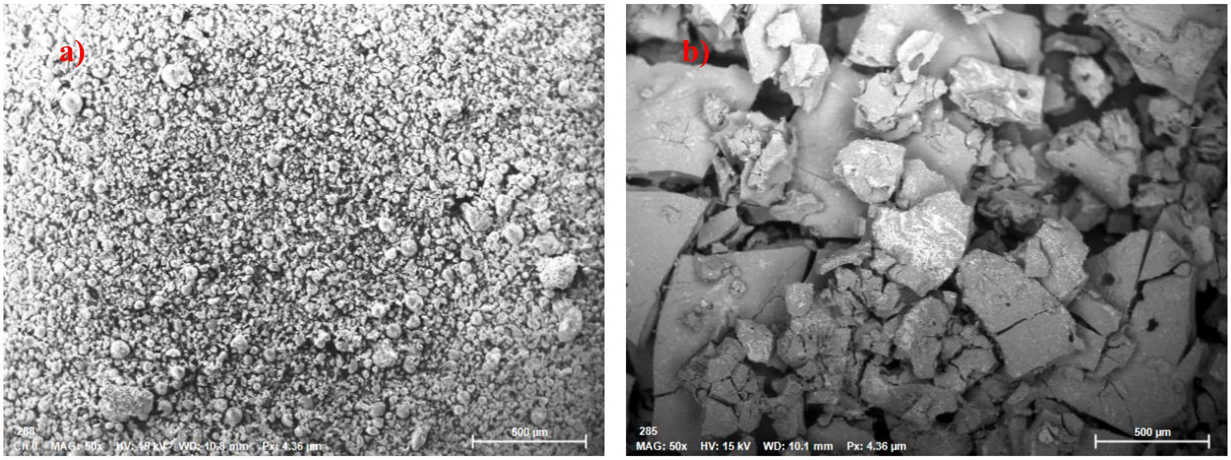

Figure 49. (a) SEM spectra of mod-HA and (b) Huma-K.

Elemental analyses of Huma-K and mod-HA (Figure 50 and Figure 51) indicated that the primary metal was potassium (K), which resulted from the treatment of leonardite with potassium hydroxyl for the extraction of these commercial humic acids. The elements carbon (C), oxygen (O), and silicon (Si) were related to the functional groups (carboxyl groups, hydroxyl/phenolic groups, aromatic rings, aliphatic chains, and silanol groups) present in humic substances. Elemental analysis of Huma-K (Figure 50) also detected the presence of aluminum (Al), iron (Fe), sodium (Na), silicon, calcium, and sulfur in Huma-K, which are the impurities in Huma-K since it is the unrefined commercial product. There are trace amounts of sulfur (S) and calcium (Ca) present in the mod-HA. The EDS mapping of Si corresponds to the EDS mapping of the O (Figure 51) indicating the Si-O-Si and/or Si-OH groups of the mod-HA.

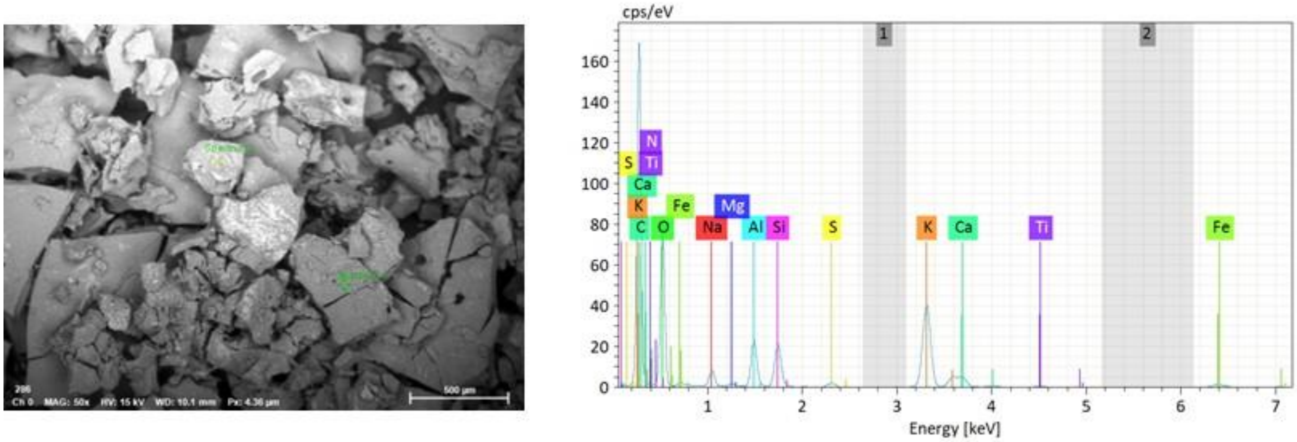

Figure 50. (a) SEM spectra of Huma-K and (b) EDS spectra of Huma-K.

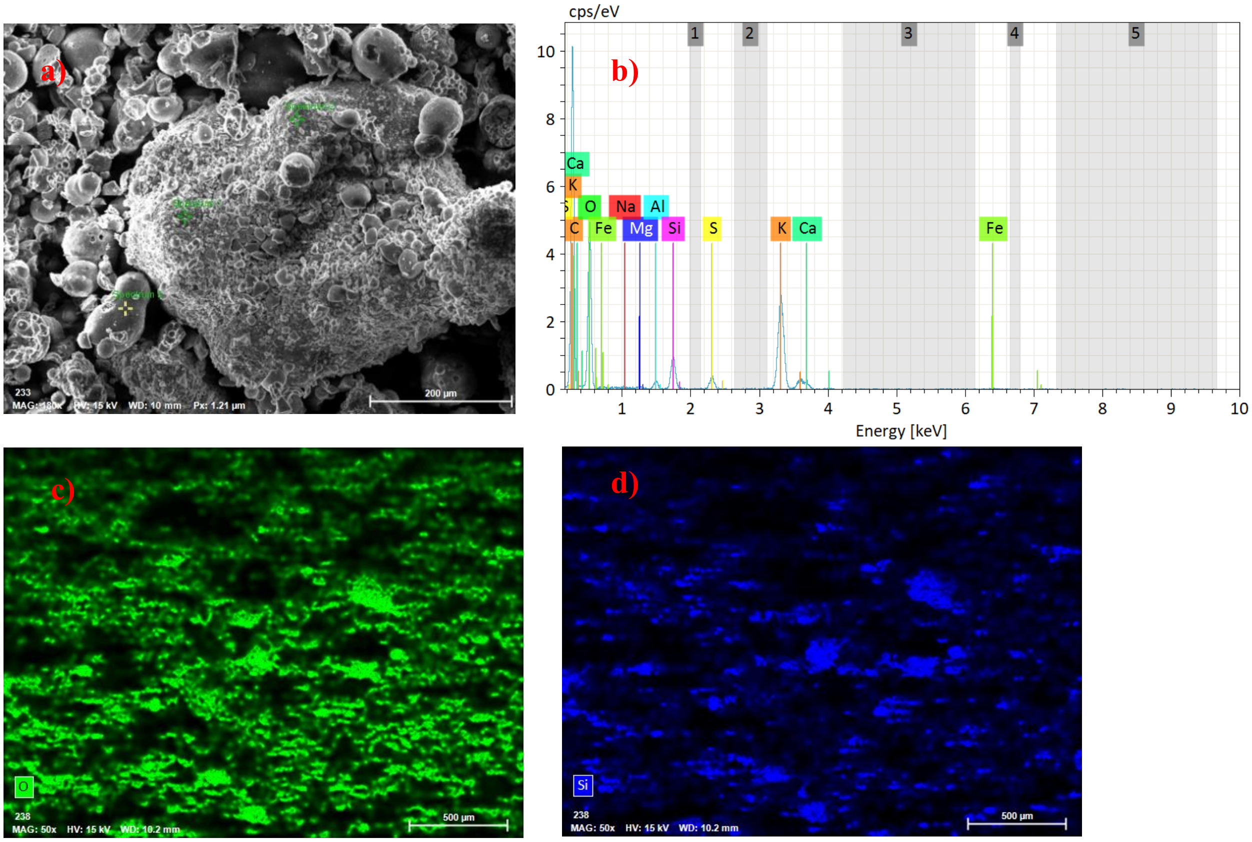

Figure 51. (a) SEM image of mod-HA , (b) EDS spectra of mod-HA , (c) EDS mapping of O , and (d) EDS mapping of Si.

Uranium sorption and desorption

Figure 52 shows the effect of pH on uranium precipitation and the trend shows that U(VI) removal due to precipitation slowly increases as the pH increases. Figure 53 shows the sorption of uranium for unfiltered and filtered samples. The trend displays an increase in sorption as pH increases until pH 5 where it then slowly decreases in a linear pattern until pH 8. Figure 54 displays the desorption percentages of U(VI) in the pH range of 4-8. Higher desorption was observed at pH 4 and 8 with 40% desorption compared to 15% desorption at pH 5-7.

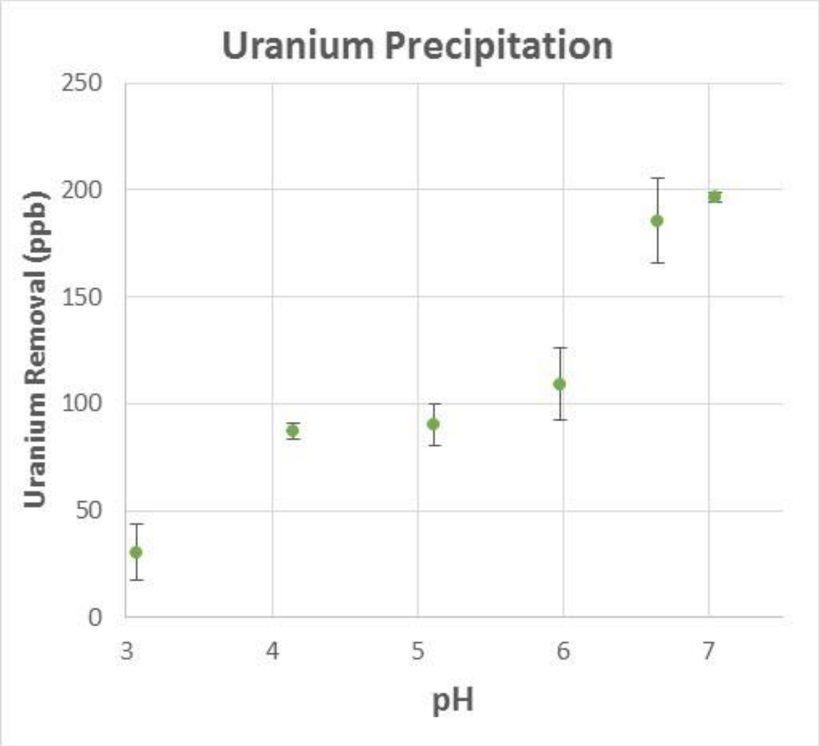

Figure 52. Uranium precipitation with change in pH.

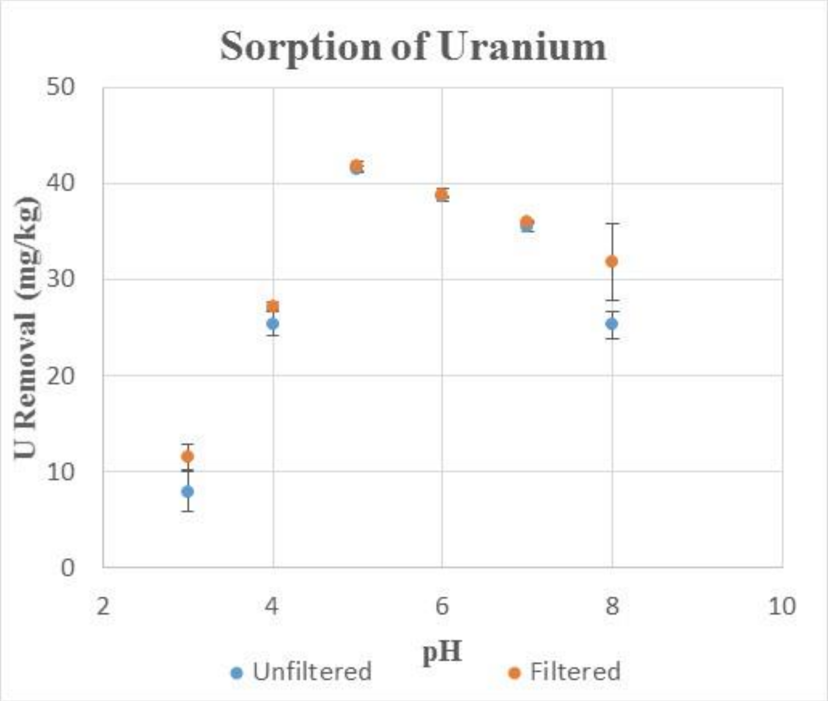

Figure 53. The effect of pH on the sorption of uranium onto mod-HA coated sediments.

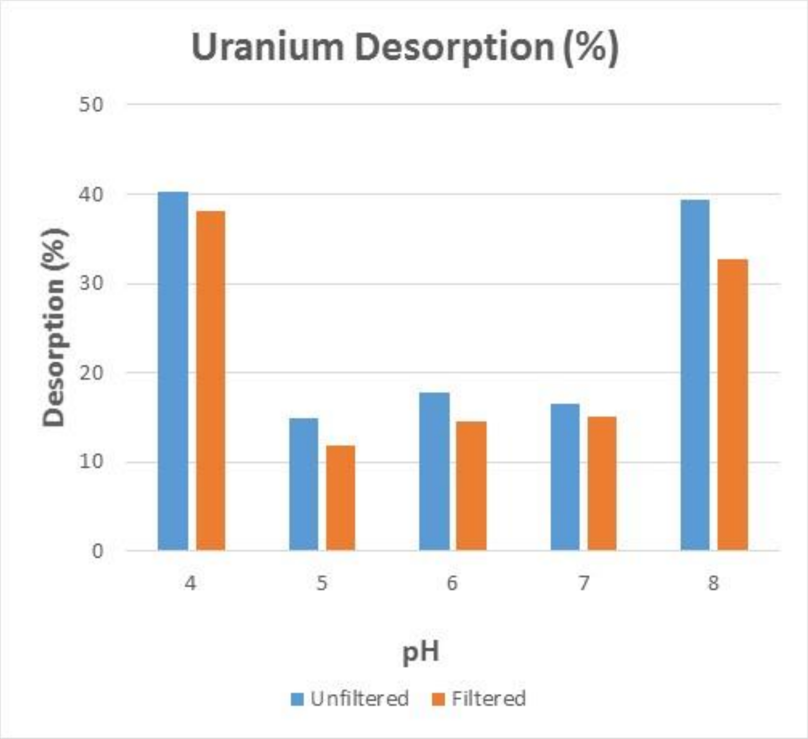

Figure 54. Percent of uranium desorption, calculated based on uranium sorbed to amount of uranium desorbed.

Figure 55 shows the amount of mod-HA desorbed with change in pH and amount of uranium sorbed onto mod-HA coated sediment. Both desorption of humic acid and sorption of U follow similar trends with an increase in pH. In Figure 56, the concentration (mg/L) of mod-HA and the desorption of uranium (mg/kg) were analyzed and displayed a trend of uranium desorption increasing with the mod-HA that is present from pH 3 to 5 and then decreasing, while the mod-HA continues increasing at pH 8.

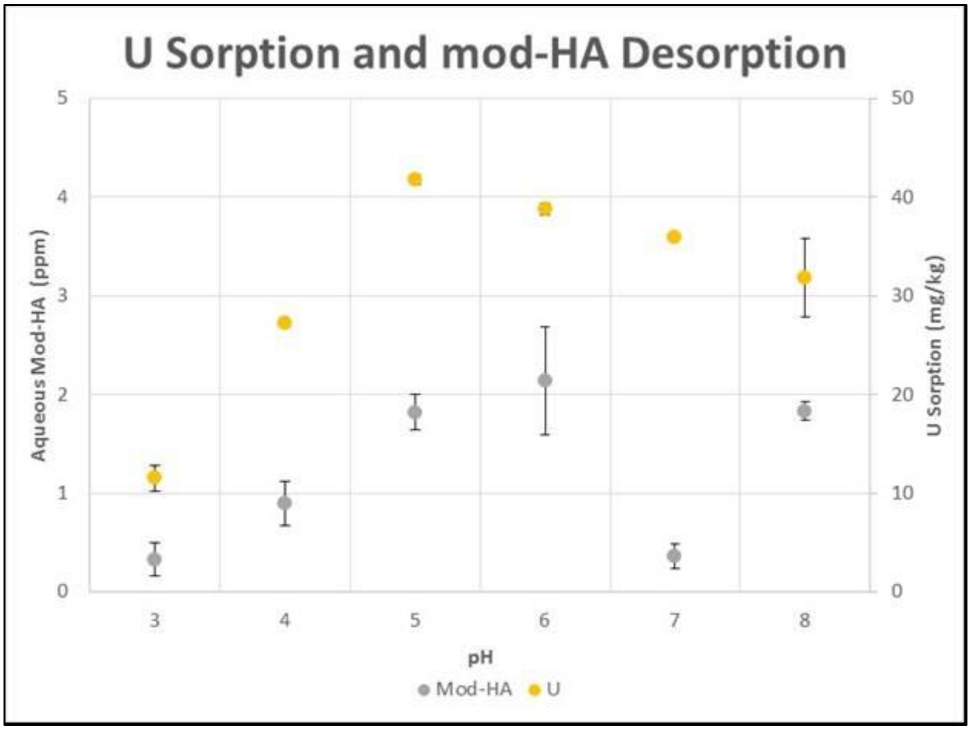

Figure 55. Effect of pH on mod-HA desorption and U sorption.

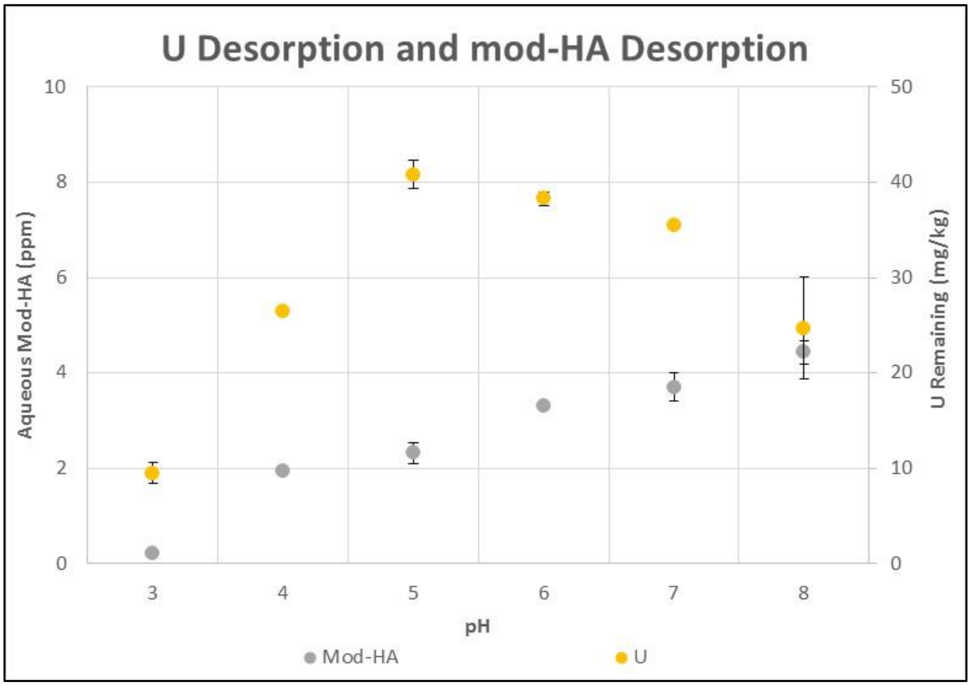

Figure 56. Effect of pH on Mod-HA desorption and U desorption (uranium remaining is shown).

Sorption of KW-30 and Uranium

Figure 57 shows the sorption of humate (mg/kg) in each sample at pH 4. The KW-30 amended sediment samples were then introduced with fresh DIW spiked with a range of U(VI) concentrations (0.025, 0.05, 0.1, 0.25, 0.5, 1 ppm). The samples were pH adjusted to pH 4 and placed on the platform shaker for 7 days, then centrifuged at 2700 rpm for 30 minutes. The supernatant was removed and analyzed on the UV-Vis for humate concentrations to estimate the amount of humate desorbed during the uranium sorption process. Figure 58 displays the concentration of humate remaining on the sediment when spiked with U(VI). The trend is similar to the sorption of humate without the presence of U(VI).

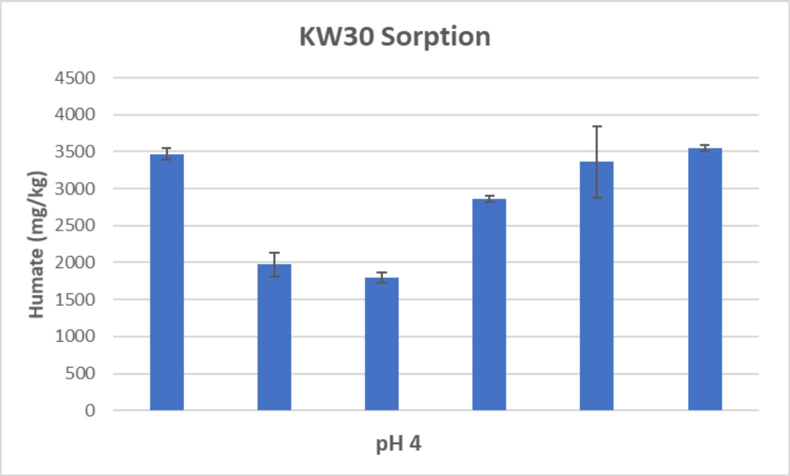

Figure 57. KW30 Humate Sorption onto SRS sediments.

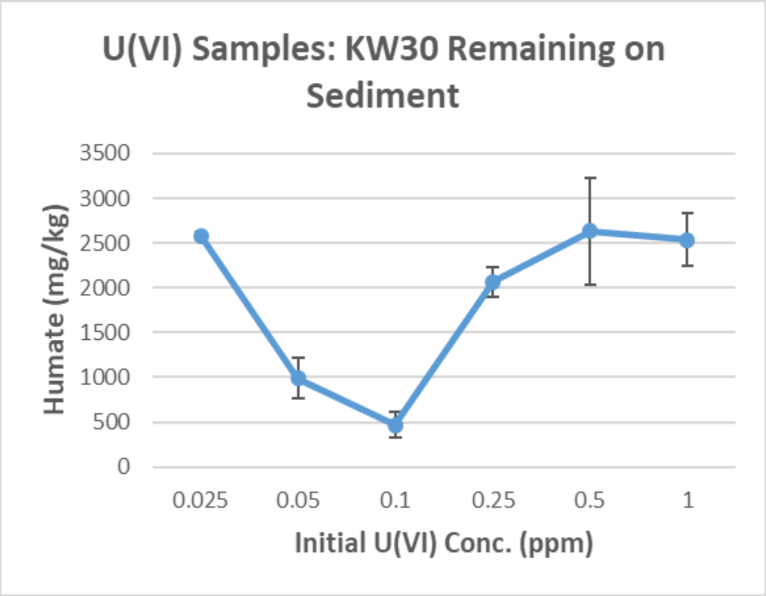

Figure 58. Humate remaining on SRS sediment in the presence of U(VI).

To avoid error in sample preparation, a bulk quantity of 50 ppm KW30 stock solution was prepared using pH 4-adjusted DIW and distributed among the sample vials and the experiment was repeated. Figure 59 shows the mod-HA sorption onto the SRS sediments with an average sorption value of ~1700 mg/kg. This is comparatively lower than in previously conducted experiments (~3500 mg/kg) and is due to the precipitation that occurs when pH adjusting the 50 ppm stock of mod-HA. A new set of KW30 samples will be spiked with humate after introducing into the vials.

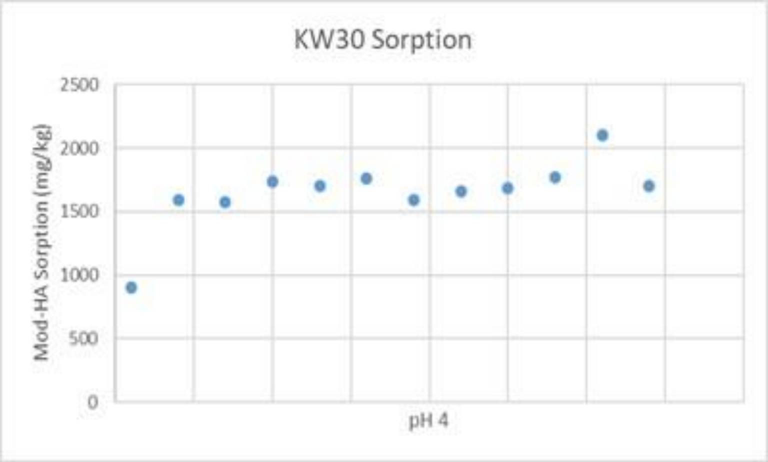

Figure 59. KW30 Humate Sorption onto SRS sediments.

A new set of samples to study the sorption of uranium on humate (KW-30) coated sediments were prepared. As shown in Figure 60, inconsistent results for samples 1 through 3 were possibly due to human error. These samples are excluded in the second part of the rest of the sample (4-12) and were used to study the sorption of uranium onto humate-coated sediments (~2300 mg/kg).

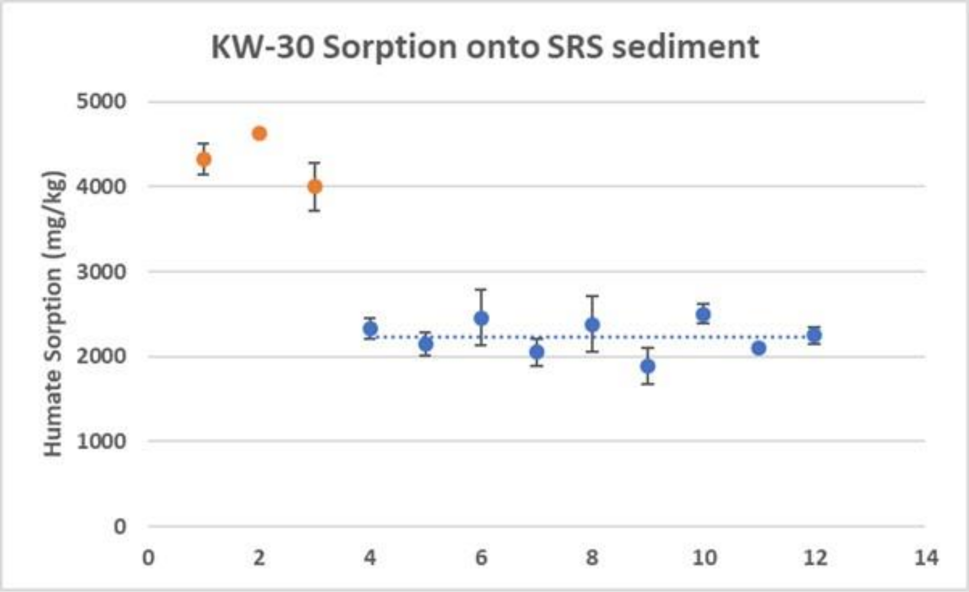

Figure 60. Sorption of KW-30 onto SRS sediment.

A volume of 20 mL of fresh uranium solution in the range of 200, 300, 400, 500, 600, 700, 800, 900, and 1000 ppb was introduced into vials containing sediment coated with KW-30. Figure 61 shows the removal of uranium with respect to equilibrium uranium concentrations was increased with an increase in uranium concentrations, however, the removal of uranium has not reached an equilibrium.

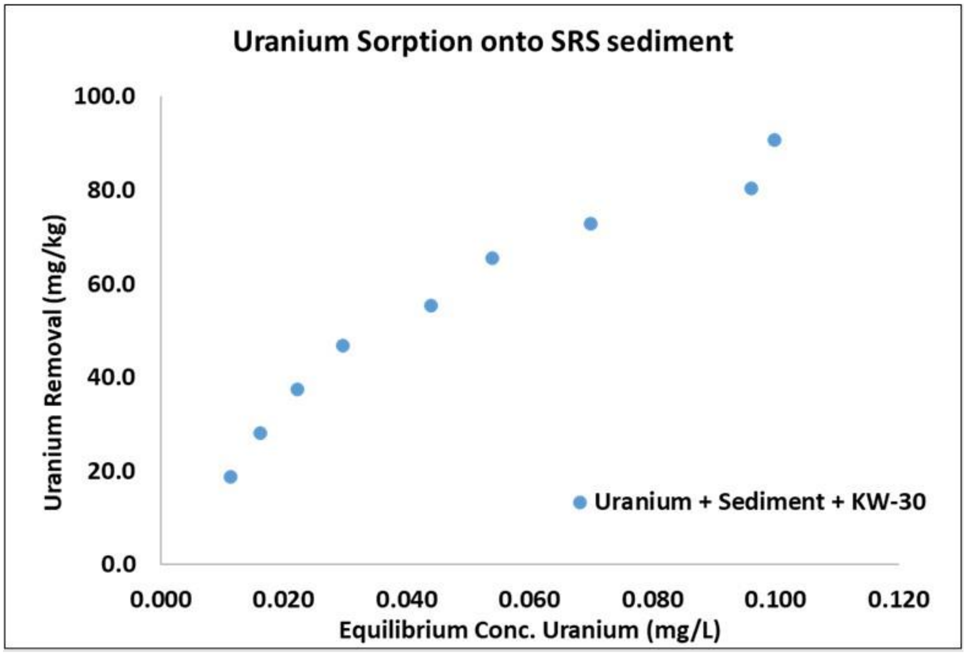

Figure 61. Sorption of uranium onto humate (KW-30)-coated SRS sediment.

The experiment was continued to include higher initial uranium concentrations by preparing triplicate samples. Figure 62 shows the KW-30 sorption data with additional samples prepared to include higher uranium concentrations. Data shows that the sorption of KW-30 has a step function (2,500 - 4,500 mg/kg) and this could be due to the particle size. SRS sediment has sand, silt and clay fractions and it is postulated that theses fractions are causing the step removal of KW-30. A new set of experiments is planned to prove this hypothesis and samples will be prepared with pure Quartz and Kaolinite to study the removal of KW-30.

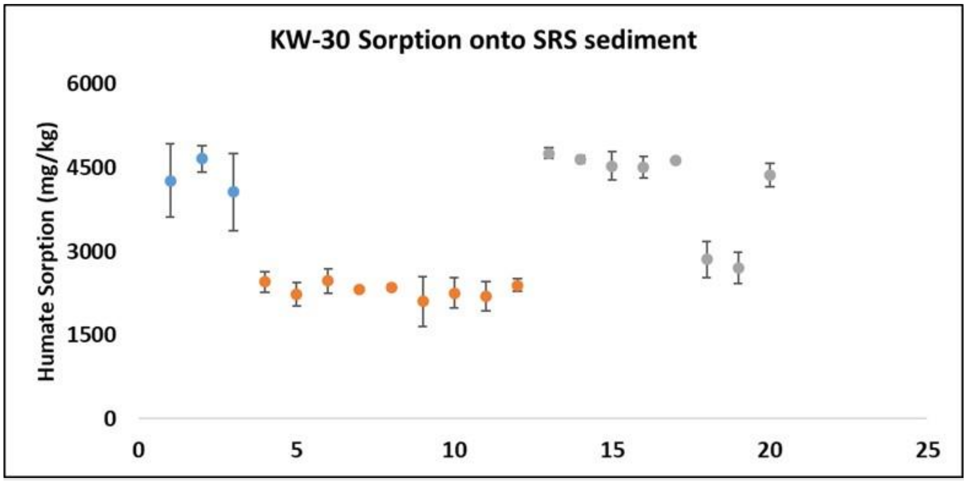

Figure 62. Sorption of KW-30 onto SRS sediment.

Comparison of data obtained from humate-free, Huma-K and KW-15 uranium sorption data with KW-30 sorption data is shown in Figure 63. Sorption of uranium onto SRS sediment coated with KW-30 is much higher compared to mod-HA (KW-15) and Huma-K coated sediment. As evident in Figure 63, the sorption of uranium in the presence of KW-30 is yet to reach equilibrium. Experiments will be conducted to extend the range of initial uranium concentration up to 20 ppm.

The current data shows sorption of uranium for the initial uranium concentration in the range of 200 ppb - 1 ppm.

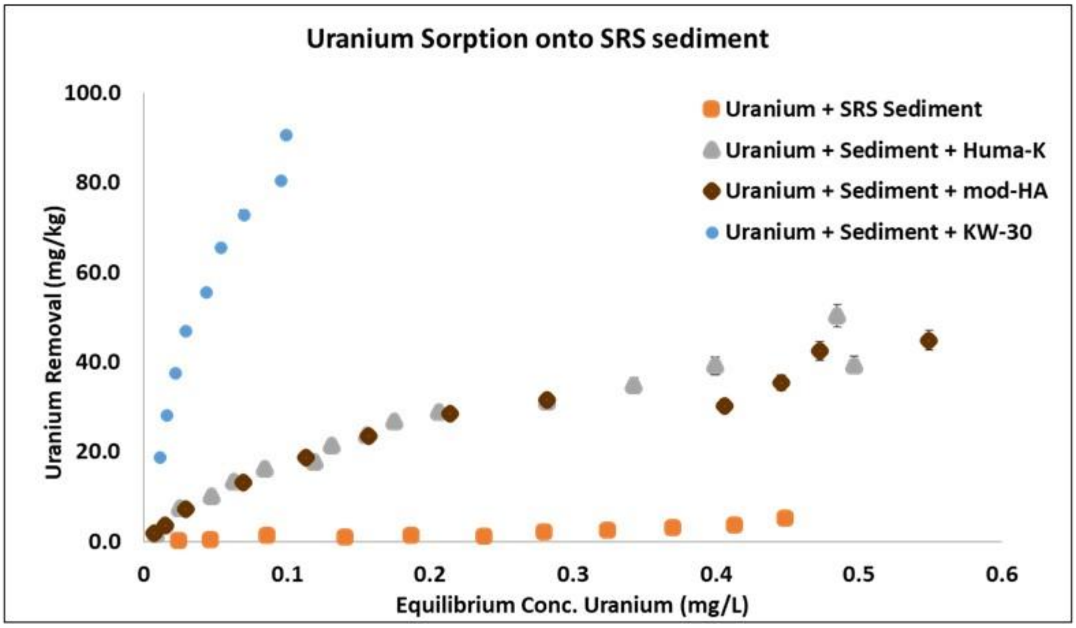

Figure 63. Sorption of uranium onto humate-coated sediment and plain sediment.

Subtask 2.2: Conclusions

Sorption of uranium is pH dependent for sediment coated with KW-15. Sorption increased as pH increased until pH 5, where it then slowly decreased until pH 8. KW-30 is shown to have much higher capacity to sequester uranium compared to Huma-K and KW-15, however further investigation is needed to find the sorption equilibrium for KW-30.

Subtask 2.2: References

Choppin, G.R., 1992. The role of natural organics in radionuclide migration in natural aquifer systems. *Radiochim. Acta* 58/59, 113.

Davis. J.A., Adsorption of natural dissolved organic matter at the oxide/water interface, 1982, 2002. Geochim. Cosmochim. Acta 46, 2381-2393.

Dong, W., Tokuanga, T. K., Davis, J. A., Wan, J., (2012). Uranium(VI) Adsorption and Surface Complexation Modeling onto Background Sediments from the F-Area Savannah River Site. Environ. Sci. Technol. 46, 1565-1571.

Evans, A.G., Bauer, L.R., Haselow, J.S., Hayes, D.W., Martin, H.L., McDowell, W.L., Pickett, J.B., 1992. Uranium in the Savannah River Site environment. Westinghouse Savannah River Co., Aiken, SC (United States), p. 95.

Gonzalez-Raymat, H., Anagnostopoulos, V.; Denham, M.; Cai, Y.; Katsenovich, Y. P., Unrefined humic substances as a potential low-cost amendment for the management of acidic groundwater contamination. Journal of Environmental Management 2018, 212, 210-218.

Gudavalli, R., Katsenovich, Y., Wellman, D., Idarraga, M., Lagos, L., Tansel, B., 2013. Comparison of the kinetic rate law parameters for the dissolution of natural and synthetic autunite in the presence of aqueous bicarbonate ions

Hay, M. B., Myneni, S. C. B., Structural environments of carboxyl groups in natural organic molecules from terrestrial systems. Part 1: Infrared spectroscopy. Geochimica et Cosmochimica Acta 2007, 71 (14), 3518-3532.

Ivanov, P., Griffiths, T., Bryan, N.D., Bozhikov, G. and S. Dmitriev, 2012. The effect of humic acid on uranyl sorption onto bentonite at trace uranium levels. *J. Environ. Monit.,* 14, 2968 - 2975.

Jiang, W., Cai, Q., Xu, W., Yang, M., Cai, Y., Dionysiou, D. D., O'Shea, K. E., Cr (VI) adsorption and reduction by humic acid coated on magnetite. Environmental science & technology 2014, 48 (14), 8078-8085.

Krepelova. A., 2007. Influence of Humic Acid on the Sorption of Uranium(VI) and Americium(III) onto Kaolinite (Dissertation).

Largitte, L. and R. Pasquier (2016). "A review of the kinetics adsorption models and their application to the adsorption of lead by an activated carbon." Chemical Engineering Research and Design 109: 495-504.

Perminova, I.V, Hatfield, K., Hertkorn, N., 2002. Use of humic substances to remediate polluted environments: from theory to practice. In the proceedings of the NATO Advance Research Workshop, Springer, P.O Box 17, 3300 AA Dordrech, The Netherland.

Trevisan, Sara, et al. "Humic Substances Biological Activity at the Plant-Soil Interface." *Plant Signaling & Behavior*, vol. 5, no. 6, 2010, pp. 635–643., doi:10.4161/psb.5.6.11211.

Zhou, T., S. Huang, D. Niu, L. Su, G. Zhen and Y. Zhao (2018). "Efficient Separation of Water-Soluble Humic Acid Using (3-Aminopropyl)triethoxysilane (APTES) for Carbon Resource Recovery from Wastewater." ACS Sustainable Chemistry & Engineering 6(5): 5981-5989.

TASK 3: CONTAMINANT FATE AND TRANSPORT MODELING FOR THE SAVANNAH RIVER SITE

The Tims Branch ecosystem represents an important applied science opportunity as a result of significant past research by the Savannah River Ecology Laboratory (SREL) and the Savannah River National Laboratory (SRNL). Tims Branch has served as an ideal testbed for development of a flow and contaminant transport model of an SRS stream that was impacted by DOE operations for 50 years and which is now recovering. The Tims Branch model being developed by FIU addresses the knowledge gaps related to the fate and transport of dissolved and sediment-bound contaminants at DOE EM sites during extreme hydrological events. Results from this study are key to evaluating the effectiveness of tin (II)-based mercury treatment of wetlands at the SRS site, and are also relevant to evaluating the potential of using this type of novel EM-developed remediation technology in other mercury-contaminated stream systems at SRS, and possibly other DOE sites, to accelerate site closure. Knowledge acquired from this research can also support model development for other contaminated SRS stream systems such as Fourmile Branch where radiocaesium (^{137}Cs), iodine-129 (I-129) and other radionuclides are of primary concern. This research will assist in developing cost-effective remediation plans integrated into the SRS Area Completion Project (ACP) and accelerate progress of the DOE EM environmental restoration mission.

Subtask 3.1: Calibration of the Tims Branch Watershed Model and Scenario Analysis

Subask 3.1: Introduction

FIU has been conducting a study using the Tims Branch watershed as a stream-scale ecosystem testbed to identify and quantify the primary hydrologic processes that contribute to streamflow, especially due to storm events. To accomplish this goal, the study was designed with the three following objectives: 1) the development and calibration of a fully distributed hydrologic watershed model of the Tims Branch watershed to predict streamflow; 2) design of the target storm events that cover a range of temporal distributions and return periods; and 3) application of the calibrated hydrologic model to predict stormflow due to designed storm events and quantify the correspondent streamflow characteristics that are important to sediment remobilization.

During the 2019-2020 period of performance FIU developed a fully distributed hydrologic watershed model, the MIKE SHE 2-dimensional (2D) land surface/3D groundwater model that simulates surface/subsurface hydrologic processes (such as overland flow, evapotranspiration, and infiltration), which was coupled with a 1D streamflow model that accounts for stream water hydraulics (such as hydraulic structures, cross-sections, and network). The hydrologic model was then calibrated against streamflow records monitored at the outlet of the Tims Branch watershed. Storm event analysis was performed for the research area to generate rainfall time series that describe storm events covering a total of 160 combinations of temporal distributions and return periods, including five average recurrence intervals (ARIs) (5y, 10y, 25y, 100y and 500y), four rainfall durations (6h, 12h, 24h and 96h), four temporal quartiles of rainfall (1st, 2nd, 3rd and 4th), and two load types (backloaded and frontloaded). The generated time series of the design storm events were applied as the driver of the calibrated hydrologic model to simulate stormflow due to designed storm events. Bed sheer stress, one of the key indicators of sediment remobilization were quantified and visualized at Steed Pond in the Tims Branch where past studies have shown that contaminants accumulate in bed sediment.

FIU's focus then turned to the Tims Branch model optimization to improve and verify the performance of the coupled hydrology and sediment transport model. This included sensitivity analysis, calibration and validation of the model as well as scenario analysis under extreme hydrological conditions. The optimization/calibration of the sediment transport model was finalized using the Advection-Dispersion (AD) and ECO Lab modules available in the MIKE 11 modeling framework. The Cohesive Sediment Transport (CST) model was developed using the AD module of MIKE 11 to simulate the cohesive sediment transport process under different design storm events. The ECO Lab module was then added to the MIKE 11 modelling framework. The sediment transport process in ECO Lab was optimized/calibrated based on the available field measurements for suspended sediment concentration. The resuspension calibration parameters in ECO Lab were set based on the velocity profile obtained from the hydrodynamic module of the MIKE 11 modeling framework. The ECO Lab module was parameterized to simulate the contaminant transport process. The fully developed integrated surface water/groundwater MIKE SHE/MIKE 11 modeling framework with the newly added ECO Lab module was then implemented to simulate the resuspension, remobilization and transport of sediment particles under various extreme storm events.

This past year (2020-2021) FIU moved on to the final phase of model development, which involves development and calibration of the contaminant transport component of the Tims Branch model. The following provides more detail on the research accomplishments during FIU Performance Year 1.

Subtask 3.1: Objectives

The principal objective of this task is to develop and test a comprehensive transport model using available hydrological modeling software and geographical information systems (GIS) tools to examine the response of Tims Branch to historical discharges and environmental management remediation actions. FIU will use the calibrated model to study transport scenarios of heavy metal contaminants of concern under extreme hydrological conditions that provide information related to inter-compartmental transfers and the environmental conditions that result in mobilization of adsorbed heavy metals in sediment, and accumulation of priority contaminants of concern due to sedimentation.

Subtask 3.1: Methodology

Contaminant Transport Modeling and Calibration - Uranium

Environmental Fate of Uranium

Antropogenic activities associated with uranium mining, milling, nuclear weapons production activities, and waste disposal practices resulted in the contamination of soil and groundwater with uranium and other radionuclides. Nuclear weapons production activities at Savannah River Site, from 1955 through 1988, caused groundwater and sediment contamination at multiple locations as a result of the release of acidic waste into unlined seepage basins (Killian et al., 1987). Uranium (U) in the environment has a complex behavior and contains several oxidation states: U (III), U (IV), U (V), and U (VI). The most common and stable form found in the oxidized environment is

U(VI). Organic carbon linked to the biogeochemical reactions taking place due to degradation is one of the factors that affect uranium mobility in the aquatic ecosystem (P.Jaffe, 2017). In addition, factors such as pH and redox conditions also affect the mobility and speciation of uranium in groundwater and surface water. The characteristics of complexing agents and the sorbing material in the environmental system control the U mobilization. Other significant impacts on the biogeochemical dynamics of the sediment and uranium desorption are the reaction rates and sorption dynamics (P.Jaffe, 2017). Wetlands existing in the TB watershed have adapted to supply oxygen to the stems of trees and plants, and as such transfer oxygen into the sediment. Because of the iron cycling as a result of low redox potentials, iron and carbon chemistries are closely studied. This process is common in wetlands and affects U fate and transport.

Preliminary Data Analysis

Preliminary work on this project has involved the development of a fully integrated surface water/groundwater MIKE SHE/MIKE 11 hydrological model of the Tims Branch watershed. This hydrological modeling framework developed by (Yan Zhou et al., 2020) and (Alam et al., 2021) contains site characterization data for the Tims Branch watershed including land use, topography, climatic drivers (precipitation, potential evapotranspiration), soil profiles, roughness characteristics, geological layers, and hydrological features such as the river network and serves as the basis for development of the contaminant transport model. This report describes the parameterization and implementation of the MIKE ECO Lab module, as well as calibration of the fully coupled MIKE model, in order to perform simulations of the contaminant transport process under extreme storm scenarios.

Field Data Collection

Surveying done in 2016 provided records of baseflow discharge in more than 18 locations along the TB stream. The average baseflow velocity in Tims Branch, A-011, and A-014 streams was approximately 2.0 m^3/s, 7.0 m^3/s, and 17 m^3/s respectively. The flow velocity was higher at the culvert in A-014 and in fact, the highest flow velocity was registered at this location. The water level was too low in Steed Pond during this site visit for any flow measusrements to be registered.

It should be taken into consideration that data collection was limited by time and location. The intention here is to use the recorded measurements as preliminary input values required for the model development; however, further data collection may be required to validate this data. In general, uranium bound to sediments and suspended solids yield important implications for water quality and water resources (Kaplan & Serkiz, 2001; Sowder et al., 1996). In case contaminated groundwater or surface water is used for irrigation water supply, U can potentially end up in the food web. Therefore, there is a need to closely monitor U-contaminated basins.

Water Quality Measurements

The total and dissolved uranium concentrations were determined. First, the water samples collected were acidified with 0.8 % nitric acid and stored in a cooler to preserve and prevent degradation. We then filtered the surface water and background uncontaminated samples, and then processed the samples following U.S. Environmental Protection Agency (USEPA) Standard Operating Procedures (SOPs), and analyzed by ICP-MS using a Nex1ON 300x mass spectrometer.

For uranium in sediment, there were a few data values from Betancourt et al., 2011 for uranium content in “sediment” collected in the summer of 2011 during a field site investigation in Tims

Branch. The average concentration of uranium in Tims Branch surface waters was calculated from data collected during previous fieldwork conducted by FIU in 2016 and 2017 (Applied Research Center, 2016; ARC, 2017). For surface waters, the average uranium concentration was measured as 0.614 ± 0.291µg/L in the main Tims Branch channel (TM). In the A-011 tributary, the uranium in the water had an average concentration of $0.040 \pm 0.014\ \mu g/L$. For Steed Pond (SP), the average surface water uranium was $1.01 \mu g/L$ and no standard deviation. Lastly, an average uranium concentration of $0.028 \pm 0.068\ \mu g/L$ was found in the A-014 tributary surface water.

Table 17. Observed Aqueous Uranium Concentrations in Tims Branch Surface Water. ***(Samples were collected during baseline conditions in the summer of 2016 and 2017, Applied Research Center, 2016; ARC, 2017)***

Location	Date Collected	Aqueous Uranium Concentrations (µg/L)
TM 1	8/29/2016	1.16
TM 2	8/29/2016	0.42
TM 3	8/29/2016	0.50
TM 4	6/22/2017	0.668
TM 2	6/22/2017	0.648
TM 3	6/22/2017	0.223
TM 4	6/22/2017	0.680
A11 1	8/29/2016	<MDL
A11 2	8/29/2016	0.02
A11 3	8/29/2016	0.04
SP 1	8/29/2016	1.01
A14 1	8/29/2016	<MDL
A14 2	8/29/2016	0.13
A14 3	8/29/2016	<MDL
A14 1	8/29/2016	<MDL
A14 1	6/22/2017	-0.013
A14 2	6/22/2017	0.000
A14 3	6/22/2017	-0.006
TM 1 Average		**0.614**
St. Dev.		0.291
A 11 Average		**0.040**
St. Dev.		0.014
SP Average		**1.010**
St. Dev.		**-**
A 14 Average		**0.028**
St. Dev.		0.068

Data Implementation

The results derived from the processed surface water samples collected in Tims Branch during the 2016 and 2017 field surveys was used to develop and calibrate the transport of suspended sediments and dissolved heavy metals in the stream. The model also uses in-situ field measurements collected from 2016-2018, including streamflow, water temperature, dissolved oxygen (DO), hydraulic conductivity, total dissolved solids (TDS), salinity, and pH. Water samples for analysis of heavy metal concentrations were also taken. Field measurements were taken at more than 18 locations in theA-014 and A-011 outfall tributaries. FIU adhered to the proper onsite health and safety measures and standard EPA field measurement procedures to ensure data accuracy and to preserve sample integrity . In addition, all instruments were operated in accordance with Section 6.8 for the use of multiparameter instruments for which the individual field measurement sensors are bundled in a sonde and placed in the water body for in situ measurements (USGS, Francesca, 2016).

Contaminant Transport Modeling and Calibration – Tin and Nickel

In addition to modeling uranium transport in Tims Branch, FIU also began collecting relevant data for development of contaminant transport models of tin and nickel as part of the long term monitoring strategy of sediment bound contaminants that may have the potential for resuspension, remobilization and redistribution during extreme storm events. Implementation of a tin-based mercury remediation technology in the Tims Branch watershed has provided records of the quantity and timing of the tin released. This has subsequently presented a unique opportunity for the tin to serve as a potential tracer for modeling sedimentation and particle transport processes in the stream, making Tims Branch an ideal testbed for evaluating the effectiveness of wetland treatment and tin (II) - based mercury treatment at the SRS site. DOE EM has highlighted the need to track the tin and to understand the impact of frequent or extreme atmospheric events on its redistribution in Tims Branch. FIU intends to utilize the data available from the tin-based remediation technology to develop a hydrological and contaminant transport model that can in future be extended to investigate other heavy metal and radionuclide contaminants of concern (e.g., nickel). Knowledge acquired from this research will also assist in developing cost-effective remediation plans integrated into the SRS Area Completion Project (ACP) and accelerate progress of the DOE EM environmental restoration mission.

FIU's efforts this year were focused on in-depth literature review of relevant reports and published journal papers on water quality monitoring in Tims Branch to gain background information related to the historical release of contaminants, particularly tin and nickel, from the SRS A/M Area into Tims Branch. FIU also communicated with SRNL scientists who were able to provide additional data resources and field measurements of contaminant concentrations and water quality data. A thorough analysis of data from the Bechtel Environmental Integrated Data Management System (BEIDMS) acquired from SRNL was performed. The spreadsheet contained mercury (Hg), nickel (Ni), arsenic (As), and uranium (U) concentrations from analysis of samples collected in the Tims Branch with only 4, 6, 4, and 9 sample events respectively for each contaminant which were spread for the period from 2004 to 2006. These sample events, unfortunately, did not overlap with the interested hydrological simulation period of 4/1/2018-6/17/2018; however, the U concentrations from this source will be valuable for contaminant model validation in the future. Sediment and biofilm data from the technical report "Tin Distribution and Fate in Tims Branch at the Savannah River Site" by Betancourt and Looney, 2011, was therefore used. The data in this report will be used for validation of the numerical model. A spreadsheet of the data in this report was not available. Therefore, the data was extracted from the PDF report and entered into an Excel spreadsheet. The sample locations in the report were assigned by approximate distances in units of feet from landmark locations and not via geographical coordinates (i.e., longitude and latitude). Therefore, in order to map the monitoring sites, it was necessary to georeference these sites using ArcGIS digitization tools. The georeferenced maps will allow the FIU team to validate the contaminant concentrations in the model grid and do further calibration and interpretation of the simulation results.

The technical report (Betancourt and Looney, 2011) provides an approximate calculation of the total mass of tin that entered Tims Branch from the air stripper treatment system from Nov. 2007 to Aug. 2011. This approximate calculation was then compared with the estimated average tin concentration in sediments. Future work involves the possible application of this methodology as an assumption for the simulation period of interest (4/1/2018 to 6/17/2018) to obtain the estimated tin concentration that entered Tims Branch watershed. Further investigation however is necessary as there are still some uncertainties associated with this methodology. Application of this methodology for simulation of Ni and U transport is also being considered.

Fieldwork Support for Model Calibration

Troubleshooting HOBO RX 3000 – Unit 3

This year FIU also continued collecting in-situ field data to support the evaluation and optimization of the contaminant transport component. Two of the three devices deployed in Tims Branch began producing anomalous data, one of which was shipped back to FIU for troubleshooting in-house at ARC as travel restrictions had been imposed due to the coronavirus pandemic. The following section describes the steps taken to repair the "Unit 3" device.

First the device was disconnected from the power AC adaptor and a full power reset of the HOBO RX 3000 was executed. The logger was placed in a 'stop logging' state by pushing the center button below the LCD. This button has a dual purpose. When the device is logging data, the button will display STOP. When the HOBO RX 3000 logger is in a 'stop logging' state, the button will display START. The solar panel connection on the device was then removed followed by removal of the battery connection.

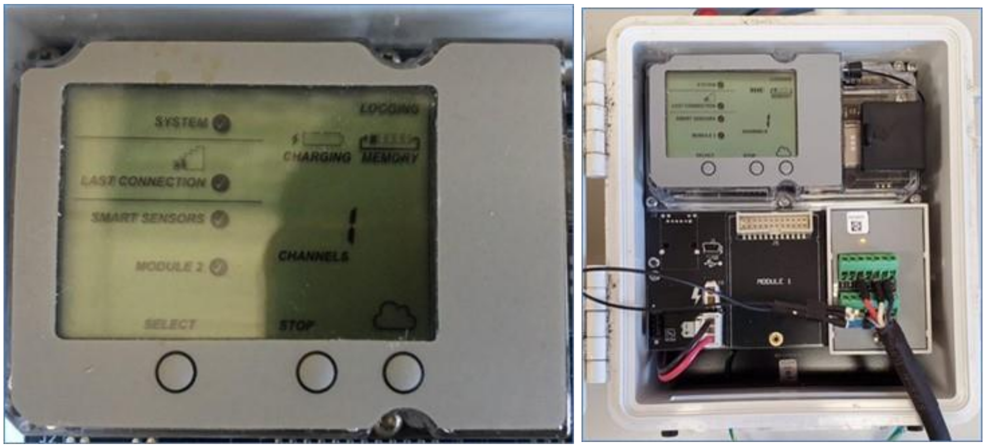

Figure 64. HOBO RX3000 housing (right) and LCD display showing the system initializing after being powered on (left). The system is currently charging, storing data, and connecting to the 3G cell signal.

While the device was powered down, the SIM card was pushed down to unlock it and then pushed back again to lock it in place. This was repeated multiple times to shave off any residues in the contacts.

After 3-4 minutes, the battery was plugged in followed by the solar panel. Power on the HOBO RX 3000 data logger was then initialized and checks were done to determine whether the device was in a normal state. A check mark next to the word 'System' on the LCD display appeared, indicating that the power cycling was effective.

Finally, the device acquired a cell connection noted by a check mark on the LCD next to "Last Connection". This process took several minutes and when completed, a cloud icon appeared in the lower right of the LCD. The 'START logging' button was then selected to begin normal logging. The cell signal was continuously monitored to see what level the logger was detecting.

*Pairing of Cyclops-7F Turbidity Meter using the Explorer indoor adapter and software***.**

In February 2021, FIU received a Cyclops-7F submersible turbidity sensor provided by an SRNL collaborator. This sensor is an accurate single-channel detector that can be used for many different applications, especially for turbidity measurements. It is designed for integration into multi-parameter systems from which it receives power and delivers a voltage output proportional to the concentration of fluorophore. The voltage output can be correlated to concentration values by calibrating with a standard of known concentration. A performance test of the sensor was conducted at FIU to ensure it functioned well with the HOBO RX3000 used for water level measurements in Tims Branch. The turbidity sensor was found to be easy to integrate with the HOBO unit. A simple preliminary test was conducted with the device using clear tap water which produced expected results. In addition, a solution was purchased with a specific dye standard with a fluorophore concentration of 100 NTU for calibration of the turbidity sensor at the time of its deployment in Tims Branch.

Figure 65. The Cyclops-7F submersible turbidity sensor being integrated into the HOBO RX3000 at FIU.

The next step was to test to ensure that measurements were being recorded in HOBOlink, which is the web-enabled software platform designed for HOBO RX3000 Remote Monitoring Systems that makes it easy to view and to manage the sensor data remotely, as the HOBO platform was being used solely for storage and retrieval of the water level data from the devices currently deployed in Tims Branch and also for configuring the devices. The Cyclops Turbidity Meter was integrated into the "Unit 3" HOBO device at FIU, and a very detailed report was developed to document details of the procedure employed

Figure 66. Turner Designs Cyclops 7-F Turbidity Sensor with Explorer adapter.

The instructions in the user manual provided with the sensor were followed accordingly. First, the software was downloaded using the USB flash drive enclosed with the device. Once downloaded, the Cyclops turbidity meter was plugged into the PC and COM7 Port was selected as input. The USB included the software platform used for visualization and manipulation of the data parameters. The Explorer platform contained a simple user interface which allowed for quick and continuous capture of data. Initial testing confirmed that the sensor was turned on and shortly after it began to record readings.

Figure 67 below describes the graphical user interface (GUI) (Turner Designs Explorer) where information from the Cyclops-7F submersible turbidity sensor such as date, time, gain and mV are displayed.

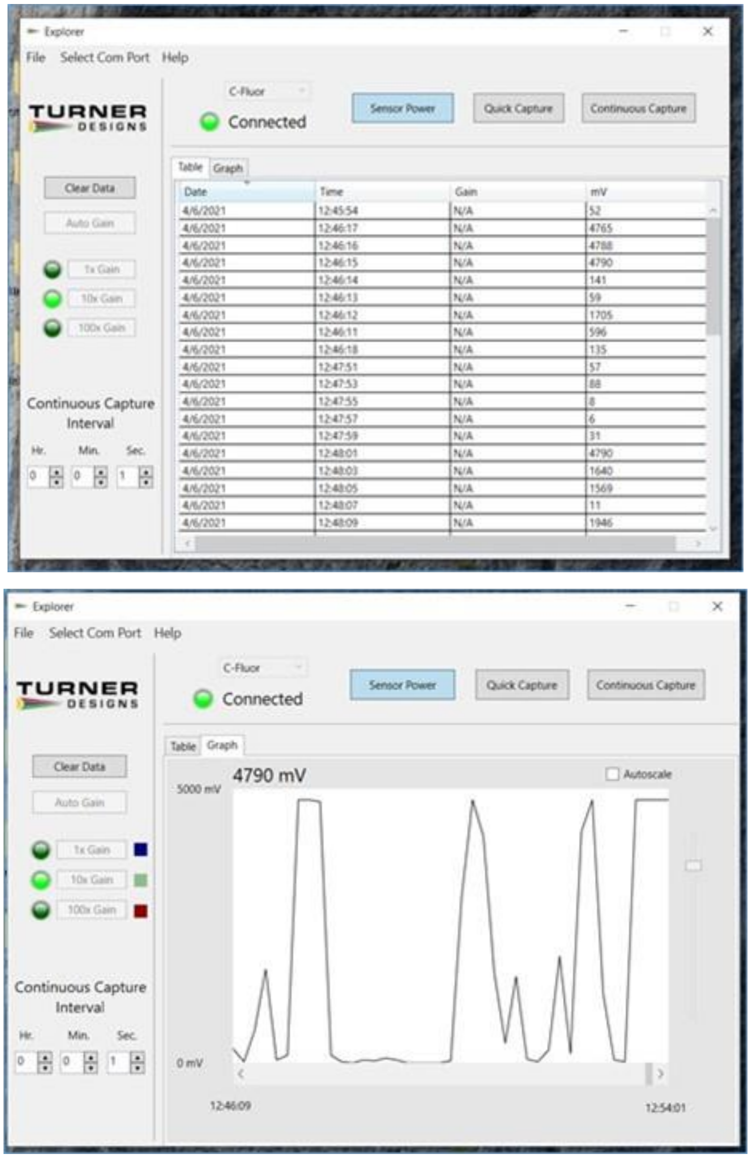

Hr. 0 Min. 0 Sec. 1

Date	Time	Gain	mV
4/6/2021	12:45:54	N/A	52
4/6/2021	12:46:17	N/A	4765
4/6/2021	12:46:16	N/A	4788
4/6/2021	12:46:15	N/A	4790
4/6/2021	12:46:14	N/A	141
4/6/2021	12:46:13	N/A	59
4/6/2021	12:46:12	N/A	1705
4/6/2021	12:46:11	N/A	596
4/6/2021	12:46:18	N/A	135
4/6/2021	12:47:51	N/A	57
4/6/2021	12:47:53	N/A	88
4/6/2021	12:47:55	N/A	8
4/6/2021	12:47:57	N/A	6
4/6/2021	12:47:59	N/A	31
4/6/2021	12:48:01	N/A	4790
4/6/2021	12:48:03	N/A	1640
4/6/2021	12:48:05	N/A	1569
4/6/2021	12:48:07	N/A	11
4/6/2021	12:48:09	N/A	1946

Figure 67. Testing of the Turner Designs Explorer software displaying both graphical and text data for the Cyclops turbidity meter.

The sensor can be used to collect data in any of the 3 different gain (range) settings. Each gain setting has its own range of concentrations. The 100x gain is the most sensitive and is used for very low concentration detection. The 10x gain is the most appropriate gain to use if you are unsure of what gain to use for your water samples. This gain has a good minimum detection limit and a good detectable range of concentrations. The 1x gain is the least sensitive gain and is reserved for utilizing the complete range of the instrument. Finally, the AUTO Gain can be selected to take advantage of the auto gain function which automatically selects the best gain to be used for the sample being read. It also provides details and graphical views of the data being collected. The data collected was stored as a .CSV file as well as the graphical visualization interface of the run time.

Integration of HOBO RX3000 with Stevens pressure transducer and Cyclops Turbidity meter

The global settings in the GUI were modified to affect all smart sensors [water level and turbidity] already logging interval data. The settings for the individual sensors were adjusted according to their user defined specs.

STEVENS pressure transducer – In this exercise, the HOBOlink interface was selected to integrate both the pressure transducer and the turbidity sensor. First, the pressure transducer was assigned to CHANNEL 1 of the HOBO device. In HOBOlink, the module configuration interval was preset to log every minute using 2 percent of the data plan. In the analog sensor login icon, CHANNEL 1 was enabled for the pressure transducer.

Initially, the current input maximum amperage was set to 20.0 mA. CHANNEL 1 was labelled [Pressure transducer] and the sensor type / input type was set to [RAW-C-20, Raw Current 0-20 mA]. Scaling was enabled and the current and scaled units were left as constants.

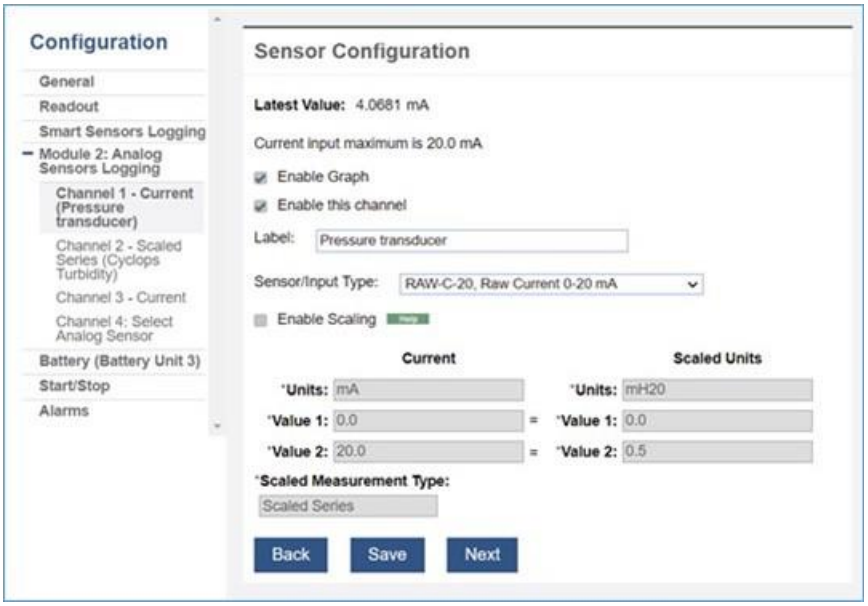

Sensor Configuration

Latest Value: 4.0681 mA

Current input maximum is 20.0 mA

☑ Enable Graph

☑ Enable this channel

Label: Pressure transducer

Sensor/Input Type: RAW-C-20, Raw Current 0-20 mA

☐ Enable Scaling

Current			Scaled Units	
*Units:	mA		*Units:	mH20
*Value 1:	0.0	=	*Value 1:	0.0
*Value 2:	20.0	=	*Value 2:	0.5

*Scaled Measurement Type: Scaled Series

Figure 68. Pressure transducer sensor configuration parameters.

Status: HOBOlink is currently experiencing delays in scheduled deliveries, exports and web service requests. We are working to bring systems back to normal operation.

Figure 69. CHANNEL 1 - Unit 3 pressure transducer mA readings integrated using the HOBOlink portal.

Cyclops Turbidity Meter – The goal here was to integrate the turbidity sensor using the HOBO RX3000. First, CHANNEL 2 was selected and the port was named [Cyclops Turbidity]. The voltage input maximum value was set to 5.0 Volts. The graph and channel were then enabled by checking the box on the analog sensors icon. The sensor/input type was set to [RAW- V-5, RAW Voltage 0-5 Vdc]. Finally, 'enable scaling' was selected.

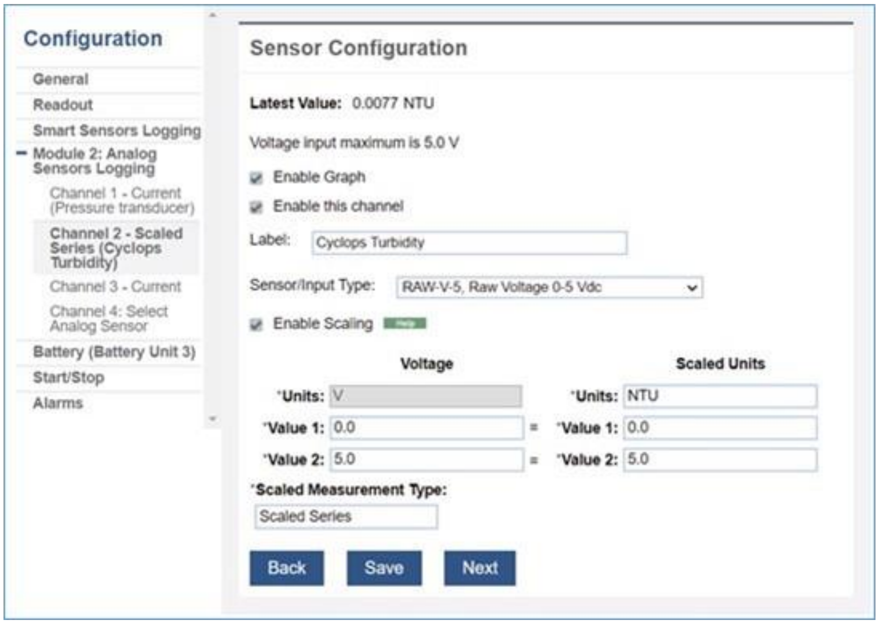

Sensor Configuration

Latest Value: 0.0077 NTU

Voltage input maximum is 5.0 V

☑ Enable Graph

☑ Enable this channel

Label: Cyclops Turbidity

Sensor/Input Type: RAW-V-5, Raw Voltage 0-5 Vdc

☑ Enable Scaling

	Voltage			Scaled Units
*Units:	V		*Units:	NTU
*Value 1:	0.0	=	*Value 1:	0.0
*Value 2:	5.0	=	*Value 2:	5.0

*Scaled Measurement Type: Scaled Series

Figure 70. Cyclops Turbidity sensor configuration.

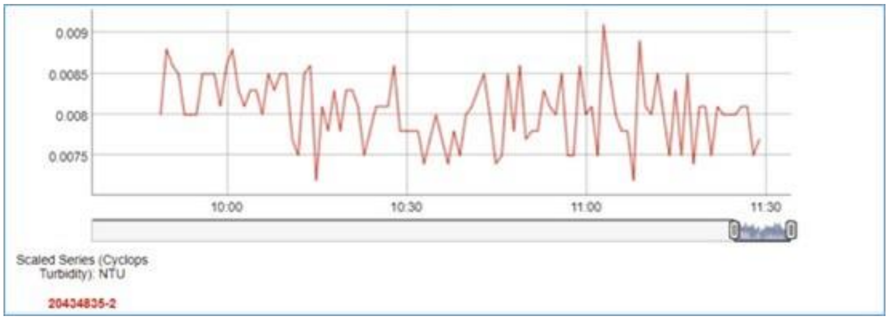

Figure 71. CHANNEL 2 - Unit 3 turbidity sensor voltage reading integrated using the HOBOlink portal.

Figure 72. Successful integration of the HOBO RX3000 with the STEVENS pressure transducer and Cyclops turbidity sensor using the HOBOlink portal.

In conclusion, all sensors were successfully integrated to work with the HOBO RX3000. Although all sensors detect a signal, they will need to be calibrated before deployment.

Preparation of the Cabling

Once readings were obtained in the HOBOlink portal, the pigtail cable was prepared with appropriate connectors for easy installation. Using connectors and heat shielding, the cable was designed for easy plug--and-play and to adapt the 10x to 100x gain port setting.

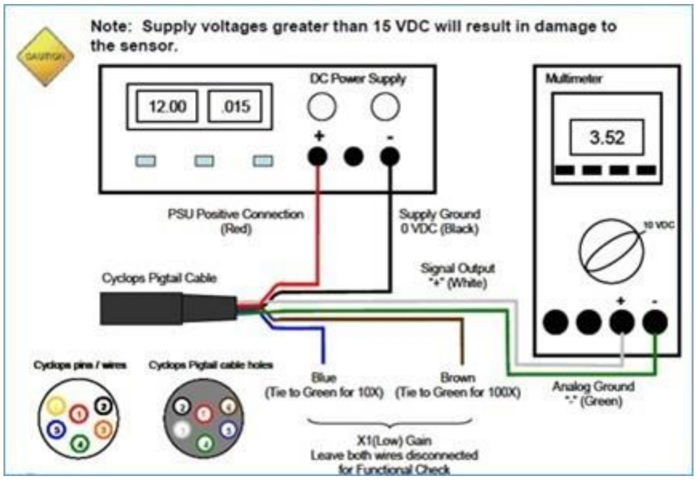

Figure 73. Schematic identifying the relationship of cable colors with intended use. Red= Positive connection, Black=ground, White=signal output, Green=analog ground, Brown=100x Gain, Blue=10x Gain.

Using this schematic, a connector was designed for fitting the male and female pigtail cabling for (10x – Green and blue) or (100x Green and brown) as displayed below.

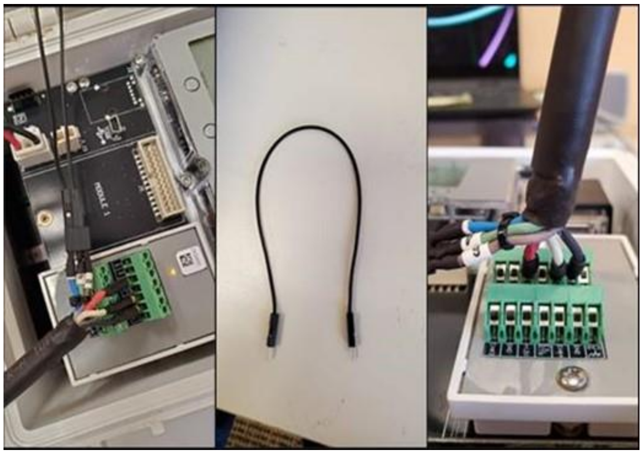

Figure 74. Cable designed for easy plug-and-play to be ready for deployment.

SRS Site Visit

FIU was able to complete fieldwork in the Tims Branch watershed at the Savannah River Site in July 2021. Assistance was provided by SRNL and SREL personnel to attain security clearance and schedule RADCON support during his visit. Routine maintenance and calibration of model inputs such as water level were conducted on the existing HOBO remote monitoring devices. The cross-sectional profile and stream height were measured for the calibration of the pressure transducer. In addition, an infrared turbidity sensor and a new battery were integrated into the HOBO system.

These changes took place at the furthest downstream location in the Tims Branch stream, near its confluence with the Upper Three Runs stream.

The fieldwork included providing technical assistance to SRNL scientist, Dr. Dan Kaplan, to install, operate and calibrate new parts for the ISCO autosampler located on the east side of Road C, just downstream of Steed Pond. The installation and calibration of this device will provide time-series data to help calibrate and further validate the hydrological model developed by FIU, continuously improving its performance over time.

Figure 75. Dr. Daniel Kaplan and DOE Fellow Juan Morales at the confluence of Tims Branch and Upper Three Runs operating the water level monitoring device (HOBO RX3000).

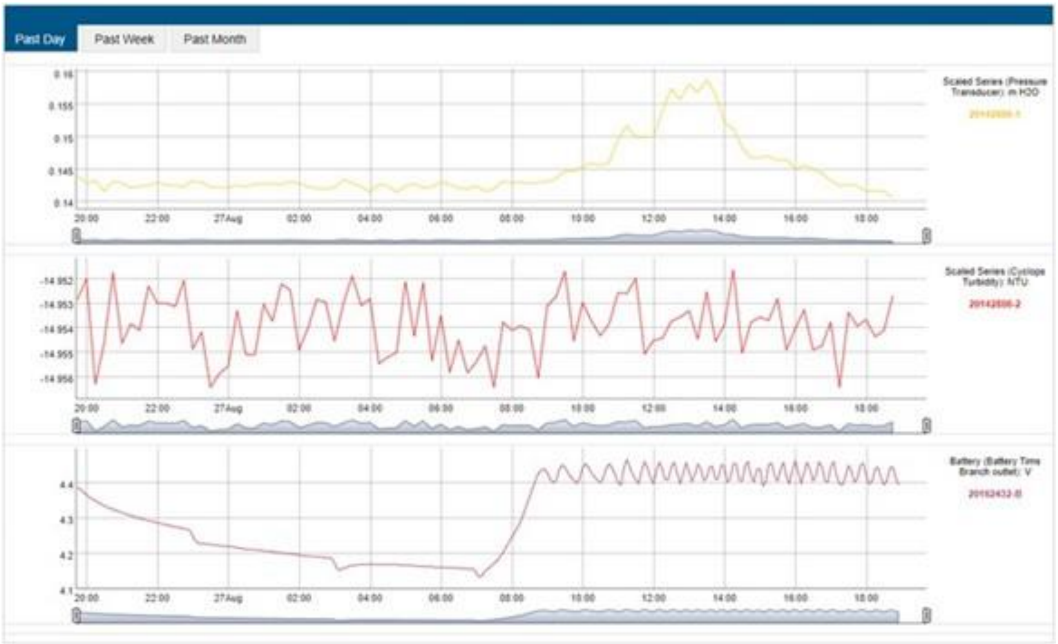

Figure 76. HOBOlink web-based graphical interface for viewing data being recorded by the turbidity sensor and pressure transducer. Both sensors were installed and calibrated in the remote monitoring device situated at the outlet of the Tims Branch stream.

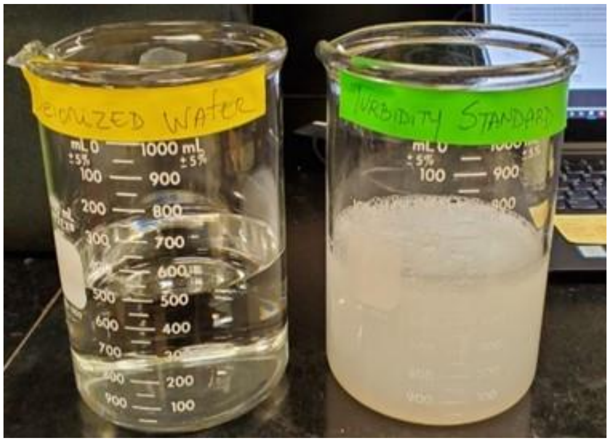

Figure 77. Calibration of Cyclops turbidity sensor using integrated EXPLORER software. The calibration was done using deionized water and a calibration standard of 1000 NTUs.

Figure 78. ISCO autosampler located in Tims Branch near Road C.

Subtask 3.1: Results and Discussion

Contaminant Transport Modeling and Calibration - Uranium

Desorption rate of uranium, K_W

The desorption rate of uranium in water (K_W) is one of the most important parameters in the model domain, which is described as dissolved and adsorbed uranium in the water along with the level of suspended solids in the stream. Several exercises were carried out varying the parameter between (0.0003/d to 30/d) . Here, we used a sensitivity analysis which allowed us to identify how influential (K_W) is and its effect on the uranium flux .

Our results show the uranium flux changing as a result of U desorption rate (1/day). Results ranged from (2.04 to 2,378 mg/s) in uranium flux in the stream. These were simulated by modifying (K_W) parameter. In conclusion, a value of $K_W =$ 0.0003 (1/day) was chosen as the best value as simulations were well correlated with the observed uranium flux values (9 mg/s) from Batson et al., 1996. As K_W decreased, the uranium flux (mg/s) remained low. Meanwhile, as K_W increased the uranium flux increased, reaching its peak of K_W = 0.03 (1/day).

Table 18. Sensitivity analysis of (Kw) as a function of uranium flux at the outlet of Tims Branch watershed. Default, Koc = 500,000 L/kg ; flow velocity = 0.397 cm/s.

Model identifier	Desorption rate (1/day)	Flux of dissolved U (mg/s)
Sim 0001	0.0003	2.04
Sim 0002	0.003	27.95
Sim 0003	0.02	881.84
Sim 0004	0.03	2,378.70
Sim 0005	0.2	209.47
Sim 0006	0.35	1,267.07
Sim 0007	3	50.24
Sim 0008	30	132.27

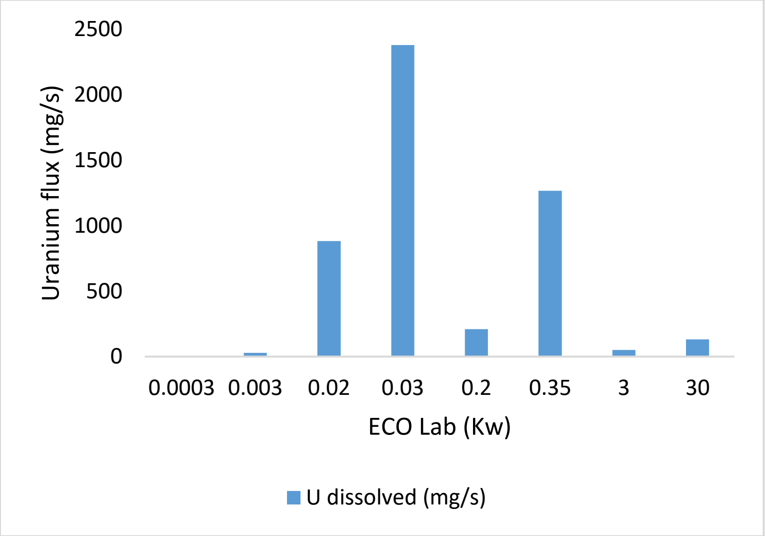

Figure 79. Sensitivity analysis using desorption rate as a function of uranium flux (mg/s).

Organic Carbon Partitioning Coefficient, K_{OC}

Organic carbon partitioning coefficient (K_{OC}) is defined as the concentration of uranium in the organic carbon component of the soil over the concentration of the uranium in the water. The K_{OC}, is suggested to affect the movement of contaminants (Sowder et al., 2003). In the model, the default K_{OC} described in ECO Lab is equal to 50,000 L/kg; a calculated K_d 2,100-6,900 L/Kg was reported in Tims Branch by Kaplan et al. (2017). Background concentrations of uranium K_d values were estimated at ~700 L/kg, at a pH of 5.5 (Kaplan et al., 2017). Also, sequential extraction results showed that uranium has a high affinity to sediments with extremely low natural organic matter concentrations. Therefore, the higher the organic carbon content, the more uranium may be adsorbed to the soil and the less the uranium will be available in the water column.

The coefficient K_d for organic compounds can be computed as the foc multiplied by the uranium – specific soil organic carbon water partition coefficient K_{OC}. Therefore, for uranium species the following formula can be used:

$$\boldsymbol{K_{d\cdot} = f_{oc} * K_{oc}} \qquad \text{Eq. 1.}$$

Given that soil can be a complex mixture of various minerals and organic matter, the fraction of organic carbon foc was examined using the EPA's Soil Screening Guidance technical report. It is known that foc is the fraction of organic matter in sediment and K_{OC} is the organic carbon partition coefficient. The fraction of organic carbon foc is important because sediment with a high foc will likely have greater potential for adsorption of contaminants, effectively limiting their mobility in the aqueous phase. EPA reports suggest that using 0.2% (0.002 g/g) as a default concentration of organic carbon for subsurface soils is a good baseline. Any concentration > 0.02% will need an explanation of the source of organic carbon being reported.

Table 19 describes the K_{oc} parameter calibration process, which resulted in an estimated 170 model runs evaluating the uranium flux at the outlet of the Tims Branch stream.

Table 19. Calibration of uranium transport model describing the parameters and methods used to obtain the best values compared against the observed data

SERIES NUMBER	REFERENCE	CALIBRATION PARAMETER
Series 1	Peer-reviewed literature [a]	K_{oc}
Series 2	Environmental report/site data [b]	K_{oc}
Series 3	Calibrated hydrodynamic model [c]	K_{oc}

a. (Denham, 1999; Serkiz et al., 2007).

b. (Betancourt et al., 2011) *and data from Bechtel Environmental Integrated Data Management System (BEIDMS©).*

c. DHI-MIKE 11 calibrated hydrodynamic model reference values (Yan Zhou et al., 2020).

Here using literature, filed derived data and hydrological modeling standards, a sensitivity analysis for K_{OC} was conducted. In conclusion, series 3 - K_{OC} values were modified from 884,960 to 1,100,000 L/Kg. Steps decided regarding the calibration of K_{OC} are illustrated below.

First series model exercises:

In the first series exercises, data from the *"Environmental availability of uranium in an acidic plume at the Savannah River Site"* was used to calculate the organic carbon partitioning coefficient (K_{OC}) parameter. In essence, the field derived K_d data from (Serkiz et al., 2007) was used to calculate the K_{Oc} parameter in ECOLab using equation 1. The recommended values of fraction of organic carbon *(foc)* were provided by (Denham, 1999) at 0.01 (unitless) and were used accordingly. Our calculated K_{OC} = 134,667 L/kg and was tested in ECO Lab. Results later confirmed, this was not in agreement with the observational values; As a result, FIU decided to use (Yan Zhou et al., 2020), initial contaminant transport model already calibrated as baseline for this exercise. A range between (1,000,000 to 1,500,000 L/kg) were simulated and results can be seen in Table 20. In conclusion, our computed model results did not fall in the best agreement with the observed values. When increasing (K_{OC}) in value, no major effect was detected in the computed U flux because it was not able to meet the observed values.

Second series model exercises:

After consultation with SRNL, it was decided that parameters such as the fraction of organic carbon (*foc*) were perceived low due to higher organic content in wetland sediment compared to typical subsurface soil. We corrected the *foc* and repeated our scenarios using the model's initial value condition to prevent the model from becoming unstable. Our calculated K_{OC} = 140,380 L/kg and was tested in ECO Lab. Table 6 illustrates the second series model exercises using the corrected *foc* and highlights the model results. After running the model, it was decided to suspend further simulations due to the significant increase in U flux in the results computed.

Third series model exercises:
In this series of exercises, the U model was dissected and brought back to default. We used similar methods as previously shown in series 1 and 2; However, this time the only parameter that we modified was K_{OC}. Here, MIKE ECO Lab enabled the estimation of the particulate and dissolved uranium in the sediments and water column. The K_{oc} values were tested from a range of 1,100,000 to 500,000 L/kg. Optimal ranges of simulated uranium flux (9.996 mg/s) were achieved by modifying the K_{oc} parameter. Following the sensitivity analysis, the value of 884,960 L/kg was selected as the best value for K_{oc} as simulation results agreed with the observed aqueous uranium values. This value of K_{oc} is still under investigation and calibration to check if the simulated peak U concentration and discharge would fall in the same time domain as expected. In general, as K_{oc} decreased the uranium in the water increased.

In general, ECO Lab contains four main subdomains that can represent uranium concentration in different model production runs. These are dissolved in the water (S_{HM}), absorbed in the water (X_{HM}) (particulate), adsorbed in the sediment (XHMS), and dissolved in the sediment pore water (SHMS).Table 22 describes the series 3 exercises in which outputs provided concerning the transport domain. In regards to the model results, the uranium flux was calculated using the maximum of April 2018 multiplied by the corresponding discharge of the day ((Max concentration in April) * (Corresponding discharge in April). This methodology falls in congruence with (Batson et al., 1996) storm measurements.

During calibration of K_{oc}, monitoring data collected by Batson et al., 1996 has been our fundamental source of observational data for baseline discharge, and a discharge that mirrors a recorded long-duration short intensity rain event. Numerically, MIKE 11 coupled with ECO Lab resulted in several output files. FIU simulated and documented several exercises used to calibrate K_{oc} , illustrated in Table 20, Table 21 and Table 22.

Table 20. Series #1 Calibration Exercises

	SERIES NUMBER	POROSITY OF SEDIMENT	DESORPTION RATE IN SEDIMENT	DESORPTION RATE IN WATER	FRACTION OF ORGANIC CARBON (SEDIMENT)	ORGANIC - CARBON PARTITIONING COEFFICIENT	URANIUM FLUX (MG/S)
ECO Lab uranium constants							
Default/ Calibrated		*Bea et al., 2013*	*Default*	*Default*	*Looney et al., 1987*	*Serkiz et al., 2007*	
Calculated/ Constant		*(pors) Constant*	*(Ks)* Constant	*(Kw)* Constant	*(foc) Calculated*	*(Koc) Calculated*	
Unit		m^3 H_20 / m^3 Bulk	Per day	Per day	dimensionless	l/kg	mg/s
Value	**Number**	**0.39**	**0.12**	**0.1**	**0.01**		
5/25/2021	00	-	-	-	-	134,667	90,210,704
5/25/2021	01	-	-	-	-	1,000,000	4.25
5/25/2021	02	-	-	-	-	1,500,000	0.008
5/25/2021	03	-	-	-	-	1,250,000	0.008
5/25/2021	04	-	-	-	-	1,125,000	1.403
5/25/2021	05	-	-	-	-	1,187,500	1.029
5/25/2021	06	-	-	-	-	1,218,750	0.946
5/25/2021	07	-	-	-	-	1,234,375	0.822
5/25/2021	08	-	-	-	-	1,248,429	0.763
5/25/2021	09	-	-	-	-	1,250,000	0.763
5/25/2021	10	-	-	-	-	1,000,000	0.763
5/25/2021	11	-	-	-	-	1,249,900	4.25

Table 21. Series #2 Calibration Exercises

	SERIES NUMBER	POROSITY OF SEDIMENT	DESORPTION RATE IN SEDIMENT	DESORPTION RATE IN WATER	FRACTION OF ORGANIC CARBON (WATER)	ORGANIC - CARBON PARTITIONING COEFFICIENT	URANIUM FLUX (MG/S)
ECO Lab uranium constants							
Default/ calibrated		*Default*	*Default*	*Default*	*BEIDMS (Dan Kaplan)*	*ARC, 2011*	
Par.		*(pors)*	*(Ks)*	*(Kw)*	*(foc)*	*(Koc)*	
Unit		m^3 H_20 / m^3 Bulk	Per day	Per day	dimensionless	l/kg	mg/s
Value	**Number**	**0.8**	**0.12**	**0.1**	**0.0424**		
7/29/2021	020	-	-	-	-	140,380	303,794,770,935, 808

1. *foc in water* =0.0424
2. *Kd*= U in soil / U in (Aq.) source- Calculated *Koc*= 140,380
3. When using Koc calculated values, meaningless U fluc results were computed. Simulation series #2 were suspended and moved onto series #3.

Table 22. Series #3 Calibration Exercises

	SERIES NUMBER	POROSITY OF SEDIMENT	DESORPTION RATE IN SEDIMENT	DESORPTION RATE IN WATER	FRACTION OF ORGANIC CARBON (SEDIMENT)	ORGANIC - CARBON PARTITIONING COEFFICIENT	URANIUM FLUX
				ECO Lab uranium constants			
Default/ calculated		*Default*	*Default*	*Default*	*Default*	*Calibrated*	
Par.		*(pors)*	*(Ks)*	*(Kw)*	*(foc)*	*(K_{OC})*	
Unit		m^3 H$_2$0 / m^3 Bulk	Per day	Per day	dimensionless	l/kg	(mg/s)
Value	**Number**	**0.8**	**0.12**	**0.1**	**0.7**	**884,765**	**9.996**
7/29/2021	031	-	-	-	-	1,000,000	15.444
7/29/2021	032	-	-	-	-	1,100,000	1.765
7/30/2021	033	-	-	-	-	1,050,000	1.815
7/30/2021	034	-	-	-	-	900,000	1.930
8/4/2021	035	-	-	-	-	500,000	459.036
8/4/2021	036	-	-	-	-	700,000	33.054
8/6/2021	037	-	-	-	-	800,000	15.372
8/9/2021	038	-	-	-	-	850,000	11.928
8/10/2021	039	-	-	-	-	875,000	11.13
8/12/2021	040	-	-	-	-	887,500	1.94
8/13/2021	041	-	-	-	-	881,250	11.088
8/13/2021	042	-	-	-	-	884,375	9.996
8/17/2021	043	-	-	-	-	885,938	1.94
8/20/2021	044	-	-	-	-	885,156	1.94
8/24/2021	045	-	-	-	-	885,156	1.94
8/24/2021	046					884,765	9.996
8/24/2021	047					884,960	9.996

1. Calibration was reached when computed U flux was compared against observed data (9 mg/s).
2. Highlighted row represents the calibrated value obtained during the sensitivity analysis.

Table 23. Summary of model (Series 3) results involving the phase shift change and U flux as a function of organic-carbon partitioning coefficient (K_{oc}).

K_OC (L/KG)	U FLUX (MG/S)
500,000	459.04
700,000	33.05
800,000	15.37
850,000	11.93
875,000	11.13
881,250	11.09
884,375	9.10
884,765	9.10
884,960	9.10
885,156	1.94
885,156	1.94
885,938	1.94
887,500	1.94
900,000	1.93
1,000,000	15.44
1,050,000	1.82
1,100,000	1.77

The selection criteria to visualize the model results were based on the manuscript titled, *"Transport of Anthropogenic Uranium from Sediments to Surface Waters During Episodic Storm Events*". The results were integrated into a DOE-FIU Research Review 2021 presentation which took place on September 14-15, 2021. Finally, due to the availability of data, results from the Series 3 exercises were selected. The (Batson et al., 1996a) approach was used to report the U flux (mg/s) as a reporting parameter. It was noted that as K_{oc} decreases in value, a higher U flux is observed, as seen in Table 22. FIU concluded that numerical calibration was achieved and a simulated value for K_{oc} = 884,765 L/Kg agreed with the observed values from (Batson et al., 1996b), although further calibration might be needed to match the peak of discharge to the peak of U concentration as expected.

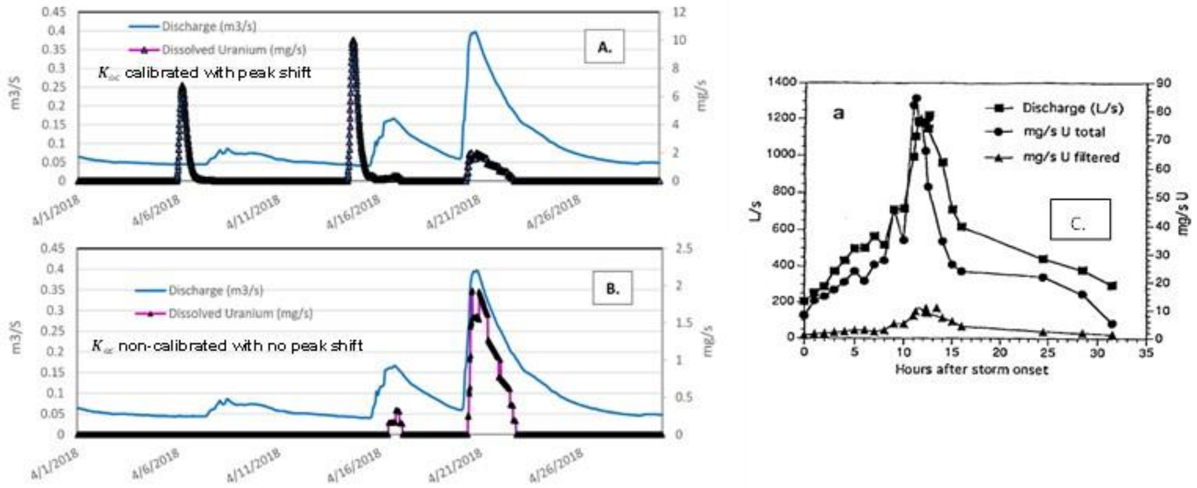

Figure 80. Simulation results highlighting the uranium flux (mg/s) and discharge (m^3/s) after a designed storm event generated in MIKE ECO Lab. Top graph A: Results have shifted in time and simulated a flux in U of 9.996 mg/s. Bottom graph B: Produced results such as 1.94 mg/s of U flux, however, it falls in agreement with the peak discharge during the time of the storm event. Right graph C: Observed data: Reference (Batson et al., 1996).

Graphs generated are a result from Table 23, highlighted shift vs no shift scenarios. FIU is currently investigating the phase shift and other calibration parameters.

Scenario Analysis and Model Results

After achieving satisfactory performance of the model through calibration of the MIKE HD, AD, and ECO Lab modules, FIU initiated the uranium transport scenario testing. The design events inserted in this exercise followed the calibration period of 02/20/2018 - 04/30/2018 and successfully generated 1-D hydrodynamic, and ECO Lab files highlighting six design storm events (5-yr, 10-yr, 25-yr, 50-yr, 100-yr, and 500-yr). The model was then reassessed and slightly modified to reduce the long run times, particularly when trying to execute the design event on 04/20/2018. This was due to the complexity of the uranium template which made initiating and loading of the warm-up period very slow. To address this issue, a shorter period (04/01/2018 to 04/30/2018) was simulated and a copy of the model was made. This reduced the simulation time from 1:50 minutes to 35 minutes. Additionally, all design events were compiled, and the scenarios were processed using parallel computing to accelerate the simulation times.

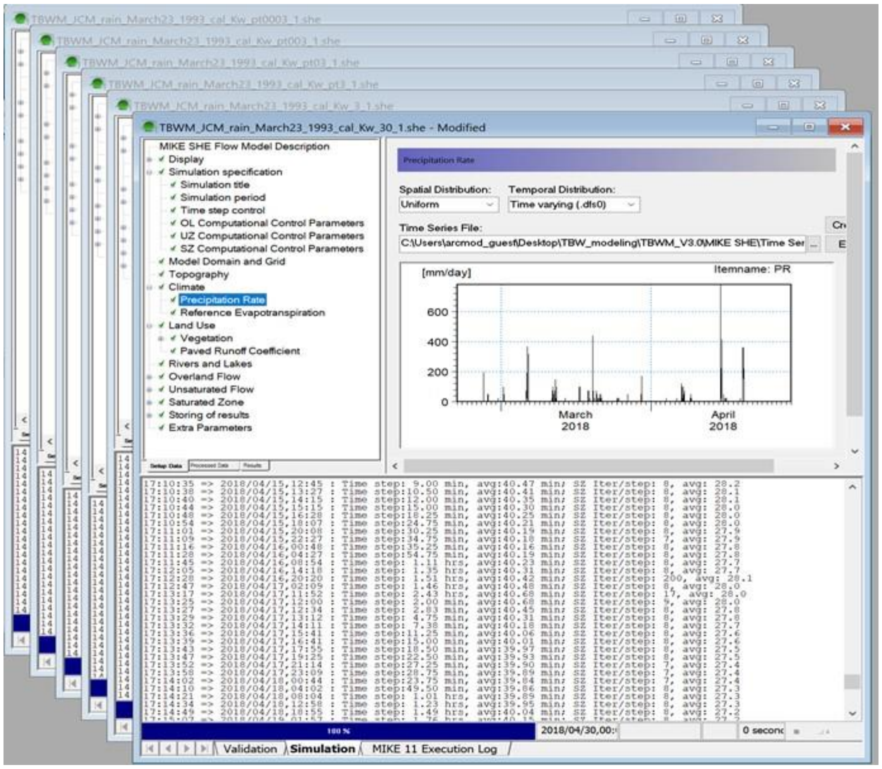

Spatial Distribution: Uniform
Temporal Distribution: Time varying (.dfs0)
Time Series File: C:\Users\arcmod_guest\Desktop\TBW_modeling\TBWM_V3.0\MIKE SHE\Time Ser

```
17:10:35 => 2018/04/15,12:45 : Time step: 9.00 min, avg:40.47 min; SZ Iter/step: 8, avg: 28.2
17:10:38 => 2018/04/15,13:27 : Time step:10.50 min, avg:40.41 min; SZ Iter/step: 8, avg: 28.1
17:10:40 => 2018/04/15,14:15 : Time step:12.00 min, avg:40.35 min; SZ Iter/step: 8, avg: 28.1
17:10:44 => 2018/04/15,15:15 : Time step:15.00 min, avg:40.30 min; SZ Iter/step: 8, avg: 28.0
17:10:48 => 2018/04/15,16:28 : Time step:18.25 min, avg:40.25 min; SZ Iter/step: 8, avg: 28.0
17:10:54 => 2018/04/15,18:07 : Time step:24.75 min, avg:40.21 min; SZ Iter/step: 8, avg: 28.0
17:11:01 => 2018/04/15,20:08 : Time step:30.25 min, avg:40.19 min; SZ Iter/step: 8, avg: 27.9
17:11:09 => 2018/04/15,22:27 : Time step:34.75 min, avg:40.18 min; SZ Iter/step: 7, avg: 27.9
17:11:16 => 2018/04/16,00:48 : Time step:35.25 min, avg:40.16 min; SZ Iter/step: 8, avg: 27.8
17:11:28 => 2018/04/16,04:27 : Time step:54.75 min, avg:40.19 min; SZ Iter/step: 8, avg: 27.8
17:11:45 => 2018/04/16,08:54 : Time step: 1.11 hrs, avg:40.23 min; SZ Iter/step: 8, avg: 27.7
17:12:05 => 2018/04/16,14:18 : Time step: 1.35 hrs, avg:40.31 min; SZ Iter/step: 8, avg: 27.7
17:12:28 => 2018/04/16,20:20 : Time step: 1.51 hrs, avg:40.42 min; SZ Iter/step: 200, avg: 28.1
17:12:47 => 2018/04/17,02:09 : Time step: 1.46 hrs, avg:40.48 min; SZ Iter/step: 8, avg: 28.0
17:13:17 => 2018/04/17,11:52 : Time step: 2.43 hrs, avg:40.68 min; SZ Iter/step: 17, avg: 28.0
17:13:25 => 2018/04/17,12:00 : Time step: 2.00 min, avg:40.68 min; SZ Iter/step: 9, avg: 28.0
17:13:27 => 2018/04/17,12:34 : Time step: 2.83 min, avg:40.45 min; SZ Iter/step: 8, avg: 27.8
17:13:29 => 2018/04/17,13:12 : Time step: 4.75 min, avg:40.31 min; SZ Iter/step: 8, avg: 27.8
17:13:32 => 2018/04/17,14:11 : Time step: 7.38 min, avg:40.18 min; SZ Iter/step: 8, avg: 27.7
17:13:36 => 2018/04/17,15:41 : Time step:11.25 min, avg:40.06 min; SZ Iter/step: 8, avg: 27.6
17:13:39 => 2018/04/17,16:41 : Time step:15.00 min, avg:40.01 min; SZ Iter/step: 8, avg: 27.6
17:13:43 => 2018/04/17,17:55 : Time step:18.50 min, avg:39.97 min; SZ Iter/step: 8, avg: 27.5
17:13:47 => 2018/04/17,19:25 : Time step:22.50 min, avg:39.93 min; SZ Iter/step: 8, avg: 27.5
17:13:52 => 2018/04/17,21:14 : Time step:27.25 min, avg:39.90 min; SZ Iter/step: 7, avg: 27.4
17:13:58 => 2018/04/17,23:09 : Time step:28.75 min, avg:39.89 min; SZ Iter/step: 7, avg: 27.4
17:14:02 => 2018/04/18,00:44 : Time step:23.75 min, avg:39.84 min; SZ Iter/step: 7, avg: 27.4
17:14:10 => 2018/04/18,04:02 : Time step:49.50 min, avg:39.86 min; SZ Iter/step: 8, avg: 27.3
17:14:21 => 2018/04/18,08:04 : Time step: 1.01 hrs, avg:39.89 min; SZ Iter/step: 8, avg: 27.3
17:14:34 => 2018/04/18,12:58 : Time step: 1.23 hrs, avg:39.95 min; SZ Iter/step: 8, avg: 27.3
17:14:49 => 2018/04/18,18:55 : Time step: 1.49 hrs, avg:40.04 min; SZ Iter/step: 8, avg: 27.2
```

Figure 81. Parallel computing was used to accelerate processing times for the design storm analysis for 1-yr, 5-yr, 10-yr, 25-yr, 100-yr, and 500-yr ARIs at 12hr - 4th quartiles with 10 percent probabilities.

In the discharge events each precipitation design from 5- to 500-year ARI was inserted within the calibration period following 04/20/2018 using the already calibrated hydrodynamic model as the warm-up period. As a result, ECO Lab simulated five stream hydrodynamic (HD) files from which data was extracted, classified, and visualized to spatially report the change in discharge for each design storm event. Out of the four rainfall durations and four quartiles, 1 to 500_year_12h_4_Q1 was used for the initial test, visualizing each design storm by a group of curves highlighting five ARIs by one load type and percentages (Figure 82). Generally, a higher ARI will result in a proportional upshifting of the curve compared to a lower ARI. Therefore, the curve of different ARIs in different load types of the same curve naturally does not fall on top of each other, with 5-year ARIs located at the bottom and 500-year ARIs at the top.

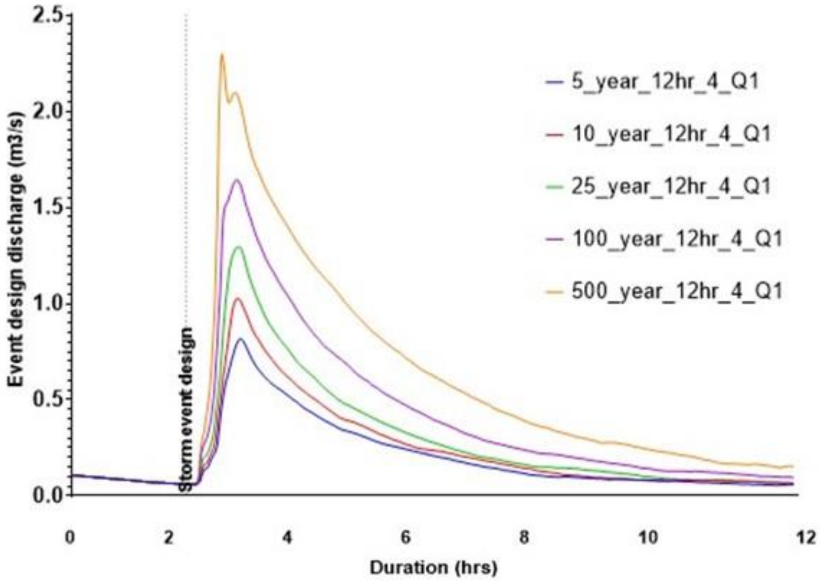

Figure 82. Event-based scenario testing hydrodynamic output files spatially and temporally representing the increased discharge after the storm event on 04/20/2018.

Uranium transport is governed by input values such as K_{oc} and desorption rates in sediment and water which are of extreme importance. This is due to the complexity of interactions in the solid and aqueous phases that make these data requirements important to reduce uncertainty.

Table 24. Results of the event-based scenario analysis highlighting transported state variables at the outlet of Tims Branch watershed and Steed Pond.

Event	Cross-sect.	Peak disch. (m3/s)	Disslv. U (mg/L)	Ads. U (mg/L)	Ads. U in sediment (g/m^2)	Susp. Solids (mg/L)	Mass of Sed. (g/m^2)
5 yr.	A	0.808	0.007	1.366	9.274	140.88	944.872
10 yr.	A	1.026	0.006	1.264	9.358	130.643	953.503
25 yr.	A	1.295	0.009	1.476	8.966	150.22	913.563
100 yr.	A	1.643	0.01	1.5	8.565	151.998	872.609
500 yr.	A	1.792	0.011	1.557	8.32	157.044	847.576
5 yr.	B	0.679	0.001	0.261	10.132	29.317	1040.005
10 yr.	B	0.828	0.001	0.563	10.134	59.422	1040.24
25 yr.	B	1.031	0.002	0.617	10.142	64.614	1041.029
100 yr.	B	1.256	0.003	0.694	10.147	72.105	1041.451
500 yr.	B	1.542	0.005	0.947	10.152	97.297	1041.899

A. Tims Branch watershed outlet B. Steed Pond outlet/ near road C
Flux of U is calculated by (Maximum discharge of event X corresponding dissolved U conc.)
The baseflow calculations were based on an average discharge of 0.127 m3/s with an average U flux of 0.54 mg/s (Hayes 1986).

In the scenario test, ECO Lab simulated five storm scenarios and U fluxes at the outlet of Tims Branch watershed. Each event simulated all five state variable outputs such as dissolved uranium (S_U), adsorbed uranium (X_U), suspended solids (X_{SS}), uranium adsorbed ($X_{U\ solid}$), and the mass of sediment (X_{SED}). As illustrated in Figure 83, all results were tabulated related to the 5-yr, 10-yr, 25-yr, 100-yr, and 500-yr ARIs at 12hr - 4th quartiles with 10 percent probabilities at the Tims Branch watershed outlet.

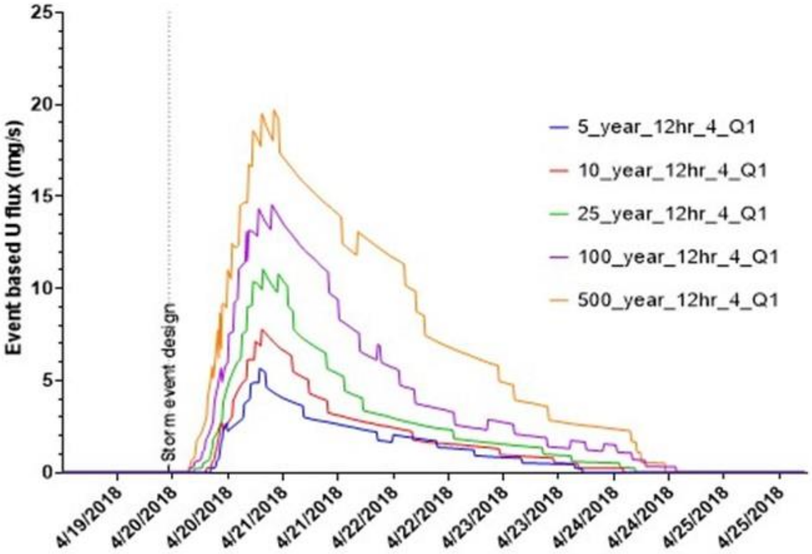

Figure 83. Event-based scenario test highlighting the U flux as a result of increased precipitation and discharge in the Tims Branch outlet. Koc=885,156 L/Kg.

Contaminant Transport Modeling and Calibration – Tin and Nickel

The contaminant monitoring sites described in the report by Betancourt and Looney (2011) were georeferenced via ArcGIS tools in ArcMap. Knowledge of the geographical location of these sites would enable calibration and validation of the contaminant transport model based on different scenarios. Table 25 provides a description of these sites.

Table 25. Contaminant Monitoring Sites Described in Report by Betancourt and Looney (2011)

Number	Site Name	Longitude	Latitude
1	Site 2	-81.734	33.333
2	Site 3	-81.732	33.333
3	Site 5	-81.731	33.333
4	Tims Branch Pond (TBP) 1	-81.718	33.334
5	Tims Branch Pond (TBP) 2	-81.718	33.326

Number	Site Name	Longitude	Latitude
6	Tims Branch Pond (TBP) 3	-81.711	33.309
7	Tims Branch Pond (TBP) 4	-81.708	33.298
8	Tims Branch Pond (TBP) 5	-81.702	33.294
9	Tims Branch Pond (TBP) 7	-81.731	33.333
10	Tims Branch Pond (TBP) 8	-81.728	33.332
11	Tims Branch Pond (TBP) 9	-81.722	33.332
12	Tims Branch Pond (TBP) 10	-81.723	33.332
13	Tims Branch Pond (TBP) 12	-81.719	33.331
14	Tims Branch Pond (TBP) 13	-81.714	33.316
15	Site 8 (Fine)	-81.728	33.332
16	Site 8 (Sandy)	-81.728	33.332
17	Site 10	-81.723	33.332
18	Site 9 (Middle)	-81.722	33.332
19	Site 9 (Edge)	-81.722	33.332
20	Site 12 (Fine)	-81.719	33.331
21	Site 12 (sandy)	-81.719	33.331
22	Site 20 BP2D	-81.716	33.32
23	Site 20 BP2C	-81.714	33.319
24	Site 20 BP2B	-81.714	33.318
25	Site 20 BP2A	-81.715	33.317
26	Site 13	-81.712	33.314
27	Site 15	-81.712	33.309
28	Site 16	-81.712	33.306
29	Site 17	-81.708	33.298

Number	Site Name	Longitude	Latitude
30	Site 19	-81.702	33.294
31	Site 18	-81.701	33.293
32	Site 14	-81.697	33.287
33	Site 1, biofilm	-81.734	33.333
34	Site 2, biofilm	-81.734	33.333
35	Site 3, biofilm	-81.732	33.333
36	Site 5, biofilm	-81.731	33.333
37	Site 9, biofilm	-81.722	33.332
38	Site 13, biofilm	-81.712	33.314

The monitored contaminant data in this report for tin, uranium, and nickel were specifically of interest in this study. Betancourt and Looney (2011) reported contaminant measurements at different sediment depths. Historical discharge and deposition of these contaminants at different times has likely resulted in their occurrence at varied sediment and soil depths. The modeling group, however, will investigate the data associated in different sediment/soil readings in the model set up. One can refer to the original report by Betancourt and Looney (2011) to study the data. Figure 84 represents the approximate locations of the Betancourt and Looney (2011) monitoring sites in Tims Branch.

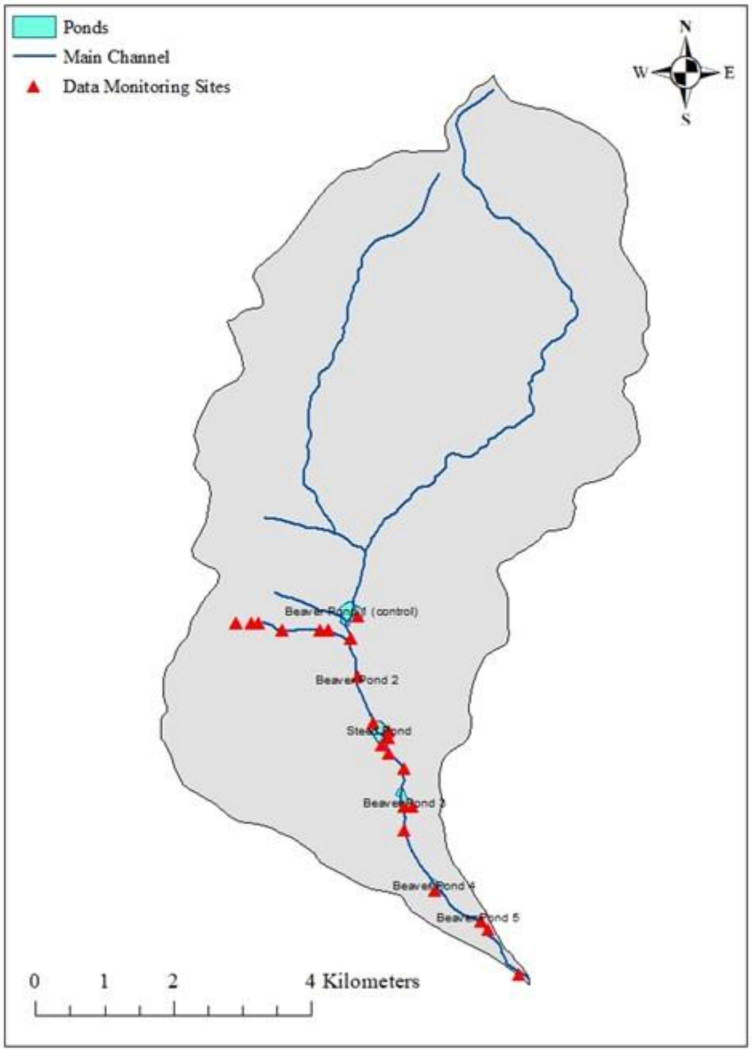

Figure 84. Contaminant monitoring sites and their approximate locations geo-referenced from report by Betancourt and Looney (2011).

To assign the boundary and initial conditions for the contaminant model, concentrations of the contaminants at the boundaries would be needed as well. The technical report by Betancourt and Looney (2011) provides theoretic mass balance calculations for tin in Tims Branch from November 2007 to August 2011. FIU applied the same methodology and made assumptions to derive an estimate of tin for the simulation period (4/1/2018 - 6/17/2018). Below, these assumptions and calculations are discussed:

i. Calculation of approximate total mass of the tin that has entered Tims Branch from M-1 Air Stripper treatment system 4/1/2018 to 6/17/2018.

   Assumptions:

   a) Q (flowrate of treated GW entering Tims Branch from the M-1 Air stripper treatment system through the A-014 outfall) = 450 gpm
   b) [Sn] (Theoretical tin concentration in treated GW from the M-1 Air stripper treatment system) = 12.88 $\mu g/L$ water

Q × [Sn] × total time (total mass of tin that has entered Tims Branch from the M-1 Airstripper system) = 2,454,545.5 L/day

Total time (April, May, and 17 days of June 2018) = 78 days

Calculations (Q × [Sn] × total time) = 2.47 Kg Sn

ii. Estimation of theoretical average approximate concentration of tin in sediments along Tims Branch, from A-014 outfall to confluence of Tims Branch with Upper Three Runs Creek.

Assumptions:

a) Assume tin is present in significant concentration only in upper 3.5 in of sediments along Tims Branch.
b) Average is calculated by assuming that sediments are evenly distributed along Tims Branch, which they are not. This assumption is necessary to calculate a theoretical average since sediments along Tims Branch have a patching distribution.
c) L (estimate of length of Tims Branch from A-014 outfall downstream to confluence of Tims Branch with Upper Three Runs Creek) = 26,000 ft
d) W (estimate of the average width of Tims Branch from A-014 outfall downstream to confluence of Tims Branch with Upper Three Runs Creek) = 6 ft
e) D (estimate of sediment depth where significant concentrations of tin are detected from the surface of the sediment bed to this depth) = 3.5 inch
f) S (estimate of density of sediments) = 1.7 $g/cm3$= 48,139 $g/ft3$
g) Total tin that has entered Tims Branch from 4/1/2018 until 6/17/2018 = 1.13 µg Sn/g sediment.

The aforementioned assumptions and calculations were discussed with SRNL research scientists. Updated information regarding the assumptions made for these calculations were also requested.

The following is an account of the work completed in September with respect to the calculations of tin in Tims Branch.

1. Calculations of the total tin input to Tims Branch

To calculate the total tin released to Tims Branch (TB) from the M-1 air stripper system, FIU acquired information from Savannah River National Lab (SRNL) which included a report with measurements of tin concentration at the inlet and outlet of the M-1 Air Stripper (2007) (SRNLSTI-2010-00393). The concentration of total tin was measured at the inlet and outlet of the M-1 air stripper during start-up and initial operations, and at the A014 Outfall, which is located 5 ft downstream of the stripper discharge. FIU created

Table 26 below based on the concentrations of total tin in the effluent from the M-1 air stripper with the initial and continuous operation of the stannous chloride treatment system (Tables 3 and 4, SRNL-STI-2010-00393 report). In the data provided, there was no monitoring data recorded for the last days of 2007, 2008, and 2009. Therefore, hypothetical days were inserted for each of the dates 12/31/2007, 12/31/2008 and 12/30/2009, with the previously monitored data in order to finalize the concentration for each of these years. These assumptions would help to assign a total accumulated tin in the TB sediment for each of these years with minimal error.

Table 26. Data summary for tin in the M-1 air stripper system outlet that entered Tims Branch from 2007 to the end of 2009. Data in the rows with bolded fonts were assumed by FIU's modeling team to be the final day of the years 2007, 2008, and 2009, with repetitive information from their previous monitoring data to help assign an accumulated tin value for each year in TB. In this study Outlet refers to the M-1 air stripper system effluent. The Outfall is located 5 feet downstream of the discharge of the stripper (Table 1 of the report by Betancourt and Looney 2011).

Date	# of days from previous reading	Q (gpm)	Q(lpd)	Tin concentration ($\mu g/L$)	Accumulated Tin from discharge (kg)
7/10/2007	Start of testing	----	----	----	----
11/5/2007	Start of facility	----	----	----	----
11/8/2007	3	525	2,863,636	1.89	0.016
11/15/2007	7	525	2,863,636	1.58	0.032
11/20/2007	5	526	2,869,091	1.82	0.026
11/29/2007	9	526	2,869,091	1.82	0.047
12/11/2007	12	459	2,503,636	1.56	0.047
12/13/2007	2	382	2,083,636	1.09	0.005
12/18/2007	5	466	2,541,818	4.31	0.055
12/20/2007	2	465	2,536,364	1.48	0.008
12/27/2007	7	469	2,558,182	4.6	0.082
12/31/2007	**4**	**469**	**2,558,182**	**4.6**	**0.047**
1/3/2008	7	454	2,476,364	3.52	0.061
1/10/2008	7	441	2,405,455	5	0.084
1/17/2008	7	461	2,514,545	10	0.176
1/24/2008	7	463	2,525,455	4.47	0.079
1/31/2008	7	380	2,072,727	1.64	0.024
2/7/2008	7	453	2,470,909	11.3	0.195
2/14/2008	7	494	2,694,545	2.11	0.040
2/21/2008	7	505	2,754,545	3.64	0.070
2/28/2008	7	431	2,350,909	6.01	0.099
10/6/2008	221	450	2,454,545	6.69	3.629
12/1/2008	56	450	2,454,545	8.84	1.215
12/31/2008	**30**	**450**	**2,454,545**	**8.84**	**0.651**
2/2/2009	63	450	2,454,545	8.84	1.367
5/11/2009	98	450	2,454,545	14.1	3.392
7/8/2009	58	450	2,454,545	20.1	2.862
8/3/2009	26	450	2,454,545	20.1	1.283
9/8/2009	36	450	2,454,545	13.5	1.193
11/30/2009	83	450	2,454,545	16.7	3.402
12/30/2009	**30**	**450**	**2,454,545**	**16.7**	**1.230**

By having the tin concentration at the outlet, the approximate total mass of tin that entered TB from the M-1 air stripper system was calculated for each timeframe with the same methodology followed by Betancourt and Looney (2011). The accumulated tin from discharge for each row was obtained as follows:

Accumulated tin = Q (GW discharge) × tin concentration at the outlet × time period involved

With this approach, the total tin that entered TB in 2007, 2008, and 2009 were obtained. Approximate inputs of tin to TB from 2010 until September 2021 resulting from the mercury treatment were also provided by SRNL. This was based on SRNL mixing the treatment reagents for use by their operating division (Area Completion Projects). Table 27 provides the accumulation of tin that entered TB in 2007, 2008, and 2009 calculated based on Table 26 and the additional data provided by SRNL.

Table 27. Deposited and Accumulated Tin in Tims Branch (for 2021, data is until September 2021)

No.	Time	Deposited tin for each year (kg)	Accumulated tin since the installation of the Air Stripper system (kg)
1	2007	0.36	0.36
2	2008	6.32	6.69
3	2009	14.73	21.42
4	2010	41.00	62.42
5	2011	51.00	113.42
6	2012	34.00	147.42
7	2013	35.00	182.42
8	2014	38.00	220.42
9	2015	43.00	263.42
10	2016	24.00	287.42
11	2017	24.00	311.42
12	2018	23.00	334.42
13	2019	21.00	355.42
14	2020	23.00	378.42
15	2021	23.00	401.42

To better observe the variations of the released tin in the TB, the deposited tin was plotted for these years. It seems that the deposited tin stabilizes between 20.0 to 25.0 kg from 2016 onwards with an approximate value of 23.0 kg.

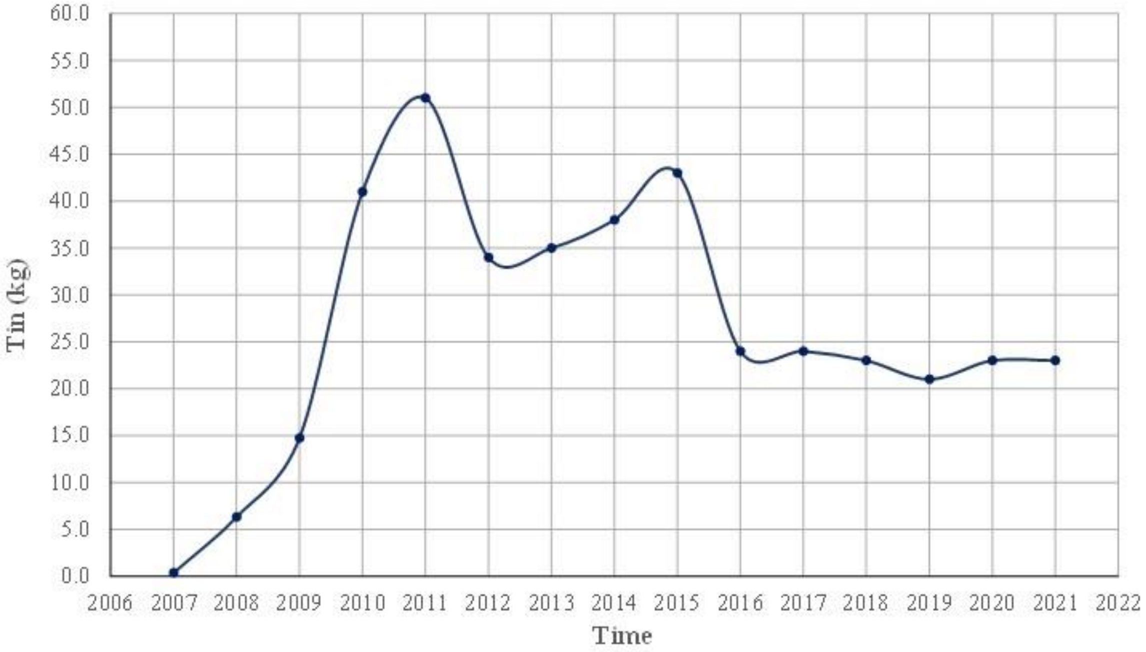

Figure 85. Estimated tin deposition in Tims Branch from 2007 to 2021.

2. Average tin concentration in sediments

In order to assign the average tin concentration along TB from A-014 outfall to the confluence of TB with Upper Three Runs Creek, the same approach, methodology, and assumptions that were made in the report by Betancourt and Looney, 2011 were used. These assumptions are:

i. L: estimate of length of TB from A-014 outfall downstream to confluence of TB with Upper Three Runs Creek = 26,000 ft
ii. W: estimate of the average width of TB from A-014 outfall downstream to confluence of TB with Upper Three Runs Creek = 6 ft
iii. d: estimate of sediment depth where significant concentrations of tin are detected from the surface of the sediment bed to this depth = 3.5 in
iv. S: estimate of density of sediments = 1.7 g/cm^3
v. All tin entering TB is accumulated in the TB sediment

Then the average tin concentration in sediment equals =

$$\frac{Total\ tin\ that\ entered\ TB\ for\ each\ year}{L\ \times W\ \times d\ \times S}$$

Table 28 provides the summary for these years.

Table 28. Average concentration of tin in sediments along Tims Branch from A-014 outfall to the confluence of Tims Branch with Upper Three Runs Creek for each individual year based on the deposited tin from Table 2-18 and the methodology provided by Betancourt and Looney (2011)

No.	Time	μg Sn / g sediment
1	2007	0.17
2	2008	2.89
3	2009	6.72
4	2010	18.72
5	2011	23.28
6	2012	15.52
7	2013	15.98
8	2014	17.35
9	2015	19.63
10	2016	10.96
11	2017	10.96
12	2018	10.50
13	2019	9.59
14	2020	10.50
15	2021	10.50

3. *Uncertainty associated with instrumentation/technique to apply observed data from Betancourt and Looney (2011) for model validation*

In the ECO Lab module, the part of the sediment layer which would be included in the modeling is the top 10 centimeters (4 in) of the soil/sediment, with the assumption that sediment/soil is homogenous. The observed data in the report by Betancourt and Looney (2011) was monitored at different soil depths, usually in 0.5, 1.0, or 1.5 inch increments. For some layers, the monitored reading was below the lower limit of either the instrument or the technique that was applied. Therefore, a threshold was used in those readings, for instance $< 12\ \mu g/g$. FIU's modeling team will communicate with SRNL to determine a scientific approach on how to handle data below the LOD for calibration and validation of the model. In the most conservative approach, all non-detects for Sn, U and Ni can be assigned the value of the LOD. EPA also recommends to report values <LOD as half the LOD. This approach assumes that all values between the LOD and zero could be present, and that the average value could be as high as half the detection limit (Helsel, 1990, EPA,1991).

To make a consistant judgement for U, Sn, and Ni, FIU decided to get the average concentration of these contaminants in the top 1.5 inches of soil/sediment from the report by Betancourt and Looney (2011). These concentrations were then mapped based on their geographical location to show their spatial distribution in Tims Branch. The spatial distribution of concentration maps provide the modeling team some insight of the contaminant deposition as well as areas where detailed modeling efforts are needed, for example Steed pond.

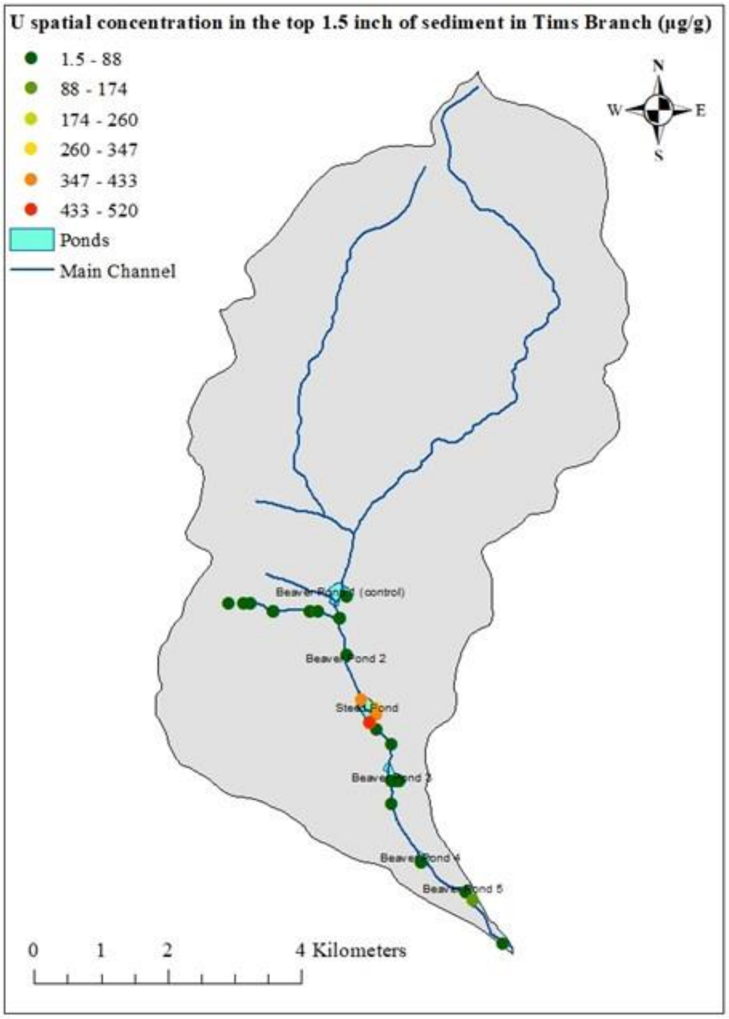

Figure 24. Spatial concentrations of uranium in Tims Branch in August 2011 based on the average concentrations in the top 1.5 inch of soil/sediment based on the data provided in the report by Betancourt and Looney (2011) .

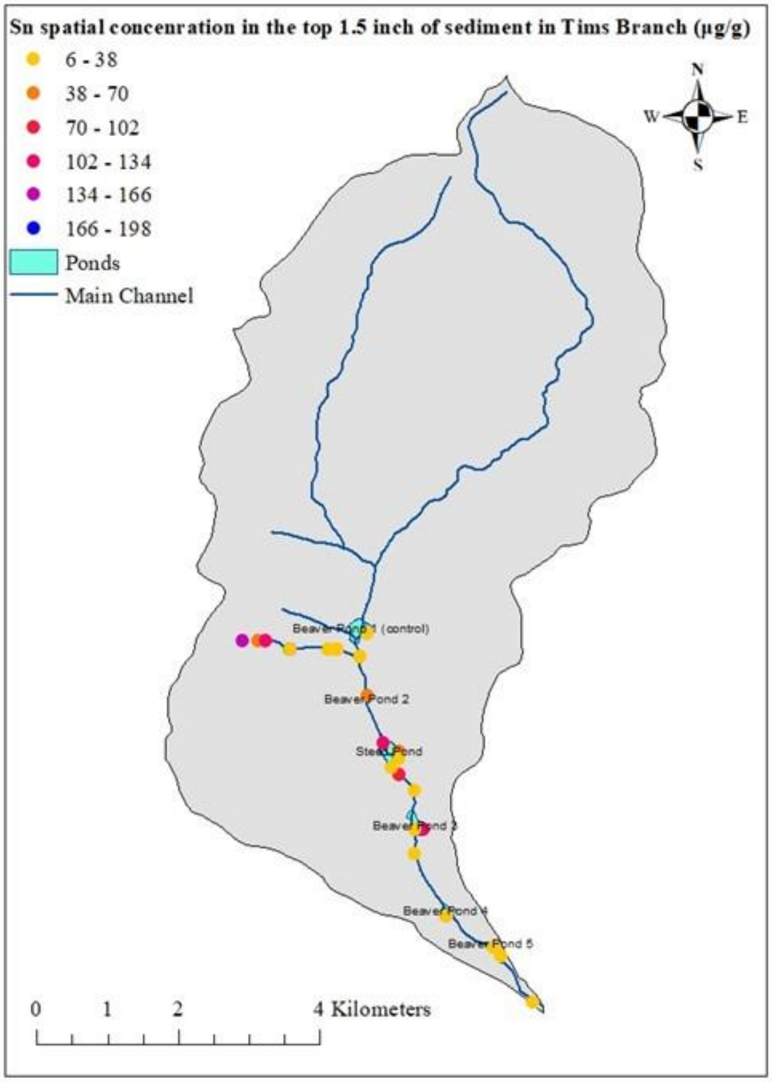

Figure 25. Spatial concentrations of tin in Tims Branch in August 2011 based on the average concentrations in the top 1.5 inches of soil/sedimentbased on the data provided in the report by Betancourt and Looney (2011).

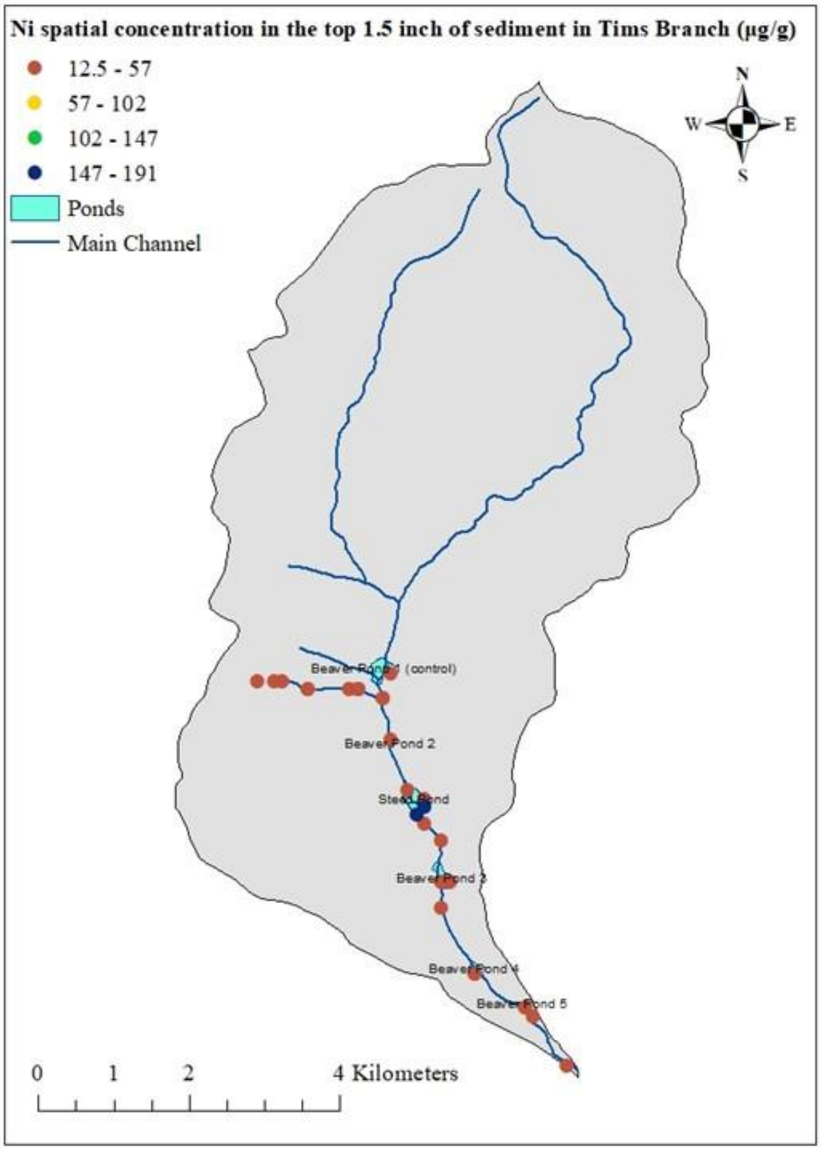

Figure 26. Spatial concentrations of nickel in Tims Branch in August 2011 based on the average concentrations in the top 1.5 inches of soil/sediment based on the data provided in the report by Betancourt and Looney (2011).

Subtask 3.1: Conclusions

Contaminant Transport Modeling and Calibration - Uranium

FIU completed the sensitivity analysis for calibration of the Tims Branch (TB) MIKE 11 ECO Lab module for the uranium (U) transport process (Milestone 2020-P2-M8), which determines the controlling variables and optimum values for parameters affecting U geochemical processes in the Tims Branch stream system. The organic carbon partition coefficient (Koc) and the fraction of organic carbon (foc) were identified as controlling variables and were thus the primary focus of the model calibration process. Simulated series tests highlight Koc to be a driver of U flux at the

TB outlet. Optimum values in Koc were determined and U flux falls in agreement with the observed data reported in published literature.

Additionally, FIU's scenario testing using Koc = 885,156 and 884,960 L/Kg, highlights our exploratory approach to describe the phase-shift error in the model results. Every effort to simulate different storm events details a novel approach to forecast uranium transport associated with contaminated sediments. The greatest amount of U was transported during the 500-year ARI peak discharge rate. Considerably, more U was transported to the TB outlet (3550 % increase for the storm simulated), (1327 % increase in Steed Pond) when compared to base flow U measurements. We identified that U transport is governed by K_{OC} for which field and literature sources were used in this exercise. The research presented the need to perform sensitivity analysis and calibrate other parameters, such as desorption rate in water (K_W) to improve the phase shift associated with the changes in K_{OC}. FIU will continue to assess the sediment and uranium transport model, explicitly addressing uncertain model inputs to ultimately estimate accurate U fluxes as a result of increased precipitation and streamflow.

Contaminant Transport Modeling and Calibration – Tin and Nickel

FIU has conducted an in-depth review of available contaminant data for tin and nickel as a continuation of the contaminant transport modeling effort in Tims Branch. FIU's aim is to utilize the existing model infrastructure developed for the uranium transport to develop contaminant transport models for other heavy metal contaminants of concern. Over the past year, the focus has been on the acquisition of data related to tin and nickel concentration and determination of significant parameters that influence their mobility in the environment under extreme meteorological conditions. Implementation of a tin-based mercury remediation technology and the subsequent release of a tin (II) oxide by-product from 2007 afterwards (Table 27, Figure 85) has provided available data to set up the boundary and initial conditions for modeling the transport of tin in Tims Branch. Subsequent field studies by Betancourt and Looney (2011) have also provided data to validate the modeling effort for uranium, tin and nickel. The data acquired and calculation methodology performed by Betancourt and Looney (2011) was used to perform theoretic mass balance calculations and decide on average concentrations of tin in Tims Branch sediment from November 2007 to September 2021 (Table 28). In the next year, FIU will continue modeling the contaminant transport process in Tims Branch by setting up the model to simulate the fate and transport of tin and nickel and possibly other heavy metals of concern using available and obtained data.

Subtask 3.1: References

Baes, C. F., & Sharp, R. D. (1983). A Proposal for Estimation of Soil Leaching and Leaching Constants for Use in Assessment Models. Journal of Environmental Quality, 12(1), 17–28. https://doi.org/10.2134/jeq1983.00472425001200010003x

Batson, V.L., P.M. Bertsch, and B.E. Herbert. 1996. Transport of anthropogenic uranium from sediments to surface waters during episodic storm events. J. Environ. Qual. 25:1129–1137.

Bea, S. A., Wainwright, H., Spycher, N., Faybishenko, B., Hubbard, S. S., & Denham, M. E. (2013). Identifying key controls on the behavior of an acidic-U(VI) plume in the Savannah River Site using reactive transport modeling. Journal of Contaminant Hydrology, 151, 34–54. https://doi.org/10.1016/j.jconhyd.2013.04.005

Betancourt, A., Looney, B. B. (2011) “Tin Distribution and Fate in Tims Branch at the Savannah River Site”. U.S. Department of Energy Office of Environmental Management under Grant No. DE-EM0000598.

Campbell, J. (2011). Porosity. Complete Casting Handbook, V(xiii), 391–464. https://doi.org/10.1016/b978-1-85617-809-9.10007-6

Denham, M. E. (1999). SRS Geology/Hydrogeology Environmental Information Document. https://doi.org/10.2172/10526

DHI Water & Environment. (n.d.). Heavy Metal MIKE ECO Lab Template Scientific Description. Retrieved January 24, 2019, from www.mikepoweredbydhi.com

EPA, U., of Radiation, O., & Air, I. (1999). UNDERSTANDING VARIATION IN PARTITION COEFFICIENT, K d , VALUES Volume I: The K d Model, Methods of Measurement, and Application of Chemical Reaction Codes. https://www.epa.gov/sites/production/files/2015-05/documents/402-r-99-004a.pdf

Fetter, C.W. 1988. Runoff and streamflow. P. 37-61. In Applied hydrology. 2nd ed. Merrill Publ., Columbus, OH.

Freer J, Beven K, and Ambroise B, 1996. Bayesian estimation of uncertainty in runoff prediction and the value of data: an application of the GLUE approach. Water Resources Research, 32 (7), 2161–2173. doi:10.1029/95WR03723

Hall J, et al., 2005. Distributed sensitivity analysis of flood inundation model calibration. Journal of Hydraulic Engineering, 131 (2), 117–126. doi:10.1061/(ASCE)0733-9429(2005)131:2(117)

Hayes, D.W., and C.D. Ouzts. 1986. Sediment transport studies in Tims Branch. Rep. DPST-86-468. E.I. du Pont de Nemours & Co, Savannah River Laboratory, Aiken, SC.

Helsel, D.R. Less than obvious; statistical treatment of data below the detection limit. Environ. Sci. Technol 24(12);1767-1774.

Hornberger G and Spear R, 1981. An approach to the preliminary analysis of environmental systems. Journal of Environment Management, 12, 7–18.

Kaplan, D.I., Buettner, S.W., Li, D., Huang, S., Koster van Groos, P.G., Jaffé, P.R., et al. In situ porewater uranium concentrations in a contaminated wetland: Effect of seasons and sediment depth. Applied Geochemistry [Internet]. 2017 Oct 1 [cited 2019 Jan 26];85:128–36. Available from: https://www.sciencedirect.com/science/article/pii/S0883292716303626#tbl1

Killian, T.H., Kolb, N.L., Corbo, P., Marine, I.W., 1987. F-Area Seepage Basins: Environmental information document. E.I. du Pont de Neumors & Co., Aiken, SC 29808 .Long, S. (2009). An Integrated Flow and Transport Model to Study the Impact of Mercury Remediation Strategies for East Fork Poplar Creek Watershed, Oak Ridge, Tennessee. https://doi.org/10.25148/etd.FI09121604

Looney, B. B., Eddy, C. A., Ramdeen, M., Pickett, J., Rogers, V., Scott, M. T., & Shirley, P. A. (1990). Geochemical and Physical Properties of Soils and Shallow Sediments at the Savannah River Site. May, 113.

Looney, B. B., Jackson, D. G., Peterson, M. J., Mathews, T. J., Southworth, G., Bryan, L., Paller, M., Eddy-Dilek, C., Halverson, N. (2010) "Assessing Potential Impacts of Stannous Chloride Based Mercury Treatment on a Receiving Stream Using Real-World Data from Tims Branch, Savannah River Site". Prepared for Karen Skubal, U.S. Department of Energy Environmental Management Office of Groundwater and Soil Cleanup (EM-32), Washington DC. SRNL-STI-2010-00393.

McCarthy, J. F., & Zachara, J. M. (1989). Subsurface transport of contaminants: binding to mobile and immobile phases in groundwater aquifers. Environmental Science & Technology, 23(5), 496–502. https://doi.org/10.1021/es00063a001

MIKE DHI. (2009). Heavy Metal Template. October.

Rheinheimer, D. S., Labanowski, J., Elsass, F., Cambier, P., & Tessier, D. (2007). Heavy metal transport modelling in soil : sorption / desorption phenomena , water fluxes and contaminant fate. Tópicos Em Ciência Do Solo, 5(1), 135–180.

Serkiz, S. M., Johnson, W. H., Wile, L. M. J., & Clark, S. B. (2007). Environmental Availability of Uranium in an Acidic Plume at the Savannah River Site. Vadose Zone Journal, 6(2), 354–362. https://doi.org/10.2136/vzj2006.0072

Soil Screening Guidance: Technical Background Document Second Edition. 1996.

United States Environmental Protection Agency, Region 3 Hazardous Waste Management Division Office of Superfund Programs 1650 Arch St. Philadelphia, PA 19103-2029.Batson, V.L., P.M. Bertsch, and B.E. Herbert. 1996. Transport of anthropogenic uranium from sediments to surface waters during episodic storm events. J. Environ. Qual. 25:1129–1137.

Subtask 3.2: Model Development for the Fourmile Branch and/or Lower Three Runs Watersheds (NEW)

Subask 3.2: Introduction

The Fourmile Branch and Lower Three Runs stream systems of the Savannah River Site have been contaminated by the historical release of radionuclides from discharged post-irradiation cooling water from on-site nuclear production facilities. The F-Area wetlands at the U.S. Department of Energy's (DOE's) Savannah River Site (SRS) has been a primary area of concern due to the presence of low-level radiological contamination in the groundwater, which originated from the disposal of 1.8 billion gallons of acidic, low-level radioactive waste from 1955 to 1988 in three unlined basins, known as the F-Area Seepage Basins. While most of the dispositioned radionuclides such as plutonium isotopes and cesium-137 sorbed to the basin soil, other mobile contaminants such as uranium (U) isotopes, strontium-90 (Sr-90), iodine-129 (I-129), technetium-99 (Tc-99), tritium (^3H), and nitrate (NO_3^-) migrated through the vadose zone into the aquifer zone contaminating the groundwater. Over time the contaminant plume migrated downstream extending from the basins approximately 600 m downgradient, resurfacing at outcrops (seep lines) in the adjacent wetlands and entering the Fourmile Branch stream system. The groundwater-surface water interface where contaminated groundwater emerges to the surface is often one of the major ecological and human health risk exposure pathways. While remediation strategies employed have been successful in sequestering the contaminants of concern, a long-term monitoring strategy is necessary at the zones of vulnerability of Fourmile Branch where there is potential for contaminant remobilization if changes in biogeochemical conditions occur that could potentially influence the release of contaminants, particularly during frequent or heavy rainfall or storm events.

Subtask 3.2: Objectives

The objective of this subtask is to assist DOE-EM by developing surface water and sediment transport models of the Fourmile Branch and/or Lower Three Runs stream systems to provide information on the potential fate and transport of major radionuclides of concern (e.g., ^{137}Cs) in these contaminated watersheds during extreme meteorological events. Knowledge acquired from the Tims Branch model development and calibration will be implemented in developing coupled surface water and sediment transport models for these contaminated SRS watersheds. Model development will be executed in the three phases: (1) data collection and pre-processing and conceptual model development, (2) hydrology model development and optimization, and (3) coupling of the hydrology model with the sediment/contaminant transport component.

Subtask 3.2: Methodology

FIU initiated the literature review and data collection activities that will support the development of a conceptual model of the Fourmile Branch watershed and future development of the Fourmile Branch hydrology model. FIU began reviewing relevant reports and journal publications to collect information on the site background, history of contamination, and applied remediation technologies to assist with characterization of the study area. FIU explored data records from federal and state databases (USGS/USDA/SCDNR), as well as data provided by SRNS, SRNL and SREL scientists as well as the SRNL Atmospheric Technologies Group. A review of available spatial and timeseries data was conducted, which included but is not limited to (i) climatic data such as rainfall and evapotranspiration, (ii) geospatial layers and associated databases including high resolution digital elevation models (DEMs), soil, geology and vegetation, (iii) hydrological conditions including records of river discharge and stage, locations of outfalls and hydraulic structures such as culverts, dams, etc., and (iv) water quality parameters relevant to transport and interactions of contaminants and sediment (such as partitioning coefficient, desorption rate, critical velocity and settling velocity). A geodatabase was developed to store and manage all the GIS data, and ArcGIS tools were applied to process the data for model input and to visualize and map the study area. Training was provided to an FIU undergraduate student (DOE Fellow) on collection of GIS data from federal, state and local online databases; GIS data management using ArcGIS geodatabases; and geoprocessing and visualization of GIS data using maps and graphs for reporting purposes. The DOE Fellow also conducted a preliminary analysis of the timeseries data records (rainfall & discharge) to identify any significant storm events (500 yr/ 100 yr/ 50 yr, etc.) as the intention is to simulate contaminant fate and transport during under extreme meteorological conditions.

Subtask 3.2: Results and Discussion

This year FIU initiated a literature review to assist with characterization of the Fourmile Branch watershed and determination of any significant model input parameters. The following are short summaries of two of the papers/reports reviewed.

- Denham, M.E., C.A. Eddy-Dilek, H.M. Wainwright, J. Thibault, and K. Boerstler, 2019. **A New Paradigm for Long Term Monitoring at the F-Area Seepage Basins, Savannah River Site.** SRNL-STI-2019-00019. Savannah River National Laboratory, Aiken, SC 29808.

In this report a team of scientists were brought together to create a new paradigm for long term-monitoring at the Savannah River Site F-Area seepage basins that have been contaminated with heavy metals and radionuclides.

From 1955 to 1988, nearly 7 billion liters of low-level radioactive waste solutions including tritium, nitrate, uranium, strontium-90, iodine-129, and technetium-99 were disposed of into 3 storage basins from which they were able to pass through the soils at the bottom of the basins, to the vadose zone and eventually into the saturated zone. Once the solutions passed through the saturated zones, they were able to enter the wetlands of Fourmile Branch, along with the Fourmile Branch stream. In 1991, low permeability caps were established over the basins in order to limit the amount of waste that was able to penetrate into the vadose zone. A pump and treat system was established in 1997 in order to address the contamination of the groundwater. This strategy extracted groundwater downgradient, and removed contaminants other than tritium. Once the contaminants were removed, the groundwater was re-injected upgradient of the basins. Unfortunately, this strategy was soon paused due to the inefficiency. Currently, a funnel and gate attenuation-based remedy is used. This remedy involves the usage of subsurface barriers that are established across the flow paths of the uppermost aquifer. The groundwater is then funneled to treatment plants where the groundwater is treated.

Currently, a natural attenuation-based remedial strategy has been implemented to address the contamination derived from the F-Area seepage basins (upstream end of Fourmile Branch). With this approach, not all of the contaminants are removed from the environment. This in situ treatment leaves contaminants in the subsurface, the basin soils, and the soils of the wetlands. Moreover, a long-term monitoring program must be used to monitor the locations where the contaminants are being attenuated, to ensure that they are not remobilized. The SWAT team (Soil and Water Assistance) has proposed using an approach used by SRNL and Lawrence Berkley National Laboratory that focuses on monitoring the systematic changes in groundwater flow and chemistry that could cause remobilization of the contaminants. This differs from a traditional mindset of primarily focusing on detecting increase of contamination. Zones of vulnerability are locations where the monitoring was focused. Systematic changes are the primary focus, as opposed to the change of contaminant concentration at a point. This new strategy will also be cost efficient.

- Lanier, T. (1997). **Determination of the 100-year flood plain on Fourmile Branch at the Savannah River Site, South Carolina, 1996 (No. 97).** US Department of the Interior, US Geological Survey.

  In 1992, USDOE partnered with USGS to investigate the aerial extent of the inundation caused by a 100-year recurrence-interval flow in Fourmile Branch at the Savannah River Site. A hydrologic analysis was made to estimate the 100-year recurrence interval flow for Fourmile Branch. Fourmile Branch is located in the upper coastal plain of South Carolina, (upper coastal plain is around 20% of the state), which consists of rounded hills and gradual slopes. It begins upstream of road F, and flows into Savannah River Swamp 11,400 feet upstream from its confluence with the Savannah river. After the swamp, Fourmile Branch becomes braided and mixes flow with the Savannah River. In this study, the downstream limit is the confluence of Fourmile Branch and Savannah River. Still, the computations in this study begin upstream of where Fourmile Branch enters the swamp due to the effect of backwater from Savannah River.

This analysis shows that both the regional-rural and urban regression equations (Regionalization of selected recurrence interval flows described by Guimaraes and Bohman(1992)) are applicable for the Fourmile Branch drainage basin. (Verified using USGS gauging location 02197342). Twenty-three years of peak flow data using the log-Pearson method was compared to the regional rural and urban-regression equations. The comparison between the peak flow data and the regional rural regression model was not similar and it was discovered this was due to the percent imperviousness. A step-backwater model was used to input the 100-year flood profile for Fourmile Branch. In the equation the drainage areas needed to be greater than 4.4 mi^2 and less then 1720mi^2. Percent imperviousness data associated with urbanized errors was obtained from Cronshey (1986). Manning's roughness coefficients which are used in the hydraulic computations were based off of field notes, photographs, and methods documented by Arcement and Schneider (1984) and Barnes (1967). Soil types in FMB were derived from the Natural Conservation Service (NRCS) and soil reports of Aiken and Barnwell counties and the Savannah River Plant Area (Rogers, 1977,1985,1990). Within this report, several man-made structures are also mentioned including:

- 4 highway bridges (A12.2, A, C, and 4 at stations 21707, 32057, 59308, and 64513)
- 1 railway bridge (crosses Fourmile Branch at station 25806)
- 5 culvert crossings (located at roads 3, A-7, C-4, E-1, and F at stations 41650, 44888, 55122, 67832, and 78720)
- 10 breached dams (located at stations 18457, 21885, 24807, 27132, 35870, 36307, 39930, 49654, 59391 and 64218)
- Roads (6-1 located at 32650), (6-2 located at 33250), (6-3 located at 34020) and (A-6 at 46475)

In addition, FIU collected geospatial data which was used to create thematic maps of the Fourmile Branch study area to have a better visualization of the watershed characteristics and stream network. The figure below shows a screenshot from ArcMap where several features are visible atop a digital orthophoto basemap. The Fourmile Branch watershed boundary can be seen highlighted in red. Other visible features include the SRS F-Area buildings, the Fourmile branch stream network, roads, wetland areas and hotspots of ^{137}Cs contamination.

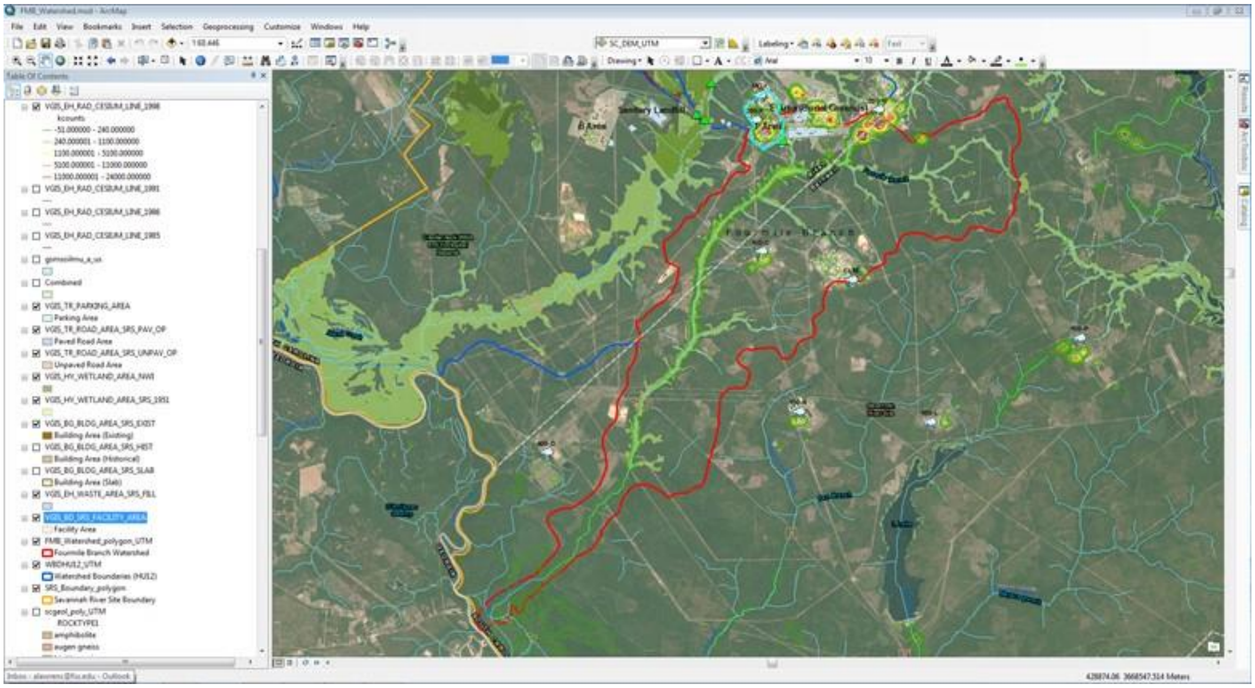

Figure 86. ArcMap view of the Fourmile Branch watershed.

A review of the available watershed polygon used to define the Fourmile Branch study area derived from the USGS Watershed Boundary Dataset (WBD) was conducted from the aspect of surface water and groundwater flows. Figure 87 displays the contours of groundwater levels within and around the delineated watershed of Fourmile Branch. A groundwater inflow or no flow boundary condition can easily be assigned to the model domain derived from the watershed boundary. The surface water flow network within the study area derived from the USGS National Hydrography Dataset (NHD) is presented in Figure 88. It is clear from this figure that the flow network is independent as it drains areas within the watershed polygon.

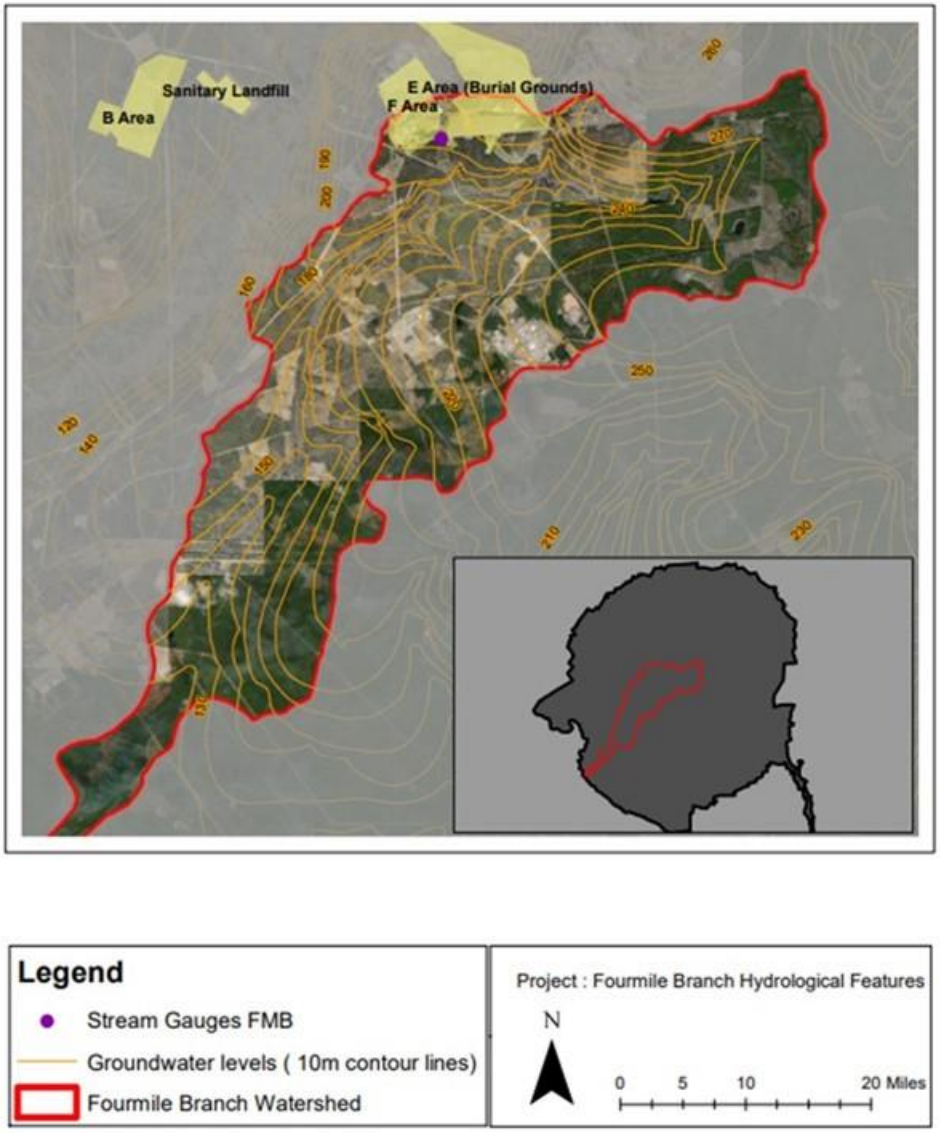

Figure 87. Contours of groundwater levels for the Fourmile Branch watershed.

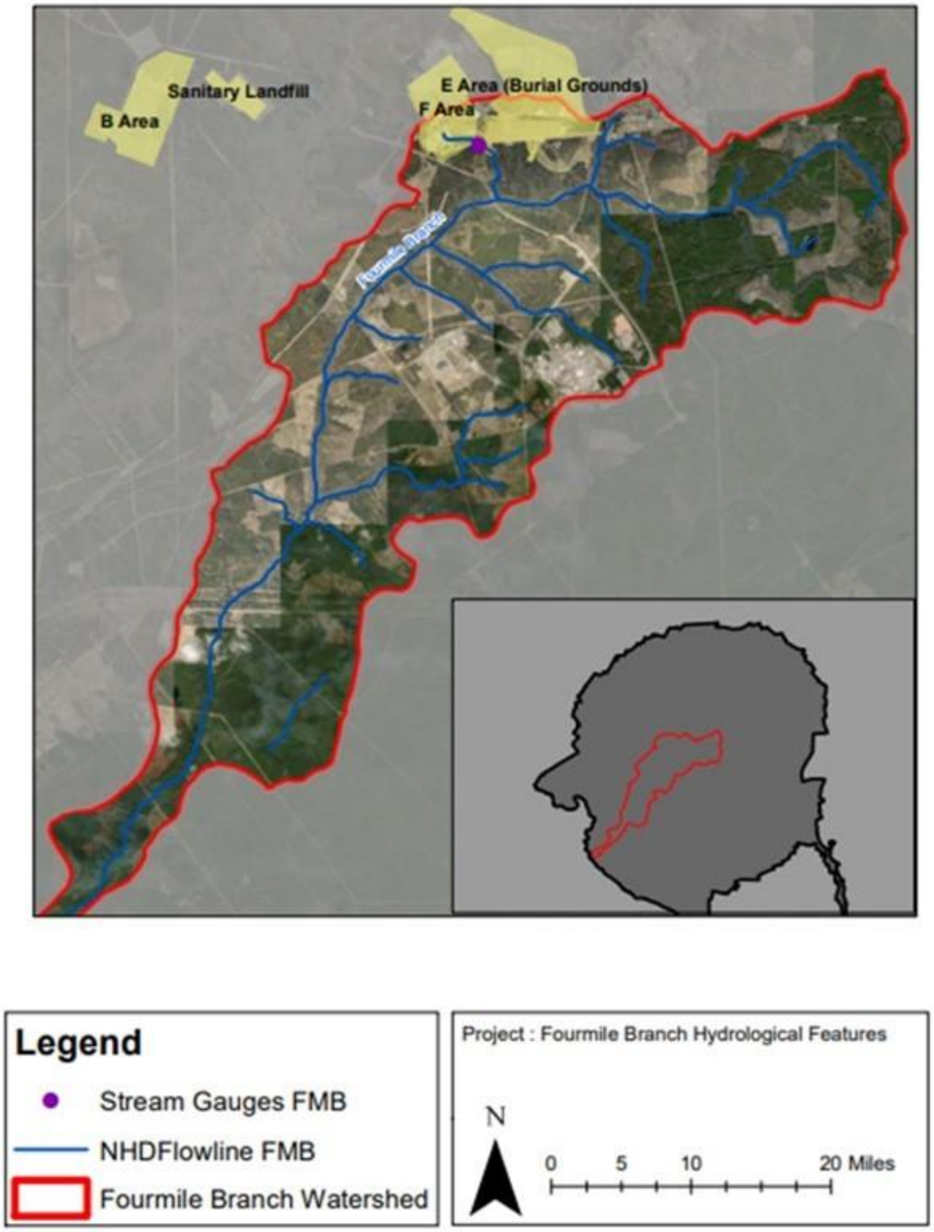

Figure 88. Surface water flow network for the Fourmile Branch watershed.

Existing data derived from the SRNS Geotechnical Engineering group for the Tims Branch modeling work was reviewed to determine if any of the datasets had a spatial extent that also covered the FMB study area and could thus be used for this subtask. As some of the data encompassed the whole of the Savannah River Site, FIU was able to use the data and just needed it to be clipped to the Fourmile Branch (FMB) watershed boundary which was the established model domain. As such FIU developed a ‘Clip’ model using ArcGIS ModelBuilder in order to automate the process of clipping several GIS shapefiles to the FMB watershed boundary. The clipping model was developed to sequentially clip each of the files grouped in the same network folder to the FMB watershed boundary. Below are screenshots of the process flow model developed, before and after views of the stream network shapefile that was processed with the

‘Clip’ model, and a table with the list of files that were clipped to the Fourmile Branch watershed boundary.

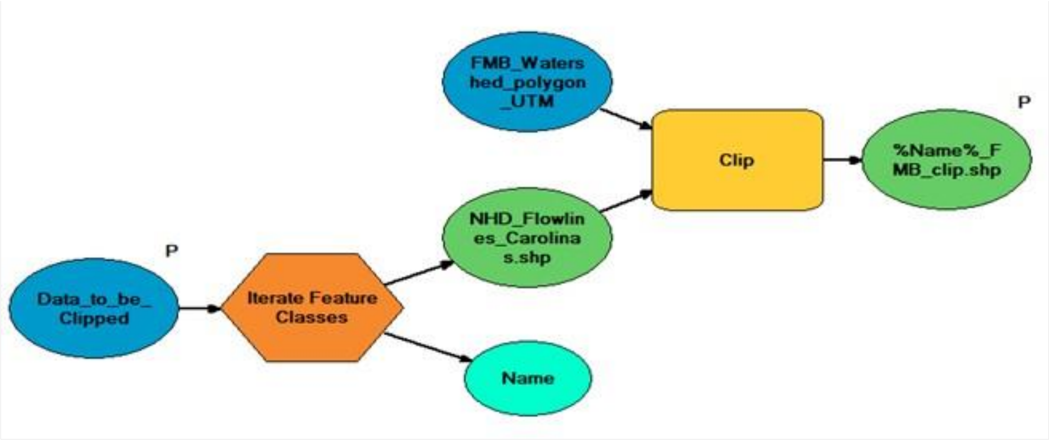

Figure 89. Screenshot of the ‘Clip’ model used to clip the GIS shapefiles to the FMB watershed boundary using ArcGIS ModelBuilder.

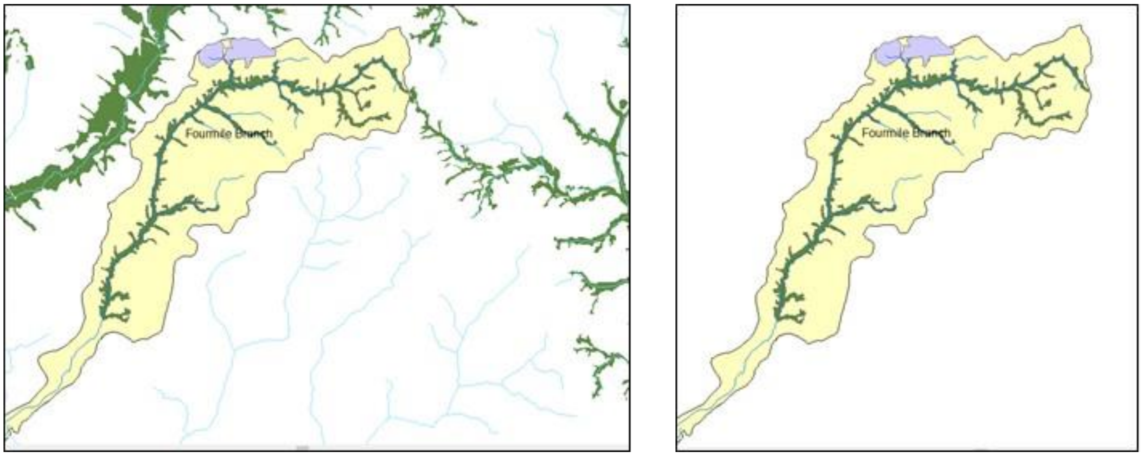

Figure 90. Stream network extending beyond the spatial extent of the Fourmile Branch watershed (left); Stream network clipped to the spatial extent of the FMB watershed (right).

Table 29. GIS shapefiles clipped to the Fourmile Branch watershed boundary.

Feature Category	File Name	Feature Type	Geometry
Biota	VGIS_FA_TES_SURVEY_AREA_SRS_FMB	shapefile feature class	polygon
Buildings	VGIS_BD_SRS_FACILITY_AREA_FMB_clip	shapefile feature class	polygon
	VGIS_BG_BLDG_AREA_SRS_EXIST_FMB_clip	shapefile feature class	polygon
	VGIS_BG_BLDG_AREA_SRS_SLAB_FMB	shapefile feature class	polygon
Contaminants	VGIS_EH_GROUNDWATER_PLUME_I_FMB	shapefile feature class	polygon

Feature Category	File Name	Feature Type	Geometry
	VGIS_EH_GROUNDWATER_PLUME_R_FMB	shapefile feature class	polygon
	VGIS_EH_GROUNDWATER_PLUME_VO_FMB	shapefile feature class	polygon
	VGIS_EH_RAD_CESIUM_LINE_1985_FMB_clip	shapefile feature class	line
	VGIS_EH_RAD_CESIUM_LINE_1986_FMB_clip	shapefile feature class	line
	VGIS_EH_RAD_CESIUM_LINE_1991_FMB_clip	shapefile feature class	line
	VGIS_EH_RAD_CESIUM_LINE_1998_FMB_clip	shapefile feature class	line
	VGIS_EH_RAD_URANIUM_LINE_1991_1_FMB	shapefile feature class	line
	VGIS_EH_RAD_URANIUM_LINE_1991_FMB	shapefile feature class	line
	VGIS_EH_RAD_URANIUM_LINE_1998_FMB	shapefile feature class	line
	VGIS_EH_WASTE_AREA_SRS_FILL_FMB	shapefile feature class	polygon
DEMs	dem_fmb_5m	raster TIFF File	
	FMB_2018_LiDAR_hillshade_5m	raster TIFF File	
	DEM_FMB_30m	raster GRID file	
Engineering Structures and Areas	BRIDGES_MAP_UTM_FMB	shapefile feature class	point
Geology	scgeol_poly_UTM_FMB	shapefile feature class	polygon
	SRS_Geology_FMB	shapefile feature class	polygon
	vgis_ge_borehole_bedrock_pt_FMB	shapefile feature class	point
	vgis_ge_core_invent_pt_1997_FMB	shapefile feature class	point
	VGIS_GE_DEPTH_BEDROCK_AREA_FMB	shapefile feature class	polygon
	vgis_ge_fault_line_1996_FMB	shapefile feature class	line
	vgis_ge_gravity_line_reg_FMB	shapefile feature class	line
	vgis_ge_gravity_pt_csra_FMB	shapefile feature class	point

Feature Category	File Name	Feature Type	Geometry
	vgis_ge_lithology_santee_FMB	shapefile feature class	polygon
	vgis_ge_magnetic_line_csra_FMB	shapefile feature class	line
	vgis_ge_magnetic_pt_csra_FMB	shapefile feature class	point
	vgis_ge_seismic_line_csra_FMB	shapefile feature class	line
	vgis_ge_sinkhole_area_usgs_FMB	shapefile feature class	polygon
	vgis_ge_sub_transect_pt_FMB	shapefile feature class	point
	vgis_ge_surf_area_kb_us_FMB	shapefile feature class	polygon
	VGIS_GE_SURF_AREA_SRS_48K_FMB	shapefile feature class	polygon
GW	vgis_hy_piezometer_pt_1998_1_FMB	shapefile feature class	point
	vgis_hy_piezometer_pt_1998_FMB	shapefile feature class	point
	vgis_hy_water_tbl_line_1995_FMB	shapefile feature class	line
	vgis_hy_water_tbl_line_1998_FMB	shapefile feature class	line
	vgis_hy_water_tbl_line_2002_FMB	shapefile feature class	line
	vgis_hy_water_tbl_line_2003_FMB	shapefile feature class	line
HydrographyNet	NHD_Flowlines_Carolinas_FMB_clip	shapefile feature class	line
	NHDWaterbody_FMB	shapefile feature class	polygon
Hydrology	VGIS_HY_STREAM_LINE_SRS_FMB	shapefile feature class	line
Land Use	NLCD2016_LandCover_UTM_FMB	raster TIFF File	
Model Domain	WBDHU12_FMB_Clip	shapefile feature class	polygon
	FMB_mask	shapefile feature class	polygon
Monitoring Stations	FMB_SRNL_Stream_Gauges	shapefile feature class	point
	FMB_USGS_Stream_Gauges	shapefile feature class	point

Feature Category	File Name	Feature Type	Geometry
	SRS_RainGauges_012419_FMB	shapefile feature class	point
	VGIS_EH_SW_DISCHRG_PT_SRS_FMB_clip	shapefile feature class	point
	vgis_im_stream_gauge_pt_FMB	shapefile feature class	point
Soils	aoi_a_aoi	shapefile feature class	polygon
	soilmu_a_aoi	shapefile feature class	polygon
	soilmu_l_aoi	shapefile feature class	line
	soilmu_p_aoi	shapefile feature class	point
	soilsf_l_aoi	shapefile feature class	line
	soilsf_p_aoi	shapefile feature class	point
Vegetation	VGIS_HY_WETLAND_AREA_NWI_FMB	shapefile feature class	polygon
	VGIS_HY_WETLAND_AREA_SRS_1951_FMB	shapefile feature class	polygon
Watershed	WBDHU12_FMB_Clip	shapefile feature class	polygon

The shapefiles generated from clipping the historical data will be used for mapping and visualization of the FMB study area to assist in conceptual model development and for generating files required for hydrological model development. In addition, the most updated versions of the more significant GIS data layers required for model development were downloaded from the online federal databases to ensure that the most recent available data is utilized in the model. These included the soil classification data from the USDA’s Natural Resources Conservation Service (NRCS) web soil survey for South Carolina (Figure 91), and the Multi-Resolution Land Characteristics Consortium (MRLC) national land cover dataset (NLCD) for 2016 (Figure 92). The soil classification data was downloaded in both GIS and tabular formats using the FMB watershed boundary as the area of interest (AOI). The 2016 NLCD was provided in the form of a raster grid file for the continental US, which was projected to the appropriate UTM coordinate system and then clipped to the extent of the FMB model domain for input into the MIKE SHE model. A digital elevation model (DEM) showing the topographical elevation can also be seen in Figure 93.

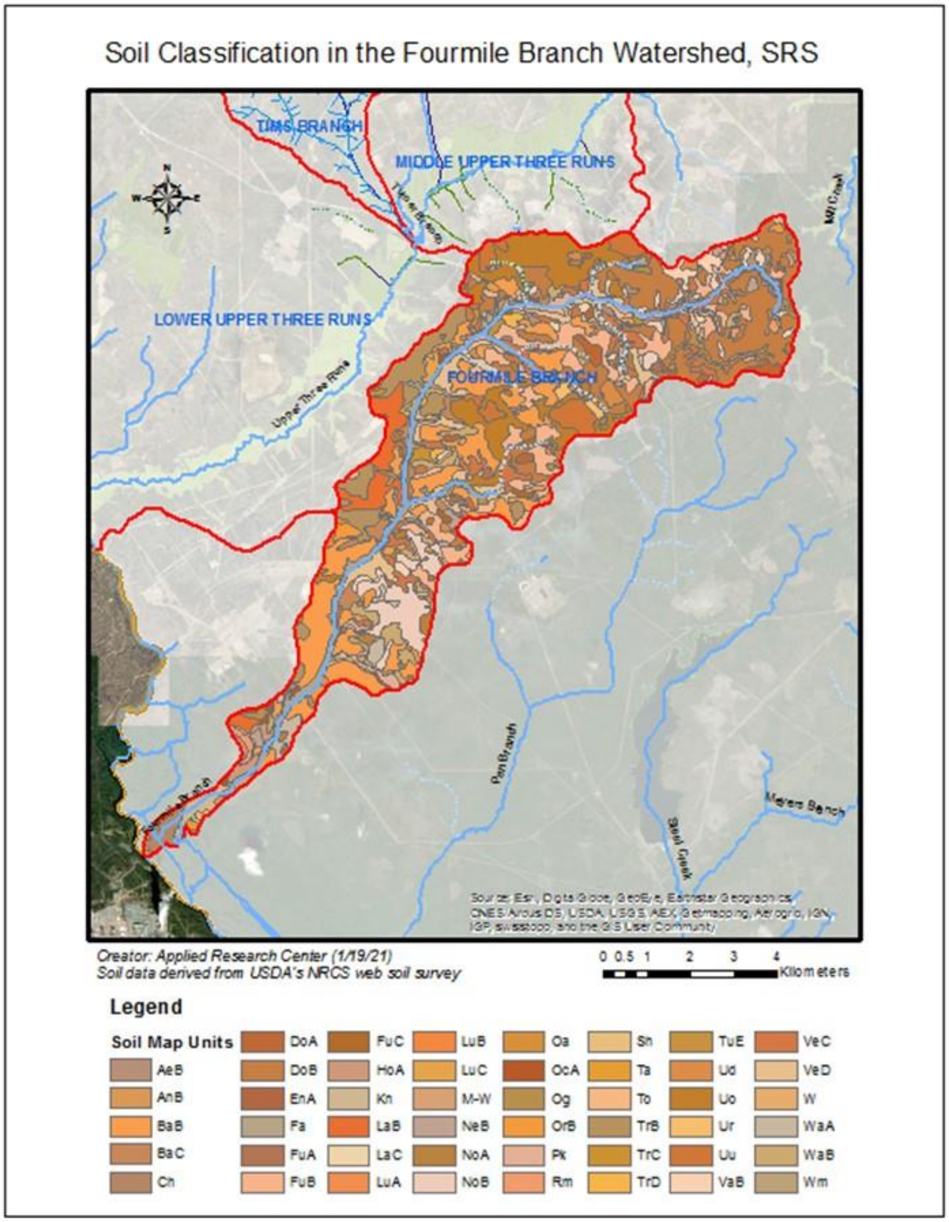

Figure 91. USDA's NRCS web soil survey soil classification (depicted by soil map unit symbols) in the Fourmile Branch watershed, SRS.

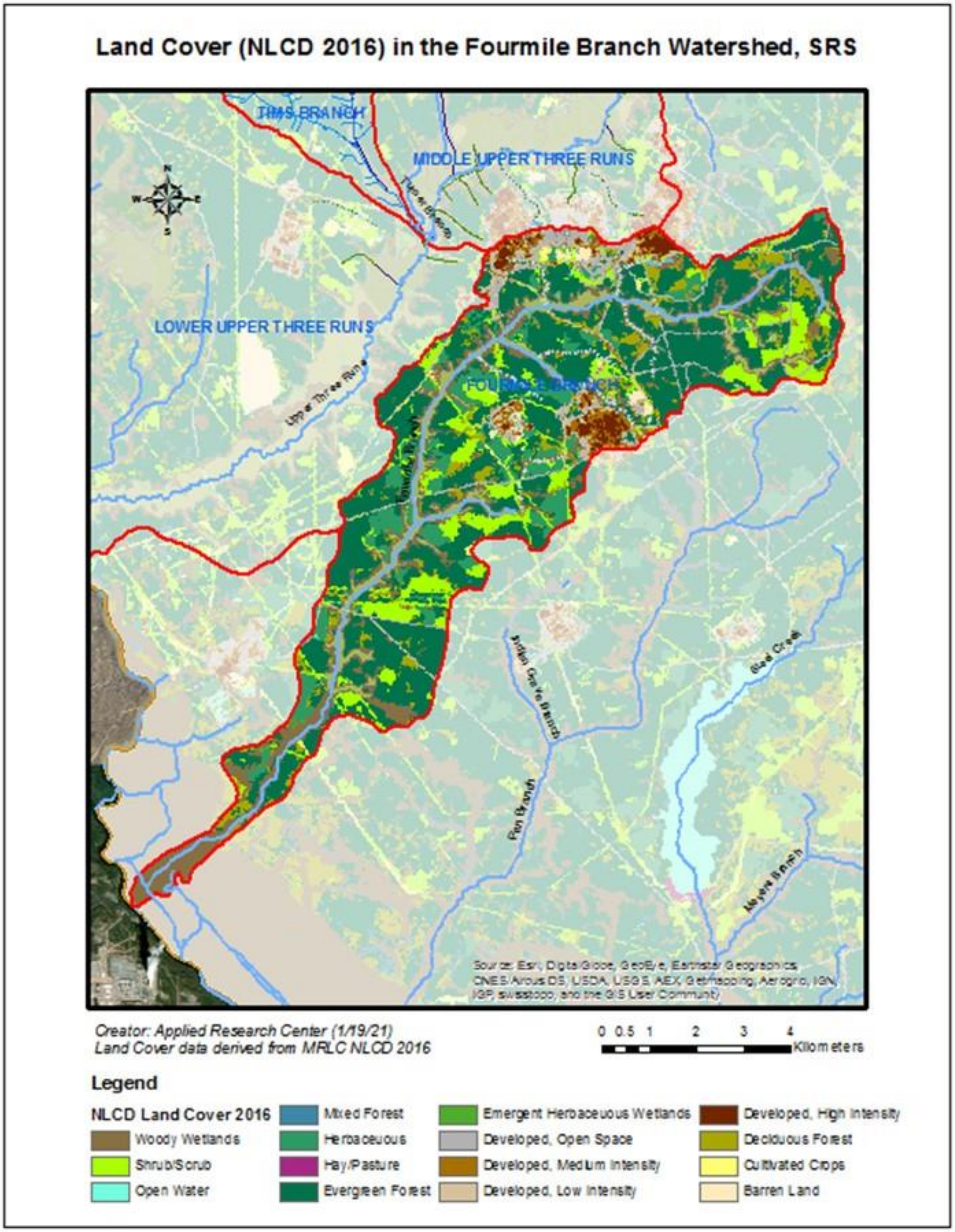

Figure 92. Land cover derived from the NLCD 2016 in the Fourmile Branch watershed, SRS.

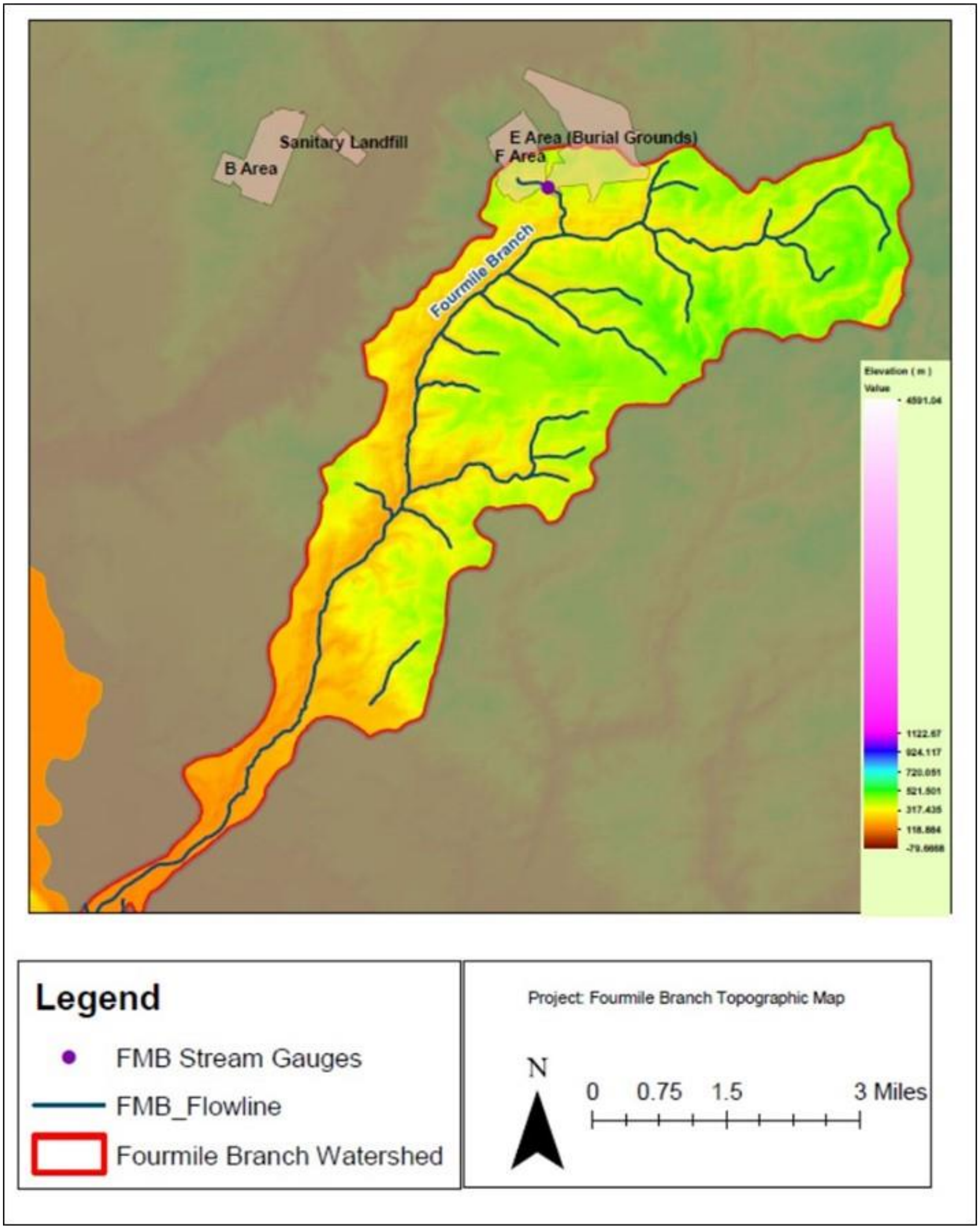

Figure 93. Topographical elevation map of the Fourmile Branch watershed, SRS.

Preliminary analysis of historical discharge data from USGS as well as rainfall data derived from the SRNL Atmospheric Technologies Group from gauges either within or in close proximity to the FMB watershed was also initiated with the intent of generating hydrographs to be used during the model calibration. Analyses were conducted on rain depth data from three rain gauges in the FMB area that recorded information at a daily scale. With the information that was received in earlier reports, FIU determined the average rain distribution per month at SRS rain gauges 200-H, 100-C, and 200-F. Rain gauge CLM was not used because it collected rainfall in 15-minute intervals. The locations of each rain gauge is displayed in the map below.

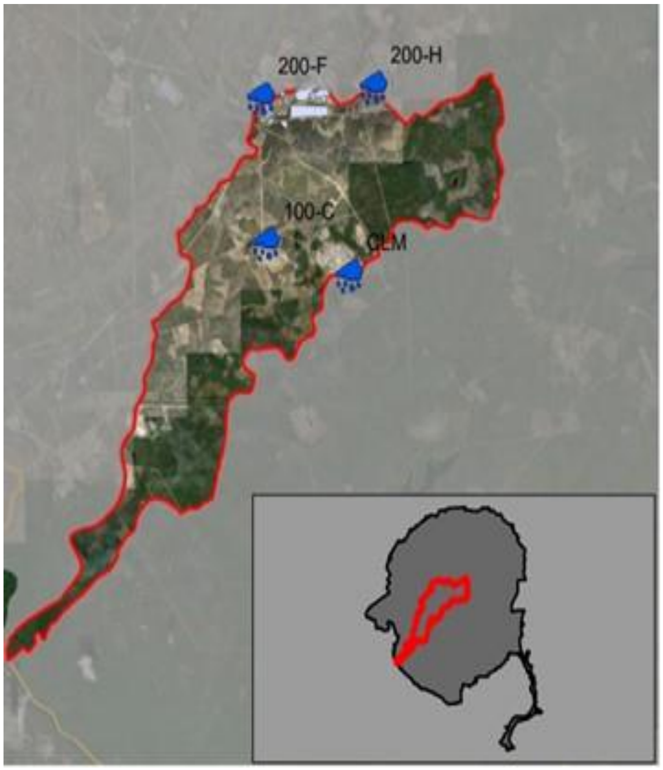

Figure 94. The locations of the rain gauges used in the monthly rainfall analysis.

In order to complete the monthly rainfall analysis, the data was organized by month from 1981-2016 (Rain Gauge 200-F began in 1961 and ended in 2016). From the graphs below, it can be predicted that within Fourmile Branch, the months of June, July, and August receive the most rainfall. This would therefore likely be a good time period to run the model for the calibration event. On the contrary, the months April, May, October, and November appear to be the months with the least amount of average rainfall depth. From the graphs, rainfall distribution was similar in each of the systems, a sign that the rain gauges were fully functional throughout the whole time period analyzed.

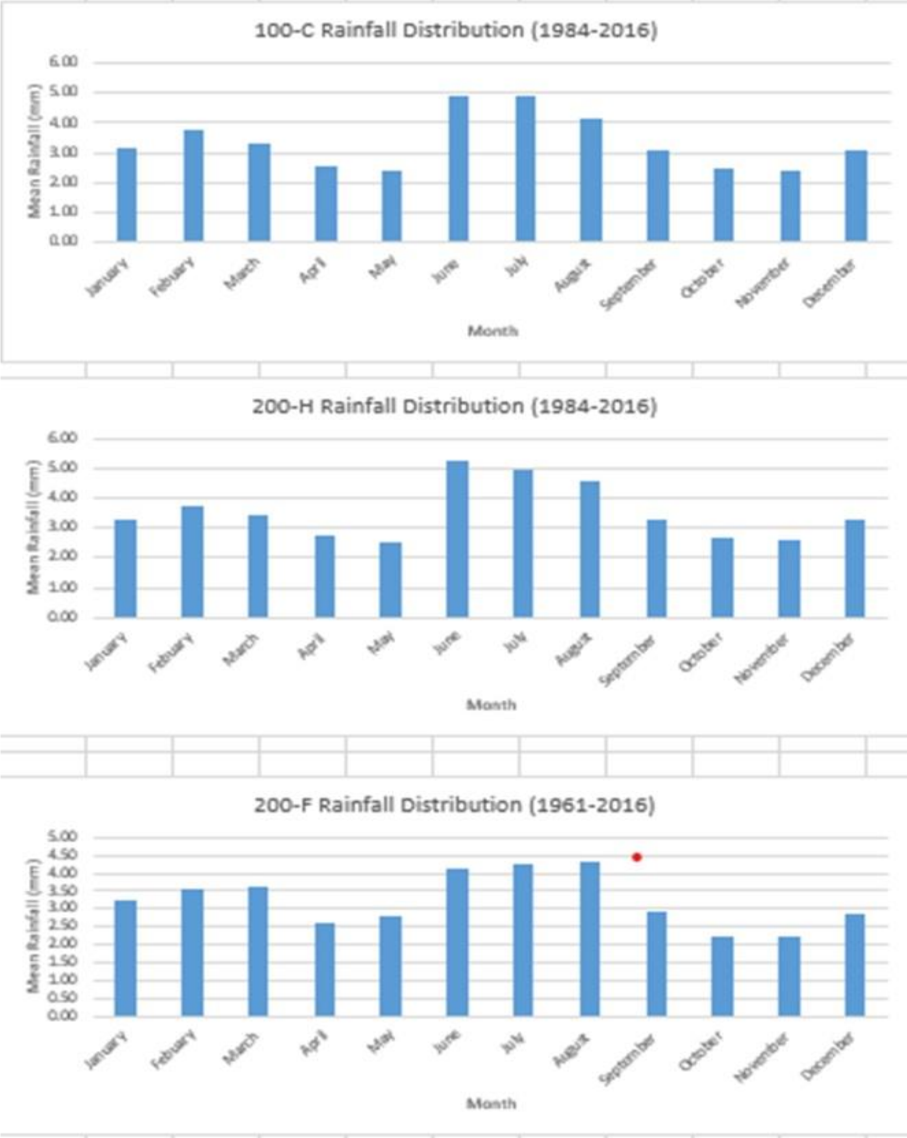

Figure 95. Average rain depths for 3 stream gauges within Fourmile Branch.

The next step was to analyze the discharge datasets within Fourmile Branch watershed to establish a correlation between rainfall and discharge and select the best suitable storm event that could be implemented when calibrating the hydrodynamic component of the model. The following map depicts the locations of the rainfall stations (blue clouds) and stream gauges (light green circles) in the FMB study area.

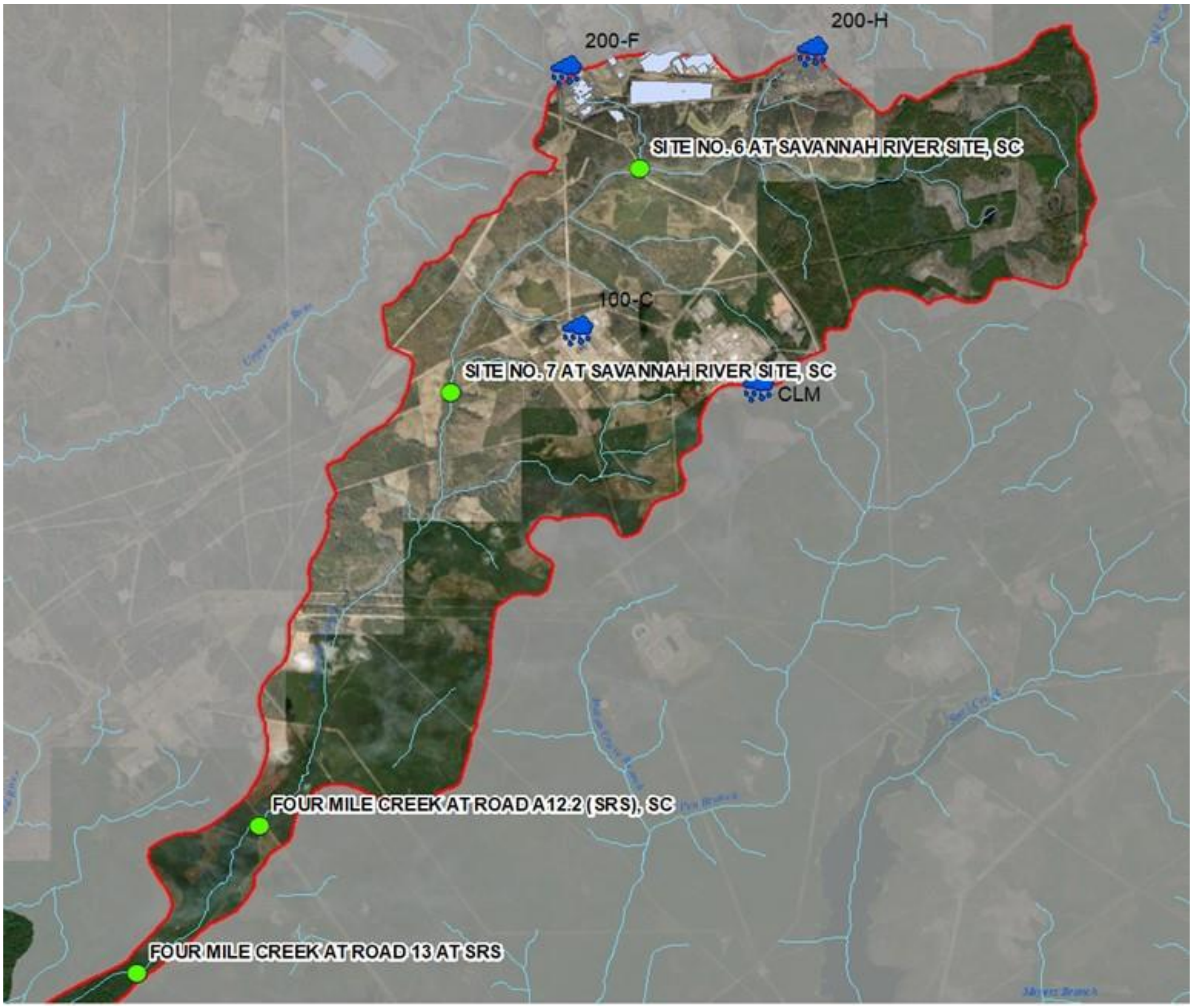

Figure 96. A map of Fourmile Branch showing the locations of nearby rainfall gauges (blue clouds) and stream gauges (light green circles).

A flood frequency analysis (FFA) was performed using data derived from USGS stream gauge #02197344 (Fourmile Creek at Road A12.2) located at the lower end of Fourmile Branch, and gauge #02197340 (Site No. 6) at the upper end of Fourmile Branch near the F/H Area. The discharge timeseries for both stream gauges for the period 1976 – 2002 were graphed for comparison (Figure 97) and analyzed to determine the annual maximum discharge at each station. It was noted that for station USGS 0217344, the median discharge values from 1976 – 1985 were far greater than the period from the 1985 – 2002 (approx. four times greater). Further investigation will be required to determine the reason for this.

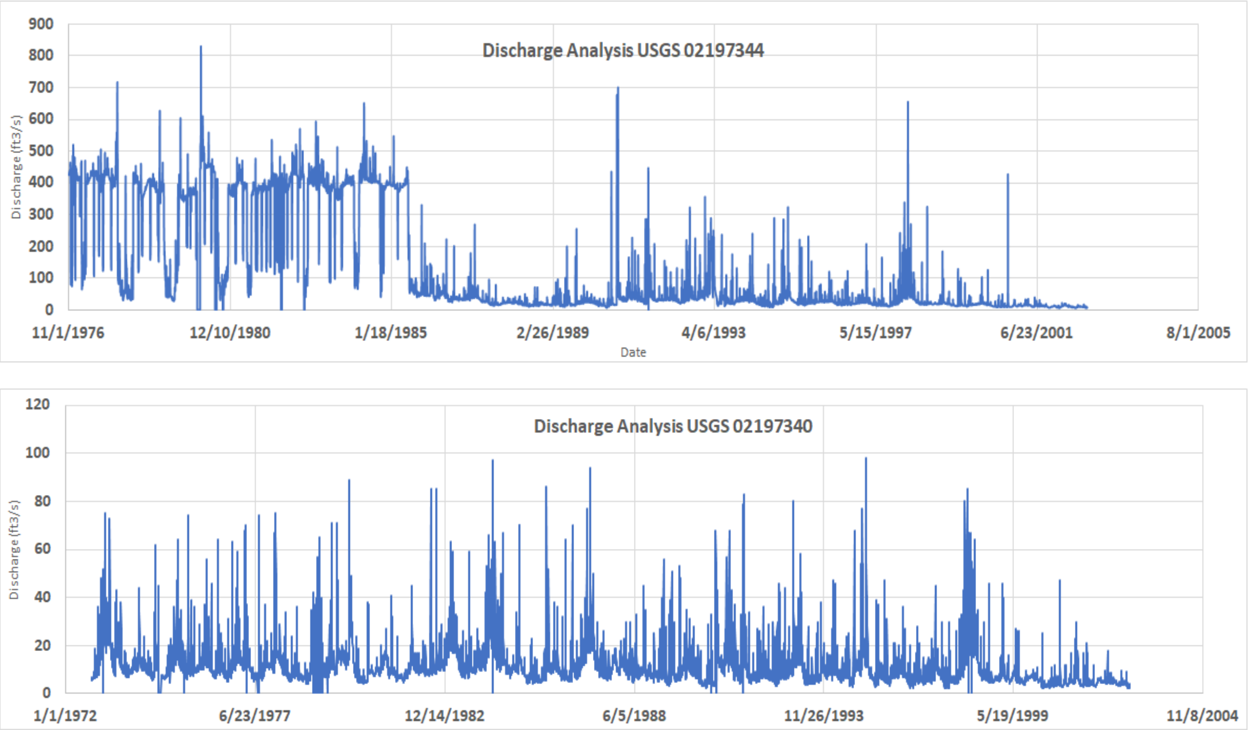

Figure 97. The discharge time series data for stream gauge USGS 0217344 (lower end of FMB) and USGS 02197340 (upper end of FMB near F/H Area).

The FFA was first conducted for USGS stream gauge #02197344, whereby the discharge values were used to calculate the average recurrence interval (ARI). The ARI describes the probability that a certain precipitation event will occur. An ARI event of 1 year is expected to occur more often than an event that is considered a 50-year event. It is more beneficial to use events with a greater ARI in the model (e.g., a 20-year ARI vs. a 5-year ARI) so that the model can be considered robust enough to be utilized as a prediction tool for rare/extreme events.

The Gumbel Distribution was used to manually conduct the FFA. The first step was to organize the discharge events from stream gauge USGS 02197344 in order from smallest to largest. The following formula was then used to estimate the ARI.

$$q_i = \frac{i-a}{N+1-2a}$$

Where,
q_i = Exceedance probability associated with a specific observation;
N = Number of annual maxima observations;
i = Rank of specific observation with i=1 being the largest to i=N being the smallest Column (C);
a = constant for estimation = 0.44 using Gringorten's method

The following formulas were then used to find the theoretical ARI for stream gauge 02197344.

$$F_x(x) = \exp\left[-\exp\left(-\frac{x-u}{\alpha}\right)\right] = p$$

Where x is the observed discharge data and u and α are the calculated parameters of the distribution. The distibution is used to calculate the theoretical estimate of ‘p’. Two columns are created, labeled ‘(x-u)/α’ and ‘p theoretical’. In order to calculate ‘p theoretical’, the value of (x-u)/a needs to be calculated first. Using the equations given below, the values of $\bar{X}$, s_x, u and α are calculated.

$$\bar{x} = \sum_{i=1}^{n} \frac{x_i}{n}$$

$$s_x{}^2 = \frac{1}{(n-1)} \sum_{i=1}^{n} (x_i - \bar{x})^2$$

$$u = \bar{x} - 0.5772\alpha$$

$$\alpha = \frac{\sqrt{6}s_x}{\pi}$$

A maximum estimated ARI of 48 years and a maximum theoretical ARI of 20 years were determined for an event that occurred in 1980 after running the formulas in MS Excel. The following graph shows the data for both the theoretical and estimated ARIs using Gumbel’s distribution.

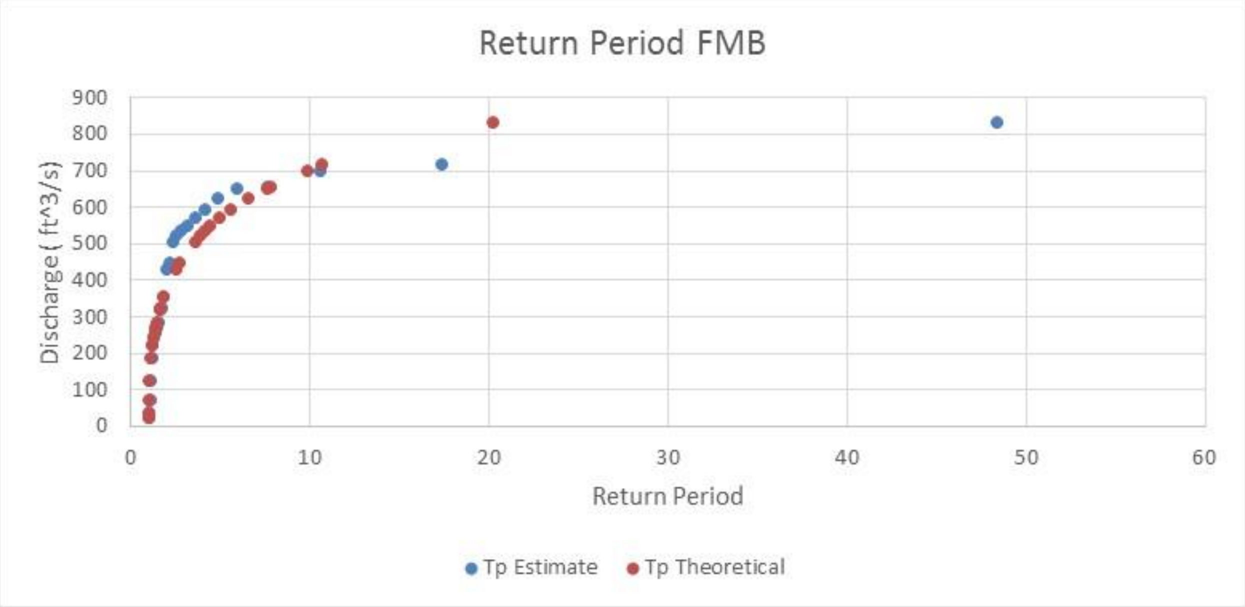

Figure 98. Graph showing the theoretical (red) and estimated (blue) ARIs derived using Gumbel's distribution.

After manually running the FFA, the process was repeated using the software FLIKE. Running the FFA through FLIKE also provided the uncertainty of each possible return period, which helps with risk management. The results derived from FLIKE are shown below.

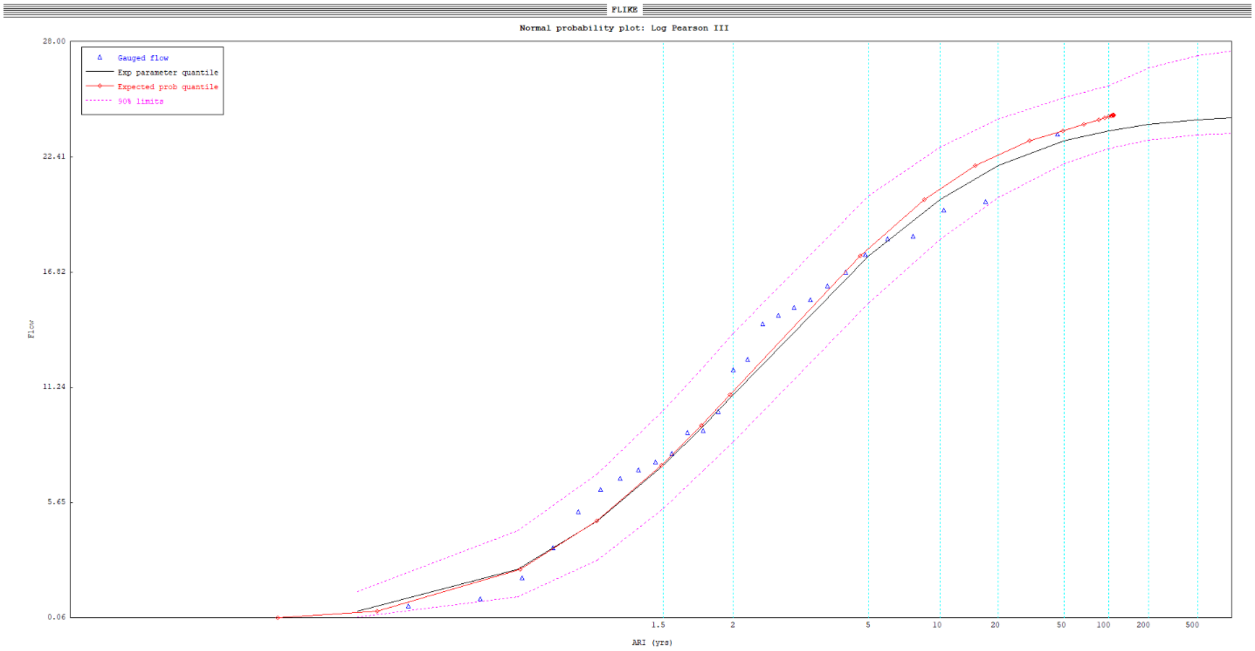

Figure 99. Graph of the discharge values in m^3/s and the correlated ARIs for each discharge value at stream gauge 02197344. This graph also includes the uncertainty, represented by the red lines. The graph provides the ability to see the minimum and maximum discharge value that is associated with each ARI.

Table 30. Table generated using FLIKE software showing each of the 27 discharge values in m^3/s in order of greatest discharge value to lowest as well as the year that these discharge values were recorded. The far right column shows the ARI of each of these events, the largest occurring in 1980 with a discharge of 23.5 m^3/s.

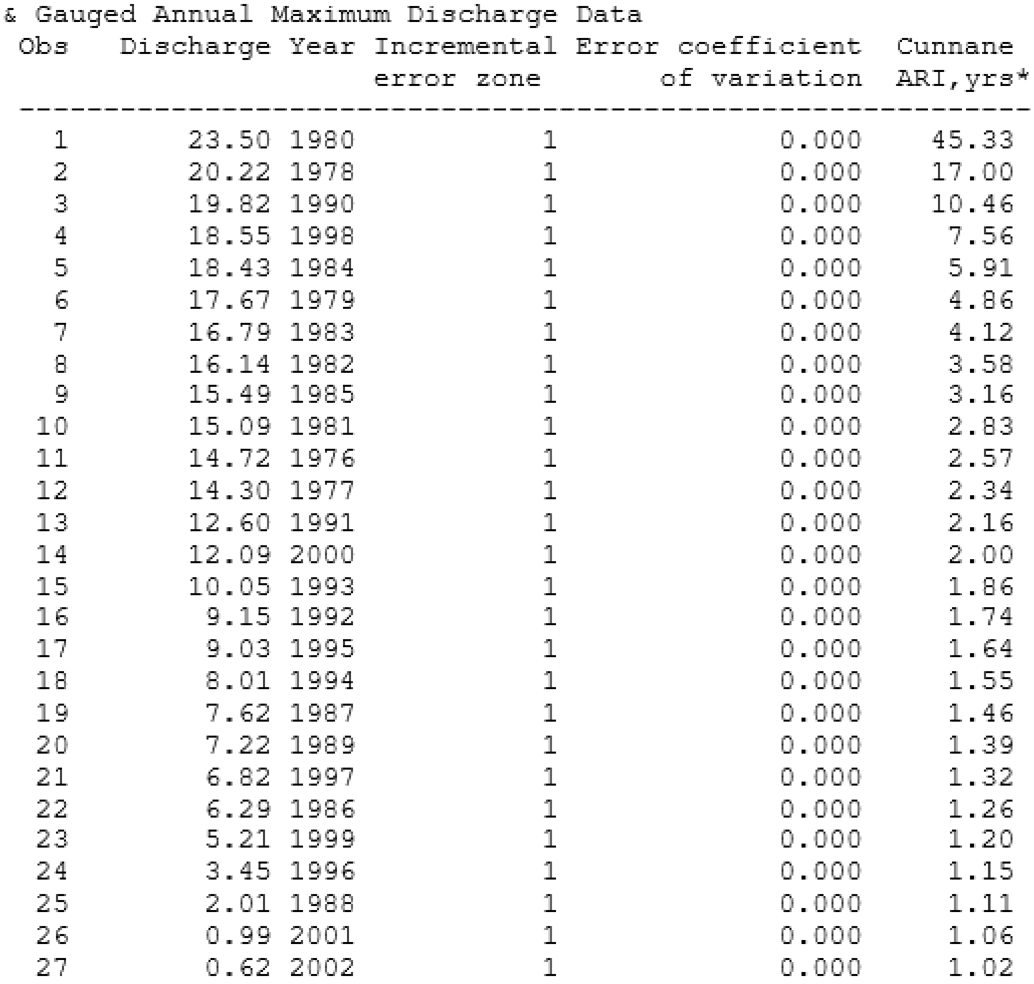

```
& Gauged Annual Maximum Discharge Data
 Obs   Discharge Year Incremental Error coefficient  Cunnane
                      error zone       of variation  ARI,yrs*
 ------------------------------------------------------------
   1       23.50 1980           1             0.000    45.33
   2       20.22 1978           1             0.000    17.00
   3       19.82 1990           1             0.000    10.46
   4       18.55 1998           1             0.000     7.56
   5       18.43 1984           1             0.000     5.91
   6       17.67 1979           1             0.000     4.86
   7       16.79 1983           1             0.000     4.12
   8       16.14 1982           1             0.000     3.58
   9       15.49 1985           1             0.000     3.16
  10       15.09 1981           1             0.000     2.83
  11       14.72 1976           1             0.000     2.57
  12       14.30 1977           1             0.000     2.34
  13       12.60 1991           1             0.000     2.16
  14       12.09 2000           1             0.000     2.00
  15       10.05 1993           1             0.000     1.86
  16        9.15 1992           1             0.000     1.74
  17        9.03 1995           1             0.000     1.64
  18        8.01 1994           1             0.000     1.55
  19        7.62 1987           1             0.000     1.46
  20        7.22 1989           1             0.000     1.39
  21        6.82 1997           1             0.000     1.32
  22        6.29 1986           1             0.000     1.26
  23        5.21 1999           1             0.000     1.20
  24        3.45 1996           1             0.000     1.15
  25        2.01 1988           1             0.000     1.11
  26        0.99 2001           1             0.000     1.06
  27        0.62 2002           1             0.000     1.02
```

Table 31. Statistical probability table showing the uncertainty of each ARI that was calculated using FLIKE.

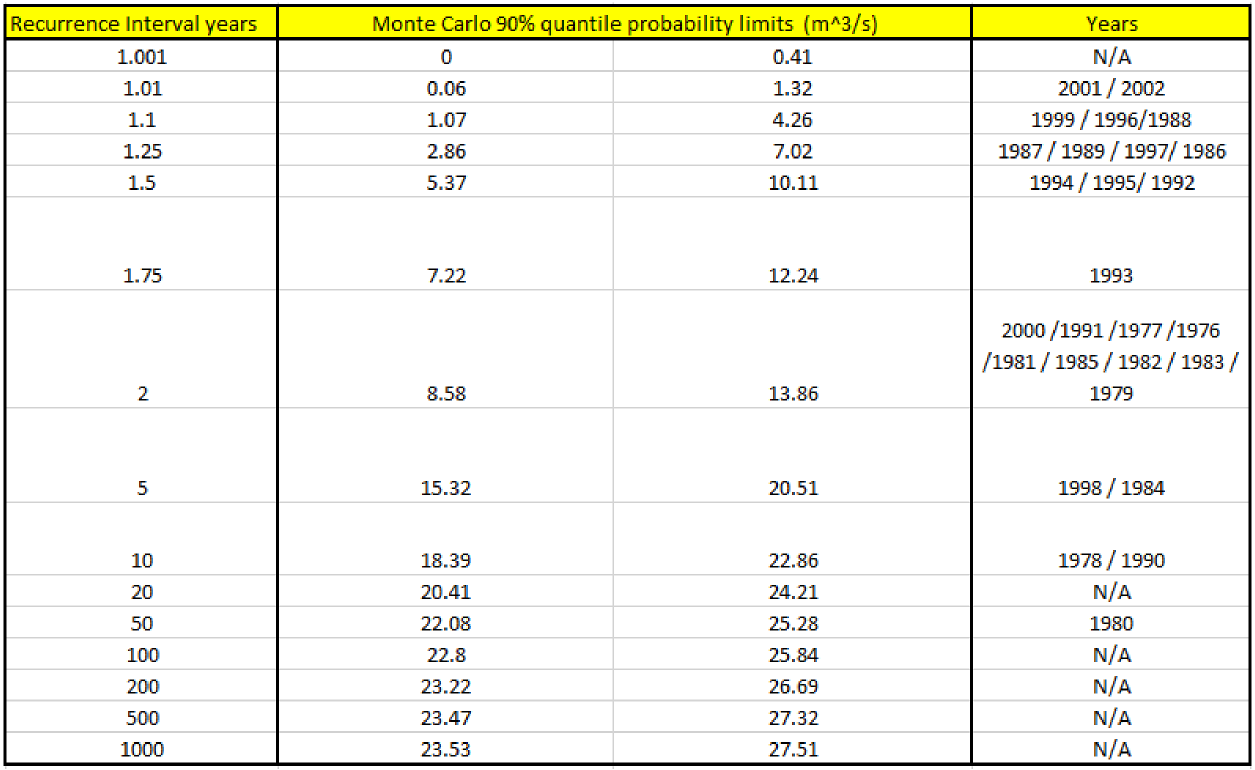

Recurrence Interval years	Monte Carlo 90% quantile probability limits (m^3/s)		Years
1.001	0	0.41	N/A
1.01	0.06	1.32	2001 / 2002
1.1	1.07	4.26	1999 / 1996/1988
1.25	2.86	7.02	1987 / 1989 / 1997/ 1986
1.5	5.37	10.11	1994 / 1995/ 1992
1.75	7.22	12.24	1993
2	8.58	13.86	2000 /1991 /1977 /1976 /1981 / 1985 / 1982 / 1983 / 1979
5	15.32	20.51	1998 / 1984
10	18.39	22.86	1978 / 1990
20	20.41	24.21	N/A
50	22.08	25.28	1980
100	22.8	25.84	N/A
200	23.22	26.69	N/A
500	23.47	27.32	N/A
1000	23.53	27.51	N/A

Table 31 shows the statistical probability of the ARIs that were calculated using FLIKE. For an ARI of 10 years, the values of discharge could range between 18.39 m^3/s and 22.86 m^3/s. The far right column shows the years that correlate with each ARI. It should be noted that these calculations are merely estimates and predictions, thus an ARI of 5 years does not mean that the event will be guaranteed to occur every 5 years. This can be seen from the information collected at stream gauge 02197344, where it was observed that it took 12 years for another 5-year event to occur. As such, the calculated ARIs are just predictions and not a certain indicator of how often an event will occur.

Based on the flood frequency analysis results, FIU contacted the SRNL climatology group to obtain detailed 15-min rainfall data for the years 1980 and 1990 from the nearby CLM meteorological station on-site SRS. This data was unfortunately not available for the time periods requested due to poor data quality. As such, FIU considered more recent sources of discharge and turbidity data and was provided an Excel spreadsheet by SRNL with both types of data for several stations along FMB ranging from 1993 – 2021. FIU reviewed and formatted the data in order to conduct another discharge analysis to identify any significant discharge events using the FLIKE statistical analysis software. Based on the outcome of this analysis, FIU will investigate whether simultaneous 15-min rainfall records are available for this time period in the next year.

Subtask 3.2: Conclusions

The work conducted over the past year under this subtask has included:

- A literature review to obtain information on the site background, history of contamination, and applied remediation technologies.

- Collection of climate, geospatial, hydrological and water quality data records from federal and state databases (USGS/USDA/SCDNR), or from SRNS and SRNL scientists and the SRNL Atmospheric Technologies Group.
- Development of a geodatabase to store and manage all the GIS data, and application of ArcGIS tools to process the data for model input and to visualize and map the study area.
- Preliminary analysis of timeseries data records (rainfall & discharge) to identify any significant storm events (500 yr/ 100 yr/ 50 yr, etc.).
- Training of an FIU undergraduate student (DOE Fellow) on geospatial mapping and analysis tools, as well as GIS and timeseries data retrieval, processing and analysis.

It should be noted that the degree and rate of progress on this subtask was impacted by the loss of technical personnel midway through the fiscal year. In addition, recent conversations with SRNL collaborators has led to a redirection of focus to better support the research activities of the Advanced Long-Term Environmental Monitoring Systems (ALTEMIS) project in the SRS F-Area. This scope revision was incited during the DOE Fellow's summer internship with Lawrence Berkeley National Laboratory (LBNL) in collaboration with Savannah River National Laboratory (SRNL), which involved assisting the ALTEMIS team in analyzing surface water parameters in the SRS F-Area and Fourmile Branch to determine if there may be any linkages between these controlling variables and the contaminants of concern within Fourmile Branch. The internship was focused on the analysis of data from surface water stations being monitored in the SRS F-Area and Fourmile Branch to provide insight about I-129 behavior/mobility in the environment and determine if there are any linkages with parameters such as flow rate, precipitation, temperature and chemistry, that may serve as controlling variables. Particular emphasis was on the spatiotemporal distribution of surface water temperature and chemistry, which are important linkages to groundwater seepages and contaminant migration from subsurface to surface. Details of the internship were documented in a report titled *"Characterization of Surface Water Dynamics within Fourmile Branch and its Linkages with Groundwater and I-129 Geochemistry"* which will be posted on the DOE Fellows website: fellows.fiu.edu.

FIU's revised work scope will also support the existing research being conducted under the ALTEMIS project and involve the development of a detailed conceptual model of the hydrological flow processes occurring within the seepline over time in response to precipitation and throughout the different seasons (i.e. lateral (shallow) surface flow vs groundwater seepage) through a detailed assessment of in situ observations. Based on this conceptual understanding, FIU will build a hydrological model focusing on the flow of groundwater downslope through the funnel and gate system, and entering the seep line – riparian zone – river network using the MIKE model.

Initially a 2D version of the model will be created to obtain an increased understanding of the flow dynamics, followed by 3D modelling of the groundwater-seepline-river network system and the role of the funnel and gate system. Subsequently, the model can be extended to include biogeochemistry focusing on the fate and transport of I-129 and other heavy metals (to be determined) in this contaminated region, focusing on remobilization of previous sequestered contaminants by temporal changes in hydrological conditions. The experience gained by the DOE Fellow during his summer internship has equipped him with knowledge and skills to support the conceptual model development under this subtask.

Subtask 3.2: References

Saksena, S. (2017, January 05). Plotting the flood frequency curve using Gumbel Distribution. Retrieved March 3, 2021, from

https://serc.carleton.edu/hydromodules/steps/166250.html

TASK 5: RESEARCH AND TECHNICAL SUPPORT FOR WIPP

Subtask 5.2: Fate of Actinides in the Presence of Ligands in High Ionic Strength Systems

Subtask 5.2: Introduction

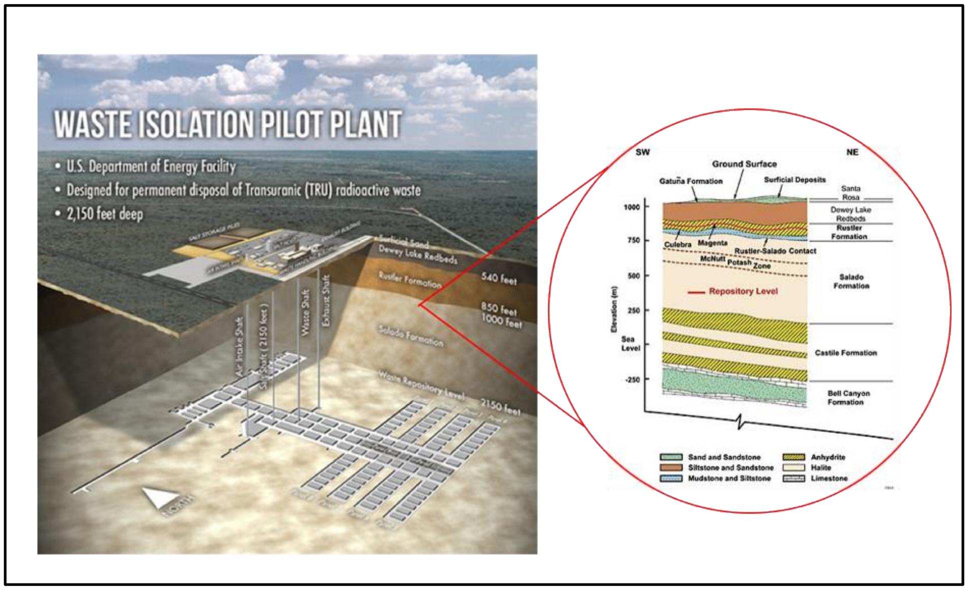

Figure 100. A rendered layout of the Waste Isolation Pilot Plant, near Carlsbad New Mexico.

The fate and transport of actinides in the subsurface poses health and environmental concern due to high radiotoxicity and long half-life. For example, actinides such as plutonium 239 (^{239}Pu) and neptunium 237 (^{237}Np) are important in performance assessment calculations for long-term stewardship of nuclear waste repositories because of their relatively long half-life ($t_{1/2}$ for ^{239}Pu = 2.4 x 10^4 and ^{237}Np = 2.14 x 10^6 years), radiotoxicity and redox chemistry (Reed and Altmaier, 2013). Moreover, under the reducing conditions expected in a deep geologic repository, Pu(IV) and Np(III) are the predominant valent states expected for plutonium and neptunium. Because the migration of actinides in the subsurface environment is largely controlled by interaction at the solid-water interface with environmental media (soil, sediment, water) a better understanding of key processes driving sorption processes can lead to a more accurate prediction of actinide mobility and development of robust transport models. Specifically, the Waste Isolation Pilot Plant (WIPP) located near Carlsbad in New Mexico is a deep underground geologic repository used for disposal of legacy transuranic (TRU) radioactive wastes. Characterized by high ionic strength pore-waters (~ 7.4 M) the WIPP resides deep (~655 m) in the bedded salts of the Permian Salado Formation that consists predominantly of interbedded halite and anhydrite layers overlying the Castile Formation (Brown et al., 1999; Brush and storz, 1996; Stein, 1985) (Figure 100). To comply with regulatory containment requirements of the U.S. Environmental Protection Agency, the U.S. Department of Energy (DOE) was required to conduct performance assessments (PAs) for a 10,000-year post-closure period. A potential release scenario envisioned in the WIPP performance assessment is groundwater intrusion through the highly transmissive Culebra Member overlying the WIPP that mobilizes nuclear wastes. In a low-probability TRU release scenario dictated by dissolved brine and radionuclide mobility, americium (Am), neptunium (Np) and plutonium (Pu) are considered the most important actinide species to be released from the WIPP environment.

The waste streams reprocessing and degradation of repository components (e.g. cellulose degradation by calcium hydroxide present in cement, steel containers) resulted in formation of significant concentrations of ligands such as citrate, EDTA, oxalate, gluconate etc. in the WIPP that can form strong complexes with metals. The iron found in the steel waste containers and lead (Pb) in the shielded containers are expected to strongly react with sulfide and compete with actinides for complexation with the organic ligands present in the WIPP brines. Along with low-probability groundwater intrusion, the presence of metal-chelating organic ligands, iron oxide minerals (magnetite), and intrinsic actinide colloids may provide a potential release pathway for migration of the actinides. Thus, a comprehensive understanding of the mobility of actinides and lanthanides in the presence of metal-chelating ligands in WIPP-relevant conditions is important to developing a robust risk assessment model.

Strong chelators such as EDTA and oxalate found in the WIPP enhance the solubility of actinides and this complexation effect has been accounted for in current PA models. However, iron, lead, sulfide species and ligands such as gluconate, a cement additive, expected in the hyperalkaline conditions of cementitious WIPP repository, have not been considered in the PA models (Brady et al., 1999; Brush and storz, 1996).

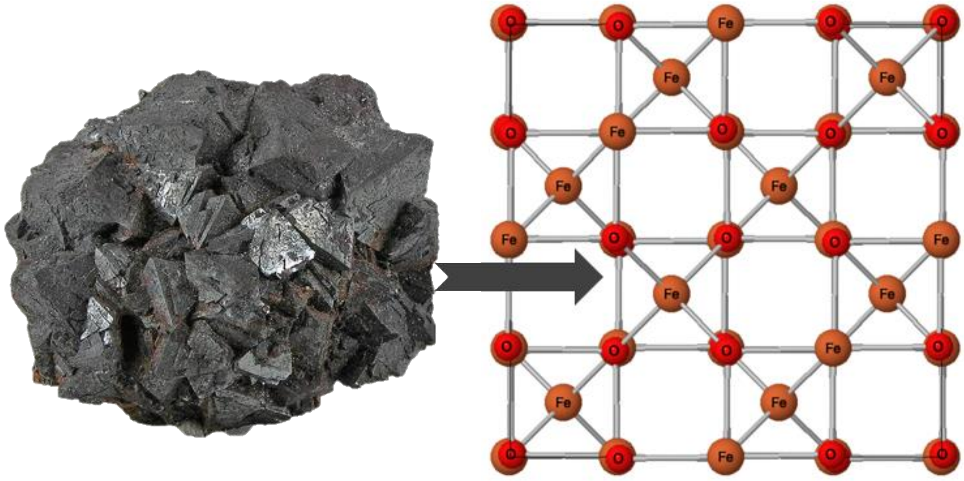

Figure 101. Magnetite mineral about 5cm wide (left) and its crystal structure (right), courtesy of mindat.org.

Thorium (Th) sorption onto natural clays, sandstone, and volcanic rocks has been shown to decrease in the presence of organic compounds (Baston et al., 1992). Previous studies have demonstrated the ability of actinides to form complexes with gluconate in a wide range of pH (Baston et al., 1992; Sawyer, 1964; Tits et al., 2005). In alkaline conditions, Th solubility increased in cement pore-waters (pH = 12) in the presence of gluconate (E. Colàs et al., 2011; Elisenda Colàs et al., 2013). In the alkaline pH range and absence of Ca, the An(IV)(OH)x(L)y species is expected to dominate the systems containing Th(IV), U(IV), Np(IV), and Pu(IV), where L is gluconate or ISA (Gaona et al., 2008). However, sorption of actinides onto WIPP-relevant iron minerals (e.g.

corrosion product, magnetite, Figure 101) and in WIPP-relevant conditions has not been well studied.

Subtask 5.2: Objectives

The key objective of this study is to elucidate the impact of gluconate and iron oxide minerals (magnetite) on actinide behavior under anaerobic conditions and high ionic strength environment expected within the WIPP repository. To accomplish this: 1) batch sorption studies were used to examine the impact of ionic strengths and gluconic acid on the sorption of actinides onto magnetite using uranium (U[VI]), neodymium (Nd[III]), and thorium (Th[IV]) as stable chemical analogs for americium/curium and plutonium; 2) experiments conducted in varying ionic strength solutions (0.1 – 5.0 *M*) and different brine types were used to assess the impact of solution chemistry and the nature of brine solutions on actinide migration; 3) two size separation steps (settling and centrifugation) were used to evaluate the formation of intrinsic actinide colloids; and 4) key variables controlling the sorption of actinides onto magnetite in the presence and absence of gluconic acid were determined. Study results will provide important parameters to update current performance assessment models.

Subtask 5.2: Methodology

Materials

Magnetite nanoparticles (97%, Iron[II,III] oxide, Fe_3O_4) were procured from Alfa Aesar (Ward Hill, MA). The magnetite (Alfa Aesar) used in these studies had a reported particle size of 44 µm and iron contents of 20% ±0.6% for Fe^{2+} and 46% ±4% for Fe^{3+}, respectively (Lagos et al., 2018). All chemicals were ACS reagent grade or better in purity and used as received. Sodium gluconate (TCI America, Portland, OR), sodium chloride, sodium bromide, sodium sulfate, potassium chloride, magnesium chloride (Fisher Scientific, Pittsburg, PA), calcium chloride, sodium bromide (Acros Organics, Geel, Belgium), sodium tetraborate (MPI Biomedicals, Santa Ana, CA) and ultrapure deionized water (>18 MΩ) were used to prepare the brines. Additionally, along with U(VI), Nd(III) and Th(IV) were used as stable analogues for Am(III) and Pu(IV), respectively, to represent the most common oxidation states of tri- and tetravalent actinides in the WIPP environment. All contaminant spikes were from stock standard solutions made in 2% nitric acid (HNO_3) from High-Purity Standards (Charleston, SC). The stock solution was stored at 4ºC and diluted to the desired final concentration for each experiment using deionized water, which was degassed with high-purity nitrogen.

The evaluated brines were spiked with a known actinide (contaminant) concentration and the pH was adjusted with either HCl/NaOH (0.1 or 1.0 *M*) to a pH value of 8 ±0.5. During the duration of the batch study, the pHs of the spiked samples were not adjusted; however, the pH (pH_R) was recorded for each sampling period using an Orion 9110DJWP electrode (Thermo Scientific). The pH_R values were subsequently converted to pcH values by the equation below (Wall et al., 2002):

$$pcH = pH_R + (0.255 \cdot m_{brine}) \qquad Eq. 1$$

where m_{brine} is the brine molality (mol/kg).

All experiments were conducted in 50 mL polypropylene centrifuge tubes (Corning CentriStar). Contaminant concentrations in experimental samples were analyzed using a Thermo Fisher

Scientific iCAP RQ inductively coupled plasma mass spectrometer (ICP-MS) with estimated quantification limits (EQL) of 1.89 ng/L, 1.12 ng/L, and 1.27 ng/L for Nd, Th and U, respectively.

Adsorption Experiments

Batch sorption experiments were used to investigate the impact of ionic strength (0.1 – 5.0 *M*) and gluconate on the sorption of Nd(III), Th(IV), and U(VI) onto magnetite in brine solutions of NaCl, $MgCl_2$ and $CaCl_2$. Experiments were conducted under a nitrogen-rich atmosphere to simulate anoxic conditions (i.e. 98% N_2: 2% H_2) expected in the WIPP environment and to prevent interaction with atmospheric CO_2. Experiments were performed in triplicates with sampling time intervals of 15 min, 60 min, 180 min, 24 h, 48 h and 7 days in the presence and absence of gluconate. Additionally, contaminant concentrations ($[M]_{initial}$ = 10 µg/L, where M = Nd, Th, U) representative of the undersaturation limit were used to spike the brines. Batch samples were not filtered because previous studies reported losses of contaminants (especially Nd) to various filter materials (e.g. paper, cellulose ester, and PTFE filters). Hence, two separation methods−settling (15 minutes) and centrifugation (20 minutes, 8000 rpm−were employed to assess the potential for colloid formation. The expected particle sizes remaining in solution after separation are estimated as follows: <6 x10^6 nm for settling and <80 nm for centrifugation, respectively. All samples were prepared in 2% HNO_3 and analyzed by ICP-MS for Nd, Th, and U.

Subtask 5.2: Results and Discussion

To better understand the impact of gluconate on adsorption behavior of U, Th and Nd onto magnetite, the conditional solid-water partitioning coefficient (K_{dc}; mL/g) was calculated according to the equations below (Eq. 2 – 3) as the ratio of solid phase concentration to dissolved concentration:

$$\boldsymbol{K_{dc}(L\,kg^{-1}) = \frac{[M]_{sld}}{[M]_{aq}}} \qquad \boldsymbol{Eq. 2}$$

$$\boldsymbol{[M]_{sld} = \frac{V_L\left([M]_{aq(0)} - [M]_{aq(t)}\right)}{[W]_{sld}}} \qquad \boldsymbol{Eq. 3}$$

Where$\boldsymbol{[M]_{sld}}$ is the amount of contaminants adsorbed onto solid phase(s) (µg/kg); $\boldsymbol{[M]_{aq(o)}}$ and $\boldsymbol{[M]_{aq(t)}}$ (µg/L) are the initial and final aqueous Nd, Th, U concentration after time (t); $\boldsymbol{V_L}$ is the volume of aqueous solution (L) and $\boldsymbol{[W]_{sld}}$ is the added mass of solid phase (kg).

Sorption in NaCl

Presented in Figure 102 are the results of batch sorption experiments investigating the impact of gluconate and two filtration methods−settling and centrifugation−over a 7-day period on sorption of 10 µg/L of Nd(III), Th(IV), and U(VI) onto magnetite in 0.1 to 5.0 M NaCl solutions.

The conditional solid-water partitioning coefficient (K_{dc}) values increased over time, approaching equilibrium at 1440 min, after which it achieved a steady state over the remaining time interval. This is in agreement with previous studies that reported 24 h to be adequate for achieving equilibrium of sorption processes to preclude significant formation of coprecipitation (Emerson et al., 2018). The batch sorption data showed that irrespective of the separation methods the removal of U and Th from NaCl solutions increased over a 7-day time period, while that of Nd was highly variable over the same time period. With increase in ionic strength from 0.1 to 5.0 M, the sorption of actinide onto batch samples decreased likely due to strong competition from copious ions for sorption sites on magnetite (Figure 102). Overall, the adsorption of U, Th, Nd onto batch samples exhibited the following trends: 0.1 M NaCl ≅ 1.0 M NaCl > 5.0 M NaCl. Irrespective of separation method, the amount of Th removed from the 0.1 – 5.0 M NaCl solutions was one to two orders of magnitude higher than that for U and Nd. The sorption trends observed for the gluconate-amended NaCl solutions were analogues to that for the gluconate-free NaCl solutions. The addition of gluconate did not enhance the solubility of U, Th, Nd as there were no differences in aqueous concentration of U, Th, Nd between unamended and gluconate-amended batch samples (Figure 102).

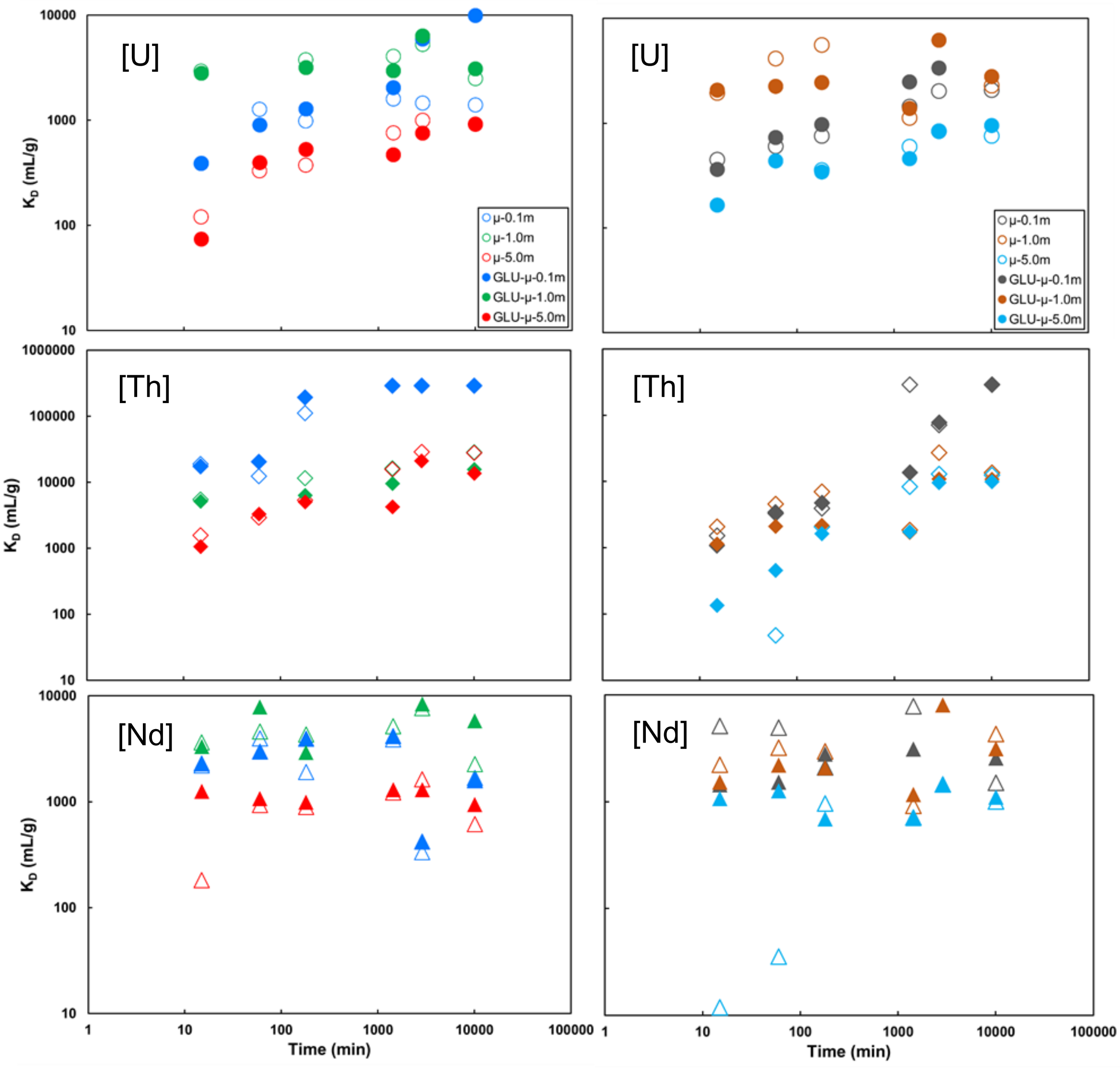

Figure 102. The K_{dc} values over time for sorption of U, Th, Nd (10 μg/L) onto magnetite suspensions (1 g/L) in filtered (right) and unfiltered (left) 0.1 - 5.0 M NaCl solutions. Filled symbols are gluconate-amended and unfilled symbols are gluconate-free samples. Error bars are based on sample triplicate; x and y axes are displayed in log scale for clarity.

$MgCl_2$ Impact on Sorption

Presented in Figure 103 are the results of batch sorption studies in magnetite-amended $MgCl_2$ solutions ($\mu = 0.3 - 15\ m$) as a function of gluconate and two filtration methods−settling and centrifugation. The conditional solid-water partitioning coefficient (K_{dc}) values for the $MgCl_2$ brines trended upward over time, approaching a steady state after a 1440-min time interval. This is in good agreement with observed decreasing trends in aqueous concentration of U, Th and Nd in the studied brine (data not shown). The batch sorption data showed that irrespective of the separation methods, the removal of U and Th from $MgCl_2$ solutions increased over a 7-day time period, while that of Nd varied over the same time period. Similar K_{dc} values were observed for U, Th and Nd in the filtered samples and unfiltered samples (Figure 103). Observed K_{dc} values for Th were higher than those for U and Nd. The decrease in actinide sorption onto batch samples as solution ionic strength increased from 0.1 to 5.0 M is indicative of an increased occupancy of sorption sites on magnetite by copious ions (Figure 103). The adsorption of U, Th, Nd onto batch samples was ranked as follows: 0.1 M $MgCl_2$ > 1.0 M $MgCl_2 \cong$ 5.0 M $MgCl_2$. Irrespective of separation method, the amount of Th removed from the 0.1 – 5.0 M NaCl solutions was one to two orders of magnitude larger than those for U and Nd. Overall, addition of gluconate does not enhance actinide solubility as there was no discernable difference in aqueous U, Th, Nd concentration between gluconate-amended samples and gluconate-free samples. Furthermore, filtration via centrifugation insignificantly impacted sorption of actinides onto magnetite as filtered samples do not significantly differ from unfiltered samples. Sorption trends observed for the gluconate-free brines were similar to that for the gluconate-amended brine (Figure 103).

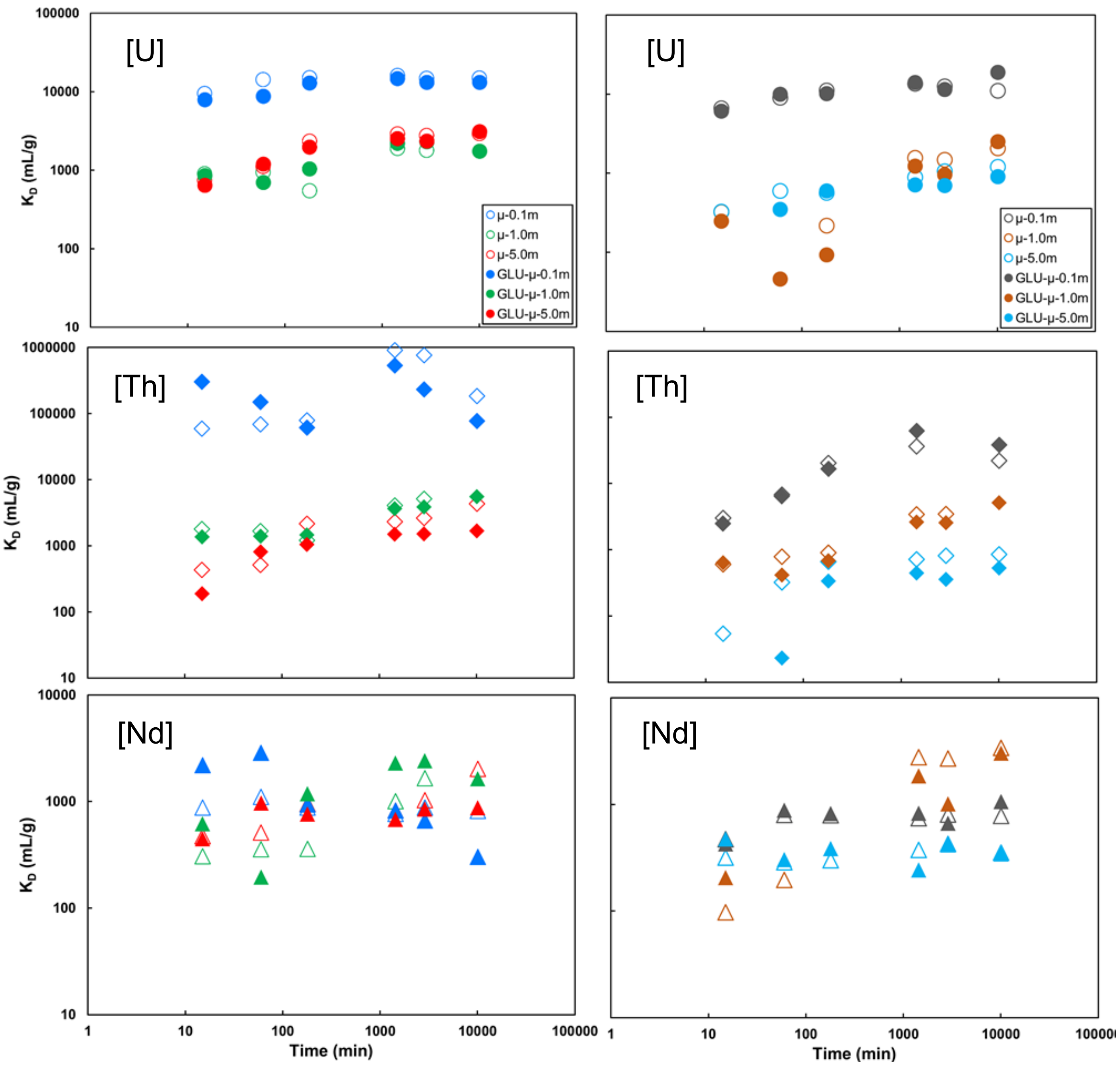

Figure 103. The K_{dc} values for sorption of U, Th, Nd (10 µg/L) onto magnetite suspensions (1 g/L) in filtered (right) and unfiltered (left) 0.1 - 5.0 M $MgCl_2$ solutions. Filled symbols are gluconate-amended and unfilled symbols are gluconate-free samples. Error bars are based on sample triplicates; x and y axes are displayed in log scale for clarity.

$CaCl_2$ Control on Sorption

The impact of gluconate and filtration methods on sorption of actinide onto magnetite-amended $CaCl_2$ solutions ($\mu = 0.3 – 15\ m$) are displayed in Figure 104. The K_{dc} values for the $CaCl_2$ brines increased over time and gradually approached equilibrium at the 1440-min time interval. This increasing trend is in good agreement with observed decreasing aqueous concentration of U, Th and Nd in the studied brine. The batch sorption data showed that the removal of U and Th from $CaCl_2$ solutions increased over the 7-day time period, while that of Nd varied significantly over time. Similar K_{dc} values were observed for actinide in the filtered samples and unfiltered samples. Calculated K_{dc} values for U, Th and Nd in the filtered and unfiltered samples were similar in magnitude. Thorium sorption onto batch samples decreased with increasing ionic strength, whereas that of U and Nd were variable (Figure 104). The sorption of actinide onto batch samples exhibited the following trends: 0.1 M $CaCl_2$ ≅ 5.0 M $CaCl_2$ > 1.0 M $CaCl_2$ for U and Nd and 0.1 M $CaCl_2$ ≅ 1.0 M $CaCl_2$ > 5.0 M $CaCl_2$ for Th (Figure 104). Overall, amendment with gluconate does not enhance actinide solubility as there was no discernable difference in aqueous U, Th, Nd concentration between gluconate-amended samples and gluconate-free samples. Furthermore, filtration via centrifugation had little impact on the sorption of actinides onto magnetite as filtered samples do not significantly differ from unfiltered samples. Sorption trends observed for the gluconate-free brines were similar to that for the gluconate-amended brines (Figure 104).

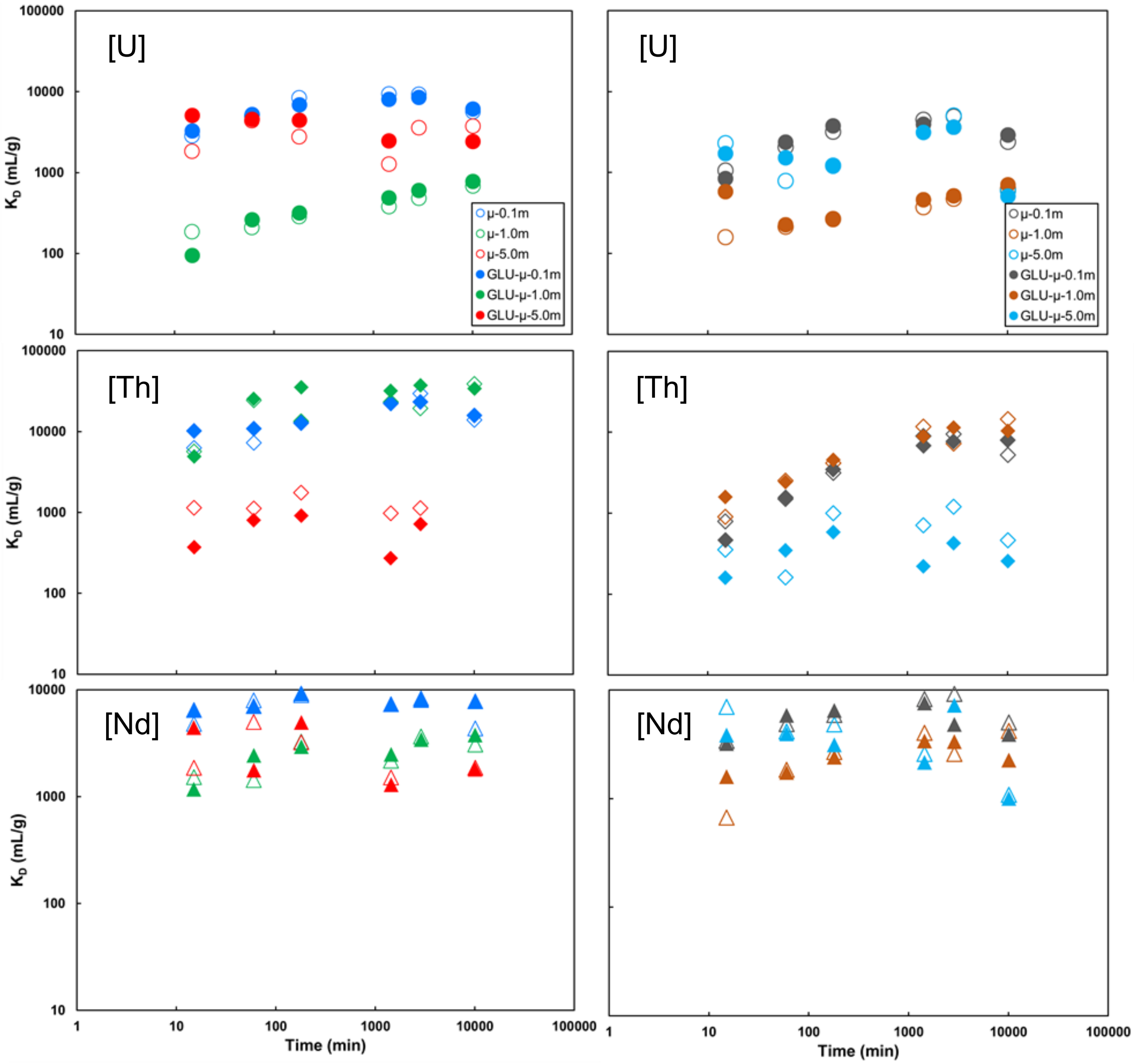

Figure 104. Progression of K_{dc} values over time for sorption of U, Th, Nd (10 µg/L) onto magnetite suspensions (1 g/L) in filtered (right) and unfiltered (left) 0.1 - 5.0 M $CaCl_2$ solutions. Filled symbols are gluconate-amended samples and unfilled symbols are gluconate-free samples. Error bars are based on sample triplicate; x and y axes are displayed in log scale for clarity.

Subtask 5.2: Conclusions

Filtration via centrifugation and amendment with gluconate of three types of brines have little impact on the adsorption of contaminants onto magnetite under the anaerobic condition employed in this study. The observed sorption trends for the gluconate-free brines were similar to that for gluconate-amended brines. Moreover, the addition of gluconate did not enhance the solubility of U, Th, Nd as there were no discernable differences in aqueous concentration of U, Th, Nd among evaluated batch samples, suggesting insignificant formation of tertiary gluconate complex with contaminants. Higher ionic-strength brines tended to increase overall solubility of the studied contaminants in the following order: $NaCl \cong MgCl_2 < CaCl_2$. Study results indicate that the contaminant concentrations employed in these batch studies did not result in formation of the tertiary gluconate complex under the predicted pH range of this study.

Subtask 5.2: References

Reed, D. T.; Altmaier, M. In Proceedings of the Third International Workshop on Actinide and Brine Chemistry in a Salt-Based Repository (ABC-Salt III), Santa Fe, New Mexico, Reed, D. T.; Altmaier, M., Eds. Los Alamo National Laboratory: Santa Fe, New Mexico, 2013; p 145.

Stein, C. L. Mineralogy in the Waste Isolation Pilot Plant (WIPP) facility stratigraphic horizon; SAND-85-0321; Other: ON: DE86000571 United States 10.2172/5203761 Other: ON: DE86000571 NTIS, PC A03/MF A01. SNL English; Sandia National Labs., Albuquerque, NM (USA): 1985; p Medium: ED.

Brush, L. H.; storz, L. J. Revised Ranges and Probability Distributions of Kds for Dissolved Pu, Am, U, Th, and Np in the Culebra for the PA Calculations to Support the WIPP CCA; Albuquerque, New Mexico, 1996.

Brown, G. O.; Lucero, D. A.; Perkins, W. G. Column Experiments for Radionuclide Adsorption Studies of the Culebra Dolomite: Retardation Parameter Estimation for Non-Eluted Actinide Species; SAND98-1005; Other: ON: DE00002672 United States 10.2172/2672 Other: ON: DE00002672 SNL English; Sandia National Laboratories, Albuquerque, NM, and Livermore, CA: 1999.

Brady, P. V.; Papenguth, H. W.; Kelly, J. W., Metal sorption to dolomite surfaces. Appl Geochem 1999, 14 (5), 569-579.

Baston, G. M. N.; Berry, J. A.; Bond, K. A.; Brownsword, M.; Linklater, C. M., Effects of Organic Degradation Products on the Sorption of Actinides. Radiochim Acta 1992, 58-9 (2), 349-356.

Sawyer, D. T., Metal-Gluconate Complexes. Chemical Reviews 1964, 64 (6), 633-643.

Tits, J.; Wieland, E.; Bradbury, M. H., The effect of isosaccharinic acid and gluconic acid on the retention of Eu(III), Am(III) and Th(IV) by calcite. Appl Geochem 2005, 20 (11), 2082-2096.

Colàs, E.; Grivé, M.; Rojo, I.; Duro, L., Solubility of ThO2·xH2O(am) in the presence of gluconate. Radiochim Acta 2011, 99 (5), 269-273.

Colàs, E.; Grivé, M.; Rojo, I.; Duro, L., The Effect of Gluconate and EDTA on Thorium Solubility Under Simulated Cement Porewater Conditions. Journal of Solution Chemistry 2013, 42 (8), 1680-1690.

Gaona, X.; Montoya, V.; Colas, E.; Grive, M.; Duro, L., Review of the complexation of tetravalent actinides by ISA and gluconate under alkaline to hyperalkaline conditions. J Contam Hydrol 2008, 102 (3-4), 217-27.

Lagos, L. E.; Katsenovich, Y.; Gudavalli, R.; Lawrence, A.; Mahmoudi, M. Environmental remediation science and technology - Year-end technical report; Applied Research Center, Florida International University: Miami, Florida, 2018.

Wall, N. A.; Borkowski, M.; Chen, J.; Choppin, G. R., Complexation of americium with humic, fulvic and citric acids at high ionic strength. Radiochim Acta 2002, 90 (9-11), 563-568.

Sockwell, K. A.; Zengotita, F.; Vento, A.; Swanson, J. S.; Reed, D. T.; Katsenovich, Y.; Emerson, H. P., The impact of ethylenediaminetetraacetic acid (EDTA) on the sorption of Nd(III), Th(IV), and U(VI) onto dolomite in WIPP-relevant brines, GWB and ERDA-6. In Waste Management, Phoenix, Arizona, 2020.

Emerson, H. P.; Zengotita, F.; Richmann, M.; Katsenovich, Y.; Reed, D. T.; Dittrich, T. M., Retention of neodymium by dolomite at variable ionic strength as probed by batch and column experiments. Journal of Environmental Radioactivity 2018, 190-191, 89-96.

TASK 6: HYDROLOGY MODELING FOR WIPP

This task was developed to support research and development activities at the Waste Isolation Pilot Plant (WIPP), the nation's only deep geologic waste repository in operation which isolates transuranic waste 2,150 feet underground within the Salado Salt Formation. Scientists and researchers are concerned about the long-term vulnerability of this karst region and thus the eventual integrity and performance of the WIPP due to the influence of characteristic surface features, such as sinkholes, swallets, and karst valleys on groundwater recharge over time. The Magenta and Culebra dolomites of the Rustler Formation which lies above the Salado Formation, are of primary concern as they extend over the WIPP. There is a need, therefore, to improve the current understanding of the regional water balance, particularly the relation between the Culebra recharge and the intense, episodic precipitation events typical of the North American monsoon. This relationship is essential for understanding the rate of propagation of the shallow dissolution front, and the impact of land-use changes around the WIPP facility on water levels and chemistry in compliance-monitoring wells. FIU has thus proposed to conduct a study in an area just west of the WIPP that has been included in the site performance assessment (PA) models known as the Nash Draw, which is an enclosed basin made up of thirty internally drained sub-basins identified from topography and field surveys. Nash Draw developed through solution and erosion of upper Permian rocks creating an array of surface features, including sinkholes, swallets, and karst valleys, and thus serves as an ideal area for this study with similar topography and representative surface hydrological features as that which overlies the WIPP. Task 6 therefore involves the development of a high-resolution digital elevation model (DEM) of Basin 6 of the Nash Draw to more accurately delineate significant surface hydrological features, as well as the development of hydrological models using the DOE-developed Advanced Simulation Capability for Environmental Remediation (ASCEM) modeling toolset. A high-resolution DEM will improve the ability of the coupled surface/subsurface flow models to simulate the hydrologic response to a range of storm events, compute the surface water balance and provide more accurate estimates of regional-scale infiltration rates/groundwater recharge. With improved estimates of the spatial and temporal patterns of recharge to force the groundwater model, predictions of halite dissolution and propagation of the shallow dissolution front will be made possible and the potential impact on repository performance quantified.

Subtask 6.1: Digital Elevation Model and Hydrologic Network

Subtask 6.1: Introduction

To study the impact of characteristic surface hydrological features on the groundwater recharge in Basin 6, in conjunction with soil properties and vegetation types, requires a revision of the current site conceptual model to couple surface water and groundwater processes, which both require a high-resolution digital elevation model (DEM) that includes channels and sink holes to account for surface water routing and return flow. This subtask therefore involves the development of a high-resolution DEM for more accurate delineation of these surface hydrological features that can influence regional groundwater recharge. A high-resolution DEM will improve the ability of the coupled surface/subsurface flow models to simulate the hydrologic response to a range of storm events, compute the surface water balance and provide more accurate estimates of regional-scale infiltration rates/groundwater recharge.

Subtask 6.1: Objectives

The objective of this subtask is to develop a high-resolution DEM of Basin 6 of the Nash Draw near the WIPP using UAV-based photogrammetry to support the development of regional surface and groundwater models by providing a more accurate ground surface representation for mesh generation, as well as a more detailed delineation of significant topographical and hydrological surface features that impact groundwater recharge. The aim is to develop the data layers for the terrestrial overland flow, channel routing, and subsurface flow processes of the regional flow models. Due to the karstic topography, local hydrologic features, such as sinkholes and brine lakes, play an essential role in the surface/subsurface water exchange in the WIPP and Nash Draw regions. As these geomorphological features are present at a very small scale (meters), a need for a high-resolution hydrological model is anticipated to accurately represent hydrological flow variability across small-scales.

Subtask 6.1: Methodology

FIU conducted a pilot study in 2020 to determine an efficient methodology for development of a high-resolution (1-m) DEM by means of a photogrammetric approach using unmanned aerial vehicles (UAVs). Aerial imagery of a small 5 km^2 area in Basin 6 of the Nash Draw, just west of the WIPP, was collected and the images were processed using photogrammetric techniques to build a high-resolution point cloud, which was then post-processed for vegetation removal, revealing the true ground surface. FIU's focus in 2021 has been on refining the vegetation removal methods and expanding the data collection to the entire Basin 6 study area.

DEM Development & Refinement

During FIU Year 1, FIU continued to work on refining the methodology for high-resolution DEM development using imagery collected in January 2020 during a pilot study in Basin 6 of the Nash Draw in New Mexico. The data was collected by means of unmanned aerial vehicle (UAV)-based photogrammetry. FIU graduate and undergraduate students (DOE Fellows) were trained on the use of photogrammetric software and techniques and drone operation to execute the required procedures. FIU applied the photogrammetry workflow (Figure 105) established in the previous performance year and processed the data for a 5 km^2 area within Basin 6 to produce a 3D point cloud.

Figure 105. Photogrammetry workflow to produce bare ground DEMs from a point cloud of the study area using RGB-based vegetation indices and machine learning technology.

The following is a brief outline of the documented photogrammetry process workflow which included field data collection, image processing and point cloud generation, DSM development and finally, an evaluation of various RGB-based vegetation removal methods to generate the best bare-ground high-resolution DEM:

1. Digital images taken in Basin 6 during a trip to Carlsbad, NM were imported into the photogrammetry software Pix4D, which is able to automatically georeference the images based on geotags embedded in images and generate an unclassified 3D point cloud.
2. Image preparation and initial analysis with Pix4D was then initiated. All of the drone images that were taken were filtered to select favorable images within duplicated areas.

This reduced the number of images from 7,407 to 5,242 and removed unsatisfactory images as well, i.e., images captured with a low light angle.

3. The coordinates of the ground control points (GCPs) were input into Pix4D, with 15 out of 87 of them serving as checkpoints (CPs) for error evaluation.
4. Two georeferencing workflows recommended by Pix4D were tested:
    a. Method A – depends on known coordinates of images and the GCPs. It allows the user to directly mark the GCPs on the images.
    b. Method B – can use images without a geotag. A fraction of the GCPs is used to match the images located in an arbitrary coordinate system with the GCPs in a known coordinate system. The rest of the GCPs are then be added during the georeferencing process, similar to Method A.

    Due to drifting of the vertical coordinates in the image geotags, the distance between the GCPs and images was deemed too far to be matched by Pix4D. Therefore, Method A could not be directly applied on the dataset even though the images had known coordinates. As a workaround, the average distance between the GCPs and images was evaluated, and an offset of GCP coordinates (-100 m) was used to bring them closer so they could be matched. After offsetting the GCPs, Pix4D successfully established matches between the GCPs and images.
5. Next, the following procedure was done using Pix4D to mark the GCPs:
    a. The rayCloud was opened by going to View > rayCloud
    b. On the left sidebar that appears under the section Layers, Tie Points was clicked followed by GCPs/ MTPs. The coordinates of 87 measured locations in the field were input from the .csv file and 14 of them were used as check points (CPs) to calculate the georeferencing accuracy.
    c. Each GCP/CP was selected from the GCPs/MTPs section one-by-one, and for each GCP/CP, a sidebar appeared on the right listing its Properties and the images in which it was visible.
    d. For each image, a blue circle shows the location of the GCP/CP estimated automatically by Pix4D. The estimated GCP/CP location is typically different from the exact location of the GCP/CP spray-marked on the ground, illustrating the error of automatic 3D reconstruction that needs to be corrected by georeferencing.
    e. The exact position of each GCP/CP was found and marked with the left click on the mouse. The clicked position appears with a yellow cross and circle. The size of the circle varies depending on the zoom level at which it was clicked.
    f. Once the GCP/CP is marked on at least two images, Pix4D recalculates the location of GCP/CP on the rest of the images, indicated by a green cross mark. This assists in marking the rest of the images.
    g. In the instances that the GCP/CP was not found in the image, the GCP name and image file was recorded onto a spreadsheet in order to further analyze the image with other programs such as Adobe Photoshop.

6. Next, a 2D digital orthomosaic and a 3D digital surface model (DSM) were created in Pix4D.
7. For the vegetation removal process, only part 14 of the point cloud was used.
8. A shapefile of a small area within part14 that was created using ArcGIS Pro was inputted into Pix4D and a reflectance map was created with six vegetation indices that were inputted manually. The resulting files were stored within Pix4D's default file folders.
9. Each VI map created was imported into ArcGIS Pro and visually inspected. For each map, up to six classes were visualized out of a total of 12 classes to determine how aggressive or conservative the index was in distinguishing vegetation.
10. Each VI map was converted into a local scene where the point cloud could be viewed in 3D and from this view, a number of threshold values were chosen, and elevation profiles created for each threshold value in order to distinguish them more easily.
11. The selected threshold value was inputted into the Python script for each VI, which separated the 3D point cloud into a vegetation only point cloud and a bare ground only point cloud.
12. The bare ground-only point cloud was then imported back into ArcGIS Pro as a LAS file and converted into a DEM.
13. Following this, cross-sections were drawn on the original DEM as well as on the filtered DEMs and an elevation profile graph was generated with all the VIs in ArcGIS Pro using the Stack Profile toolbox.
14. From the elevation profile graph, the differences in the resultant DEMs can be evaluated to select an optimal VI and threshold value.
15. The second method used ArcGIS Pro's own 3D point cloud classification. The unclassified 3D point cloud was imported into ArcGIS Pro and the point cloud was classified. The bare-ground point cloud was then converted from a LAS file to a DEM using the conservative method.

Sinkhole Detection

The generated DEM of Basin 6 will be used to delineate and extract sink holes and other topographical features of interest using ArcGIS geoprocessing tools. These extracted features will be converted to GIS shapefiles and incorporated during the mesh generation stage of development of the Amanzi-ATS model. This year FIU began testing various sinkhole detection and extraction methods that were derived from an in-depth literature search. The shapefile generated from each method employed was then compared to a GIS shapefile created by Andrea Goodbar, an Environmental Scientist at the New Mexico Environment Department, based on a ground survey of Basin 6.

UAV Field Survey of Basin 6

After completing the pilot study to extablish an efficient photogrammetry workflow for developing the Basin 6 DEM, FIU initiated plans to extend the coverage area beyond the 5 km^2 pilot study area to the complete Basin 6 area (~24 km^2). In preparation for this expanded field survey, the FIU research team of staff and students (DOE Fellows) began training on the operation of unmanned aerial vehicles in an empty parking lot of the FIU Engineering Center. A demonstration of the DJI Phantom 4 RTK drone was given by one of ARC's postdoctoral associates and instructions were provided on the creation of a flight plan, how to set up the drone for takeoff and how to collect images, amongst other topics. Drone testing was carried out in accordance with FAA Unmanned Aircraft Systems (UAS) regulations.

Figure 106. Drone Demonstration at the Applied Research Center.

In addition, an online video was reviewed which provided further instructions on the drone operation: (https://www.youtube.com/watch?v=go03aFUPqrM&ab_channel=AerialMediaPros).

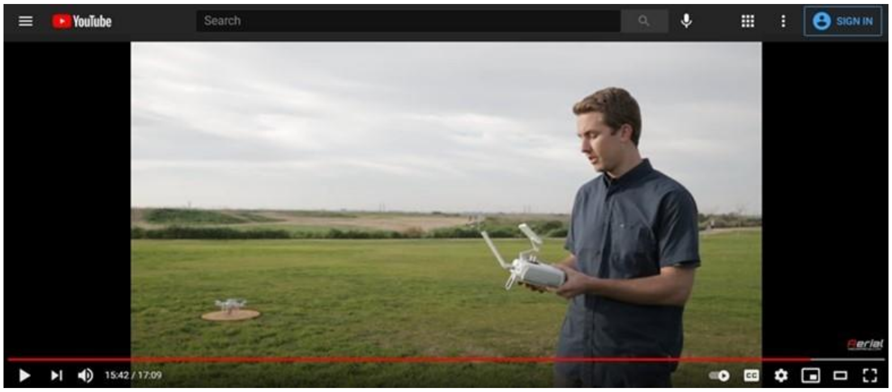

Figure 107. Screenshot of online video instruction of the DJI Phantom 4 RTK drone operation.

The research team then tested the drone during another flight session where a sample flight plan was created using the controller and over 40 images were taken of the parking lot at an altitude of 80 ft and a velocity of 6 m/s.

Figure 108. DOE Fellow, Gisselle Gutierrez-Zuniga, during the DJI Phantom 4 RTK flight session.

The images taken were then downloaded and pre-processed using the photogrammetric software program Pix4D. The image post-processing methodology was demonstrated to other members of the hydrological modeling team by the DOE Fellow who previously visited the study site and had experience processing the data. An introduction was given to Pix4Dmapper, where it was demonstrated how to import and georeference the drone images, generate a 3D point cloud, orthomosaic, reflectance map, and digital surface model (DSM). Additionally, the training covered the procedure for visualizing the results created by Pix4D, such as the DSM, using ArcGIS. Below are the processed images and resultant DEM derived from this exercise.

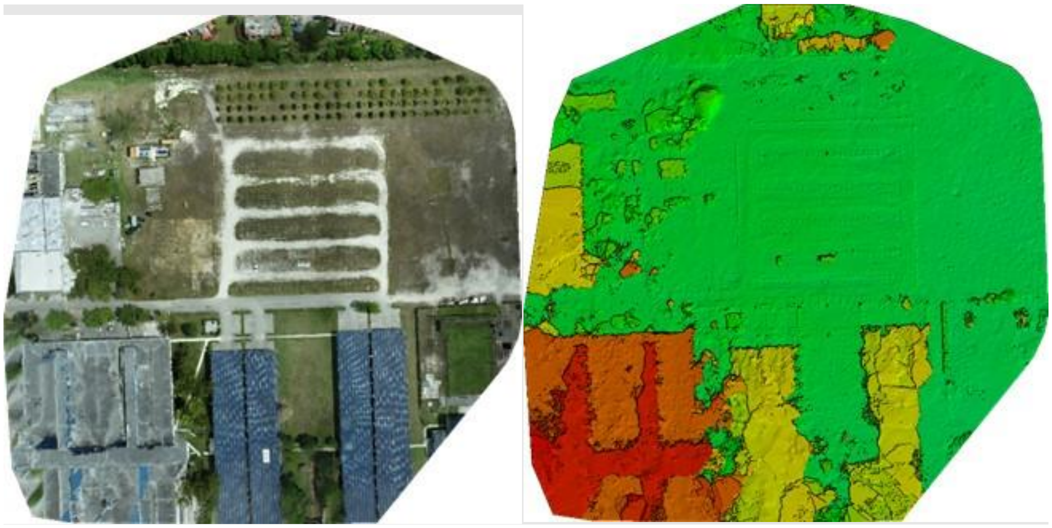

Figure 109. Orthomosaic (left) and corresponding sparse digital surface model (DSM) before densification of the test area around FIU's Engineering Center.

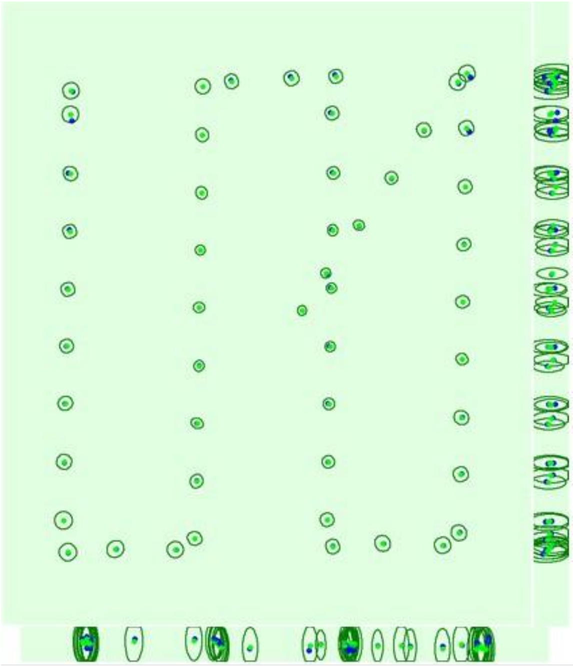

Figure 110. Offset between initial (blue dots) and computed (green dots) image positions as well as the offset between the GCPs initial positions (blue crosses) and their computed positions (green crosses) in the top-view(XY plane), front-view (XZ plane), and side-view (YZ plane). Dark green ellipses indicate the absolute position uncertainty of the bundle block adjustment result.

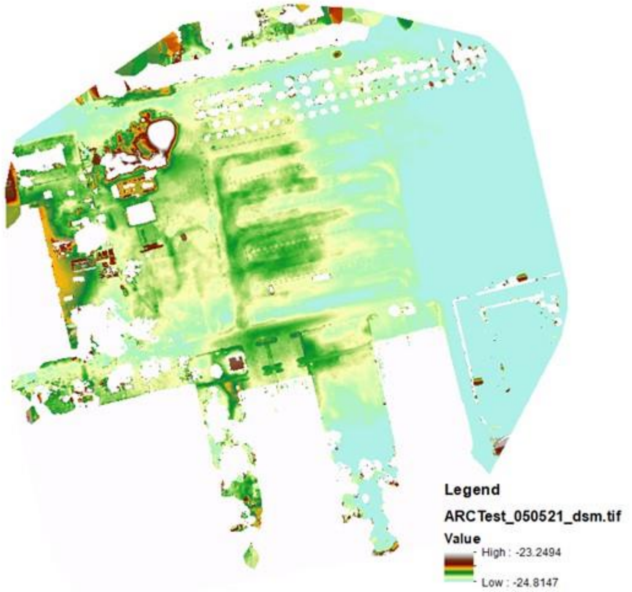

Figure 111. DEM of resolution of 2.6 cm generated by Pix4D after densification.

In July, FIU prepared the flight plan for a UAV-based aerial survey of Basin 6 of the Nash Draw just west of the WIPP in Carlsbad, NM which was scheduled for August 2021. The images captured during this trip will be used to generate a high-resolution DEM which will be used as input to the ATS-Amanzi model. The Basin 6 study area to be surveyed encompasses approximately 24 km^2 and was considered for this study as it contains many of the topographical, hydrological and geological features characteristic of the region surrounding the WIPP. The aim was to cover approximately 5 km^2 every day for five days. The 5 km^2 plots were outlined on Google Earth Pro for the purpose of easily exporting kmz/kml files that can be imported into the DJI Phantom 4 RTK drone. Based on lessons learned during a previous trip, the following conditions/parameters were also taken into consideration:

- Ground control points (GCPs) should be marked at every takeoff for accurate georeferencing.
- Recommended flying hours are from 10 AM-2 PM to reduce the impact of shadows in the images.

The following outlines the operating procedure developed for the Basin 6 survey:

1. ***Site Map & Drone Mission***

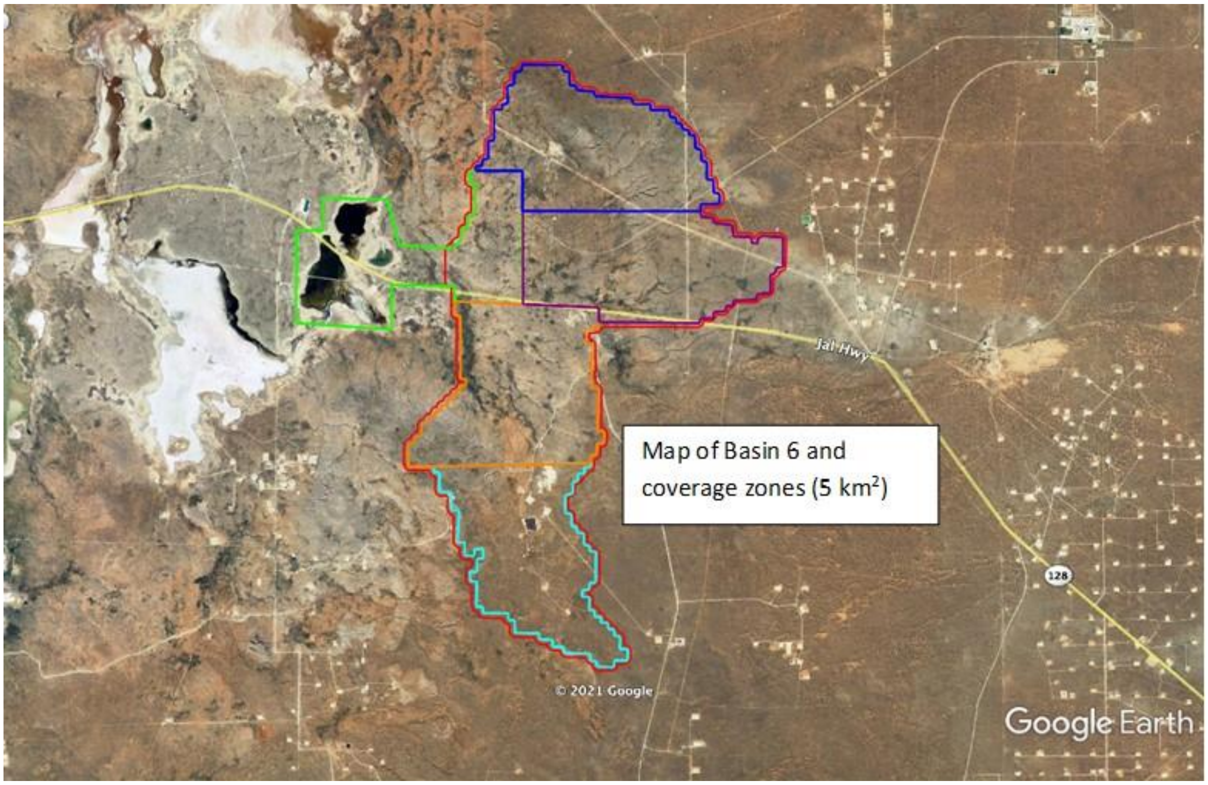

2. ***Personal Protective Equipment***
   - Hard hat
   - Visibility vest
   - Puncture resistant/steel-toe boots
   - Water
   - Sunscreen
3. ***Forms of Communication***
   - Mobile phones
   - Walkie Talkies

4. ***Nearby aviation facilities***
   - Cavern City Air Terminal
     - 1505 Terminal Dr., Carlsbad, NM 88220 (30 miles from WIPP site)
5. ***Emergency Contingencies and Response Plan***

In case the flight operation needs to be terminated, the Remote Pilot in Command (RPIC) and Visual Observer (VO) will have reliable phone signals with charged phones (and with portable chargers) to contact with Air Traffic Control (ATC). The cell phone signal has been tested at the site during a previous trip to Carlsbad, NM and deemed strong. The sUA will use the aircraft's take off position as the home point which is recorded by the DJI software powering on the aircraft. The sUA will be automatically sent to the home point for its landing destination which will all be controlled via controller. This home point will be located on a flat surface for the sUA to land safely.

6. ***Description of Emergency Procedures***
   - In case of an accident resulting in severe injury to a person the location and name of the closest emergency hospital is located in the following section of the aviation plan. Injured person will be transported to the nearest hospital with the help of the flight crew. All procedures address Part 107 requirements. In the case of an accident resulting in severe injury to any person or any loss of consciousness or $500+ of property damage, the RPIC will report the accident to the FAA within 10 days of the accident.
   - In the case of an accidental fire from the drone batteries, a fire extinguisher will be present at the site.
7. ***Name and location of nearest emergency facility (e.g., hospital)***
   - Carlsbad Medical Center
     - 2430 W Pierce St, Carlsbad, NM 88220
     - Phone: (575) 887-4100
     - 35 miles from site
8. ***Standard Operating Procedures***
   - Summarized drone safety procedure
     1. The target location is a remote open area in Carlsbad, New Mexico. No obstruction towers, trees, or power lines are located at the site. A preflight inspection was performed to be aware of the project's environment. Since there are no obstructions present, they will be effectively avoided by choosing a clear takeoff and landing area. A flight height of 100 ft AGL will be maintained for surveying after takeoff. Therefore, the possibility of collision with structures is minimal.
     2. A visual observer (VO) will also be assisting to ensure avoidance of any non-participating aircraft. The RPIC and the VO will have constant communication with clear phrases to signify specific events or observations in the case that there is an approaching aircraft or if the sUA is deemed too close to an approaching aircraft. All air operations will be monitored via radio

CTAF frequency 122.8 to assure situational awareness throughout the survey. If that is the case, the sUA will be manually lowered 50 ft by the RPIC and hover until the area is cleared of any risk. There will be a designated working area where the sUA will be taking off from and landing. Once the sUA is in air, the RPIC has the capability to track its altitude172 and location with the sUA's GPS and barometer sensor capability to ensure the altitude of 100 feet is maintained

3. The high-resolution live video feed transmitted from the sUA will also keep the RPIC and VO aware of surrounding obstacles and any incoming aircraft over a range of flight altitude between AGL and 100 ft AGL.
4. A combination of built-in indicator lights, attached strobe light and high contrast neon decal will be used by the VO and RPIC to improve the sUA's visibility and to maintain visual line of sight (VLOS) for at least 3 statute miles.

9. *Summarize procedure for preflight mission briefings with crew*

- Crew members are instructed to park GSA vehicles away from dry vegetation upon arrival to site.
- The flight crew will gather outside of the surveyed area where there will be a briefing of risk assessment and prevention. Crew members will obtain walkie talkies for ease of communication as well as wear suitable PPE for flight missions. The location of the emergency information will be demonstrated along with the location of the cooler with water.
- For the prioritization of flight crew member safety, areas where sUA is collecting data overhead such as pictures from RGB cameras and lidar data will be avoided.
- Flight logging and maintenance records will be maintained.

10. *Aircraft Descriptions*

- Make/Model (with image)
    - DJI Phantom 4 RTK

Small UAS Certificate of Registration

Registered Owner: **Eduardo Rojas**

Manufacturer: **DJI**

Model: **WM334R**

Serial Number: **0V2SH5JRA30041**

Registration Number: **FA3WNKY34F**

Issued: **06/29/2021** Expires: **06/29/2024**

*This Small UAS Certificate of Registration **is not an authorization to conduct flight operations** with an unmanned aircraft. Operations must be conducted in accordance with applicable FAA requirements. The operator of the aircraft is responsible for knowing and understanding what those requirements are. For more information on flying requirements, please visit the FAA website at **www.faa.gov/uas**.*

For U.S. citizens, permanent residents, and certain non-citizen U.S. corporations, this document constitutes a Certificate of Registration. For all others, this document represents a recognition of ownership.

Operators of unmanned aircraft must ensure they comply with the appropriate safety authority from the FAA and economic authority from the DOT.

- FAA Registration (include copy)
- Aircraft Description (e.g., rotary wing, hexa-copter):
    - Quad-copter
- Maximum Gross Take-Off Weight:
    - 1391 g
- Maximum Speed:
    - 31 mph (P-mode)
    - 36 mph (A-mode)
- Maximum Flight Endurance:
    - Number of batteries used for flight:
        - 1 battery
    - Number of backup batteries:
        - 12 batteries
    - Flight time for each flight:
        - Approximately 30 minutes per battery
- Propulsion: 6 m/s (automatic flight); 5 m/s (manual control)
- Maximum Wind Resistance: 10 m/s or 22 mph
- Sensors: RGB camera
- Ground Control Station:
    - Mobile phone and DJI Controller

1. *Declaration of Airworthiness*

Declaration of Conformity

Product: Phantom 4
Model Number: WM330A
Manufacturer's Name: *SZ DJI TECHNOLOGY CO., LTD.*
Manufacturer's Address: *14th floor, West Wing, Skyworth Semiconductor Design Building NO.18 Gaoxin South 4th Ave, Nanshan District, Shenzhen, Guangdong, China*

We, *SZ DJI TECHNOLOGY CO., LTD.*, declare under our sole responsibility that the above referenced product is in conformity with the applicable requirements of the following directives:

RED Directive:	2014/53/EU
EMC Directive:	2014/30/EU
Low Voltage Directive:	2014/35/EU
RoHS Recast Directive:	2011/65/EU
WEEE Directive:	2012/19/EU
REACH Regulation:	2006/1907/EC

Conformity with these directives has been assessed for this product by demonstrating compliance to the following harmonized standards and/or regulations:

Safety	EN 60950-1: 2006+ A11:2009+ A1:2010+A12:2011+A2:2013
EMC	EN 301 489-1 V2.1.1(2017-02) EN 301 489-3 V2.1.1(2017-03) EN 301 489-17 V3.1.1 (2017-02)
Radio	EN 300 328 V2.1.1 (2016-11) EN 300 440 V2.1.1 (2017-03)
Health	EN 62311:2008
RoHS	2011/65/EU
WEEE	2012/19/EU
REACH	2006/1907/EC

Software*: V01.02.06.02

*Note: Updated software will be released by manufacturer to fix bugs and improve the performance after the product placed on the market. All updated versions released by the manufacturer have been verified to be complied with the applicable regulations. All RF parameters (e.g., RF power, frequency) are not accessible to end users and cannot be changed by any third parties.

Signed for and on behalf of: *SZ DJI TECHNOLOGY CO., LTD.*
Place: Shenzhen, China Date: 2017-05-16
Name: Mingyu Wang Position: VP of R&D

CE

Signature:

1 / 1

2. Flight Crew

Remote Pilot(s) in Command (RPIC)

- Eduardo Rojas
- Gisselle Gutierrez-Zuniga

Visual Observer

- Mackenson Telusma

3. Drone Mission Hazards and Mitigation Measures

The following matrix was adapted from a similar matrix which addresses typical hazards for sUAS operations at remote LM sites in western Colorado, which have similar terrain to the Basin 6 study site.

Category	Hazard Description (if applicable)	Mitigation Measure
Stored Energy (Batteries)	Lithium ion batteries if misused, mishandled, and improperly packaged can short circuit, overheat, and possibly cause a fire.	Batteries are inspected periodically as well as properly charged to prevent short circuits. The lithium ion batteries used for the survey will be housed in a portable battery case to mitigate the risk of overheating or igniting a fire. A fire extinguisher will also be present in case of fire.
Drop Zones (strikes from falling objects)	Awareness of drop zones is important to avoid sUAS collisions with parachuting operations	This hazard will be avoided because the survey will take place in a remote area.
Proximity to overhead power lines and/or obstructions	Powerlines and obstructions are deemed hazardous to air navigation. Close proximity with drones can cause collisions.	No overhead power lines or obstructions are located on or near the surveyed site. Therefore, there is no risk with proximity to drone surveys.
Plants/Insects	Insect stings can cause the RPIC to lose focus and control of the operation. Thorns from the vegetation may cause cuts and/or abrasion to the skin.	This risk will be mitigated by pausing the flight mission and returning to the home point upon being stung by insect. In case the affected participant is allergic to the sting, a bee

Category	Hazard Description (if applicable)	Mitigation Measure
		sting kit will be present on site. Additionally, the flight crew will be wearing appropriate PPE to ensure vegetation will not cause injury.
Animals/Wildlife	Wildlife can disrupt the scheduled survey if located in the vicinity of the surveyed area. Rattlesnakes are common and can pose a risk to flight crew members walking the project site.	In the case that there is wildlife present, the operation will be discontinued until the wildlife is out of the area. Flight crew members will mitigate encounters with rattlesnakes and other potential wildlife in the area by maintaining visual awareness of the ground.
Weather Conditions	heat can cause electronic malfunction as well as impact the overall well-being of the flight crew.	Weather conditions will be monitored daily up until the day of the flight to be aware of temperatures, high winds, thunderstorms and other conditions that may cause the flight to be discontinued. A weather mobile app will aid in actively monitoring weather conditions. The RPIC will respond to heat or potential rain by ceasing operations based on timing. Under FAA Part 107 regulations the RPIC will maintain a minimum distance of 500 ft below clouds and a minimum of 2000 ft horizontally from a cloud. The RPIC will take control of the drone and return to home point if weather conditions and excessively

Category	Hazard Description (if applicable)	Mitigation Measure
		low cloud cover persist.
Terrain	Terrain where the flight crew will be walking on is a layer of rocks as well as various thorny vegetation. Additionally, there are sinkholes located throughout Basin 6.	All flight crew members will use puncture-proof hiking shoes or ankle support shoes to reduce the risk of tripping and reduce the chances of being punctured by vegetation.
Communication Limitations	The cell is 25 km^2 in size and communication may become limited.	The cell phone signal has been tested at the site and deemed strong. Flight crew members will have walkie talkies to communicate amongst one another in case of any emergency.
Emergency Evacuation Limitations	In the scenario where an aircraft suddenly approaches and enters the working area space.	The RPIC and the VO will have constant communication with clear phrases to signify specific events or observations in the case that there is an approaching aircraft or if the sUA is deemed too close to an approaching aircraft. If that is the case, the sUA will be lowered 50 ft by the RPIC and hover until the area is cleared of any risk. In case the flight operation needs to be terminated, the RPIC and VO will have reliable phone signals with charged phones (and with portable chargers in

Category	Hazard Description (if applicable)	Mitigation Measure
		case the phone battery is low) to contact Air Traffic Control (ATC). The cell phone signal has been tested at the site and deemed strong.
Heat & Illness Prevention	Recent weather conditions in Carlsbad, NM have been high temperatures which can cause heat illness and dehydration.	To prevent heat illness flight crew members will drink plenty of water to stay hydrated, utilize sunscreen to protect from the sun, and wear protective PPE (hat and dri-fit long-sleeved shirts). Water will be taken in a cooler for flight crew members.
Aviation Fatigue	Surveying of the site will take various flight hours and days to gather data. This prolonged duration of flight can be a risk for developing aviation fatigue and tiredness.	This hazard will be mitigated by getting sufficient sleep the night prior to the flight. In the case where fatigue leads to difficulty with a flight mission, the sUA can automatically return to the home point. The sUA also has GPS mode which will allow the drone to pause during the flight mission, if necessary.
Other	Loss of control with sUA	When connection is lost between the RPIC and the sUA, the sUA has the built-in capability to automatically return to its “home point” which will be the landing zone. During this process, as the sUA moves closer to RPIC, RPIC will attempt to regain control of the sUA.

4. *Drone Mission Risk Assessment*

(Assess the risks involved with the planned mission.)

Project: UAV Survey of Basin 6	**Flight Date(s):** August 9-13, 2021

Pre-Mitigation Hazard Ratings (List and describe hazards.)	**Severity**	**Likelihood**	**HRI, Risk Level**
High winds – Operating outside of the approved project area.	II	B	1, Unacceptable
Mishandling stored energy - Improperly packaged and mishandled lithium ion batteries resulting in fire hazard	III	B	1, Unacceptable
Drop Zones - Risk of sUAS collisions with parachuting operations	II	D	1, Unacceptable
Obstructions - Power Lines and obstructions pose hazard to air navigation	II	D	4, Acceptable
Fall Hazards - Project area on mostly flat terrain	II	E	1, Unacceptable
Wildfires - Parking on dry vegetation can lead to wildfire	I	D	1, Unacceptable
Wildlife - If present on the project area can disrupt gathering of remote sensing data. Present rattlesnakes can be a hazard for flight crew monitoring project sites.	IV	C	2, Tolerable
Weather Conditions - If turbulent winds, rain, or extreme heat are present they pose a high-risk hazard to the crew members and sUA	II	A	1, Unacceptable
Terrain - Rocky terrain of project area poses a tripping risk	II	C	2, Tolerable
Communication Limitations - May lack phone service due to remote location	IV	D	1, Unacceptable

Emergency Evacuation Limitations - Approaching aircraft	I	D	2, Tolerable
Heat & Illness - High temperatures lead to heat illness and dehydration	II	B	1, Unacceptable
Aviation Fatigue - Prolonged flight of sUAS can result in tiredness	III	C	2, Tolerable
Loss of control with sUAS - sUAS loses connection with RPIC	II	B	3, Tolerable
Post-Mitigation Hazard Ratings (List and describe mitigation controls.)	**Severity**	**Likelihood**	**HRI, Risk Level**
High winds – Operating parameter of XX mph steady winds is lower than the operational limitation of XX mph; pilot is experienced in operating model of UAS	IV	D	4, Acceptable
Mishandled stored energy - Batteries inspected periodically; will be housed in portable battery cases for safe keeping. A fire extinguisher will be present in case of fire.	IV	D	3, Tolerable
Drop Zones - No drop zones are located at or with any proximity to work area confirmed on sectional chart of study site	IV	E	4, Acceptable
Obstructions - No overhead power lines or obstructions are located within the vicinity. A preflight site inspection is performed to confirm mitigation.	IV	E	4, Acceptable
Fall Hazards - Crew members will pace walk across the terrain and place attention where they step.	III	C	4, Acceptable
Wildfires - Crew members will park in designated areas with no vegetation.	II	D	4, Acceptable
Wildlife - Wildlife present in the project area will cause the flight to be paused until wildlife is off the area. Prevention from encountering rattlesnake or being bitten is to monitor the ground careful	IV	D	4, Acceptable
Weather Conditions - weather conditions will be monitored day by day. In the case of heavy rain and thunderstorms the flight can be discontinued. For wind speeds, if the wind speed is within the sUA's flying limit the mission will continue.	IV	D	4, Acceptable

Terrain - All flight crew members will war hiking shoes or ankle supported shoe to reduce risk of tripping.	II	D	4, Acceptable
Communication Limitations - The cell phone signal has been tested at the site and deemed strong. Flight crew members will have walkie talkies to communicate amongst one another in case of any emergency.	III	D	4, Acceptable
Emergency Evacuation Limitations - If that is the case, the sUAS will be lowered 50 ft by the RPIC and hover until the area is cleared of any risk. In case the flight operation needs to be terminated, the RPIC and VO will have reliable phone signals with charged phones (and with portable chargers in case the phone battery is low) to contact Air Traffic Control (ATC).	IV	D	4, Acceptable
Heat & Illness - To prevent heat illness flight crew members will drink plenty of water to stay hydrated and utilize sunscreen to protect from the sun. Water will be taken in a cooler for flight crew members. Hats, sunglasses, and bright dri-fit long sleeved shirts will be worn to protect from heat.	II	C	4, Acceptable
Aviation Fatigue - This hazard will be mitigated by getting sufficient sleep the night prior to the flight. In the case where fatigue leads to difficulty with a flight mission, the sUA can automatically return to the home point. The sUA also has GPS mode which will allow the drone to pause during the flight mission, if necessary.	IV	E	4, Acceptable
Loss of control with sUA - When connection is lost between the RPIC and the sUA, the sUA has the built-in capability to automatically return to its "home point" which will be the landing zone. During this process, as the sUA moves closer to RPIC, RPIC will attempt to regain control of the sUA.	II	D	4, Acceptable
Overall Risk Assessment Rating	**Acceptable**		

RISK ASSESSMENT KEY

Severity Table

Description	Category	Hazard Severity
Catastrophic	I	Death or serious injury, irreversible or significant environmental/ biological impact, destruction of public property, and/or destruction of UAS.
Critical	II	Injury resulting in hospitalization and/or permanent partial disability, major public property damage, reversible significant environmental/biological impact, significant reduction in safety margins, and/or major UAS damage. Damage to property over $500.
Marginal	III	Minor injury, minor public property damage, minor incident with little impact on safety margins, and/or minor UAS damage requiring repair. Damage to property under $500.
Negligible	IV	Not serious enough to cause injury to the crew and public, public property, the sUAS, or safety margins.

Likelihood Table

Description	Level	Specific Event
Frequent	A	Likely to occur frequently; or likely to occur twice or more a year.
Probable	B	Will occur several times in the life of the system; or will occur once a year.
Occasional	C	Likely to occur within the life of the system; or likely to occur once every few years.
Remote	D	Unlikely but possible to occur in the life of the system; or may occur once.
Improbable	E	So unlikely, it can be assumed that occurrence may not be experienced.

In August, the FIU team traveled to Carlsbad, NM to conduct the UAV-based survey of the entire Basin 6 study area, the details of which are provided in the next section of this report.

Subtask 6.1: Results and Discussion

DEM Development & Refinement

This section describes the results of the photogrammetry workflow applied by FIU to process the Basin 6 imagery collected in January 2020. FIU applied several vegetation identification and removal methods found in peer reviewed literature with the aim of producing a high-resolution bare-ground DEM which can be used in the hydrological models and for delineation of the significant surface features of interest (i.e., stream network, sink holes, gulley, swallets, etc.). The results of the automatic point cloud classification in ArcGIS using a subset of the collected point cloud in Basin 6 can be seen below. Figure 112 shows the images produced using two different classification types, standard and conservative, which are more suitable for relatively flat surfaces. These images were visually compared to determine the better approach.

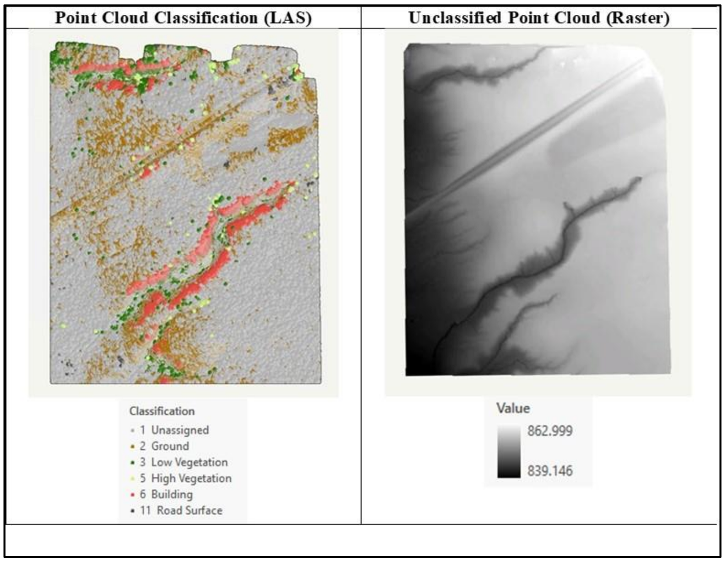

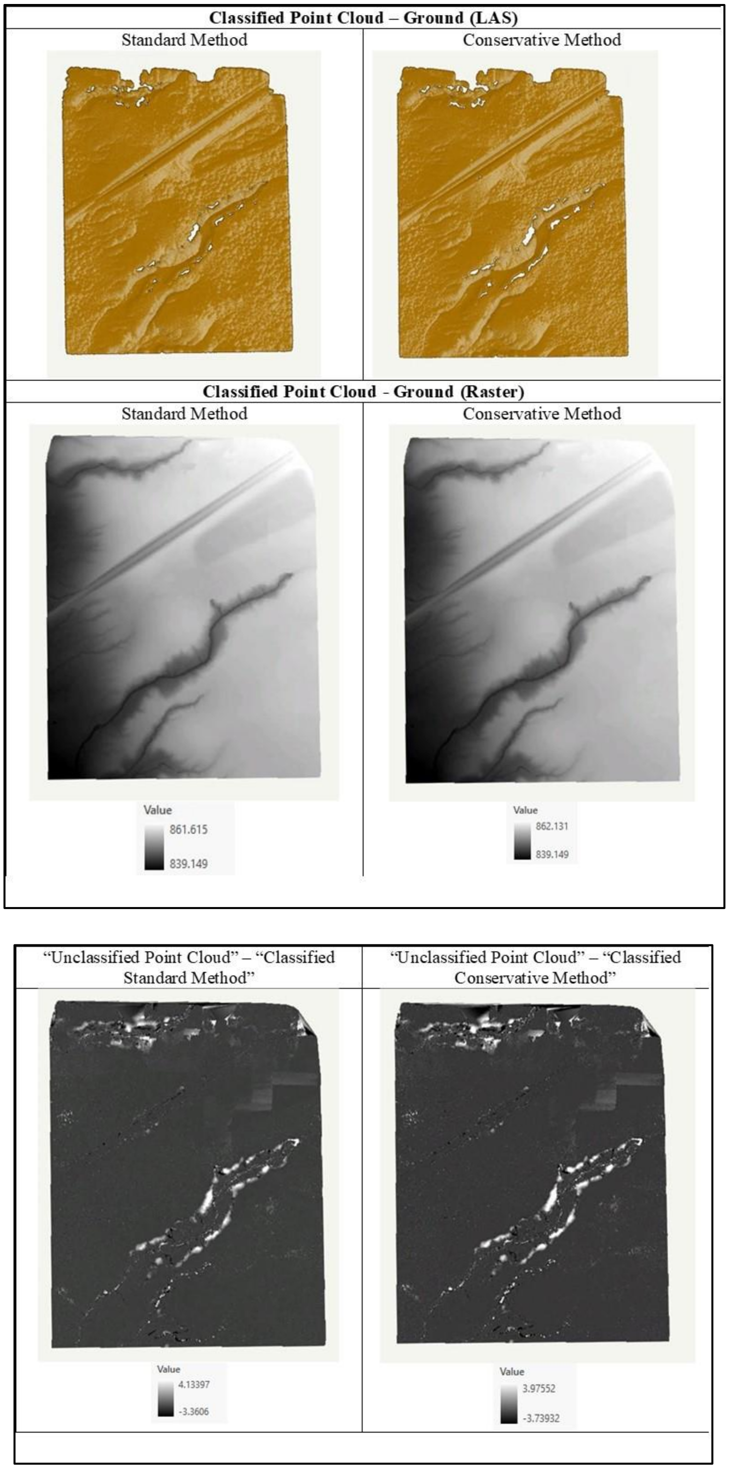

Figure 112. Images produced for visual comparison of two different automatic point cloud classification types, standard and conservative, for vegetation identification.

The conservative method was considered superior to the default method and was therefore selected to compare to the vegetation index (VI)-based vegetation removal method. Using Pix4D, a reflectance map was created for the test area and then VI maps were calculated for all six VIs (Table 32) including the Red-Green Index (RGI), Red-Green-Blue Index (RGBVI), Green-Leaf

Index (GLI), Visible Atmospherically Resistant Index (VARI), Normalized Green-Red Difference Index (NGRDI), and Enhanced Red-Green-Blue Vegetation Index (ERGBVI).

Table 32. Vegetation Indices

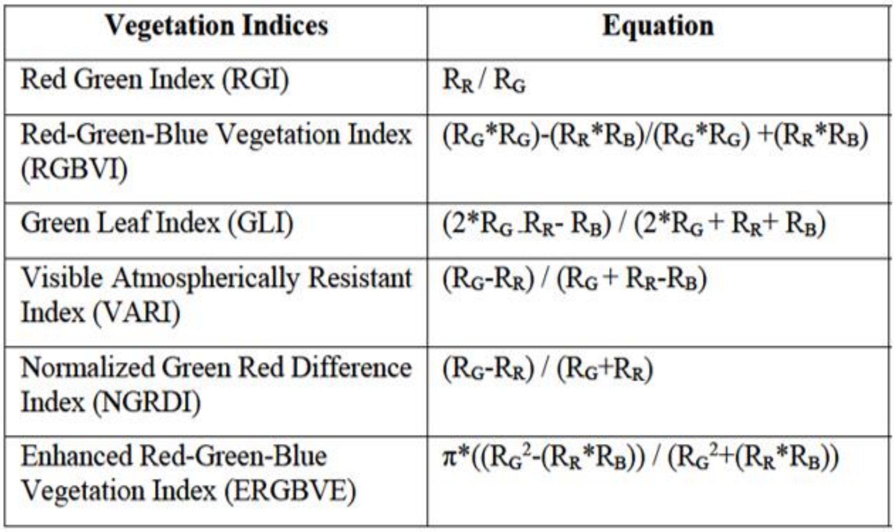

Vegetation Indices	Equation
Red Green Index (RGI)	R_R / R_G
Red-Green-Blue Vegetation Index (RGBVI)	$(R_G*R_G)-(R_R*R_B)/(R_G*R_G) +(R_R*R_B)$
Green Leaf Index (GLI)	$(2*R_G - R_R - R_B) / (2*R_G + R_R + R_B)$
Visible Atmospherically Resistant Index (VARI)	$(R_G-R_R) / (R_G + R_R-R_B)$
Normalized Green Red Difference Index (NGRDI)	$(R_G-R_R) / (R_G+R_R)$
Enhanced Red-Green-Blue Vegetation Index (ERGBVE)	$\pi*((R_G^2-(R_R*R_B)) / (R_G^2+(R_R*R_B))$

The VI raster maps (.tiff format) were imported into ArcGIS Pro for visualization. After importing each of the VI raster maps into ArcGIS Pro 4, threshold values out of a total of 12 classes were selected and visualized using black masks. This enables the visualization of the coverage of vegetation identified with different criteria, and thus facilitates selection of an optimal threshold value for each VI, which is described in following steps. Figure 113 gives an example of the RGBVI-based vegetation identification with the threshold value ranging from -0.178 to -0.092 where vegetation was masked in black.

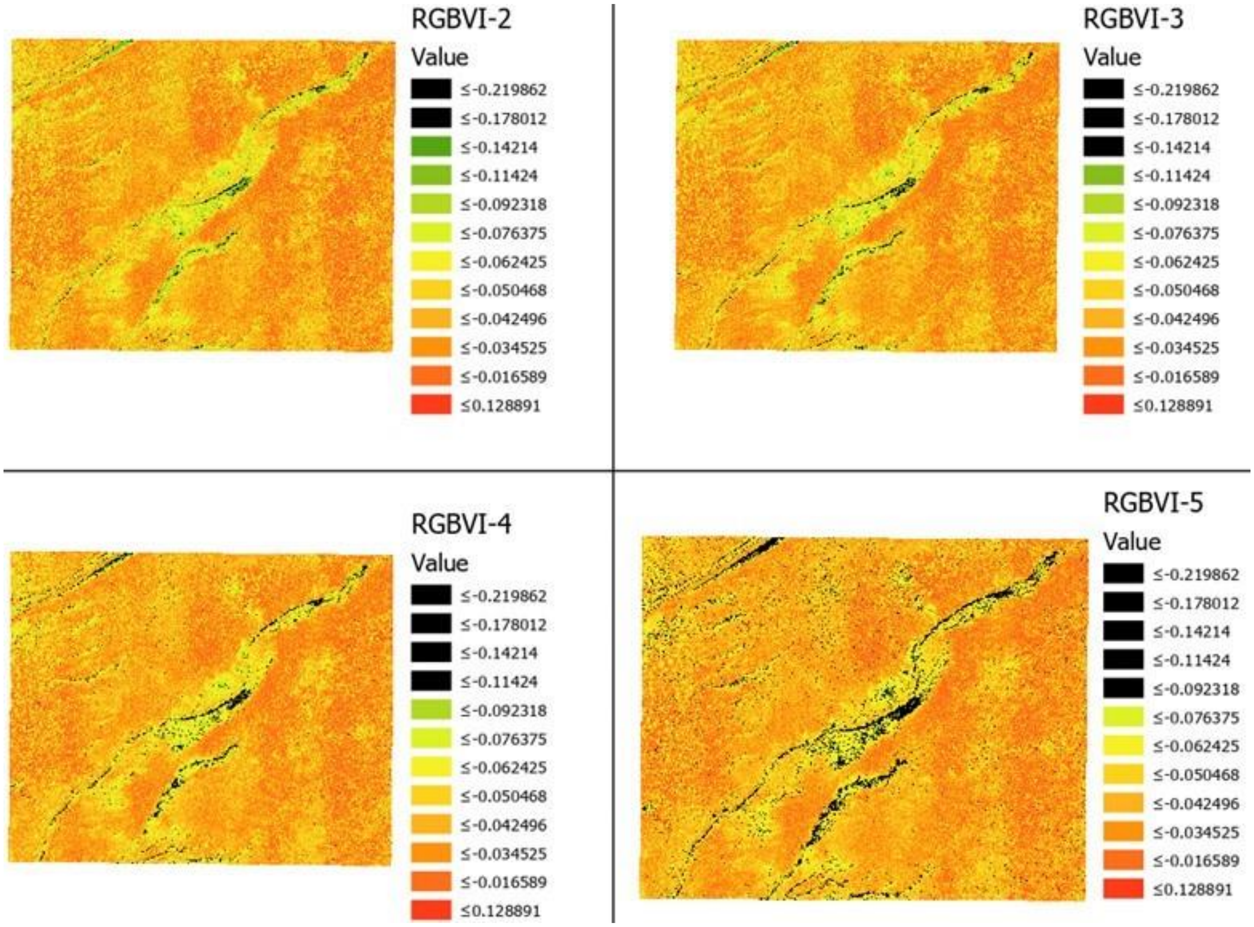

Figure 113. Red-Green-Blue Vegetation Index (RGBVI)-based vegetation identification with the threshold value ranging from -0.178 to -0.092, where vegetation was masked in black.

After selecting 4 threshold values for each of the VIs using a raster map, libLAS was used to separate the photogrammetric 3D point clouds (.las format) into land and vegetation based on the threshold values. Figure 114 is an example of the python script using the RGBVI and Figure 115 shows a 3-dimensional view of the point cloud after vegetation was removed.

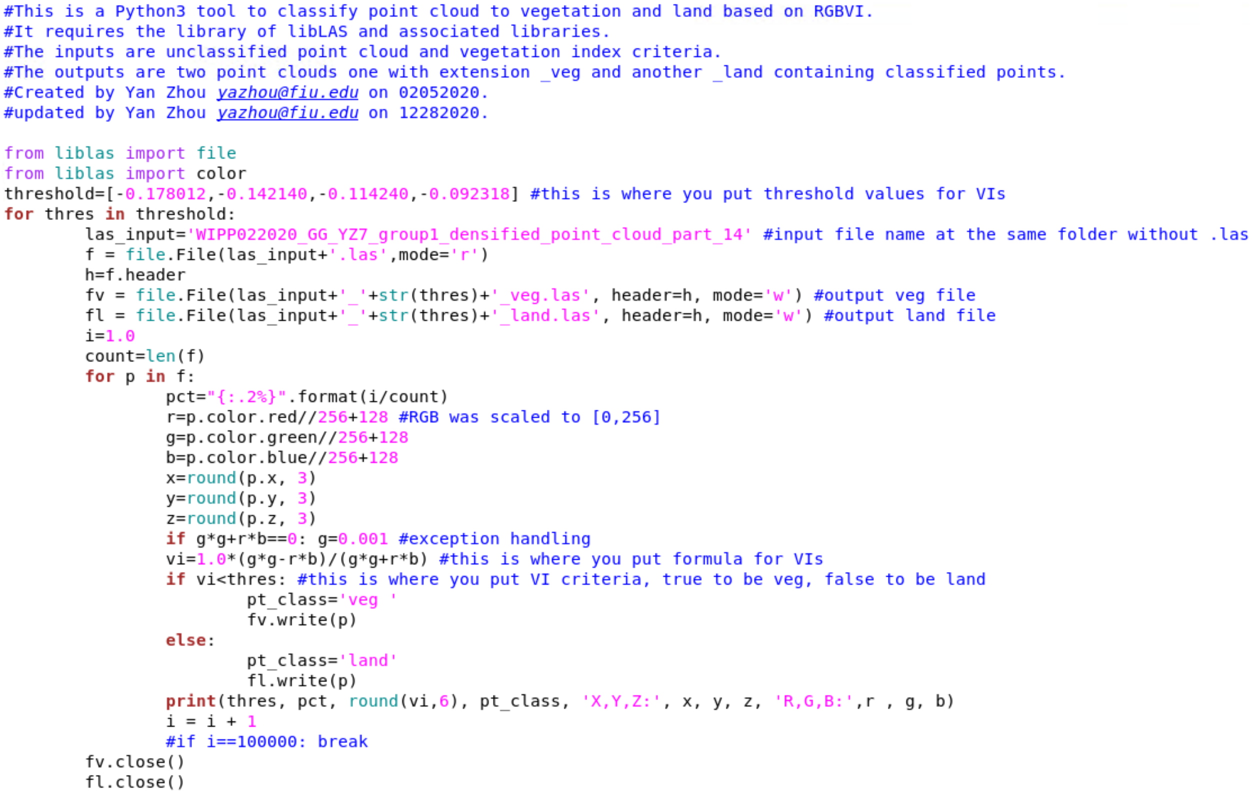

```
#This is a Python3 tool to classify point cloud to vegetation and land based on RGBVI.
#It requires the library of libLAS and associated libraries.
#The inputs are unclassified point cloud and vegetation index criteria.
#The outputs are two point clouds one with extension _veg and another _land containing classified points.
#Created by Yan Zhou yazhou@fiu.edu on 02052020.
#updated by Yan Zhou yazhou@fiu.edu on 12282020.

from liblas import file
from liblas import color
threshold=[-0.178012,-0.142140,-0.114240,-0.092318] #this is where you put threshold values for VIs
for thres in threshold:
        las_input='WIPP022020_GG_YZ7_group1_densified_point_cloud_part_14' #input file name at the same folder without .las
        f = file.File(las_input+'.las',mode='r')
        h=f.header
        fv = file.File(las_input+'_'+str(thres)+'_veg.las', header=h, mode='w') #output veg file
        fl = file.File(las_input+'_'+str(thres)+'_land.las', header=h, mode='w') #output land file
        i=1.0
        count=len(f)
        for p in f:
                pct="{:.2%}".format(i/count)
                r=p.color.red//256+128 #RGB was scaled to [0,256]
                g=p.color.green//256+128
                b=p.color.blue//256+128
                x=round(p.x, 3)
                y=round(p.y, 3)
                z=round(p.z, 3)
                if g*g+r*b==0: g=0.001 #exception handling
                vi=1.0*(g*g-r*b)/(g*g+r*b) #this is where you put formula for VIs
                if vi<thres: #this is where you put VI criteria, true to be veg, false to be land
                        pt_class='veg '
                        fv.write(p)
                else:
                        pt_class='land'
                        fl.write(p)
                print(thres, pct, round(vi,6), pt_class, 'X,Y,Z:', x, y, z, 'R,G,B:',r , g, b)
                i = i + 1
                #if i==100000: break
        fv.close()
        fl.close()
```

Figure 114. Python script using libLAS to separate a 3D point cloud based on the RGBVI.

Figure 115. Example of the 3D point cloud before (left column) and after (right column) vegetation removal.

For each VI, digital elevation models (DEMs) were generated from each libLAS file that was created using four different threshold values selected. A subtraction between the DEMs of the lowest and highest threshold values of each VI resulted in output DEMs with highlighted areas (as seen in red in Figure 116 below) representing areas of highest variation in elevation. Based on this result, for each threshold value, the method by Asters et al (2019) was implemented where cross-sections were drawn on the DEM from the libLAS file of that threshold value in several of the highlighted areas as on the subtracted DEMs to determine the elevation values at representative locations of different slopes/landscapes. This process was repeated for each threshold value of each VI and the results compared. Figure 116 shows the cross-sections drawn on the subtracted ERGBVI DEMs.

Figure 116. Output of subtracted rasters of ERGBVI with threshold values of -0.690367 and -0.558956 highlighting areas of greatest variation between each DEM in red.

Line feature classes to represent cross-sections were created on the red areas that were of stark difference and an elevation profile graph of each threshold value for each VI was created using the Stack Profile tool on ArcGIS Pro.

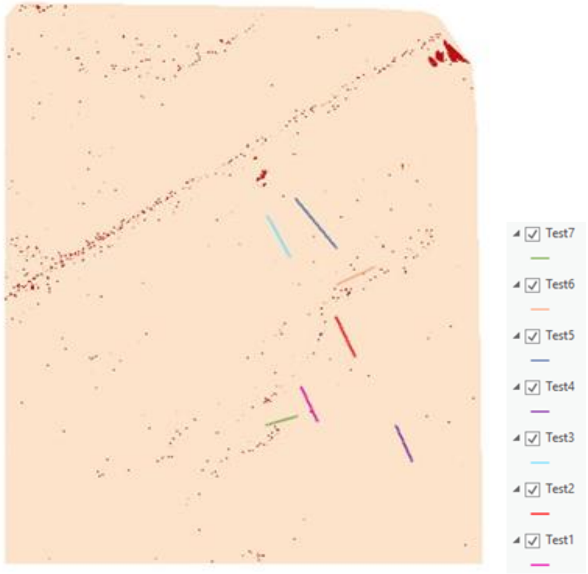

Figure 117. Test lines drawn on DEM from subtracted ERGVI rasters to determine best area to create profile graph.

The Feature Class Line (Test 7) with the most variations between each threshold value for ERGBVI was chosen and drawn on the remaining VIs and elevation profile graphs were created for each one. Line Test 7 is on the bank of the gully (referred to now as Section A-A') and another cross-section was chosen on a land sink (Section B-B').

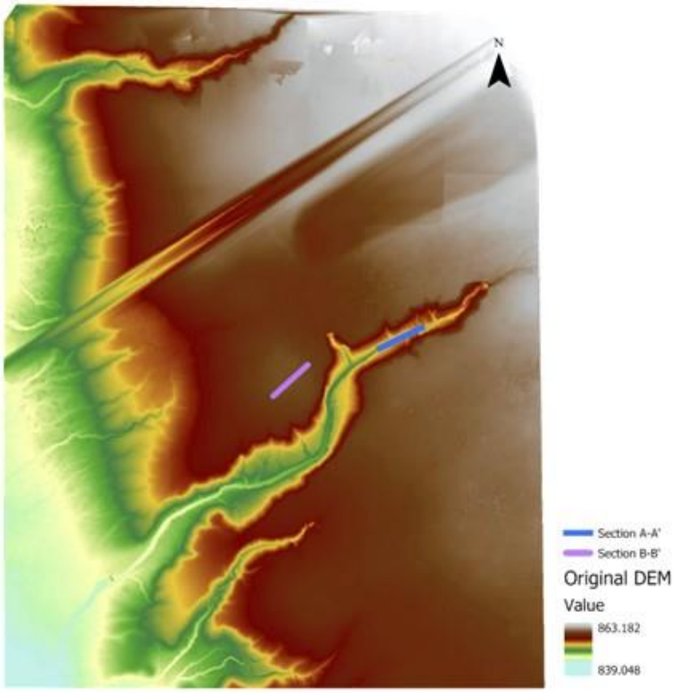

Figure 118. Unfiltered DEM with cross-sections highlighted.

Upon visual inspection of the point cloud and the profile graphs of each VI, the best threshold values were chosen as follows:

- ERGBVI (-0.4436193)
- GLI (0.074329)
- NGRDI (-0.16606)
- RGBVI (-0.14214)
- RGI (1.483579)
- VARI (-0.157247)

These threshold values were plotted on a profile graph and compared as seen in Figure 119.

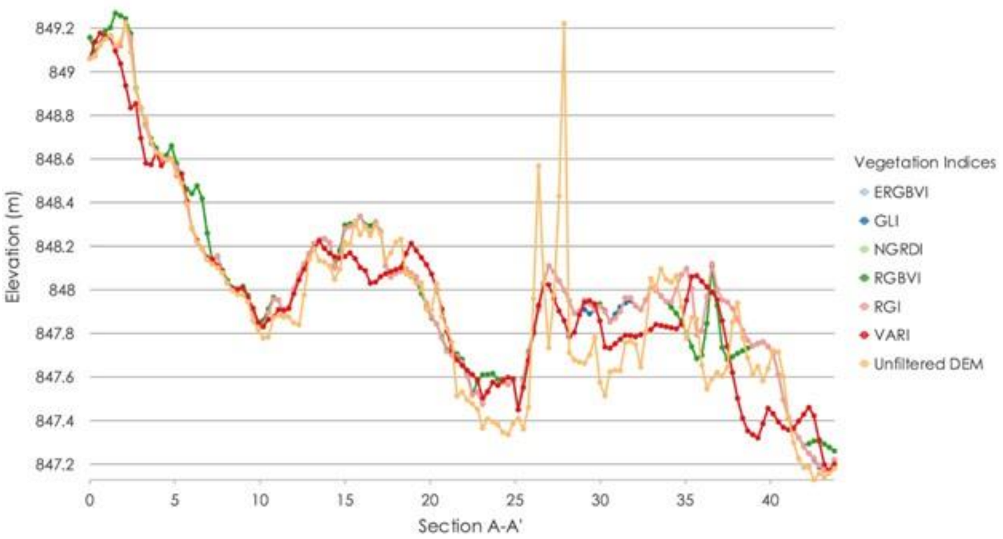

Figure 119. Profile graph of Section A-A' of each VI.

This completed the workflow to evaluate various vegetation removal methods to generate the best bare-ground digital elevation model to be used for the development of the WIPP regional land surface model, however, based on the results it was still difficult to make a distinction as to which VI and threshold value was superior. FIU therefore proceeded with a further assessment of the vegetation removal methods by creating additional cross-sections on the DEMs that were generated using different threshold values for each vegetation index (VI). The purpose of the additional cross-sections was to have a more representative variation in surface topography, hoping that the elevation profile graphs generated at the cross-sections will enable a more conclusive assessment as to which VI and threshold value produce the best results. Therefore, for each DEM, elevation profile graphs of the cross-sections were plotted and compared to determine the best VI and threshold value that distinguishes the vegetation from the bare ground.

The orthomosaic images of the current study area were also downloaded from Pix4D in order to inspect obtrusive areas that were causing additional height to be added in the profile graph of the cross sections of the digital elevation models of the various vegetation indices. From the orthomosaic images, it can be seen that there are many shadows present throughout the study area as a result of the angle at which the drone captured the images and the positioning of the sun. Using the orthomosaic images and the subtracted DEMs of the highest and lowest threshold values of the VIs, additional cross-sections were drawn in the areas where there were obvious shadows present and where there were not any visually apparent shadows. This was done in order to determine if shadows played a role in the addition of height in the profile graphs, thus impacting the results that determine which VI or threshold values are most effective at detecting vegetation.

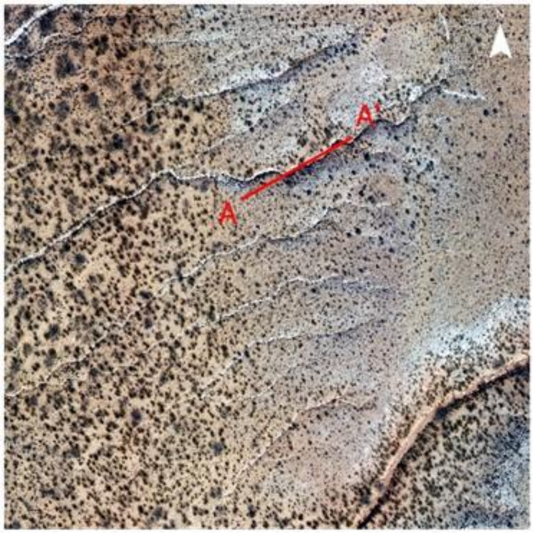

Figure 120. Cross-section A-A' (41.32 m) drawn in shaded area on unfiltered DEM.

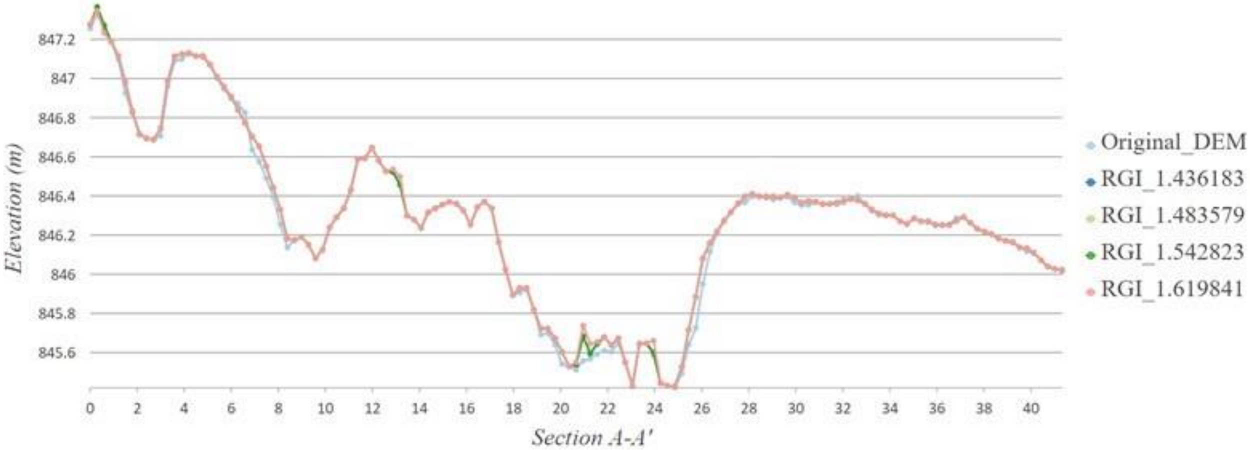

Figure 121. Elevation profile graph of cross-section A-A' (in meters) using Red-Green Index (RGI) thresholds.

Based on the profile graphs, it was concluded that the shadows do likely impact the end results and as such a literature review on shadow detection and removal techniques was conducted. A study by Agarwal et al (2020) implemented the use of a DJI Phantom 3 to collect aerial imagery, processed the imagery on Pix4D, and applied four techniques to detect and remove shadows from the orthomosaic images (Background Subtraction, Gray Level Threshold, RGB to LAB Color Space, Texture Based). The Background Subtraction method and Gray Level Threshold method which produced the best results were further investigated to determine if they could be done in a three-dimensional approach. A pseudocode was provided by Agarwal et al, but it was challenging to develop a Python code based on this. Further research was therefore conducted to find a code that would accurately detect and remove shadows. A study by Deb et al (2014) created a workflow to detect shadows by converting the RGB values to a YCbCr color space and creating a mask based on the intensities of the values in the image. To remove the shadow, average pixel intensities of the shadow and non-shadow areas are calculated and added to the Y channel followed by calculating the ratio between average shadow pixels and non-shadow pixels. Once this was done, the color space was converted back to RGB and a final image with no shadows is produced. The code was provided on the author's GitHub (https://github.com/mykhailo-mostipan/shadow-removal) and was tested by FIU on a smaller area within Basin 6; however, the final image produced appeared to only include the mask of the shadows detected.

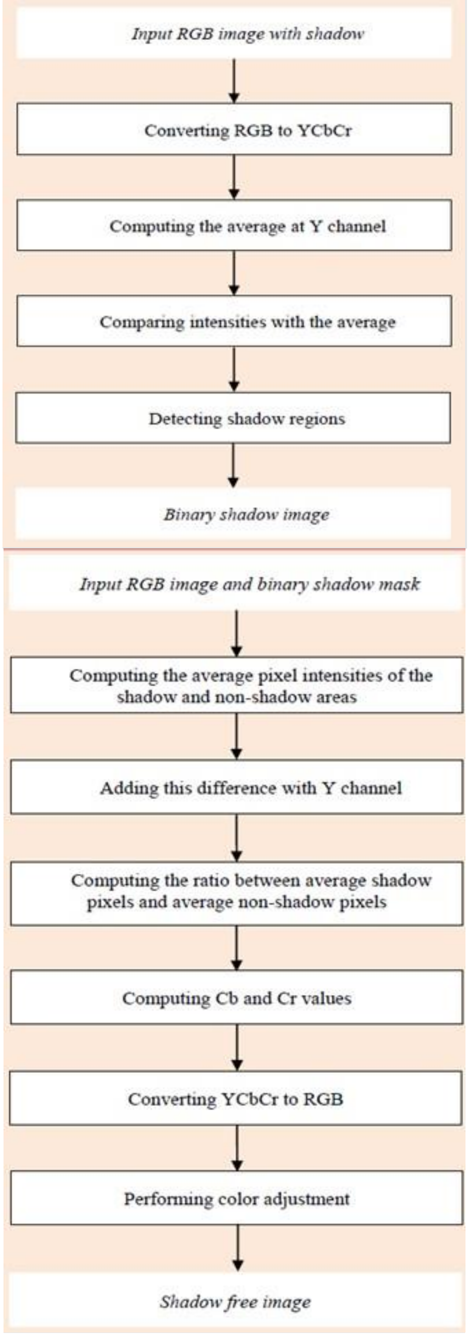

Figure 122. Workflow for shadow removal by Deb et al (2014).

Figure 123. Final image with shadows detected using code provided by Deb et al (2014).

Further investigation was conducted to determine why the script by Deb et al (2014) was not working on Spyder. The script was also tested on Matlab which the authors originally used to run the script, but the script was unable to successfully run. The Python script by Deb et al (2014) is divided into two steps: shadow detection and shadow removal. As the attempts to run the complete script through Spyder and Matlab were unsuccessful, where the resulting images displayed a mask of the shadows highlighting but not removing them, it was decided to conduct a further test by running the code for each of the two steps separately. This was also unsuccessful as the shadow detection code did not identify any shadows or produce a mask as previously seen, and instead only displayed the untouched input image.

Another script found on GitHub (https://github.com/cdbharath/shadow_detection_and_removal) was investigated; however, an issue was encountered when attempting to download one of the packages required (PyTorch) on the Windows computer in the research laboratory at FIU. The installation was finally successful when downloaded on a Mac computer and the code was able to successfully create a black and white mask of the shadows detected. With this script, an unsupervised segmentation algorithm employing autoencoders is used for detecting shadow regions. A Gabor filter was designed to identify the texture features in the images. Additionally, illuminance transfer techniques are deployed to remove the shadow regions with the help of the acquired textures.

Sinkhole Detection

The generated DEM of Basin 6 will be used to delineate and extract topographical features such as drainage basins, brine lakes, channels, sink holes, discharge points and other relevant hydrological features using ArcGIS geoprocessing tools, which will be essential for LSM development. This year FIU began testing previously researched sinkhole detection methods on the DEM that was generated for the Basin 6 Pilot Study Area using the imagery collected in early

2020. The MDTA method employs ArcGIS Model Builder to run a series of geoprocessing tools that ultimately produces a shapefile of sinkholes. Another sinkhole detection method, the Sinkhole Mapper Toolbox, was based on using Python coding to create a toolbox where a set of parameters are to be entered and a shapefile of sinkholes will be produced. When testing these methods, it was found that the GEOTIFF file of the DEM was unable to be read and as a result, the point clouds generated by Pix4D were converted to DEM/raster format. Once this was done both methods ran smoothly. A preliminary map using the default parameter values was created and compared to the sinkhole locations recorded by Andrea Goodbar, an Environmental Scientist at the New Mexico Environment Department. Efforts are now focused on improving the parameters in order to get a result that is better correlated with the inventory of sinkholes provided by our DOE collaborators.

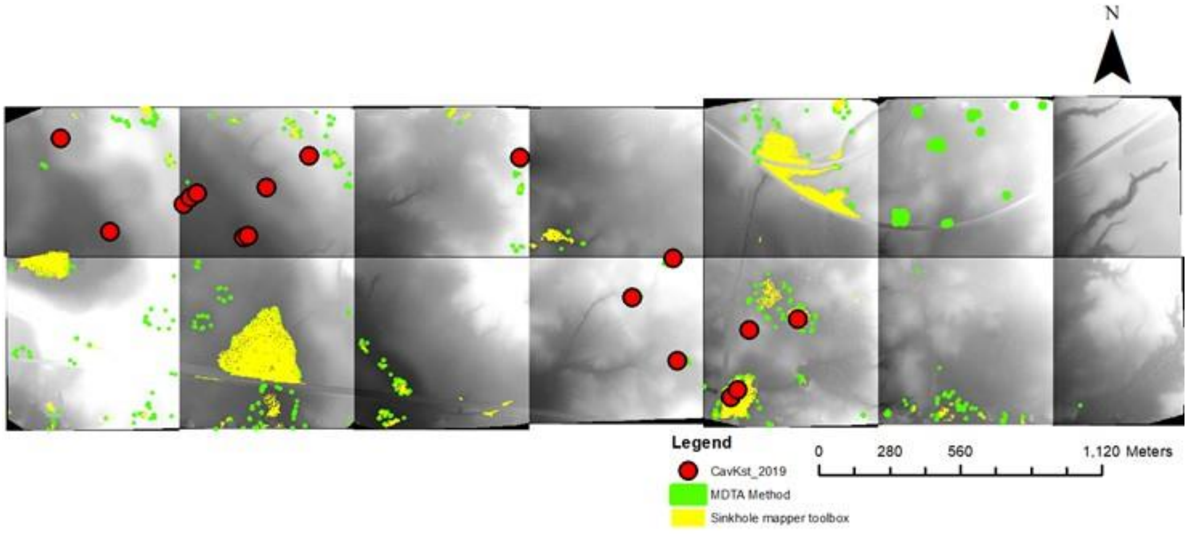

Figure 124. Map of sinkholes identified by Andrea Goodbar, MDTA Method, and Sinkhole mapper toolbox.

UAV Field Survey of Basin 6

After completing the pilot study to extablish an efficient photogrammetry workflow for developing the Basin 6 DEM, FIU proceeded to extend the coverage area beyond the 5 km^2 pilot study area to the complete Basin 6 area. A team comprised of two DOE Fellows and an FIU ARC Research Specialist traveled to Carlsbad, NM to complete the UAV-based survey of Basin 6. As formerly mentioned, Basin 6 contains several hydrological features characteristic of the region such as sink holes, brine lakes and gullies that can be significant contributors to the groundwater recharge and thus serves as an ideal representative study area for taking a proof-of-concept approach to developing a workflow that would provide a more accurate estimate of the regional water balance. The aim of this trip was to repeat the survey conducted the previosu year, however this time covering the entire Basin 6 area (approx. 24 km^2) as well as a small area (approx. 4 km^2) where several brine lakes are located west of Basin 6. The FIU team was successful in covering approximately 22 km^2, about 6 km^2 short of the complete study area. More than 38,000 images were collected using a DJI Phantom 4 drone equipped with a real-time kinematic (RTK) GPS. Accurate coordinates of 20 ground control points were measured with a Trimble GNSS Receiver for improved accuracy and calibration of the photogrammetry process. The current focus will now be on processing the imagery collected using the photogrammetry workflow established from the pilot study, including geo-referencing and tests of different vegetation removal approaches.

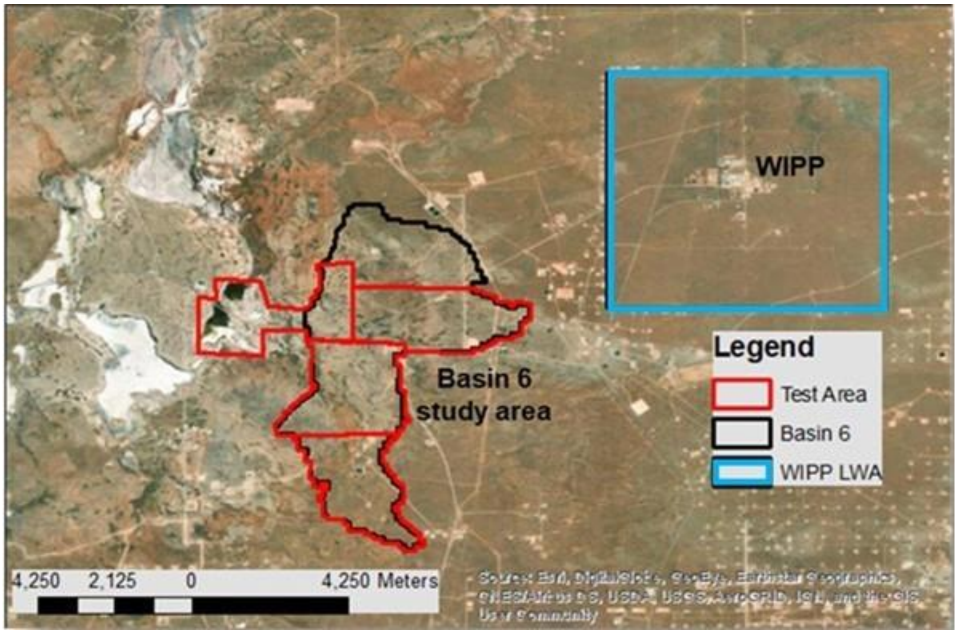

Source: Esri, DigitalGlobe, GeoEye, Earthstar Geographics, CNES/Airbus DS, USDA, USGS, AeroGRID, IGN, and the GIS User Community

Figure 125. Basin 6 study area (completed survey area in red) in Carlsbad, NM.

Figure 126. DOE Fellow Gisselle Gutierrez-Zuniga conducting a drone flight.

Figure 127. Field team consisting of DOE-EM Fellow Gisselle Gutierrez-Zuniga, DOE-LM Fellow Eduardo Rojas, and FIU ARC Research Specialist Mackenson Telusma.

Figure 128. Field image (left) and drone image (right) of a gulley captured during the aerial survey conducted by FIU in Basin 6, Carlsbad, NM.

Figure 129. Field image (left) and drone image (right) of a brine lake captured during the aerial survey conducted by FIU in Basin 6, Carlsbad, NM.

Subtask 6.1: Conclusions

DEM Development & Refinement

Although several vegetation indices (VIs) were evaluated, preliminary results were inconclusive and indicate a need for a greater number of cross-sections that will be more representative of the variation in surface topography, so that a more conclusive assessment can be made. It was also determined that LiDAR data of the land surface should also be collected, which will serve as the ground truth to enable a quantitative evaluation of the result.

A literature review was also initiated to investigate additional vegetation removal methods from high-resolution DEMs for comparison with the previous RGB-based methods employed. Sentinel imagery of the Basin 6 pilot study area was previously downloaded and will now be used to apply six different vegetation indices. Additionally, the high-resolution DEM of the pilot study area was scaled to the same resolution as the Sentinel imagery which will allow for a comparative analysis of the vegetation removal accuracy.

In FIU Year 2 the team will also continue to assess the performance of various RGB-based vegetation removal methods (e.g. libLAS Python, Pix4D and ArcGIS) and select the most suitable approach for the generation of a high-resolution DEM for Basin 6. Furthermore, FIU will continue an evaluation of the shadow effect observed, due to the time of day collected, on the quality of the DEM.

Sinkhole Detection

The resulting high-resolution DEM in FIU Year 2 will be evaluated for the presence of sinkholes to be compared to a previously performed in-situ based inventory. Also, FIU will evaluate the physical characteristics of the soils at different depths (e.g. texture, porosity, etc.) from available observations and databases and collect additional data while visiting the site for additional validation. The generated DEM and surface information of Basin 6 will be used to delineate and extract topographical features such as drainage basins, brine lakes, channels, sink holes, discharge points and other relevant hydrological features using ArcGIS geoprocessing tools, which will be essential for hydrological model development.

UAV Field Survey of Basin 6

FIU has begun transferring the aerial imagery collected in Basin 6 near the WIPP in New Mexico from the SD cards to an external hard drive. The current focus will now be on processing the imagery collected using the photogrammetry workflow established from the pilot study, including geo-referencing and tests of different vegetation removal approaches. There are a total of 38,807 images, amounting to 346 GB. Currently, FIU is investigating the fastest and most efficient method of processing the data. Two potential options include (1) splitting the project into multiple projects and then merging them on Pix4Dmapper, and (2) using Pix4Dmatic which is designed to process projects that are over 10,000 images. For FIU Year 2 the FIU team will revisit the site and finalize the UAV observations. FIU will continue to train undergraduate and graduate students (DOE Fellows) on UAV photogrammetry methods and provide mentorship and field experience through student summer internships in collaboration with Los Alamos National Laboratory (LANL), Carlsbad Field Office (CBFO) and Pacific Northwest National Laboratory (PNNL) scientists.

Subtask 6.1: References

Agarwal, A., Kumar, S., & Singh, D. (2020). An Adaptive Technique to Detect and Remove Shadow from Drone Data. *Journal of the Indian Society of Remote Sensing*, 1-8.a

Anders, N., Valente, J., Masselink, R., & Keesstra, S. (2019). Comparing Filtering Techniques for Removing Vegetation from UAV-Based Photogrammetric Point Clouds. Drones, 3(3), 61.

Deb, K., & Suny, A. H. (2014). Shadow detection and removal based on YCbCr color space. *SmartCR*, *4*(1), 23-33.

Goodbar, A. K., Powers, D. W., Goodbar, J. R., & Holt, R. M. (2020). Karst and sinkholes at Nash Draw, southeastern New Mexico (USA).

Sadeghi-Tehran, P., Virlet, N., Sabermanesh, K., & Hawkesford, M. J. (2017). Multi-feature machine learning model for automatic segmentation of green fractional vegetation cover for high-throughput field phenotyping. Plant methods, 13(1), 103.

Sandino, J., Gonzalez, F., Mengersen, K., & Gaston, K. J. (2018). UAVs and machine learning revolutionising invasive grass and vegetation surveys in remote arid lands. Sensors, 18(2), 605.

Serifoglu Yilmaz, C., & Gungor, O. (2018). Comparison of the performances of ground filtering algorithms and DTM generation from a UAV-based point cloud. Geocarto international, 33(5), 522-537.

Skarlatos, D., & Vlachos, M. (2018). Vegetation removal from UAV derived DSMS, using combination of RGB and NIR imagery.

Yilmaz, V., Konakoglu, B., Serifoglu, C., Gungor, O., & Gökalp, E. (2018). Image classification-based ground filtering of point clouds extracted from UAV-based aerial photos. Geocarto international, 33(3), 310-320.

Zhang, C., & Xie, Z. (2013). Object-based vegetation mapping in the Kissimmee River watershed using HyMap data and machine learning techniques. Wetlands, 33(2), 233-244.

Subtask 6.2: Model Development

Subtask 6.2: Introduction

This subtask involves the development of regional groundwater model (GWM) of Basin 6 of the Nash Draw near the WIPP site, using the Advanced Simulation Capability for Environmental Management (ASCEM) modeling toolset to improve the current understanding of regional and local groundwater flow in the vicinity of the WIPP. A state-of-the-art open-source surface hydrological model will also be developed to provide surface process parameters (e.g. infiltration rate) for input into the ASCEM GWMs to compute the surface water balance, and derive estimates of groundwater recharge. This subtask will provide an extensible, multi-scale land-atmosphere modeling capability for conservative, coupled and uncoupled prediction of the hydrological cycle components in the WIPP area and surrounding region. This will simplify the upper boundary condition for flow in Culebra that is currently externally specified without consideration of water fluxes due to surface processes like runoff, infiltration and evapotranspiration. Coupling of the surface hydrological model with the ASCEM GWMs leads to more accurate predictions of groundwater flow patterns, including horizontal flow (e.g., potentiometric surface, flow direction, vertical flow into transmissive units, and the effect of density on flow direction). With improved estimates of the spatial and temporal patterns of recharge to force the GWM, predictions of halite dissolution and propagation of the shallow dissolution front will be made possible and the potential impact on repository performance quantified.

Subtask 6.2: Objectives

The objective of this subtask is to develop a groundwater model for Basin 6 of the Nash Draw near the WIPP site using the ASCEM toolset coupled with a selected surface hydrological model to account for the surface and near-surface processes. These models will be used to compute the water balance across multiple scales and to reduce uncertainties in recharge estimates. The spatial distribution of recharge as well as groundwater flow rates and directions derived from these models will be used to estimate the rate of halite dissolution and the rate of propagation of the shallow dissolution front, both of which have the potential to affect post-closure repository performance.

Subtask 6.2: Methodology

Groundwater Model Development: ASCEM Training

In Performance Year 1, the FIU team continued training virtually on the ASCEM modeling toolset that was initiated in the previous year under the guidance of PNNL and CBFO collaborators. ASCEM is an open source and modular computing framework that incorporates new advances and tools for predicting contaminant fate and transport in natural and engineered systems and includes both a platform with integrated toolsets (Akuna) and a high-performance computing multi-process simulator (Amanzi) (Freedman *et al.* 2014). FIU's training was focused on the Akuna toolsets for model setup, database management, sensitivity analysis, parameter estimation, uncertainty quantification, and visualization of both model setup and simulation results.

Surface Hydrological Model Development: Amanzi-ATS Training

FIU also continued the review and evaluation of various open-source surface hydrological models (e.g., Community Land Model (CLM) and WRF-Hydro, among others) and after consultation with collaborators from CBFO, PNNL and LANL, it was decided to make use of the Advanced Terrestrial Simulator (ATS) to simulate the near-surface hydrological response (i.e. infiltration and evapotranspiration) and how this impacts groundwater recharge. ATS is an ecosystem-based, integrated, distributed hydrology simulator that is built on the underlying multi-physics framework provided by Amanzi, the high performance computing simulator developed in the ASCEM program used for environmental applications to provide flexible and extensible flow and reactive transport simulation capability. The output of the ATS model includes predictions of infiltration rates over selected regions of interest, such as sinkholes, and groundwater recharge, and hence ensembles of ATS simulations facilitate sensitivity and uncertainty analysis of groundwater and surface water flows.

FIU began virtual training on ATS to develop a detailed understanding of the ATS-Amanzi model. This training was initiated on a weekly basis led by LANL scientists; however, FIU experienced a setback due to loss of technical personnel midway through the fiscal year. To ensure continuity of the work scope during FIU's search for a substitute Post-Doc and Senior Research Scientist, FIU continued the training in the form of a student (DOE Fellow) internship throughout the summer of 2021, during which FIU staff participated in weekly Zoom meetings to facilitate knowledge transfer. The internship incorporated training on many of the hydrological modeling skill sets required for the research work being conducted at FIU ARC. FIU also prepared slides and presented the work conducted under this subtask during the annual DOE-FIU Cooperative Agreement Program Review.

Subtask 6.2: Results and Discussion

Groundwater Model Development: ASCEM Training

FIU's training on Akuna enabled successful development and execution of a sample test case using the HPC (high-performance computer) Cori provided by NERSC and visualization of the result of the hydrologic components using VisIt, an open-source interactive parallel visualization and graphical analysis tool for viewing scientific data.

An existing Culebra MODFLOW model was also shared by the CBFO collaborator, where the majority of model inputs for the MODFLOW model could be applied for the ASCEM groundwater model. FIU then began learning data preprocessing tools (e.g., LaGriT) and creating data layers for the ASCEM model including conversion of the MODFLOW inputs. Figure 130 shows preliminary examples of preprocessed data layers including a digital elevation model (DEM) of Basin 6 at the resolution of 10 meters, and the initial head for the Culebra formation from the MODFLOW model.

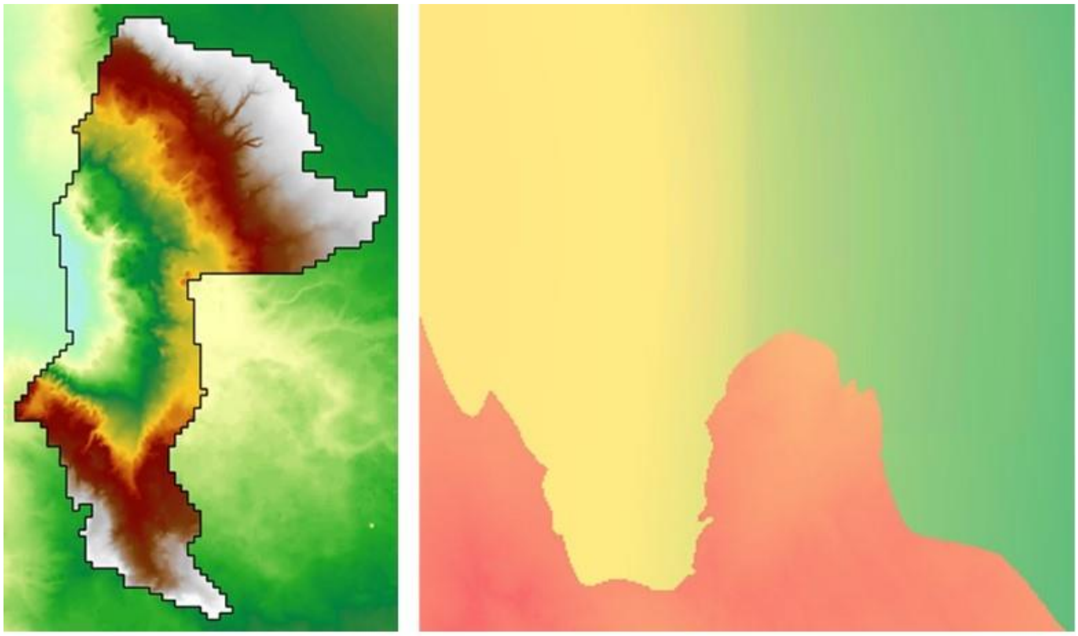

Figure 130. Digital elevation model (DEM) delineated for Basin 6 based on 10-meter resolution DEM acquired from USGS (left) and initial head for the Culebra formation acquired from the MODFLOW model (right).

FIU began to employ the Culebra MODFLOW model input to define the model components for the ASCEM Basin 6 groundwater model. The inputs included lower/upper boundaries, initial hydraulic head, transmissivity, anisotropy, recharge and storativity. Figure 131 shows an example of the initial hydraulic head in the context of Basin 6, which could assist with the definition of model boundaries.

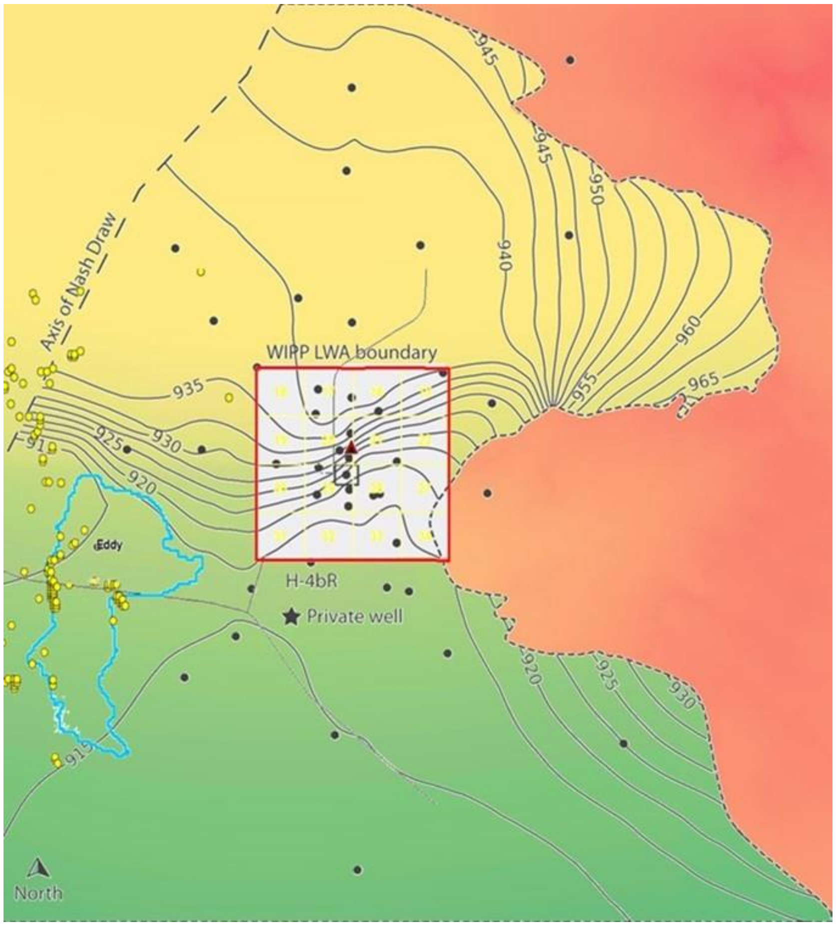

Figure 131. Initial hydraulic head in the of the Culebra MODFLOW model in the context of Basin 6.

Initially, technical difficulty was encountered setting up the proper environment for the python application of LaGriT, pyLaGriT, as one of the dependencies, General Mesh Viewer (GMV), required an alternative Linux environment. FIU ARC's IT support was however able to quickly resolve the issue and the pyLaGriT environment was properly configured.

Next the model input from the Culebra MODFLOW model was georeferenced (using the WIPP Land Withdrawal Act (LWA) boundary as anchor points) and visualized in ArcGIS Pro, including lower/upper boundaries, initial hydraulic head, transmissivity, anisotropy, recharge and storativity. Figure 132 shows the bottom boundary of the Culebra formation in the context of Basin 6 as an example, which could assist the definition of the model boundaries.

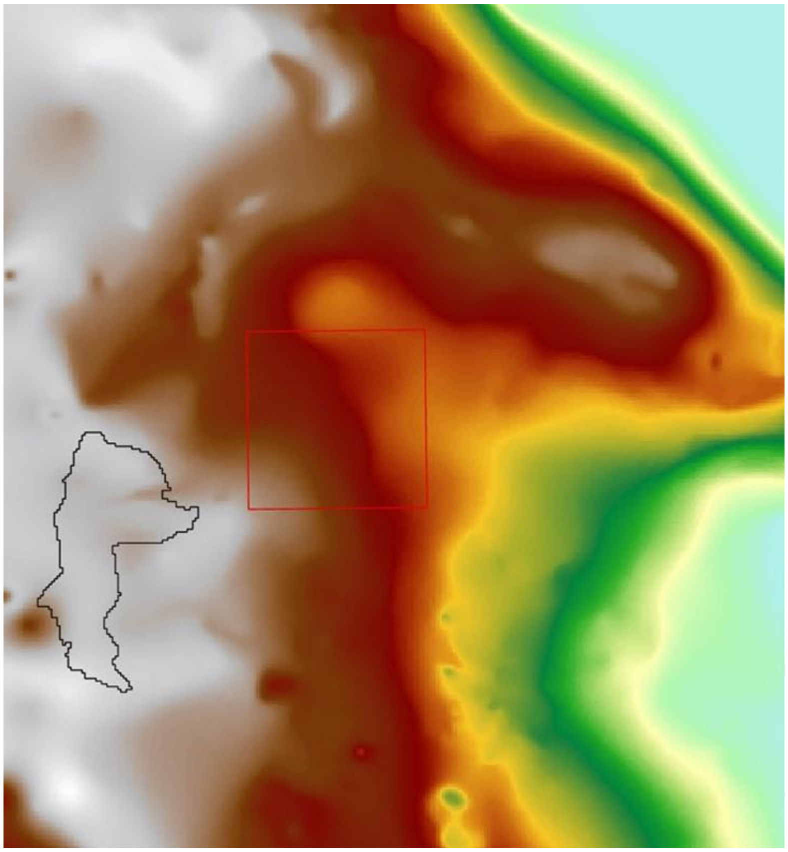

Figure 132. Bottom boundary of the Culebra MODFLOW model where the WIPP LWA boundary is outlined in red and Basin 6 is outlined in black.

Surface Hydrological Model Development: Amanzi-ATS Training

As formerly mentioned, FIU began virtual training on ATS to develop a detailed understanding of the ATS-Amanzi model, which was initiated on a weekly basis led by LANL scientists. This training was transitioned to a DOE Fellow student summer internship upon the departure of the technical leads on this subtask from FIU to ensure continuity of the work and maintain the knowledge transfer. Training of FIU staff will resume once the positions of the technical leads have been filled.

The DOE Fellow began her virtual summer internship with Los Alamos National Laboratory on June 1, 2021. The focus was primarily on the Amanzi-ATS training required for development of an integrated hydrology model of Basin 6 near the Waste Isolation Pilot Project (WIPP) site to investigate groundwater recharge; therefore, the first step was to become familiar with the platform and tools required to generate the input files for the ATS model. An overview of the tools and open-source software to be used was given, as well as an introduction to mesh generation with TINerator for creating uniform and variable resolution meshes, focusing on surface flow and surface features.

An example Jupyter notebook using TINerator was reviewed, which showed the steps to load a DEM, perform a watershed delineation, and generate a triangulated mesh, a volumetric mesh and a surface mesh. The visualization software, ParaView, which can be used to visualize the created mesh, was also demonstrated. Once this example notebook was reviewed, a new Jupyter notebook was generated for a smaller watershed named Borden. A mesh was generated using TINerator after which efforts were focused on developing the input files for the ATS model.

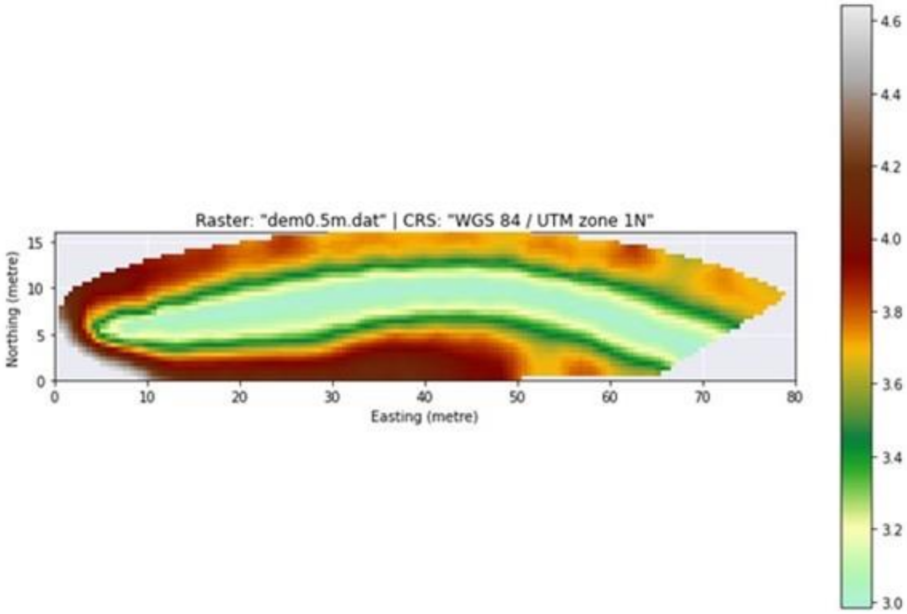

Figure 133. Digital elevation model (DEM) with a resolution of 0.5 meters of the Borden watershed.

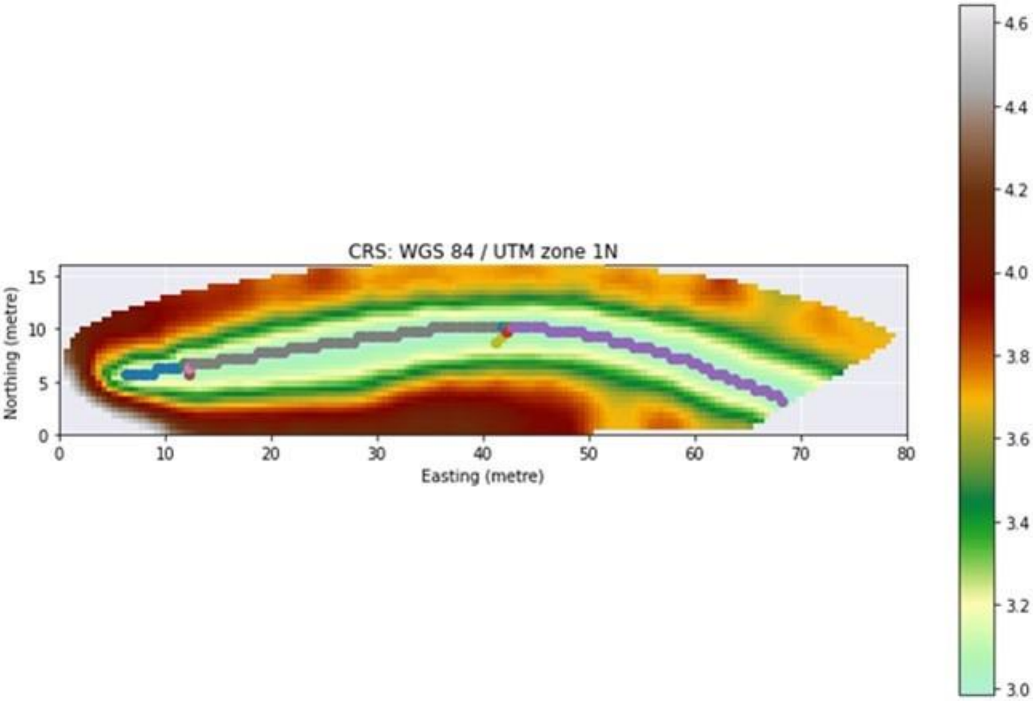

Figure 134. Watershed delineation on Borden watershed.

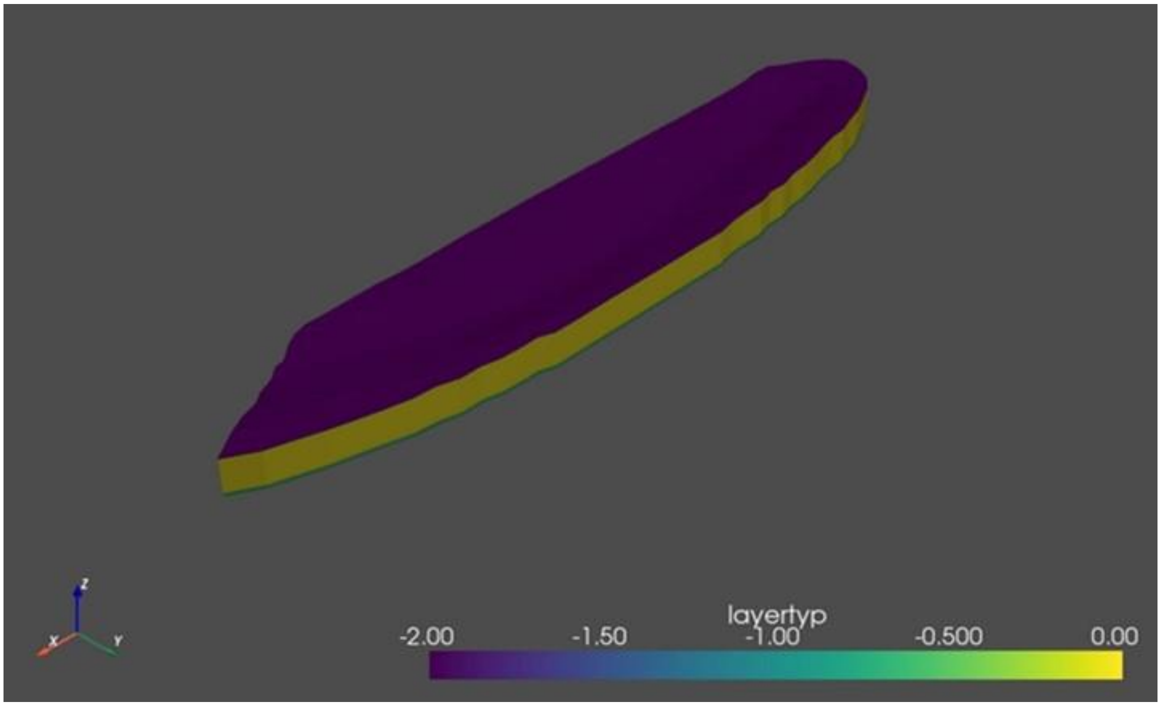

Figure 135. Surface mesh of the Borden watershed generated using TINerator.

The next task assigned was to setup and run surface water flow simulations with different rain events to explore the impact of different mesh resolutions and refinement, to visualize the surface flow results using VisIT and to expand the mesh generation with TINerator to create a more realistic subsurface mesh. A surface water flow simulation of a 12-hour rainfall event using ATS was conducted, after which the visualization software programs, ParaView and VisIT, were explored using the output files created from the ATS simulation. Training was also received on how to use Git and ssh keys in order to upload files and connect remotely from a Mac computer terminal.

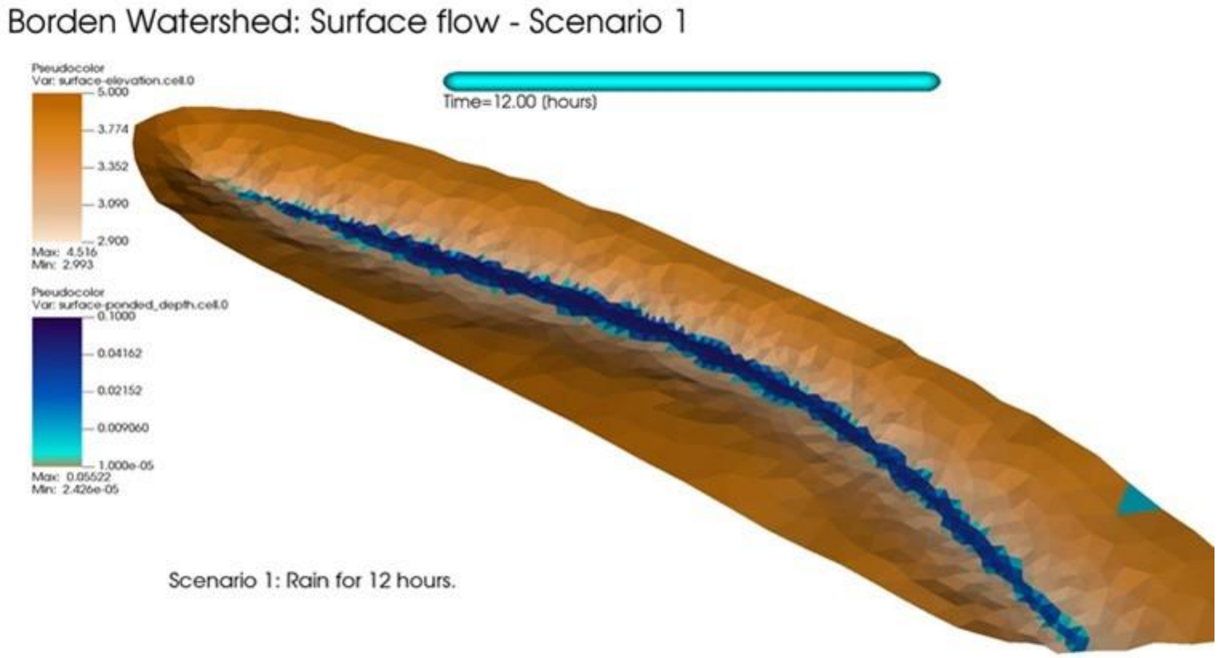

Figure 136. Simulation of overland flow with a rainfall event of 12 hours using ATS.

During the internship a workflow for ATS model development was established using a small subset of the Basin 6 study area for testing. FIU will continue to work under the guidance of LANL collaborators to implement this workflow for the entire Basin 6 study area.

Subtask 6.2: Conclusions

During FIU Year 1, FIU's research under this subtask has included training on the ASCEM toolset provided by PNNL collaborators, which included getting familiar with the Akuna interface; use of an existing Culebra MODFLOW model to extract several model inputs that could be applied to FIU's preliminary groundwater model development; training on data preprocessing tools and creating layers for the groundwater model; and training on the ATS code under the guidance of our LANL collaborators to begin development of an integrated surface water/groundwater hydrological model of Basin 6.

During FIU Year 2, FIU will initiate the development of the ATS-Amanzi model of the Basin 6 study domain using the data derived from Subtask 6.1. Hydrological, climate and topography datasets will be collected from DOE and various national database platforms. Furthermore, FIU will continue improving our understanding of the groundwater models available in the ASCEM modeling platform for the Culebra Dolomite Member (Culebra) of the Permian Rustler Formation, which is a potential radionuclide release pathway from the WIPP as started in Year 1. Given the uncertainty of the impact of small-scale hydrological features on infiltration and groundwater recharge, FIU proposes to use both the high-resolution DEM developed in Subtask 6.1 as well as other available coarser-scale DEMs (e.g. at 10, 30 or 90 m resolution).

For FIU Year 2 the workflow established during the student summer internship at Los Alamos Laboratory will be employed for the Basin 6 study area to perform a series of ATS simulations, including the generation of meshes from the DEM data, setting up of meteorological forcing data, development of input files for the ATS, executing simulations on local or remote systems, and analyzing the output. Jupyter notebooks will be utilized to detail each of the steps in this workflow.

Additionally, Amanzi provides an advanced mesh infrastructure for the ATS that is capable of reading large 3D meshes in parallel, subsetting meshes, managing multiple meshes, and deforming them. For this project, the open-source Python module TINerator will be used for the creation of unstructured 3D and 2.5D meshes from GIS data sources. With TINerator, a DEM can be imported and an unstructured triangulated mesh generated to represent the surface topography in the ATS model. This unstructured mesh can then be further refined (smaller triangles) near selected topographic features, such as stream networks and sinkholes. The topographic features can be identified in a number of ways, including externally provided shapefiles and internal processing by TINerator of the DEM. The development of the ATS model for Basin 6 will require the development of an unstructured mesh using TINerator and will serve as the input for the ATS.

The ongoing ATS training designed and executed by LANL will be held one day per week to support Basin 6 ATS model development. The remaining training will be reactive in nature as it will be designed based on the technical needs from FIU. Once developed, in subsequent years (FIU Years 3 and 4) the ATS will be coupled with the ASCEM GWM to gain an improved understanding of how infiltration variability at the land surface impacts groundwater recharge (using ATS) and how this subsequently impacts regional groundwater flow.

Subtask 6.2: References

Beauheim, R. L. (2009). Collection and integration of geoscience information to revise the WIPP hydrology conceptual model. In *Approaches and challenges for the use of geological information in the safety case for deep disposal of radioactive waste*.

Coon, E. T., Moulton, J. D., & Painter, S. L. (2016). Managing complexity in simulations of land surface and near-surface processes. Environmental modelling & software, 78, 134-149.

Corbet, T. F., & Knupp, P. M. (1996). *The role of regional groundwater flow in the hydrogeology of the Culebra Member of the Rustler Formation at the Waste Isolation Pilot Plant (WIPP), southeastern New Mexico* (No. SAND-96-2133). Sandia National Lab, Albuquerque, NM (United States).

Freedman, V. L., Agarwal, D., Bensema, K., Finsterle, S., Gable, C. W., Keating, E. H., Krishnan, H.. Lansing, C., Moeglein, W., Pau, G. S. H., Porter, E., Scheibe, T. D. *Akuna: An Open Source User Environment for Managing Subsurface Simulation Workflows.* American Geophysical Union, Fall Meeting 2014.

Hart, D. B., McKenna, S. A., & Beauheim, R. L. (2009). *Calibration of the WIPP culebra transmissivity fields* (No. SAND2009-7334C). Sandia National Lab.(SNL-NM), Albuquerque, NM (United States); Sandia National Laboratories,, Carlsbad, NM.

Hayes, A. (2019). *Culebra Hydrologic Model in WIPP Performance Assessment* (No. SAND2019-4432PE). Sandia National Lab.(SNL-NM), Albuquerque, NM (United States).

Sampson, K., & Gochis, D. (2018). *WRF Hydro GIS Pre-Processing Tools, Version 5.0 Documentation.* Boulder, CO: National Center for Atmospheric Research, Research Applications Laboratory.

Wehbe, Y., Temimi, M., Weston, M., Chaouch, N., Branch, O., Schwitalla, T., Wulfmeyer, V., Zhan, X., Liu, J. and Al Mandous, A. (2019). *Analysis of an extreme weather event in a hyper-arid region using WRF-Hydro coupling, station, and satellite data.* Natural Hazards & Earth System Sciences, 19(6).

Yucel, I., Onen, A., Yilmaz, K. K., & Gochis, D. J. (2015). *Calibration and evaluation of a flood forecasting system: Utility of numerical weather prediction model, data assimilation and satellite-based rainfall.* Journal of Hydrology, 523, 49-66.

Zeitler, T. R. (2016). *WIPP Performance Assessment* (No. SAND2016-8142PE). Sandia National Lab.(SNL-NM), Albuquerque, NM (United States).

TASK 7: ENGINEERED MULTI-LAYER AMENDMENT TECHNOLOGY FOR MERCURY REMEDIATION ON THE OAK RIDGE RESERVATION

Task 7: Introduction

Legacy wastes from past weapons production and industrial uses from coal-fired power plants to artisanal gold mining have resulted in over 3,000 mercury-contaminated sites globally (Kocman et al., 2013). As increased economic activity and disposal of mercury-added products continue to offset concerted efforts to reduce mercury releases to the environment, there is the growing need for sustainable and cost-effective remediation technologies to combat mercury contamination (Futsaeter and Wilson, 2013). Remediation of mercury poses long-term challenges due to its persistent geochemistry, bioaccumulative effect and continuous cycling through the environment. Moreover, the existence of diffuse mercury sources further complicates technology development efforts for mercury remediation in freshwater stream systems, such as the East Fork Poplar Creek (EFPC), Oak Ridge, Tennessee (Southworth et al., 2010).

As a case study, EFPC, a 26-kilometer low-gradient stream in Oak Ridge, Tennessee received from the headwater at Y-12 (National Security Complex) approximately 128,000 ±35000 kg of mercury (Hg) from 1950 to 1963, resulting in contamination of floodplain soils, surface water and streambed sediment of the EFPC ecosystem (Brooks and Southworth, 2011). Despite remedial actions in the early 1980s that significantly reduced Hg inputs at the source zone in Y-12, EFPC is still classified as an impaired waterbody due to elevated concentrations of Hg in soil, water and biota. Annual mercury and methyl mercury fluxes to EFPC from streambank soil is estimated as 38.6 kg and 5.6 g, respectively (Watson et al., 2016). Streambank soils and Y-12 discharge account for the vast majority of mercury export from the EFPC watershed. Although floodplain runoff and infiltration exert some influence on Hg flux to the EFPC stream system, these contributions are small compared to Hg flux from Y-12 and streambank soil. The spatial distribution, speciation and the extent of Hg contamination have been well documented in several studies within EFPC in the last few years (Peterson et al., 2018; Riscassi et al., 2016; Southworth et al., 2010). Approximately 60% of mercury exiting Y-12 is in the dissolved inorganic phase (Hg^{2+}) which becomes increasingly complexed with natural dissolved organic matter (DOM, at ~3 mg/L) with distance downstream (Dong et al., 2010a).

Typically, mercury remediation technology involves either the reduction of its bioavailability for methylation or flux to the environment. While sorbent amendments are affective at sequestering mercury, they are less effective at reducing mercury bioavailability for methylation (Katherine A. Muller and Brooks, 2019; K. A. Muller et al., 2019). Moreover, fouling problems of sorbents can lead to potential leaching of constituents and particles into waterbodies, thereby severely limiting their applications for Hg sequestration (Johs et al., 2019). Mercury fate and transport in EFPC are governed by its strong interaction with dissolved organic matter, which renders Hg^{2+} binding to sorbents and removal from the water column by strong reductants, such as stannous chloride ($SnCl_2$), problematic (Dong et al., 2010b; Liang et al., 2010). It has been shown that DOM can outcompete mercury for sorption sites on amendment materials such as activated carbon (AC) and biochar, decreasing the overall effectiveness of these materials for mercury sequestration

(Katherine A. Muller and Brooks, 2019). The reduction in overall effectiveness is attributed to AC-DOM interaction rather than the direct interaction between AC and Hg (Eckley et al., 2020).

Despite ubiquitous use of amendments for in-situ sequestration of organic contaminants, large-scale application of sorbents for mercury remediation is uncommon (Gilmour et al., 2013; Gomez-Eyles et al., 2013; Schwartz et al., 2019; Wang et al., 2020; Wang et al., 2019). Mercury sorbents may be highly effective in mitigating mercury releases into the environment; however, their large-scale use may be cost-prohibitive and less effective in the presence of DOM.

Task 7: Objectives

The main objective of this study is to evaluate a suite of sustainable sorbents for cost-effective removal of mercury in the presence of DOM. The specific goal of this study is to evaluate the effectiveness of these sustainable sorbents to remove mercury in the presence of DOM. As such, the scope of this study was to determine the maximum sorption capacity, kinetics and adsorption mechanism to inform effective design of remediation technologies for mercury capture.

Task 7: Methodology

A suite of sorbent media was evaluated for removal of aqueous mercury (Hg^{2+}) phase(s) from contaminated creek water (Table 33). The investigated sorbent materials included the following: (1) Biochar (Biochar Now); (2) Sorbster (Sorbster, Inc.), (3) Si-thiol (Biotage®), (4) Mackinawite blended powdered activated carbon (Redox Solutions, LLC), (5) Powdered activated carbon (Cabot Corporation), 6) Organoclay PM-199 (CETCO Minerals Technologies), 7) Filtrasorb 300 (Calgon Carbon Corporation) and (8) RemBind (RemBind Pty Ltd). The sorbents were evaluated due to their sustainability, low-cost (except Si-thiol) and anticipated high adsorption capacity for aqueous mercury. Most of these sorbent media were either carbon-based materials or functionalized silica/clays (Table 33).

Table 33. A list of evaluated sorbent media for mercury sorption.

Sorbents	Description	Manufacturer
Powdered activated carbon (Norit SedimentPure PAC)	Finely milled activated carbon particles produced from lignite coal	Cabot Corporation, Boston, MA
Mackinawite (FeS) blended powdered activated carbon	An equal blend of abiotically synthesized mackinawite and finely ground carbon produced from lignite coal	Redox Solutions, Carmel, IN
Biochar	Charcoal, anaerobically produced via high-temperature, slow pyrolysis of plant biomass (mostly wood chips)	Biochar Now, LLC, Loveland, CO
Filtrasorb 300	Granular activated carbon produced from bituminous coal via reagglomeration process	Calgon Carbon Corporation, Moon Township, PA
Silica thiol (Si-Thiol)	A silica gel (backbone) modified with sulfur-containing organic compound (1-propanethiol)	Biotage LLC, Charlotte, NC
RemBind	Powdered carbon-mineral blend of aluminum oxyhydroxide, activated carbon, clays and other proprietary additives	RemBind Pty Ltd, Thebarton, Australia
Sorbster	An activated alumina blended with iron oxide and sulfur	Sorbster, Inc., Euclid, OH
Organoclay PM 199	Sodium bentonite clay modified with quaternary ammonium	CETCO Mineral Technologies, Hoffman Estates, IL

Mercury Standards

A mercury stock standard traceable to NIST SRM 3133 was purchased from Alfa Aesar (Ward Hill, MA). The as-received stock solution (Specpure®) containing 1,000 ± 5 µg/mL Hg^{2+} in 5% HNO_3 was stored at 4ºC and was diluted to the desired working concentration for the batch sorption studies using 5% HNO_3.

Artificial Creek Water (ACW)

An artificial creek water (solution) was employed in these batch sorption studies. The ACW solution is a simulant whose chemical composition closely mimics natural, uncontaminated creek water chemistry found in EFPC. The composition of the ACW is as follows: 41.5 mg/L Ca^{2+}, 27.38 mg/L Na^+, 1.89 mg/L K^+, 12.05 mg/L Mg^{2+}, 14.83 mg/L Cl^-, 197.06 mg/L NO_3^-, and 33.86 SO_4^{2-} (Goñez-Rodríguez et al., 2021). All chemicals were ACS reagent grade or better in purity and used as received. Sodium chloride, sodium nitrate, sodium sulfate, potassium nitrate, magnesium nitrate (Fisher Scientific, Pittsburg, PA), calcium nitrate (Acros Organics, Geel, Belgium), and ultrapure deionized water (>18 MΩ) were used to prepare the ACW. The pH of the ACW was adjusted with either HNO_3 or NaOH (0.1 or 1.0 M) to a pH value of 8 ±0.5.

Batch Sorption Studies

Batch sorption studies were performed to determine mercury adsorption (percent removal) onto sorbent media as a function of time (kinetic) and varying concentration (isotherms) in an artificial creek water solution (ACW) adjusted to a pH value of 8 ±0.5. For the kinetic studies, sorbent ratios ranging from 0.1-10 g/L were added to ACW that was spiked with a known Hg^{2+} concentration (500 ±75 µg/L) without adjustment of pH. Whereas, to determine the adsorption capacity of the sorbent media, equilibrium studies were performed in batch reactors amended with sorbent dosages ranging from 1 to 10 g/L and a fixed Hg^{2+} concentration of 1,000 µg/L without adjustment of suspension pH. All slurry mixtures were stirred on a slow shaker at 100 rpm for 2,880 min (equilibrium studies) and up to 4,320 min (kinetics studies) at 25°C (room temperature). At each time interval, the suspensions were centrifuged with a Sorvall Legend Micro 17 centrifuge (Thermo Scientific, Inc.) at 9,000 rpm for 10 min. Approximately 0.1– 0.2 g of the filtrate volumes were transferred to quartz boats in which Hg^{2+} concentrations were analyzed with a DMA-80 evo (Milestone, Inc.). Sorption coefficient (K_d), kinetic and sorption capacity values were subsequently calculated from the filtrate concentrations using rate equations and adsorption isotherms.

The rate equations (Eq.1 – Eq. 8) given below were used to assess the kinetics of Hg^{2+} sorption onto the studied sorbent material(s).

The percent adsorption or removal efficiency (R_E) and adsorbed amount (Q_t) of Hg^{2+} were computed as follows:

$$\mathbf{R_E\ (\%) = \frac{C_0 - C_t}{C_0} \times 100} \qquad \mathbf{Eq. 1}$$

$$\mathbf{Q_t = \frac{V(C_0 - C_t)}{m}} \qquad \mathbf{Eq. 2}$$

$$\mathbf{K_d = \frac{(C_0 - C_t)}{C_t} \times \frac{V}{m}} \qquad \mathbf{Eq. 3}$$

where C_0 is the initial aqueous Hg^{2+}concentration in the sorbent-free solution (Hg^{2+} concentration at the beginning of the experiment); C_t (mg/L) is the effluent final Hg^{2+} concentration after equilibration with the sorbents; K_d (mL/g) is the distribution coefficient; V is the volume of suspension (L); and m is the mass of added sorbent phase(s) (g).

The pseudo-first order, PFO (Langergren's equation) is expressed below (Lagergren, 1898):

$$\mathbf{\ln(Q_e - Q_t) = \ln Q_e - k_1 t \quad (Linear\ form)} \qquad \mathbf{Eq. 4}$$

$$\mathbf{Q_t = Q_e\left(1 - e^{-k_1 t}\right) \quad (Nonlinear\ Form)} \qquad \mathbf{Eq. 5}$$

The expressions of the pseudo-second order (PSO) are given below (Blanchard et al., 1984):

$$\mathbf{\frac{t}{Q_t} = \frac{1}{k_2 Q_e^2} + \left(\frac{1}{Q_e}\right) t \quad (Linear\ form)} \qquad \mathbf{Eq. 6}$$

$$\mathbf{Q_t = \frac{Q_e^2 k_2 t}{1 + k_2 Q_e t}} \quad \textbf{(Nonlinear form)} \qquad \textbf{Eq. 7}$$

The initial adsorption rate *h* is derived from the expression: $h = k_2 Q_t^2$

The intraparticle diffusion model is useful for distinguishing rate-controlling steps and predicting reaction pathways and adsorption mechanisms. This kinetic model is dependent on the porosity, size of particles, solution concentration and agitation velocity. Its linearized expression is as follows (Weber Jr and Morris, 1963):

$$\mathbf{Q_t = k_p \sqrt{t} + C} \quad \textbf{(Linear Form)} \qquad \textbf{Eq. 8}$$

where Q_t (mg/g) and Q_e (mg/g) are the amount of Hg^{2+} adsorbed at time *t* (min) and at equilibrium, respectively; k_1 (1/min) is the pseudo-first-order rate constant; k_2 (g/mg × min) is the pseudo-second-order rate constant; k_p is the intraparticle diffusion constant (mg/g × $min^{1/2}$); and *C (*mg/g) is the liquid film or boundary layer thickness.

The Langmuir adsorption isotherm describes monolayer adsorption onto homogeneous finite sites of sorbent surfaces without interaction between adsorbed molecules (i.e., the adsorbate species). When the observed experimental data are well described by the Langmuir model, the R_L (a dimensionless separation factor; *Eq. 11*) is especially useful for predicting the favorability of the adsorption process based on the initial concentration of the adsorbate (Hg^{2+}). When $R_L > 1$, the adsorption is considered unfavorable; $R_L = 1$, the adsorption is linear; $0 < R_L < 1$, the adsorption is favorable, and when $R_L = 0$, the adsorption is irreversible.

The Freundlich isotherm describes multilayer adsorption onto heterogeneous surfaces that are characterized by interaction among adsorbates.

The Langmuir equations are expressed below (Langmuir, 1918):

$$\mathbf{\frac{1}{Q_t} = \left(\frac{1}{Q_m K_L}\right)\frac{1}{C_t} + \frac{1}{Q_m}} \quad \textbf{(Linear model)} \qquad \textbf{Eq. 9}$$

$$\mathbf{Q_t = \frac{Q_m K_L C_t}{1 + K_L C_t}} \quad \textbf{(Nonlinear model)} \qquad \textbf{Eq. 10}$$

$$\mathbf{R_L = \frac{1}{1 + K_L Q_m C_0}} \qquad \textbf{Eq. 11}$$

The expressions for the Freundlich equations are as follows (Freundlich, 1906):

$$\mathbf{\log Q_t = n \log C_t + \log K_F} \quad \textbf{(Linear model)} \qquad \textbf{Eq. 12}$$

$$\mathbf{Q_e = K_F C_t^n} \quad \textbf{(Nonlinear model)} \qquad \textbf{Eq. 13}$$

where K_L (L/mg) is the Langmuir constant related to the affinity between the adsorbate (Hg^{2+}) and sorbent, and it is essentially the reciprocal of the concentration at which the sorbent is 50% saturated; Q_m (mg/g) is the maximum monolayer adsorption capacity of the sorbent; K_F [(mg/g)/(mg/$L)^n$] is the Freundlich constant characterizing the adsorption strength; and n is the dimensionless Freundlich intensity parameter related to adsorption intensity and/or surface heterogeneity.

Studies have shown that errors associated with experimental data are typically transformed during the linearization of adsorption data. Thus, non-linearized regression analyses were conducted on the original form of the adsorption equations. Nonlinear regression typically involves the minimization of error distribution between the experimental data and predicted values. The estimation of the pertinent sorption parameters in the nonlinear models was performed using experimental data. The estimated values were subsequently used for validation by comparing the predicted values with the observed values over the duration of the batch sorption experiments.

The modeling errors for the nonlinear models were evaluated with the sum of squared errors (SSE), which is the difference between the predicted and measured adsorption values as follows:

$$\mathbf{SSE} = \sum_{\mathbf{i}}^{\mathbf{n}} (\mathbf{O_i} - \mathbf{P_i})^2 \qquad \mathbf{Eq.\,14}$$

where is O_i and P_i are experimental and model-predicted values, respectively.

The minimization of SSE was performed in a Microsoft Excel spreadsheet using the add-in Solver coupled with the generalized reduced gradient nonlinear algorithms. A small SSE value is indicative of the quality and predictive performance of the model to accurately fit the observed experimental data. Moreover, the determination coefficient (R^2), an indicator of the model precision and therefore the quality of the fit, was calculated as follows ([Lima et al., 2015; Schwarz, 1978):

$$\mathbf{R^2} = \mathbf{1} - \left(\frac{\sum_{\mathbf{i}}^{\mathbf{n}} (\mathbf{O_i} - \mathbf{P_i})^2}{\sum_{\mathbf{i}}^{\mathbf{n}} (\mathbf{O_i} - \overline{\mathbf{O}}_{\mathbf{i}})^2} \right) \qquad \mathbf{Eq.\,15}$$

where $\overline{O}_i$ is the average value of observed experimental data. To evaluate the robustness of models, the differences in Bayesian Information Criteria (ΔBIC) were employed. The expression is given in the equation below (Schwarz, 1978):

$$\mathbf{BIC} = \mathbf{nLn}\left(\frac{\mathbf{SSE}}{\mathbf{n}}\right) + \mathbf{pLn(n)} \qquad \mathbf{Eq.\,16}$$

where *n* is the number of data points and *p* is the number of parameters in the fitting model

The ΔBIC is defined as the difference between a BIC value from one model (e.g. Langmuir model) and BIC value from another model (e.g. Freundlich model). When the $\Delta\text{BIC} \leq 2$, there is no significant difference between the applied models; $2 < \Delta\text{BIC} < 6$, there is a high probability that the model with the lower BIC value is the most appropriate; $6 < \Delta\text{BIC} < 10$, there is high probability that the model with the lower BIC is the better fitting model, and $\Delta\text{BIC} > 10$, it can be predicted with a high degree of confidence that the model with the lower BIC is the better fitting model (Schwarz, 1978).

Physiochemical Properties

The SEM secondary electron micrographs for select untreated sorbent media are presented in Figure 137. The morphology of the untreated materials ranges from irregular to spherical (Figure 137B-F), to platy (Figure 137A) particles that clustered into larger agglomerates. The SEM sizes of the particles typically range from 0.5 – 60 µm. BET surface area and particle sizes reported in literature and by the manufacturers are displayed in Table 34. Surface area ranges from 60.7 to 588 m^2/g, while particles sizes varied from 1 to 1000 µm, respectively. The PAC and Si-thiol sorbents exhibited highest BET surface areas and smallest particle sizes among the evaluated materials.

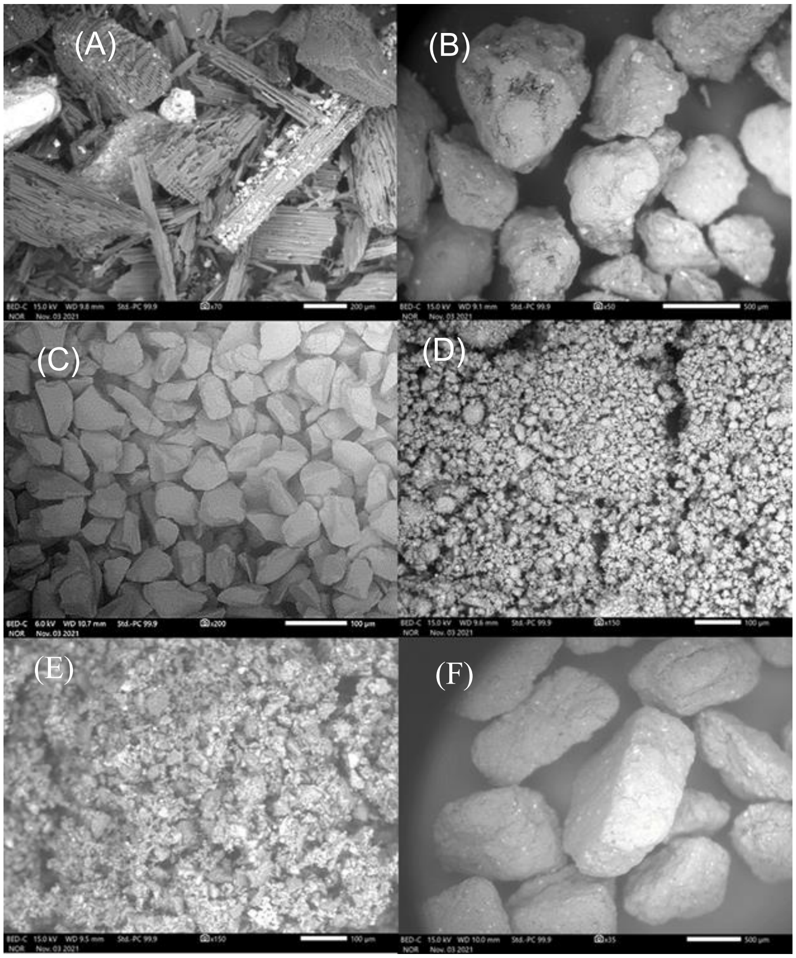

Figure 137. SEM micrographs of uncoated, select sorbent media at various magnifications; Biochar (A, 70x), Filtrasorb 300 (B, 50x), Si-thiol (C, 200x) Sorbster (D, 150x), FeS+PAC (E, 150x), Organoclay PM 199 (F, 35x)

Table 34. Physiochemical Properties of Select Sorbent Media

Sorbents	BET surface Area (m^2/g)	Particle size (μm)	Reference
Powdered activated carbon (PAC)	588	44 - 74	Cabot Corporation
Mackinawite (FeS) blended PAC	436	0.05 - 200	Jeong et al. 2008
Biochar	219.4	300 - 700	Jiang et al. 2017
Filtrasorb 300	N/A	800 -1000	Calgon Carbon Corp
Silica thiol (Si-thiol)	500	40 - 63	Biotage LLC
RemBind	123.4	500	Braunig et al. 2021
Sorbster MM-1	N/A	420 - 840	Sorbster Inc.
Organoclay PM 199	60.7	74	Santamarina et al. 2002

Task 7: Results and Discussion

The effect of sorbent concentrations as a function of time on mercury adsorption onto a suite of sorbent media were investigated and results of the batch kinetic studies are presented in Figure 138 and Figure 139. The kinetic data demonstrated a steady state adsorption of mercury onto the evaluated media, approaching equilibrium within 4,320 min. Increasing the sorbent dosages resulted in faster kinetics of mercury sorption onto the evaluated sorbents. For PAC, FeS+PAC, Sorbster and Si-thiol, adsorption was rapid, with >90% of the equilibrium concentration adsorbed within 10 min. Extension of the adsorption duration up to 1,440 min (data not shown) did not appreciably alter the established equilibrium adsorption of Hg^{2+} onto these sorbents. The sorbents were ranked by the rate of mercury sorption as follows: PAC > Sorbster > FeS+PAC > Si-thiol ≅ RemBend > Biochar > Filtrasorb > Organoclay.

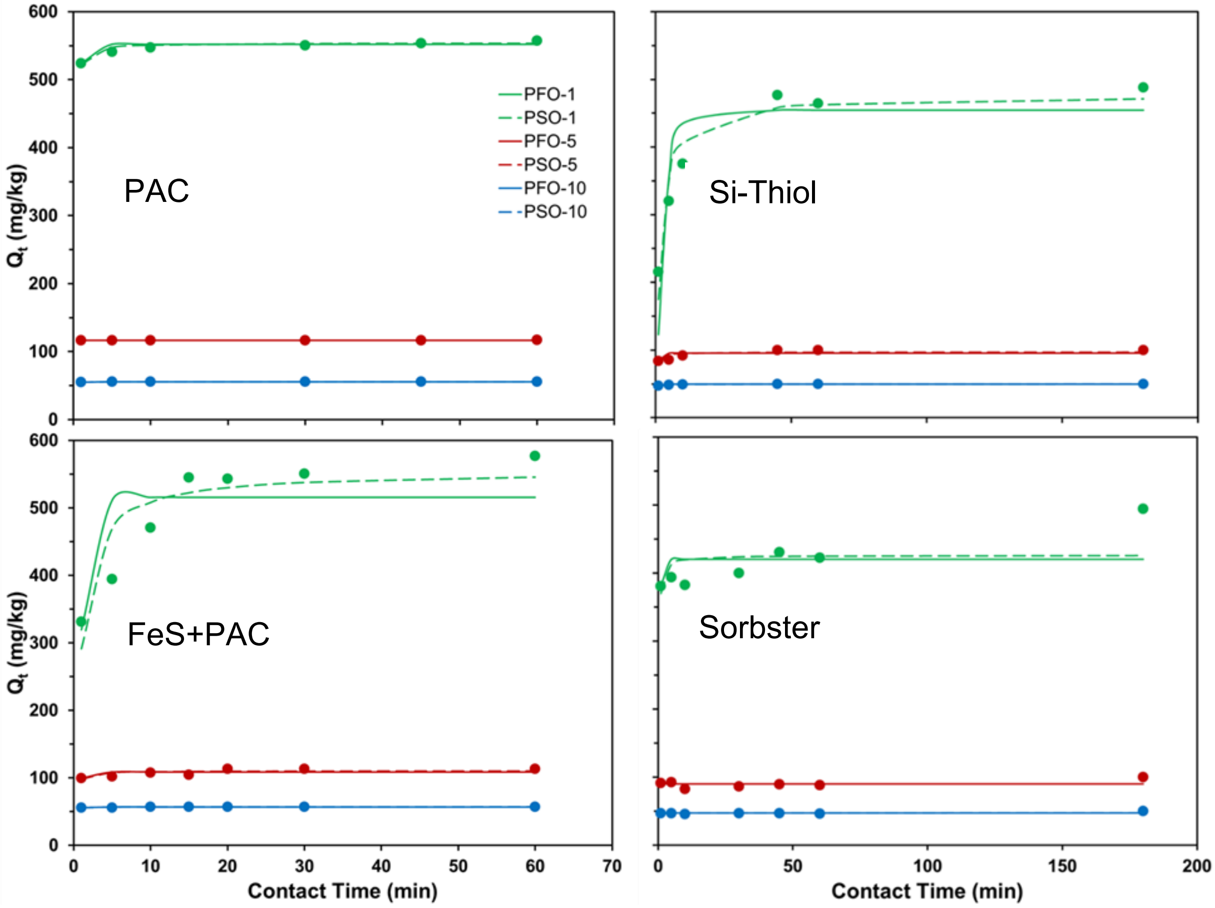

Figure 138. The nonlinear pseudo first and pseudo second order plot for Hg^{2+} adsorption onto a suite of sorbents media in ACW at pH = 8. Experimental conditions included a Hg^{2+} concentration of 500 ±75 µg/L µg/L, solid:liquid ratio of 1 g/L (S-1), 5 g/L (S-5) and 10 g/L (S-10), contact time of 60 – 180 min, and two replicates.

As linearization of adsorption models could yield meaningless parameters, nonlinear equilibrium and kinetic adsorption models were employed to model adsorption data. Furthermore, linearized equilibrium and kinetic adsorption models that provide high R^2 values close to unity are considered unreliable. The correlation coefficient (R^2) of the nonlinear pseudo-second-order kinetic model was generally higher than that for the nonlinear pseudo-first-order kinetic model. Moreover, the ΔBIC values were typically greater than 2, corroborating the applicability of the pseudo-second-order model as the best predictor of kinetic parameters for Hg^{2+} adsorption onto the studied sorbent media.

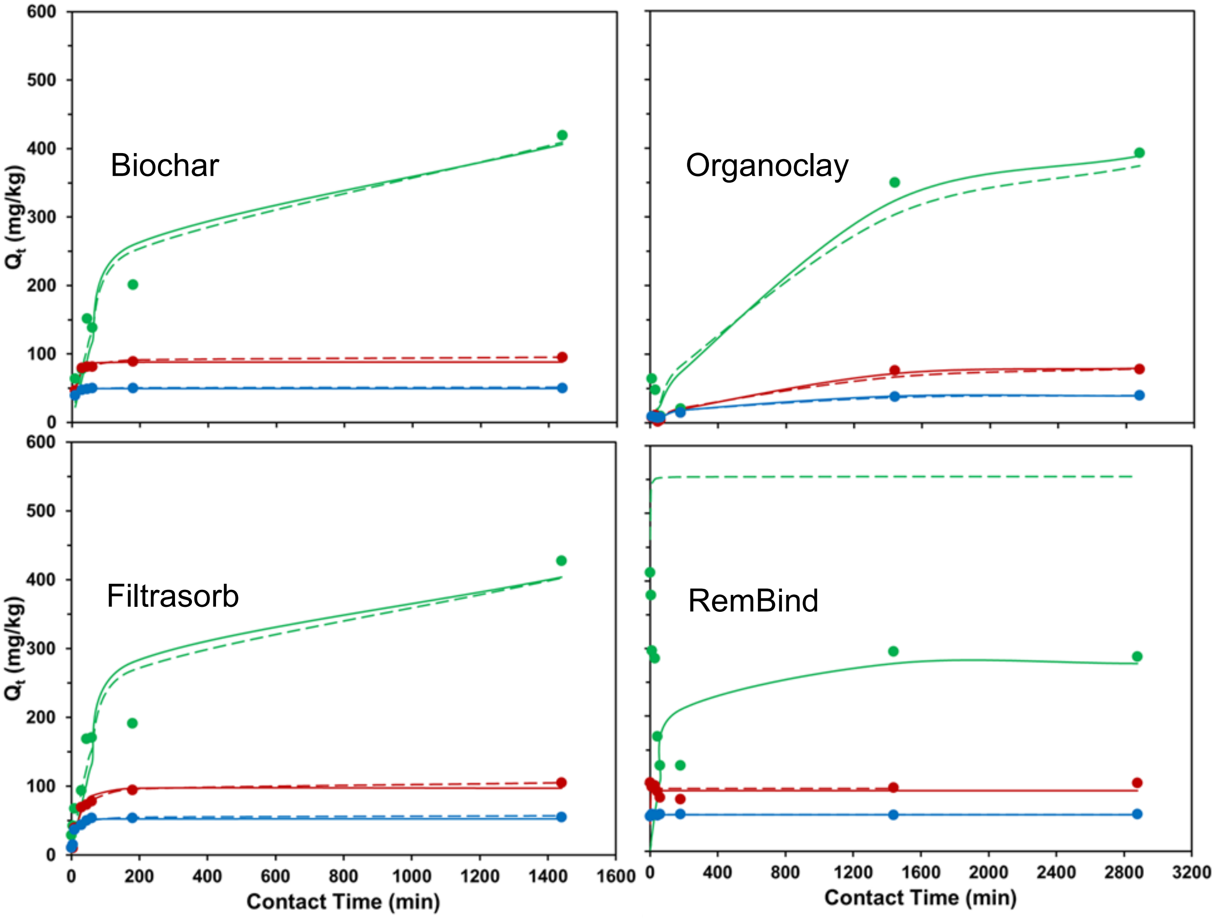

Figure 139. The nonlinear pseudo first and pseudo second order plot for Hg^{2+} adsorption onto a suite of sorbents media in ACW at pH = 8. Experimental conditions included a Hg^{2+} concentration of 500 ±75 µg/L µg/L, solid:liquid ratio of 1 g/L (S-1), 5 g/L (S-5) and 10 g/L (S-10), contact time of 1440 – 2880 min, and two replicates.

The adsorption kinetic is primarily controlled by intra-particle (pore) diffusion when a plot of Q_t against $\sqrt{t}$ is linear and passes through the origin, whereas a plot yielding multiple linear regions is considered an adsorption process governed by a multistep mechanisms. In Figure 140 the intraparticle diffusion plots are non-linear with multiple linear regions that can be grouped into different linear stages over the studied time interval. The initial steep stage accounts for the external mass transfer of Hg^{2+} from the bulk solution to the external surface of the adsorbent material through the hydrodynamic boundary film or layer (film or external diffusion). The later stage of the model is attributed to the pore diffusion (migration of the Hg^{2+} from the adsorbent exterior into the pores of the adsorbent, along pore-wall surfaces, or both) and gradual equlibration of the adsorption process. Thus, the adsorption of Hg^{2+} onto all evaluated sorbent media is primarily controlled by film diffusion. A similar adsorption mechanism was observed with higher sorbent dosages employed in this study. The values of the observed intercept (C) were positive, indicating the influence of boundary layer (film diffusion) restriction on the adsorption process.

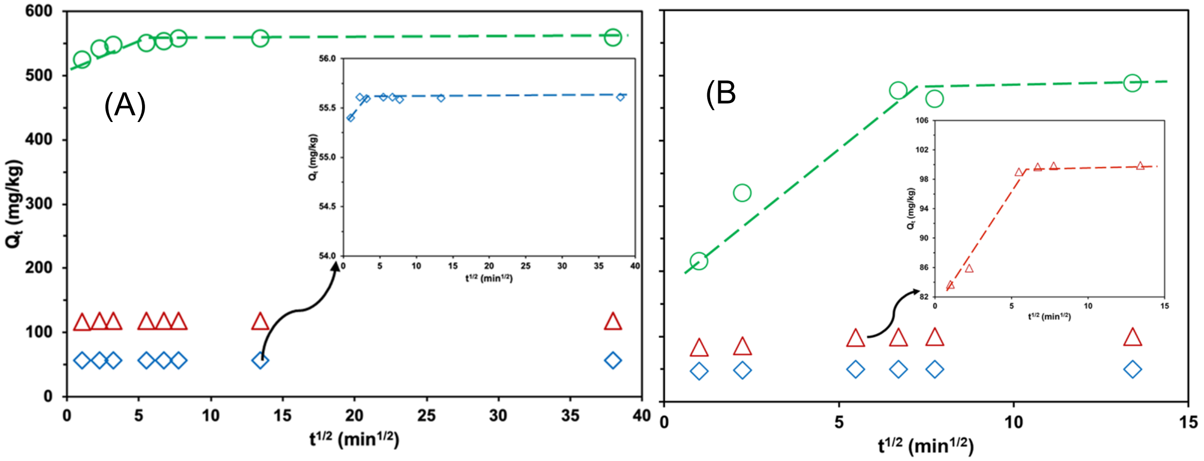

Figure 140. The intraparticle diffusion plot for adsorption of Hg^{2+} by PAC (A) and Si-thiol (B) media in ACW at pH = 8. Experimental conditions included a Hg^{2+} concentration of 500 ±75 µg/L, Solid:liquid ratio of 1 g/L (S-10, unfilled circle), 5 g/L (unfilled triangle) and 10 g/L (unfilled diamond); two replicates. Inset shows a close-up of the plots.

Task 7: Conclusions

Eight low-cost sorbent media were evaluated for mercury removal from a contaminated freshwater stream whose composition mimics that of the EFPC ecosystem. Kinetic parameters computed with kinetic models demonstrated that the nonlinear pseudo-second-order model is a better fitting model compared to the nonlinear pseudo-first-order model to describe observed experimental data (ΔBIC > 2). Furthermore, kinetic data suggest liquid film diffusion was the rate-limiting step that controls mercury sorption. Increasing concentrations of sorbents added to the batch reactors resulted in faster kinetics of mercury sorption. Overall, the rate of mercury adsorption onto the studied sorbent media was ranked in the following order: PAC > Sorbster > FeS+PAC > Si-thiol ≅ RemBend > Biochar > Filtrasorb 300 > Organoclay PM 199. These facile sorbents may provide sustainable solutions for cost-effective remediation of mercury in contaminated environments.

Task 7: References

Kocman, D.; Horvat, M.; Pirrone, N.; Cinnirella, S., Contribution of contaminated sites to the global mercury budget. *Environ Res* 2013**,** *125*, 160-70.

Futsaeter, G.; Wilson, S., The UNEP Global Mercury Assessment: Sources, Emissions and Transport. *E3S Web of Conferences* 2013, *1*, 36001.

Southworth, G. R.; Greeley Jr, M. S.; Peterson, M. J.; Lowe, K. A.; Ketelle, R. H.; Floyd, S. B. *Sources of Mercury to East Fork Poplar Creek Downstream from the Y-12 National Security Complex: Inventories and Export Rates*; ORNL/TM-2009/231; Oak Ridge National Lab. (ORNL), Oak Ridge, TN (United States); Oak Ridge Electron Linear Accelerator: 2010; p Medium: ED.

Brooks, S. C.; Southworth, G. R., History of mercury use and environmental contamination at the Oak Ridge Y-12 Plant. *Environ Pollut* 2011**,** *159* (1), 219-228.

Watson, D. B.; Brooks, S. C.; Mathews, T. J.; Bevelhimer, M. S.; DeRolph, C.; Brandt, C. C.; Peterson, M. J.; Ketelle, R., Evaluation of Lower East Fork Poplar Creek Mercury Sources. 2016, Medium: ED; Size: 128 p.

Peterson, M. J.; Brooks, S. C.; Mathews, T. J.; Mayes, M. A.; Johs, A.; Watson, D. B.; Muller, K. A.; Gonez Rodriguez, L.; Derolph, C. R.; Surendrannair, S. *Mercury Remediation Technology Development for Lower East Fort Poplar Creek - FY2018 Update*; ORNL/SPR-2018/912 United States 10.2172/1490603 ORNL English; ; Oak Ridge National Lab. (ORNL), Oak Ridge, TN (United States): 2018; p Medium: ED; Size: 59 p.

Riscassi, A.; Miller, C.; Brooks, S., Seasonal and flow-driven dynamics of particulate and dissolved mercury and methylmercury in a stream impacted by an industrial mercury source. *Environ Toxicol Chem* 2016**,** *35* (6), 1386-400.

Dong, W.; Liang, L.; Brooks, S.; Southworth, G.; Gu, B., Roles of dissolved organic matter in the speciation of mercury and methylmercury in a contaminated ecosystem in Oak Ridge, Tennessee. *Environmental Chemistry* 2010, *7* (1).

Muller, K. A.; Brandt, C. C.; Mathews, T. J.; Brooks, S. C., Methylmercury sorption onto engineered materials. *J Environ Manage* 2019**,** *245*, 481-488.

Muller, K. A.; Brooks, S. C., Effectiveness of Sorbents to Reduce Mercury Methylation. *Environmental Engineering Science* 2019**,** *36* (3), 361-371.

Johs, A.; Eller, V. A.; Mehlhorn, T. L.; Brooks, S. C.; Harper, D. P.; Mayes, M. A.; Pierce, E. M.; Peterson, M. J., Dissolved organic matter reduces the effectiveness of sorbents for mercury removal. *Sci Total Environ* 2019**,** *690*, 410-416.

Dong, W.; Liang, L.; Brooks, S.; Southworth, G.; Gu, B., Roles of dissolved organic matter in the speciation of mercury and methylmercury in a contaminated ecosystem in Oak Ridge, Tennessee. *Environmental Chemistry - ENVIRON CHEM* 2010, *7*.

Liang, L.; Gu, B.; Brooks, S. C.; Miller, C. L.; He, F.; Elias, D.; Watson, D. B.; Peterson, M. J., Challenges and opportunities of mercury remediation in East Fork Poplar Creek, Oak Ridge, Tennessee (Invited). In *AGU Fall Meeting Abstracts*, 2010; Vol. 2010.

Eckley, C. S.; Gilmour, C. C.; Janssen, S. E.; Luxton, T. P.; Randall, P. M.; Whalin, L.; Carrie, A., The assessment and remediation of mercury contaminated sites: A review of current approaches. *Science of the Total Environment* 2020, *707*.

Gilmour, C. C.; Riedel, G. S.; Riedel, G.; Kwon, S.; Landis, R.; Brown, S. S.; Menzie, C. A.; Ghosh, U., Activated carbon mitigates mercury and methylmercury bioavailability in contaminated sediments. *Environ Sci Technol* 2013, *47* (22), 13001-10.

Gomez-Eyles, J. L.; Yupanqui, C.; Beckingham, B.; Riedel, G.; Gilmour, C.; Ghosh, U., Evaluation of biochars and activated carbons for in situ remediation of sediments impacted with organics, mercury, and methylmercury. *Environ Sci Technol* 2013**,** *47* (23), 13721-9.

Schwartz, G. E.; Sanders, J. P.; McBurney, A. M.; Brown, S. S.; Ghosh, U.; Gilmour, C. C., Impact of dissolved organic matter on mercury and methylmercury sorption to activated carbon in soils: implications for remediation. *Environ Sci Process Impacts* 2019**,** *21* (3), 485-496.

Wang, A. O.; Ptacek, C. J.; Blowes, D. W.; Finfrock, Y. Z.; Paktunc, D.; Mack, E. E., Use of hardwood and sulfurized-hardwood biochars as amendments to floodplain soil from South

River, VA, USA: Impacts of drying-rewetting on Hg removal. *Sci Total Environ* 2020**,** *712*, 136018.

Wang, A. O.; Ptacek, C. J.; Blowes, D. W.; Gibson, B. D.; Landis, R. C.; Dyer, J. A.; Ma, J., Application of hardwood biochar as a reactive capping mat to stabilize mercury derived from contaminated floodplain soil and riverbank sediments. *Sci Total Environ* 2019**,** *652*, 549-561.

Goñez-Rodríguez, L.; Johs, A.; Lowe, K. A.; Carter, K. E.; Löffler, F. E.; Mayes, M. A., Evaluation of engineered sorbents for the sorption of mercury from contaminated bank soils: a column study. *Environmental Science and Pollution Research* 2021**,** *28* (18), 22651-22663.

Lagergren, S., About the theory of so-called adsorption of soluble substances *Kungliga Svenska Vetenskapsakademiens, Handlingar* 1898**,** *24 (4)*, 1-39.

Blanchard, G.; Maunaye, M.; Martin, G., Removal of heavy metals from waters by means of natural zeolites. *Water Research* 1984**,** *18* (12), 1501-1507.

Weber Jr, W. J.; Morris, J. C., Kinetics of adsorption on carbon from solution. *Journal of the sanitary engineering division* 1963**,** *89* (2), 31-59.

Langmuir, I., The adsorption of gases on plane surfaces of glass, mica and platinum *Journal of the American Chemical Society* 1918**,** *40* (9), 1361-1403.

Freundlich, H. M. F., Uber die Adsorption in Losungen. *Zeitschrift für Physikalische Chemie* 1906, *57*, 385-470.

Schwarz, G., Estimating the dimension of a model. *The annals of statistics* 1978, 461-464.

Lima, É. C.; Adebayo, M. A.; Machado, F. M., Kinetic and Equilibrium Models of Adsorption. In *Carbon Nanomaterials as Adsorbents for Environmental and Biological Applications*, Springer International Publishing: 2015; pp 33-69.

CONFERENCE PARTICIPATION, PUBLICATIONS, AWARDS & ACADEMIC MILESTONES

Peer-reviewed Publications

Silvina A. Di Pietro, Hilary P. Emerson, Yelena Katsenovich, Timothy J. Johnson, Ryan M. Francis, Harris E. Mason, Maxwell Marple, April Sawvel, and James E. Szecsody. Solid phase characterization and transformation of illite mineral with gas-phase ammonia treatment, 2021. *Journal of Hazardous Material, in print*

Boglaienko, D., J. A. Soltis, R. K. Kukkadapu, V. E. Holfeltz, G. B. Hall, Y. Du,L. E. Sweet, E. C. Buck, C. U. Segre, H. P. Emerson, Y. Katsenovich, T. G. Levitskaia. Spontaneous Redox Continuum Reveals Sequestered Technetium Clusters and Retarded Mineral Transformation of Iron, July 2020. *Communications Chemistry– Nature*. DOI 10.1038/s42004-020-0334-x.

Boglaienko, D., O. Qafoku, R. K. Kukkadapu, L. Kovarik, Y. P. Katsenovich, D. E. Cherkasov, H. P. Emerson and T. G. Levitskaia. Elemental iron: reduction of pertechnetate in the presence of silica and periodicity of precipitated nano-structures. *Environ. Sci.: Nano*, 2021, 8, 97-109. DOI: 10.1039/D0EN00897D.

Di Pietro, S. A., H. P. Emerson, Y. Katsenovich, N. P. Qafoku, and J. E.Szecsody. Phyllosilicate mineral dissolution upon alkaline treatment under aerobic and anaerobic conditions, 2020. *Applied Clay Science, v.189, p.105520.*

Dickson, J., N. A. Conroy, Y. Xie, B. A. Powell, J. C. Seaman, M. I. Boyanov, K. M. Kemner, D. I. Kaplan. Surfactant-modified siliceous zeolite Y for pertechnetate remediation (2020). Chemical Engineering Journal, v. 402, p. 126268. doi.org/10.1016/j.cej.2020.126268.

Katsenovich, Y. P., R. Trimino Gort, R. Gudavalli, J. Szecsody, V. Freedman, and N. P. Qafoku. Silicon concentration and pH controls over competitive or simultaneous incorporation of iodate and chromate into calcium carbonate phases. *Applied Geochemistry* 128 (2021) 104941.

Looney, B. B., H. H. Vermeulen, T. L. White, A. J. Boggess, E. D. Fabricatore, T. B. Peters, and J. O. Dickson. Vapor-Liquid Partitioning of Methylmercury Compounds: Fundamental Data to Support the Savannah River Site Liquid Waste System. United States: N. p., 2021. Web. doi:10.2172/1804664.

Pagan, J., M. Pryor, R. Deepa, J. M. Grace III, O. Mbuya, R. Taylor, J. O. Dickson, V. Ibeanusi, Ashvini Chauhan, G. Chen, A. Anandhi. Sustainable Development Tool Using Meta-Analysis and DPSIR Framework — Application to Savannah River Basin, U.S. (2020). JAWRA (Journal of the American Water Resource Association). V. 56, p. 1059-1082. doi.org/10.1111/1752-1688.12872.

Publications Under Review:

Gonzalez-Raymat, H., Gudavalli, R., Denham, M., Cai, Y, and Y. Katsenovich. *In situ* sequestration of uranium from contaminated groundwater using a low-cost unrefined humic substance (In preparation).

Conference Presentations

The Project 2 team presented three posters and three oral presentations during the professional sessions of the 2021 Waste Management Symposia (WM2021), as well as four undergraduate student posters, and five graduate student posters. As the conference was held virtually, the team prepared and submitted pre-recorded videos for each of the poster and oral presentations.

Three oral presentations based on the Project 2 research were also delivered at 57th Annual Meeting of the Clay Mineral Society which was held virtually in Richland, WA.

Oral Presentations (presenter is underlined)

Alam, M. S., Zhou, Y., Yancoskie, A., Lawrence, A., Morales, J., Charles, S., Laogs, L., Looney, B. B., Seaman, J. *Sediment Transport Modeling Under Extreme Storm Events in the Tims Branch Testbed, Savannah River Site, SC – 21290.* WM2021 Conference Proceedings, March 7- 11, 2021 Virtual.

Di Pietro, S., Emerson, HP, Qafoku,N, and JE Szecsody. *Effects of Variable Redox Conditions and Alkaline Treatment in Phyllosilicate Minerals.* Presented at 57th Clay Mineral Society Conference held virtually in Richland, WA, October 18-23, 2020.

Kandel, S., Y. Katsenovich, R. M. Asmussen, A. K. Sockwell and R. Gudavalli. *Effect of Grout Impacted Water on the Glass Dissolution Behavior at Various Temperature.* Waste Management 2021 Virtual Conference, Phoenix, AZ, March 2021.

Katsenovich, Y., R. Trimino Gort (DOE Fellow), R. Gudavalli, N. P. Qafoku, J. Szecsody, V. Freedman, L. Lagos, October 2020. *Incorporation of Iodate in Calcium Carbonate at Variable pH and Si Concentrations.* Presentation for the 57th Annual Meeting of the Clay Mineral Society, Oct 18-23, 2020.

Sockwell, AK, F Zengotita, A Vento, D Reed, J Swanson, J Dickson, Y Katsenovich, and H Emerson. *Mobility of Actinides (+3, +4, and +6) in the Presence of Dolomite - Effect of EDTA and Ionic Strength.* Presented at 57th Clay Mineral Society Conference held virtually in Richland, WA, October 18-23, 2020.

Zhou, Y., Alam, M. S., Lawrence, A., Yancoskie, A., Morales, J., Laogs, L., Looney, B. B., Seaman, J. *Hydrologic Modeling and Storm Analysis for Technology Evaluation and Long-Term Monitoring in the Tims Branch Testbed – 21247.* WM2021 Conference Proceedings, March 7- 11, 2021 Virtual.

Poster Presentations (presenter is underlined)

Bustillo, O. (DOE Fellow), R. Gudavalli, L. Lagos. *Interaction of Hydroxyapatite and Uranium in Groundwater at the Old Rifle Site to Facilitate Site Remediation.* Waste Management 2021 Virtual Conference, Phoenix, AZ, March 2021.

Delarosa, K. (DOE Fellow), R. Gudavalli, Y. Katsenovich, P. Pham, L. Lagos. *Effect of modified-HA on the Sequestration of Uranium in acidic groundwater at the Savannah River Site.* Waste Management 2021 Virtual Conference, Phoenix, AZ, March 2021.

Di Pietro, S. A., (DOE Fellow), Y. Katsenovich, H. P. Emerson. *Illite Physicochemical Transformation upon NH3 Gas Treatment.* Waste Management 2021 Virtual Conference, Phoenix, AZ, March 2021.

Dickson, J., A. Vento, Y. Katsenovich, A. K. Sockwell, J. S. Swanson, D. T. Reed. *Organic Ligand Control on Mineral Stability in High Ionic Strength Matrices: Implication for Actinide Mobility In WIPP-relevant Environment.* Waste Management 2021 Virtual Conference, Phoenix, AZ, March 2021.

Doughman, M. (DOE Fellow), Y. Katsenovich, L. Lagos. *Competing Attenuation Processes for Mobile Contaminants in Hanford Sediments.* Waste Management 2021 Virtual Conference, Phoenix, AZ, March 2021.

Doughman, M. (DOE Fellow), Y. Katsenovich, L. Lagos, K. O'Shea. "*Competing Attenuation Processes for Mobile Contaminants in Hanford Sediments*". ACS Fall 2021 Meeting, Atlanta, GA, August 22-26, 2021 (Virtual).

Gudavalli, R., K. De La Rosa, P. Pham, H. Gonzalez Raymat, B. Looney, Y. Katsenovich, L. Lagos. *Low Cost Humate as an Amendment for Uranium Remediation.* Waste Management 2021 Virtual Conference, Phoenix, AZ, March 2021.

Guiterrez, G., and Zhou, Y.. *Comparison of Vegetation Filtering Methods for UAV-Based Photogrammetry to Generate High-Res Bare-Surface DEM Near the WIPP Land Withdrawal Act (LWA) Boundary, New Mexico.* WM2021 Conference, March 7- 11, 2021 Virtual. [Student poster].

Katsenovich, Y., R. Trimino Gort, R. Gudavalli, N. P. Qafoku, J. Szecsody, V. Freedman, L. Lagos. *Incorporation of Iodate and Chromate in Calcium Carbonate Phases at Variable pH and Si Concentrations.* Waste Management 2021 Virtual Conference, Phoenix, AZ, March 2021.

Morales, J., Bramer, L., Lagos, L., and K. Waters. *Investigation of Heavy Metal Biomarkers for the Assessment of Remediated Surface Waters*. WM2021 Conference, March 7- 11, 2021 Virtual. [Student poster].

Pham, P. (DOE Fellow), R. Gudavalli. *Characterization of KW-15 modified humic acid - a potential in-situ technology for uranium remediation at the SRS.* Waste Management 2021 Virtual Conference, Phoenix, AZ, March 2021.

Stevens, C., Alam, M., Zhou, Y., Lawrence, A., Looney, B. and J. Seaman. *A Modeling Exercise to Examine the Variation in Sediment Transport Process Under Different Erosion and Precipitation Criteria at Steed Pond, Tims Branch Watershed, Savannah River Site, SC.* WM2021 Conference, March 7- 11, 2021 Virtual. [Student poster].

Tuya, N. (DOE Fellow), R. Gudavalli, H. Gonzalez-Raymat, L. Lagos. *Influence of Environmental Factors on Iodine Attenuation and Release in Savannah River Site Wetlands Sediments.* Waste Management 2021 Virtual Conference, Phoenix, AZ, March 2021.

Vento, A. (DOE Fellow), J. Dickson, Y. Katsenovich. *Investigation and analysis of dolomite dissolution in variable ionic-strength systems relevant to the WIPP.* Waste Management 2021 Virtual Conference, Phoenix, AZ, March 2021.

Academic Milestones

Silvina Di Pietro (DOE Fellow) succesfully defended her PhD thesis “Uranium Fate and Mineral Transformations upon Remediation with Ammonia (NH_3) Gas” and graduated with the PhD degree in chemistry in Fall 2021.

DOE Fellow Mariah Doughman graduated with M.S. Degree in chemistry in Spring 2021 and continued to pursue Ph.D. in chemistry at FIU.

Alexis Vento (DOE Fellow) succesfully defended his M.S. thesis “Dolomite Dissolution and Contaminant Adsorption in the Presence of EDTA in Different Ionic Strength Solutions” and graduated with MS degree in Environmental Engineering in Summer 2021.

Jonathan Williams succesfully defended his M.S. thesis “Competitive Reductive Removal of Cr(IV) and Tc(VII) via Zero Valent Iron” and graduated with M.S. degree in biomedical engineering in Spring 2021.

Amanda Yancoskie (DOE Fellow) graduated with M.S. degree in environmental engineering in Fall 2021.

DOE Fellows Nathalie Tuya and Katherine De La Rosa graduated with B.S. degree in environmental engineering in Spring 2021.

ACKNOWLEDGEMENTS

Funding for this research was provided by U.S. DOE Cooperative Agreement #DE-EM0005213. FIU’s Applied Research Center would like to acknowledge the commitment of DOE-EM to this specific Environmental Remediation Science and Technology project and to all the collaborators at DOE-EM HQ and the National Labs for support of the research being conducted as part of the Cooperative Agreement. The partnership between DOE EM and FIU has also resulted in the development and training of outstanding minority STEM students that will benefit this country as a whole.

FIU also gratefully acknowledges Thomas Beasley from FIU FCAEM facilities for his assistance with the SEM/EDS analyses.

APPENDIX

The following documents are available at the DOE Research website for the Cooperative Agreement between the U.S. Department of Energy Office of Environmental Management and the Applied Research Center at Florida International University: https://doeresearch.fiu.edu

FIU Year 1 Annual Research Review Presentations:

1. FIU Research Review - Project 1
2. FIU Research Review - Project 2
3. FIU Research Review - Project 3 – D&D
4. FIU Research Review - Project 3 – IT ML
5. FIU Research Review - Project 4 & 5
6. FIU Research Review - Project 4 - DOE Fellow Aurelien Meray
7. FIU Research Review - Project 4 - DOE Fellow Gisselle Gutierrez
8. FIU Research Review - Project 4 - DOE Fellow Jeff Natividad
9. FIU Research Review - Project 4 - DOE Fellow Mariah Doughman
10. FIU Research Review - Project 4 - DOE Fellow Philip Moore
11. FIU Research Review - Project 4 - DOE Fellow Sebastian Story
12. FIU Research Review - Project 5 - DOE Fellow Eduardo Rojas
13. FIU Research Review - Project 5 - DOE Fellow Olivia Bustillo
14. FIU Research Review - Wrap Up - Project 1
15. FIU Research Review - Wrap Up - Project 2
16. FIU Research Review - Wrap Up - Project 3 – D&D
17. FIU Research Review - Wrap Up - Project 3 – IT ML
18. FIU Research Review - Wrap Up - Project 4
19. FIU Research Review - Wrap Up - Project 5